Topology Optimization of Elastoplastic Structures

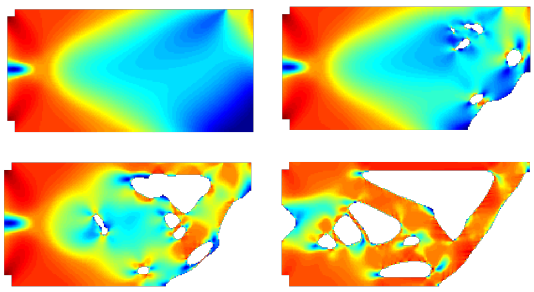

Mengxiao LI

School of Engineering and the Built Environment

Edinburgh Napier University

Thesis submitted in partial fulfilment of the requirements of Edinburgh Napier University, for the award of

Doctor of Philosophy

January 2019

Abstract

Topology optimization technique has been used as an efficient tool that optimizes material layout within a given space to obtain the desired functional performance. So far, topology optimization has been mainly focused on linear problems and less attention has been paid on nonliear design, although accounting for the material nonliearity can significantly influence the optimized structure layout.

Research studies undertaken in this thesis considered material elastoplasity in combination with the SIMP based topology optimization method, particularly for two-phase structure in which different plastic material model is adopted for each phase. This expands the optimization scope in nonliear design in further applications.

Since the structural nested framework that nonliear analysis is repeatedly solved for every updated topology, is very computationally expensive. This research also proposed to apply the transient coupled nonliear system to BESO method for nonliear structural design, as a result, a stable topological evolution was achieved, and results converged after a much smaller number of iterations.

In addition, this research originally proposed a topology optimization method for plastic strain minimization design, to accommodate the diverse design purpose. By means of several examples of equivalent plastic strain minimization, in comparison with the results obtained from the elastic stiffness-based design, elastoplastic stiffness-based design, it is revealed that materials are much more efficiently used, and the plastic strain and von Mises stress are more evenly distributed within the design domain.

Acknowledgements

This thesis is submitted in partial fulfillment of requirements for achieving the degree of Ph.D at the Edinburgh Napier University. Supervisors were Dr. Johnson Zhang (director of study), Dr. Khokhar Aamir (supervisor), Dr.Barreto Gonzalez Daniel (additional adviser) and Dr.Binnie, David (Independent panel member) from the School of Engineering and the Built Environment.

I would first appreciate the fully funded scholarship provided by the Edinburgh Napier University during the period January 5^{th} 2015 - January 5^{th} 2018. Many thanks to my supervisors for their helpful suggestions throughout the work on this thesis. I am really grateful to Johnson again for his invaluable discussion and endless support to help me out with challenges encountered in both academic and non-academic fields. Also, thanks to Ian Smith from Ian Smith Geotech Ltd who recommended me at the early Ph.D application. Finally, I would like to thank my family for their love, trust, and support.

Contents

List of Figures

List of Tables

1

Introduction

1.1 Structural type

1.1.1 Composite structure

Composite structure has drawn a wide attention from both research and design communities in various areas such as structural engineering and aerospace fields due to the diverse design purpose and increasingly high demand on mechanical characteristic and weight savings. In other words, materials constituting the composites can be placed easily into a free-form combination to achieve a specific and more desirable design, e.g. increase in strength, toughness, erosion resistance and anti-fatigue ability compared to using single materials. Currently, a two-phase composite in which one of the materials as a reinforcing part embedded into the other material matrix in the form of strips, sheet, or grids, has become attractive for many practical applications. The material candidates for both phases can be steel, aluminium, polymer, wood or concrete, etc. Therefore, a concurrent need of distributing materials of composites efficiently arises to maximize contribution of each material.

1.1.2 Discontinued or disturbed structure

Structural concrete domain can be categorized into two regions: B (Bernoulli or Beam) - regions where plane-section assumptions apply, and D (Disturbed or

Discontinuity)-regions which are defined by parts of a structure with nonlinear strain distribution due to sharp geometrical changes in structures. The approach for B-region design is maturely established and can be easily achieved by beam or Bernoulli theory and cross-sectional analysis. While in the structural design for D-region, traditional approaches for slender beams are appropriate. The failure mode in such structure is normally presented as shear failure rather than flexural failure. Therefore, achieving a proper analysis and design for disturbed members in concrete structures such as pile caps, deep beams, transfer thick plates, corbels, structural members with opening holes, and beam-column joints has been a challenge for decades. A typical illustration of B-region and D-region in structures are shown in Fig.1.1.

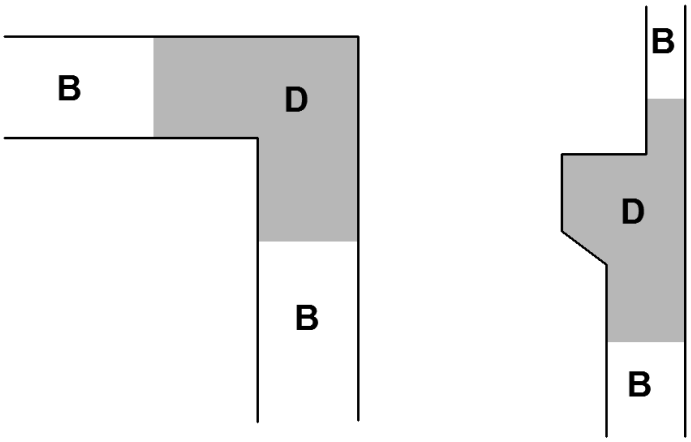

Figure 1.1: B and D-region in structural members

In this thesis, the optimized design of composite structure (e.g, reinforced concrete structure) takes the material elastoplasticity of each candidate into account. Also, the design for deep beams, beam with openings or L-shape brackets are used to produce optimization benchmarks.

1.2 Structural optimization technique

Structural optimization aims to achieve the best performance for a structure under loading conditions, while satisfying various constraints such as geometrical

or mechanical constraints. To describe the "best", weight, cost, stiffness, stress, displacement or critical load, etc., can be set up as objective functions to be minimized or maximized. Also, these measures can be formulated as constraints within an optimization problem. The design parameters generally required in the structural optimization problem statement are presented as follows [1]:

- Objective function (f): A function that is used to classify designs. For every possible design, f returns a number which indicates the goodness of the design. Usually, f measures mean compliance, material quantity, displacement in a given direction, effective stress or cost of production.

- Design variable ($\mathbf{x}$): A vector that describes the design, and which can be updated during optimization procedure. It may represent geometry or choice of material. When it describes geometry, it may relate to a sophisticated interpolation of shape or it may simply be the area of a bar, or the thickness of a sheet. For a density-based optimization, the design variable is generally assigned with material density.

- State variable ($\mathbf{y}$): A function or vector that represents the response of the structure. For a mechanical structure, response means displacement, stress, strain or force, etc.

As can be seen, there are two sets of variables: design variables $\mathbf{x}$ and state variables $\mathbf{y}$, which are coupled via a state equation, e.g., finite element equation in an elastic condition: $\mathbf{K}(\mathbf{x})\mathbf{U} = \mathbf{F}$, that for given values of the design variables give values of the state variables.

The following shows an example of optimization problem statement where a specified objective function f with respect the design variable $\mathbf{x}$ and the state variable $\mathbf{y}$ is formulated and multiple constraints are considered, i.e. behaviour constraints, design constraints, and equilibrium constraints (FE (finite element)

state equation) as

$$\begin{aligned} \min \quad & f(\mathbf{x}, \mathbf{y}) \\ s.t. \quad & \sum_{e=1}^{N_{ele}} v_e x_e \leq v^* \\ & g_i(\mathbf{x}, \mathbf{y}) \leq g_i^*, \quad (i = 1, 2, ..., M) \\ & x_{\min} \leq x_e \leq x_{\max}, \quad (e = 1, 2, ..., N_{ele}) \\ & \mathbf{K}(\mathbf{x})\mathbf{U} = \mathbf{F} \end{aligned} \tag{1.1}$$

where x_e depicts the design variable for every element; v^* is the prescribed target volume fraction of the design domain; g_i illustrates the i^{th} behaviour constraint and M is the total number of constrains. $\mathbf{K}(\mathbf{x})$ represents the global stiffness matrix with respect to design variable $\mathbf{x}$; $\mathbf{U}$ is the global displacement vector taking the role of the state variable $\mathbf{y}$; and $\mathbf{F}$ denotes the external load vector applied on the structure.

In terms of the geometrical optimization problem of mechanical structures, there are mainly three categories of design variables: sizing variables, shape variables and topology variables. A brief introduction of the corresponding optimization methods subject to various type of design variables is given in the following subsections.

1.2.1 size optimization

Size optimization is the earliest method to improve the structural behaviour and save the amount of material used by varying the size variable, i.e., cross sectional area of the truss element or the thickness of the plate. A size optimization example is shown in Fig.1.2.

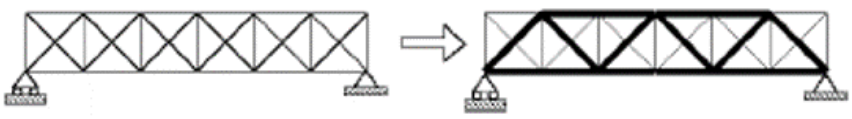

Figure 1.2: Size optimization of a truss structure [1]

1.2.2 shape optimization

In this optimization case, the design variable represents the form or contour of the predefined geometrical boundaries, while the connectivity of the structure is not changed through shape optimization. A shape optimization problem performed on a continuous structure is presented in Fig.1.3. Good examples of size

Figure 1.3: Shape optimization of a continuous structure [1]

optimization and shape optimization can be found in Christensen et al.[1].

1.2.3 Topology optimization

Topology optimization has been used widely in mechanical components such as wing designs and has become an extremely active research area in recent decades and been applied to many other design fields such as structural engineering [5]. For discrete structures such as trusses or frames, the topology optimization method is applied to find the optimised connectivity of nodes. For continuous structures, the topology optimization method is utilized to design the optimised location and geometry of cavities in the design domain. Fig.1.4 shows a topology optimization problem of a two-dimensional continuous structure. Other examples of this type of optimization can be reviewed in previous summary works [1, 6]. The art of structural (topological) optimization is to determine where to locate

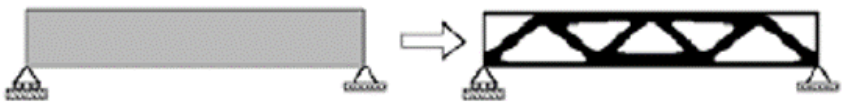

Figure 1.4: Topology optimization of a continuous structure [1]

structural cavities as referred by Robert Le Ricolai. In comparison with other types of structural optimization approach, topology optimization technique provides more flexibility for designers to create a completely novel concept design,

especially for a continuous structure. The only required quantities in the problem are the applied loads, the possible support conditions, the volume of the structure to be constructed and possibly some additional design constraints such as the location and size of prescribed cavities or solid areas. Using this method, the detailed physical size and the shape and connectivity of the structure are not required to be estimated before design [6].

1.3 Overview of topology optimization approach

As mentioned in Section 1.2.3, topology optimization methods are generally classified into discrete and the continuous, depending on the structural form. The former one is mainly based on the ground structure approach [7]. And various methods are developed to solve the ground structure problem using either direct approaches (e.g. mathematical programming algorithms), or indirect approaches (e.g. optimality criteria algorithms). Here, the present review of this research focuses on topology optimization of continuous structures. Four approaches are generally considered: homogenization method, continuous density-based optimization method, evolutionary optimization technique (discrete density-based optimization method), and level set approach. They are introduced in section 1.3.1, section 1.3.2, section 1.3.3 and section 1.3.4, respectively. In this research thesis, the density-based topology optimization method and the evolutionary optimization technique are used as the basis of methodology.

1.3.1 Homogenization method

Numerical methods for topology optimization of continuous structures have undergone an active development since the landmark paper [2]. They proposed the homogenization method where the design domain can be divided into finite cell, and each cell consists of an individual micro-structure. Thus, the method of homogenization enables to compute the optimal distribution of such a composite material in a given domain. An example of a structure with composite microstructure is presented in Fig.1.5.

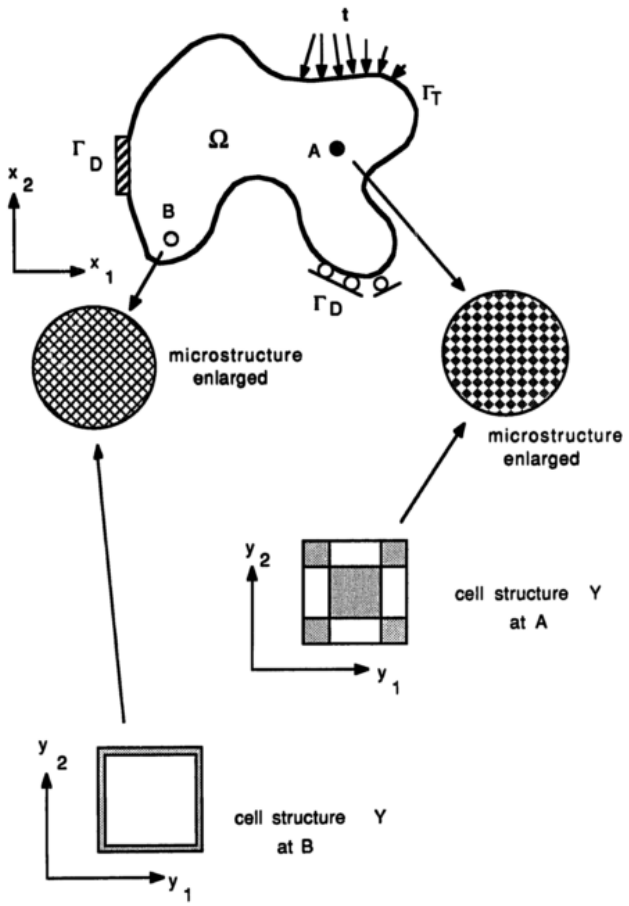

Figure 1.5: A structure with composite microstructure [2]

However, due to its relatively large amount of design variables, complicated sensitivity analysis, and essential post-processing penalization phase transferring the individual microstructure into a continuous solid layout, its use is limited in practical engineering applications.

1.3.2 Density-based optimization method

Soon after the introduction of homogenization method, the so-called SIMP (Simplified Isotropic Material with Penalization) was suggested by Bendsoe [8] and others [9, 10]. Originally, it was introduced to minimize the complexity of the homogenization approach and improve the convergence to solid-void solutions. Later, a physical justification of SIMP was proposed in Bendsoe and Sigmund et al [11]. In this approach, the solid isotropic design domain is discretized into finite elements with density value from 0 (void) to 1 (solid). However, the void material is generally treated as a very soft material, with design variable equal to 0.001, to reduce the singularity phenomenon. Thus, the continuous design variables are interpreted as material densities, and a power-law is used to penalize the initial material properties, which is given as follows:

$$E(\rho_e) = \rho_e^p E_0 \tag{1.2}$$

where E_0 is the material initial Young's modulus, ρ_e is the elemental material density, and p represents the penalization parameter. When $p = 1$, the so-called variable-thickness-sheet problem appears, in which the design domain covers the whole range of material values from 0 to 1. Hence, in order to generate a solid-and-void layout for continuous structure, the penalization value p is normally over 1 to penalize the intermediate density. The SIMP model also names penalized or proportional fictitious material model. It is found that set up the value of p too low or too high either causes too much grey scale or too fast convergence to local minima. The value that guarantee a good convergence to almost 0-1 solutions is $p = 3$ [12].

1.3.3 Evolutionary optimization technique

Opposite to the homogenization and SIMP method having a mathematical basis, the evolutionary structural optimization (ESO) belongs to the heuristic-based optimization methods. From an engineering point of view, this approach is attractive due to its simple concept of removing low efficient material from a structure. It is relatively easier to integrate with finite element analysis.

In terms of the heuristic-based optimization method, it is initially based on the fully stressed design principle that a small portion of the material within the structural domain will be eliminated due to low stress value. ESO is firstly proposed by Xie and Steven [13, 14], and later, Querin et al.[15] presented an additive evolutionary structural optimization method (AESO) where the initial design domain is defined based on the minimum possible load transfering route. At the beginning, the structure is overly stressed, then material is added to reduce the localised high stresses. The deficiencies of the conventional ESO method is that removed elements cannot be reintroduced in the subsequent iteration even if they are considered rewarding. Therefore, the bi-directional evolutionary structural optimization method (BESO) [16] is developed with the capability of allowing elements to be removed and added simultaneously.

In the early BESO method, the number of elements to be removed and added in each iteration is determined separately with a rejection ratio (RR) and an inclusion ratio (IR) respectively. However, due to the fact that selecting values of RR and IR is subjective, ranking elements for removing and reintroducing separately is illogical, and the number of optimizing iterations is significantly high, the BESO has undergone further development. Huang and Xie et al. [17] utilize a standard adjoint gradient-based analysis and a filtering scheme to obtain more reliable results and topologies, which is regarded as a similar strategy as that is adopted in the SIMP density approach. In comparison with SIMP, the design variables representing the corresponding material densities in the design domain are discrete (0 or 1) rather than continuous (from 0 to 1). Therefore, the modified BESO approach can also be considered as a discrete density-based optimization method. The BESO method is further developed to address the issues of building

up a proper statement of the optimization problem, checkerboard pattern, mesh-dependency and convergence of solution [18]. Its advantage of achieving a discrete "black and white" layout without existence of gray area is attractive, however, it is difficult to solve the optimization design with multiple constraints due to lack of mathematical theory support.

1.3.4 level set approach

Level set (LS) method, also regarded as an evolutionary approach, is developed to track the motion of the structural boundaries under a speed function and in the presence of potential topological changes. In the LS approach [3, 19, 20, 21], the boundary of the design is defined by the zero level contour of the level set function and the structure is defined by the domain where the level set function takes positive values. Fig.1.6 shows a LS optimization design problem of a two-bar structure, that starts from a full design domain (left) and from an initial domain with a single hole (right).

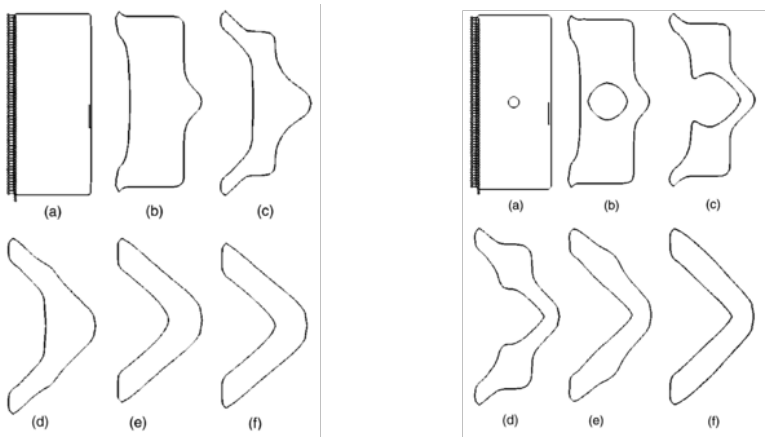

Figure 1.6: Results of the iteration in the level set optimization for a two-bar example [3]

Note that the LS method mainly focus on structural boundary design and apply to problems of structural optimization involving multi-physics and/or multi-domains. Hence, its main advantage does not benefit the purpose of this research of achieving an optimized material distribution in a given single or multiphase

structure. Moreover, as discussed in Section 1.3.1, the homogenization method usually produce not manufacturable structure. Therefore, based on the literature review, most of the research works use density-based or evolutionary topology optimization method for structural layout design.

1.4 Structural analysis

According to the description about structural optimization formulation provided in section 1.2, the objective function is generally followed by inequality constraints. The response obtained from the structural analysis of the design domain (assigned with any value of design variables) can be formulated as equality constraints, which are used in the optimization procedure. Therefore, the structural optimization design algorithm can be regarded as a nested framework, in which the structural analysis is nested in the optimization procedure and is repeatedly solved for every updated topology.

The finite element analysis (FEM) is the most prominent numerical technique to perform structural analysis of any given physical phenomenon. FEM method is developed to solve complicated partial differential equations (PDEs) in approximate sense, which is opposite to find exact solution that satisfy both governing equations at all points of area of interest and boundary conditions, e.g. finite difference method (FDM). Nowadays, FEM method is widely used in the modelling and analysis of many mechanical applications related to civil engineering field. It is able to replace the single complicated shape with an approximately equivalent network of simple elements, namely the finite element mesh. The type of element can be one-dimensional rods, two-dimensional triangles or quadrilaterals, or three-dimensional blocks. The accuracy of calculation is considerably influenced by the mesh condition, which means that larger amount of elements and smaller size of element to be used would result in more accurate results. However, a computational cost may arise from finer mesh. The elemental stiffness matrix is calculated based on the shape function and then combined into a global matrix representing the stiffness of the whole system using a merging technique in a reduction process. Afterwards, the equilibrium equations on nodal points and

governing equations of stress-strain relationship is solved to obtain the structural response. A typical FEA process is given as follows:

1. Define design domain and mesh condition.
2. Set up material properties.
3. Apply boundary conditions and loads.
4. Solve the boundary value problem.
5. Output results (e.g. displacement, stress, strain, natural frequency, etc.)

The structural analysis can be divided into three main categories: linear static analysis, nonlinear static analysis and dynamic analysis. A brief introduction of both linear and nonlinear system at a static state are given in the following Section 1.4.1 and Section 1.4.2, respectively.

1.4.1 Linear structural analysis

With a given external load, the internal force is generated for resisting any deformation to achieve the equilibrium of the two forces. Generally, for elastic structure, a force-displacement relationship is linear where the deformation is proportional to the loading, and the structure return back to its initial position on unloading. The algebraic set of equation to be solved in the finite element analysis is expressed as

$$\mathbf{KU} = \mathbf{F} \tag{1.3}$$

where $\mathbf{K}$ is the global stiffness matrix; $\mathbf{U}$ is the nodal displacement vector, and $\mathbf{F}$ is the external load vector. Upon imposing the geometrical boundary condition, Eq.(1.3) is solved for the unknown displacement vector. In linear FEM analysis, for a 2D design problem with acceptable mesh condition, the computational cost of solving this equation is generally rapid, especially by taking the advantage of stiffness matrix which is symmetric, sparse and can be stored in a compact manner. The force vector, as well as the unknown displacement vector, is stored in one-dimensional array of length equal to the number of degrees of freedom.

In linear elastic optimization design problem, Eq.(1.3) can be regarded as an equality constraint, producing structural response that are used to evaluate the objective and the constraint in the optimization procedure.

1.4.2 Nonlinear structural analysis

In the linear analysis, structures return to their original form, and there are no changes in loading direction and magnitude and material properties remain the same. However, nonlinear analysis is required when material deformation is partially irreversible or geometry changes resulting in stiffness changes is assumed. Generally, structural nonlinearity may be caused by nonlinear material, nonlinear deformations on displacements, nonlinear boundary condition and nonlinear loading condition. Since this thesis focus on topology optimization design of structures considering more realistic material property, the structural analysis procedure associated with material nonlinearity is mainly discussed herein.

1.4.2.1 Classical material elastoplasticity model

For one-dimensional (1D) structural elements, such as steel bars or trusses, the stress-strain relation is easily obtained through the uniaxial tension test. While for multidimensional elements, stress is a tensor with up to six components. Thus, an equivalent stress/strain ratio is developed to present the multidimensional stress/strain state.

In the year of 1864, due to most material fail by shear deformation, Tresca proposed to use the maximum shear stress criterion as the material failure criterion. As known that deformation consists of dilatation and distortion changes, and plastic deformation is related to the distortion part of the total strain, which is so called the deviatoric strain. For pure shear deformation, shear strain is the only nonzero strain component that is equivalent to the deviatoric strain. While, for those deviatoric strain having nonzero volumetric (normal) strain, it is difficult to use the deviatoric strain or stress as the yield criterion as it is not a scalar. Thus, the distortion energy criterion is developed as its nature of scalar quantity, and is defined by removing the volumetric part from the strain energy.

The deviatoric stress is defined as

$$\mathbf{s} = \boldsymbol{\sigma} - \sigma_m \mathbf{1} = \mathbf{I}_{dev} : \boldsymbol{\sigma} \tag{1.4}$$

with

$$\sigma_m = \frac{1}{3}(\sigma_{11} + \sigma_{22} + \sigma_{33}) \tag{1.5}$$

$$\begin{aligned} &\mathbf{1} = [\delta_{ij}] \\ &I_{ijkl} = (\delta_{ik}\delta_{jl} + \delta_{il}\delta_{jk})/2 \\ &\mathbf{I}_{dev} = \mathbf{I} - \frac{1}{3}\mathbf{1} \otimes \mathbf{1} \end{aligned} \tag{1.6}$$

where σ_m is the mean stress; $\mathbf{1}$ is the second-order unit tensor and $\mathbf{I}$ is the fourth-order unit symmetric tensor. The von Mises yield criterion is developed based on the distortion energy theory to state that material yields when the equivalent stress σ_e reaches the yield stress σ_y obtained from the uniaxial tensile test. The equivalent stress can be expressed as follows:

$$\begin{aligned} &\sigma_e = \sqrt{3J_2} \\ &J_2 = \frac{1}{2}\mathbf{s} : \mathbf{s} = \frac{1}{6}[(\sigma_{xx} - \sigma_{yy})^2 + (\sigma_{yy} - \sigma_{zz})^2 + (\sigma_{zz} - \sigma_{xx})^2] + \tau_{xy}^2 + \tau_{yz}^2 + \tau_{xz}^2 \end{aligned} \tag{1.7}$$

where J_2 is the second invariant of the deviatoric stress. The von Mises yield criterion is given by

$$f = ||\mathbf{s}|| - \sqrt{\frac{2}{3}}\sigma_y \tag{1.8}$$

with

$$||\mathbf{s}|| = (\mathbf{s} : \mathbf{s})^{\frac{1}{2}} \tag{1.9}$$

In this thesis, Drucker-Prager yielding criterion is also considered to perform pressure dependent materials such as concrete or soil. It is achieved by adding a hydrostatic term, and the details are presented in Chapter 4.

Eq.(1.8) presents the material with constant yielding stress, which is called elastic perfectly plastic, while for some materials, the yielding stress itself varies following the evolution of plastic deformation. A simplified plot describing the post yielding behaviors is presented in Fig.1.7, and two types of hardening model are given in Fig.1.8.

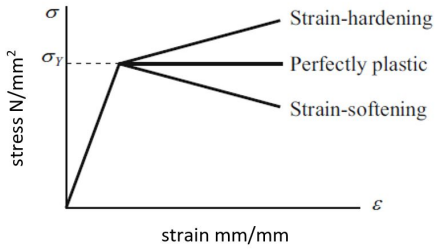

Figure 1.7: Post-yielding behaviors of material [4]

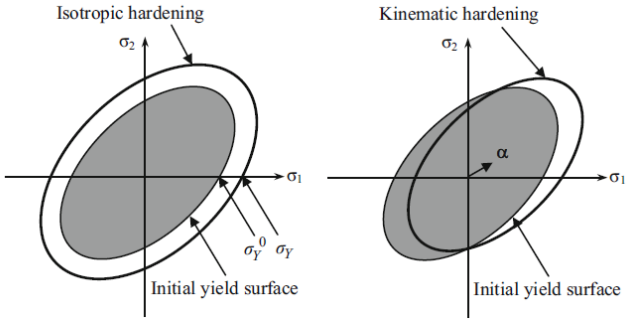

Figure 1.8: Hardening rules in two dimension [4]

In the isotropic hardening, the yield surface continuously develop based on the plastic deformation, while it remains constant but moves parallel with the hardening line for the kinematic hardening. Moreover, many materials show a combined behavior of isotropic and kinematic hardening, i.e., the yield stress grows and the yield surface moves simultaneously following the plastic response. For a material associated with a combined hardening rule, the yield surface is further defined as

$$f = ||\boldsymbol{\eta}|| - \sqrt{\frac{2}{3}}[\sigma_y^0 + (1-\phi)He_p] = 0 \tag{1.10}$$

with

$$\begin{aligned} \boldsymbol{\eta} &= \mathbf{s} - \mathbf{a} \\ \mathbf{a} &= \sqrt{\frac{2}{3}}\phi He_p \frac{\boldsymbol{\eta}}{||\boldsymbol{\eta}||} \end{aligned} \tag{1.11}$$

where $\boldsymbol{\eta}$ is the shifted stress; $\boldsymbol{a}$ is the back stress; σ_y^0 is the initial yield stress; ϕ is a parameter stating the combined effect (so called the Bauschinger effect) in

the range between 0 and 1. When ϕ equals to 0, the material corresponds to the isotropic hardening and 1 for the kinematic hardening.

Small deformation elastoplasticity is assumed that the total strain and strain rate can be decomposed into elastic and plastic parts as

$$\begin{aligned} \boldsymbol{\epsilon} &= \boldsymbol{\epsilon_e} + \boldsymbol{\epsilon_p} \\ \dot{\boldsymbol{\epsilon}} &= \dot{\boldsymbol{\epsilon_e}} + \dot{\boldsymbol{\epsilon_p}} \end{aligned} \tag{1.12}$$

The stress is associated with the elastic strain by a forth-order constitutive tensor $\mathbf{D}$, thus the rate form can be formulated as

$$\begin{aligned} \dot{\boldsymbol{\sigma}} &= \mathbf{D} : \dot{\boldsymbol{\epsilon_e}} \\ &= (\lambda + \frac{2}{3}\mu)(tr(\dot{\boldsymbol{\epsilon}}) - tr(\dot{\boldsymbol{\epsilon_p}}))\mathbf{1} + 2\mu\mathbf{I}_{dev} : (\dot{\boldsymbol{\epsilon}} - \dot{\boldsymbol{\epsilon_p}}) \\ &= (3\lambda + 2\mu)\dot{\epsilon_m} + 2\mu(\dot{\mathbf{e}} - \dot{\mathbf{e_p}}) \end{aligned} \tag{1.13}$$

with

$$\begin{aligned} &\mathbf{D} = (\lambda + \frac{2}{3}\mu)\mathbf{1} \otimes \mathbf{1} + 2\mu\mathbf{I}_{dev} \\ &\mathbf{1} : \dot{\boldsymbol{\epsilon}} = tr(\dot{\boldsymbol{\epsilon}}) = 3\dot{\epsilon_m} \\ &tr(\dot{\boldsymbol{\epsilon_p}}) = 0 \end{aligned} \tag{1.14}$$

where λ and μ are the lame's constant, $\mathbf{e}$ and $\mathbf{e_p}$ are the deviatoric strain and deviatoric plastic strain tensor. More specifically, the volumetric and deviatoric part of the stress can be further expressed as

$$\begin{aligned} \dot{\sigma_m} &= (3\lambda + 2\mu)\dot{\epsilon_m} \\ \dot{\mathbf{s}} &= 2\mu(\dot{\mathbf{e}} - \dot{\mathbf{e_p}}) \end{aligned} \tag{1.15}$$

It can be found that the volumetric stress is independent of plastic deformation, which is consistent with the fact that the yield function is defined using the deviatoric stress alone. In order to obtain the elastic strain, plastic strain is determined by

$$\dot{\boldsymbol{\epsilon_p}} = \gamma\frac{\partial g}{\partial \boldsymbol{\sigma}} \tag{1.16}$$

where g is the flow potential, which is associated with the yield function in this thesis. And the parameter γ is known as plastic consistency multiplier. The

Kuhn-Tucker condition as stated in Eq.(1.17) should be satisfied.

$$\begin{aligned} \dot{\lambda} &\geq 0 \\ f &\leq 0 \\ \dot{\lambda} f &= 0 \end{aligned} \tag{1.17}$$

When the material stay at the elastic state, the corresponding yield function $f < 0$ and there is no plastic deformation ($\gamma = 0$). While in the plastic state where the value of γ is positive, the stress on the yield surface $f = 0$. When the state varies, four possible situations may occur

1. Elastic loading $\dot{\gamma} = 0$, $f < 0$, and $\dot{f} < 0$
2. Elastic unloading just after yielding $\dot{\gamma} = 0$, $f = 0$, and $\dot{f} < 0$
3. Neutral loading $\dot{\gamma} = 0$, $f = 0$, and $\dot{f} = 0$
4. Plastic loading $\dot{\gamma} > 0$, $f = 0$, and $\dot{f} = 0$

1.4.2.2 Numerical integration

The FEM analysis for elastoplastic material is performed within an iteratively incremental scheme that include the increment part and the iteration part. The full loading force or displacement is divided into finite incremental steps, and in static problem, the time increment can be regarded being consistent with the load increment. In the displacement-controlled analysis, the displacement at a certain time is prescribed, while in the force-controlled method, force is known and the corresponding displacement is obtained by an assumption of elastic force-displacement relationship at the initial stage. And then, the strain increment on a local level is computed. The stress, internal plastic variables at every integration point are calculated and corrected until the internal force is infinitely approaching to the external force.

Assuming the state variables, i.e. stress, plastic variables, are known at time t_n, the updated value at time t_{n+1} is an internal procedure based on the given strain increments. Here, the return-mapping algorithm is introduced, which consists of two steps. Firstly, a trial stress is calculated by assuming the incremental

strain from time t_n to time t_{n+1} is purely elastic. According to the Kuhn-Tucker condition, when the trial value of yield function $f^{trial} < 0$, the plastic multiplier $\dot{\gamma} = 0$. This means the trial stress is within the elastic domain, and other state variables are updated equal to the predicted trial values. However, when the trial value of yield function $f^{trial} > 0$, plastic deformation occurs ($\dot{\gamma} > 0$) and the yield function at time t_{n+1} must equal to 0 ($f^{n+1} = 0$). This is the second step of projecting the trial stress onto the yield surface. The detailed return-mapping algorithm is given in Chapter 4 based on the specified material elastoplasticity.

1.4.2.3 Solution to nonlinear equilibrium

Once the internal structural response, i.e., stress, strain or plastic variables, are determined, they can be used to solve the nonlinear equilibrium equation. The internal energy can be expressed as

$$W = \int\int_{\Omega} \boldsymbol{\epsilon}(\mathbf{u})^T \boldsymbol{\sigma} d\Omega = \mathbf{u}^T \int\int_{\Omega} B^T \boldsymbol{\sigma} d\Omega = \mathbf{u}^T \sum_{i=1}^{N} (\mathbf{B}^T \boldsymbol{\sigma} \mathbf{J})_i w_i = \mathbf{u}^T \mathbf{f}_{int} \quad (1.18)$$

where i represents the integration point, N is the total number of integration points, $\mathbf{J}$ is the Jacobian between the physical and reference elements, w is integration weight, $\mathbf{u}$ is the nodal displacement vector, and $\mathbf{f}^{int}$ is the internal force vector. The residual representing the equilibrium btween the external and internal force can be written as

$$\mathbf{R} = \mathbf{f}_{ext} - \mathbf{f}_{int}(\mathbf{u}) = 0 \quad (1.19)$$

The external load applied to the structure is assumed to be independent of deformation, whereas the internal force depends on the displacement in a nonlinear form. Generally, an iterative method of Newton-Raphson method is used to solve nonlinear equilibrium.

$$\mathbf{K}\Delta\mathbf{u} = \mathbf{R} \quad (1.20)$$

The evaluation of displacement increment is updated iteratively until the residual is less than a tolerance value. When the tangent stiffness matrix $\mathbf{K}$ obtained in the first iteration is repeatedly used in the following iteration, this is so called as Modified Newton-Raphson method, which less effort made on factorizing $\mathbf{K}$

iteratively, but may converge slowly to the solution. When $\mathbf{K}$ is evaluated at every iteration, the procedure is known as Fully Newton-Raphson Method. It may result in more computational cost but converged in less iterations.

Here, two most common types of incremental approach: force control and displacement control have been described.

Force incremental method

In the force incremental method, the prescribed external force can be divided into several loading steps. More specifically, $\mathbf{f}_{ext}$ starts from one increment and increases incrementally till reaches the prescribed value of external load. At the time increment n and the current iteration i, the deformation and tangent stiffness at the former step $i-1$ are known, then the iterative equilibrium can be formulated as

$$ {}^{n}\mathbf{K}^{i-1}\Delta\mathbf{u} = \mathbf{f}_{ext} - {}^{n}\mathbf{f}_{int}^{i-1} \tag{1.21} $$

A FEM procedure for a single increment problem can be outlined in the following steps:

1. Define initial nodal displacement $\mathbf{u}_0$.
2. Determine the incremental force at the specified p^{th} degree of freedom Δf_p.
3. Set force vector $\Delta\mathbf{f}_{ext}$ with value at p^{th} degree of freedom equals to Δf_p.
4. Solve $\mathbf{K}_0\Delta\mathbf{u}_1 = \Delta\mathbf{f}_{ext}$ where $\mathbf{K}_0$ relates to $\mathbf{u}_0$.
5. Set $\mathbf{u}_1 = \mathbf{u}_0 + \Delta\mathbf{u}_1$.
6. Compute internal forces $\mathbf{f}_{int}^{i}$ and residual $\mathbf{R} = \Delta\mathbf{f}_{ext} - \mathbf{f}_{int}^{i}$.
7. If the convergence is satisfied, then stop otherwise continue.
8. Compute the tangent stiffness matrix $\mathbf{K}_i$.
9. Solve equilibrium $\mathbf{K}_i\Delta\mathbf{u}_2 = \mathbf{R}$.
10. Set $\mathbf{u}_{i+1} = \mathbf{u}_i + \Delta\mathbf{u}_2$.
11. Set $i = i + 1$ and return back to step 6.

Displacement incremental method

In case of displacement incremental method, the external force can be regarded as a reference force $\hat{\mathbf{f}}_{ext}$ that equal to 1 on the degree of freedom with prescribed displacement applied and 0 on others. Hence, the expression of iterative equilibrium corresponding to displacement control method is given as

$$ {}^{n}\mathbf{K}^{i-1}\Delta\mathbf{u} = {}^{n}\varphi\hat{\mathbf{f}}_{ext} - {}^{n}\mathbf{f}_{int}^{i-1} \tag{1.22} $$

where φ is the load factor to be calculated at every iteration. The procedure for single increment of loading following Batoz and Dhatt [22] can be described as

1. Define initial nodal displacement $\mathbf{u}_0$, fixed external force vector $\hat{\mathbf{f}}_{ext}$ and initial load factor φ_0.
2. Determine the incremental displacement at the specified p^{th} degree of freedom Δu_p.
3. Solve $\mathbf{K}_0\Delta\mathbf{u}_1 = \hat{\mathbf{f}}_{ext}$ where $\mathbf{K}_0$ relates to $\mathbf{u}_0$.
4. Calculate $\Delta\varphi = \frac{\Delta u_p}{\Delta u_{1p}}$.
5. Set $\mathbf{u}_1 = \mathbf{u}_0 + \Delta\varphi\Delta\mathbf{u}_1$, $\varphi_1 = \varphi_0 + \Delta\varphi$.
6. Compute internal forces $\mathbf{f}_{int}^{i}$ and residual $\mathbf{R} = \varphi_i\hat{\mathbf{f}}_{ext} - \mathbf{f}_{int}^{i}$.
7. If the convergence is satisfied, then stop otherwise continue.
8. Compute the tangent stiffness matrix $\mathbf{K}_i$.
9. Solve equilibriums $\mathbf{K}_i\Delta\mathbf{u}_1 = \hat{\mathbf{f}}_{ext}$ and $\mathbf{K}_i\Delta\mathbf{u}_2 = \mathbf{R}$ simultaneously.
10. Compute $\Delta\varphi = -\frac{\Delta u_{2p}}{\Delta u_{1p}}$.
11. Set $\mathbf{u}_{i+1} = \mathbf{u}_i + \Delta\mathbf{u}_2 + \Delta\varphi\Delta\mathbf{u}_1$, $\varphi_{i+1} = \varphi_i + \Delta\varphi$.
12. Set $i = i + 1$ and return back to step 6.

2

Research Outline

2.1 Research motivation

In recent decades, topology optimization technique as an efficient tool has attracted much attention from both academic and industrial engineering community.

To design discontinued structure, such as deep beam or transfer plate, etc., a solution of creating strut-and-tie model (STM) is proposed and recorded in the associated design codes (e.g., BS EN 1992-1-1:2004 [23]). However, for purpose of achieving the most optimal design layout or solving the cases under complex loading and boundary conditions, nowadays, extensive studies emerge with applying optimization technique to structural design.

Also, some commercial package of FEM modelling and analysis include topology optimization solver to meet the structural requirements of a part assembly while saving material and reducing costs. For example, Abaqus Topology Optimization Module (ATOM) helps engineers to refine designs and produce components that are lightweight, rigid and durable. It starts with an initial model and be governed by a set of objectives and constraints. An optimum design is produced by modifying the properties of the material in selected elements, effectively removing elements from the analysis.

However, the optimization solver is limited to particular cases and further research is required on unsolved or more complicated problems, especially for

nonlinear optimization design. Firstly, the topology optimization module is restricted to only single part or structural member, where the removal elements in the design domain is assigned with mass and stiffness that is small enough to ensure they no longer participate in the overall structural response. To some extent, this consists with the concept of achieving a STM model and in the post design process, different material may be adopted for struts and ties respectively, but it is far from realistic design. Some structures consist of multiple materials having distinguished properties, such as reinforced concrete assembly is made by concrete and steel. Therefore, topology optimization design of structure while taking material realistic nonlinearity for each phase into account remain a challenge with limited research works. Secondly, in Abaqus, the objectives applied to a topology optimization process is limited to those that have been maturely investigated, i.e., strain energy (a measure of structural stiffness), frequencies, internal and reaction forces, weight and volume. However, more internal variables in structural response are necessarily considered as an objective or constrain in the optimization design problem when looking into from a different point of view for various functional design purpose. Therefore, in this thesis, both FEM structural analysis and optimization iterative algorithm are programmed and performed in Matlab. This enables to embed the sensitivity analysis into the incremental FEM analysis and solve them simultaneously to save the computational cost, rather than breakdown into separate parts by storing extensive information of structural response that used in sensitivity analysis for all increments in structural analysis stage.

Regarding to topology optimization, two methods are generally undertaken: the heuristic evolutionary method (BESO method) and mathematical SIMP based optimization method. They are also regarded as discrete density based method in which the design variable coupled with element equal to either 0 or 1, and continuous density based method where the density of elements is assumed to vary continuously from 0 to 1. BESO method mainly benefit from easily implementing researchers' novel idea into algorithms but less support from mathematical theory of achieving the optimal solution. While the SIMP-based optimization method may have difficulty in achieving a discrete "black and white" layout due to the existence of elements with intermediate density. In this thesis, these two

methods are both involved in separate research aspects to achieve the optimized layout due to their particular advantage and drawbacks.

This thesis focus on application of topology optimization in structural mechanics from two perspectives: the feasibility of optimization method to be applied and capacity of incorporating with elastoplastic structural mechanics for single or composite structures. The main contribution is related to the framework of optimizing multi-phase material with distinct elastoplasticity at each phase, since the investigation regarding to elastoplastic structural optimization is rare and only reached a preliminary stage. Also, equivalent plastic strain-based optimization method is proposed, which is firstly discussed to authors' best knowledge.

A summary of the research aspect is described in Section 2.2.

2.2 Summary of research

The main motives of each research aspects are hereby presented.

Aspect 1: Optimized design of steel layout in RC Structure structure (Chapter 3 of the thesis)
Reinforced Concrete (RC) is the most well known composite structure and used worldwide. Research studies about how to design structure with D-region properly can be recited as follows: STM method is initially proposed based on stress trajectories and engineers' empirical practice, which is an effective approach but usually uncertain. Afterwards, truss topology optimization method is applied to seek the best truss (steel reinforcement) layout in the design domain based on ground structure theory where the initial truss layout is predefined and has significant influence on the resulting truss topology. Continuous topology optimization method is also applied due to its advantage of achieving a novel layout without restriction from original design domain. The continuum optimization of single material structure can be regarded as an alternative to achieve STM design. Gradually, incorporating different mechanical properties of concrete and steel into topology optimization has emerged, e.g., add yield constraint on material phase. Furthermore, RC structure is not only a two-material but a two-scale design problem, in order to consider the realistic volumetric ratio of steel used

into the continuum concrete, a hybrid truss-continuum model is developed. More specifically, the truss ground structure and continuum finite elements are combined onto a mesh of shared nodes where tension members are presented by truss elements resulting in reinforcing steel design while continuum elements are implemented as concrete to carry compression. Although, it solves the two-scale problem and simultaneously taking two separate material phase (steel and concrete) into account, the steel is assumed to be unable to work in compression, which is consistent with the STM mechanism but oppose to the realistic material property.

Therefore, this paper proposed a truss-embedded-continuum model and incorporated with the evolutionary optimization technique. Firstly, it succeeds in considering two distinct material scales by modelling reinforcing bar as truss and concrete as continuum elements. Secondly, both tension and compression are acceptable in steel, also, a modified variable updating scheme is developed to consider the contribution of concrete in tension. Thirdly, opposite to the conventional truss or truss-continuum topology optimization method that bothered with the impact from the predefined ground structure, a heuristic orientation finding scheme is proposed and added into the BESO algorithm to enable the truss adjust itself orientally in a continuum element. Two numerical examples are used to present the effectiveness of the proposed algorithms. The result shows an optimized reinforcement layout in both topology and orientation.

However, there are still some limitations encountered in this study. Although the asymmetric property of concrete is taken into account by setting the approximate allowable value of strain in tension and compression as index to effect the design variable update scheme, the behaviour of both steel and concrete are assumed to be linear and elastic in structural analysis. This is still far from incorporating more precise material feature, e.g. elastoplasitcity, into optimization algorithms. In order to nest the structural analysis into every optimization iteration and consider the nonliearity and post yielding behaviour for both steel and concrete, the distinct scale problem is neglected in the next research study. This is due to some obstacles encountered, e.g., it is difficult to determine a consistent constitutive tensor at any material point for an embedded model as its discrete nature. Therefore, to simplify the problem, both concrete and steel are

modelled as continuous elements and the continuous density-based SIMP optimization method is used, which means the element is either concrete or steel or a kind of smeared concrete-steel material.

Aspect 2: Using continuous density-based optimization method for nonlinear composite structure (Chapter 4 of the thesis)
In this research study, the proposed framework is applicable for not only the reinforced concrete model but any composite structure having same or distinct elastoplasticity. Research studies about using topology optimization for continuous structure design are briefly recited here and a detail review is given in Chapter 4.

Initial studies focused on implementing topology optimization on single or multiphase elastic material design, however, linear elastic material model is not appropriate when there are material points exceeding the elastic range. Therefore, research emerged to optimize structure taking their material nonlinearity into account. However, few studies consider material nonlinearity for a multiphase optimization problem. Especially, when the yield criteria and the post yielding performance (e.g. hardening model) applied to each material phase is different. Also, the von Mises plastic material model is adopted in majority studies and all works employ the isotropic hardening rule. While some materials, e.g., polycrystalline metals, present a mixed property of isotropic and kinematic hardening.

Therefore, due to the increasing demanding of topology optimization technique in efficiently distributing material phases for composite structure, it is necessary to consider more types of hardening rules following multiple yield criteria and incorporate with topology optimization method to achieve a more realistic and reliable design. The proposed method and framework are implemented and illustrated by three numerical examples. In-depth analysis to the numerical results have revealed the significant impact of selection of plasticity and hardening model on the results of topology.

Aspect 3: Using Discrete Density-based Optimization Method for Nonlinear Structure (Chapter 5 of the thesis)

As can be concluded from the former research study (Aspect 2), it is successful to optimize two-phase structure taking their individual yielding and post yielding behaviour into account, however, there are several problems arise when the SIMP density optimization method is used for multiphase nonlinear structural design.

Firstly, although a gradually reduced filtering scheme is proposed and employed to eliminate the gray scale areas in the topology, this optimization still failed to achieve a distinct convergence of "0-1" layout. In the design domain, for the elements that develop large plastic deformation or little deformation, it is easy to determine which material phase is effective, while for elements that show in-between level of strain, not very large or very small, presenting in gray scale. This is an unsolved issue that has also been observed in previous research studies [24, 25]. Secondly, due to a nested framework is performed by embedding partial sensitivity analysis into structural analysis, and nesting the structural analysis into the optimization procedure. The number of structural analyses to be solved is equal to the number of optimization iterations. Moreover, in a path-dependent nonlinear analysis, several increments are needed to converge at every certain displacement level. Therefore, the computational cost relates to the number of time increments defined and the total number of optimization iterations. In the former study, most problems require at least 300 design iterations to reach a distinct layout, and after that, no significant changes in the topology and objective value. Hence, computational burden is non-negligible during design.

BESO method seems to be an alternative effective tool due to their advantage of obtaining a distinct "0-1" layout in a certain number of design iterations, which solves the problems discussed above.

In the evolutionary optimization field, calculation of sensitivity numbers that determine the removal and addition of every element is considerably important. And it straightforwardly influence the stabilization of evolutionary procedure and convergence of topology. Limited research studies consider to use BESO method for nonlinear structural design and the sensitivity analysis applied is always simplified or approximated, e.g. only take the global constitutive equation into account. Afterwards, additional approaches are applied, e.g., damping scheme on sensitivity numbers, admission volume ratio of limiting the number of recovered elements at each iteration, filtering scheme of gradually decreasing the filtering

radius, to smooth the sensitivity number. Reference works are reviewed in Chapter 5. Therefore, an accurate calculation of sensitivity number is particularly vital for using BESO method for nonlinear design.

This research aspect contributes to apply a transit coupled nonlinear system that consider the elastic and plastic transit state when calculate the sensitivity numbers in the BESO algorithms. The stable evolutionary process is observed and convergent topology is achieved without applying any additional scheme mentioned above. Two design problems show the reliability and effectiveness of the proposed method. Also, in the nonlinear analysis, the tangent stiffness between the stress and strain rate is further modified to be consistent with the time integration algorithm, based on the fact that a finite size of time increment is used in the time integration algorithm. This enables to achieve quadratic convergence during the Newton-Raphson iteration to further save computational cost.

Aspect 4: Plastic Strain-based Topology Optimization for Nonlinear Structure (Chapter 6 of the thesis)
As can be observed from previous researches[24, 26, 27, 28, 29] relating to use optimization method for nonlinear structural design. Majority of studies take maximizing the energy absorption capacity as their purpose, which is theoretically similar to maximizing the stiffness (minimize the compliance) for an elastic structure. It can be achieved by maximizing the total strain energy, minimizing the complementary elastic work, maximizing the absorbed plastic work or maximizing the end-compliance under prescribed displacement loading condition. Apart from compliance or energy based optimization problem, stress based topology optimization design emerged as another attractive and challenging area to minimize the maximum stress or restrict stress to an allowable value.

However, from research studies focus on nonlinear analysis of elastoplastic structure, I realized that plastic strain is obviously an important internal tensor. For instance, for an elastic-perfectly-plastic structure, the yield stress remain constant while the plastic deformation grows under further loading of force or displacement. Also, for elastoplastic structure with strain-hardening model, the yield surface moves or expands along the plastic deformation. Furthermore, the non-reversible deformation in response to the applied force would deteriorate the

material strength. Thus, in the optimization design procedure for a nonlinear structure, plastic deformation is essentially taken account as an optimization objective or constraint. To authors' best knowledge, there yet no studies about plastic strain based optimization problems.

This possibly due to the challenges encountered: (i) local nature of strain. They exist on every material integration point rather than can be expressed in a global form. (ii) structure may partially enter the plastic state. Plastic strain equals to 0 for material staying at the elastic state. (iii) 'singularity' problem. Elements with low density may present high equivalent plastic strain, which resists the optimization algorithm from removing them.

This study solved the first difficulty mentioned above by using a global quantity, that accumulate all equivalent plastic strain on every Gauss points, to approximate local plastic strain. And the nature of BESO evolutionary method prevents the 'singularity' phenomenon raised from elements with intermediate density. Also, for a material point, its sensitivity may vary by several orders of magnitude due to the uncertain state (plastic or elastic). Hence, a damping scheme is proposed to stabilize the topology evolution.

This study successfully deals with a formulation for topology optimization of elastoplastic structures that aims at minimizing the maximum equivalent plastic strain subject to material usage constraint. Two numerical examples are presented to discuss the features of the achieved optimized designs along with performances of the adopted procedure. Comparison with the compliance based optimization results points out the difference in the resulting topology, equivalent stress and equivalent plastic strain distribution.

3

Optimized Design of Steel Layout in RC Structure

3.1 Introduction

In structural concrete design, disturbed regions, so called as 'D-regions', have been a challenge for decades. Opposed to 'B-regions' (Bernoulli or Beam regions) where design procedure is maturely established according to beam theory and cross-sectional analysis, D-region is defined by a structural part with nonlinear strain distribution, for which traditional approaches for slender beams are not appropriate for design. Current practice towards design and analysis of such regions of the structure is using strut-and-tie model (STM) [30] which is well known as a generalization of truss analogy model [31]. The concrete struts represent elements in compression while the tensile ties are carried by steel reinforcements.

However, the selection of STM is usually uncertain, especially for an irregular RC structural member under complicated loading and boundary conditions, because it is mainly based on stress trajectories, load path methods or empirical observations. The optimization technique has been regarded by researchers as an efficient tool to distribute reinforcements within the concrete structure.

Initially, the discrete topology optimization based on the truss ground structure approach, that allows the truss topology design problem to be viewed as a generalized sizing problem, has been used to search for the optimal STMs in

reinforced concrete structures [32, 33]. The continuous reinforced concrete domain is discretized by a predefined layout where the fixed truss ties correspond to the actual reinforcements and the ties with cross-sectional areas equal to zero or nearly zero are removed through the topology optimization process. In both works of Biondini [34] and Ali and White [35], an automatic search technique for truss models consistent with the elastic stress trajectories in reinforced concrete members were proposed based on ground structure approach and linear mathematical programming technique. Also, genetic algorithms have been applied to truss topology optimization to seek the best layout of the location of reinforcing ties and compressive struts within the reinforced concrete beam [36]. More recently, Amir and Sigmund [37] developed a truss topology optimization method by embedding a truss ground structure into a concrete continuum damage model, so that the distribution of embedded steel reinforcement is optimized. However, the predefined ground structure has dominant influence on the resulting topology, which mainly depend on the intuition and experience of designers.

As opposed to truss topology optimization that require designers to define node locations and element connections a priori, using continuum topology optimization to achieve a novel layout design of reinforced concrete structures has attracted a large amount of researchers in recent years [38, 39, 40, 41, 42, 43, 44].

However, these studies all proposed to use a truss-like structure obtained from single-material topology optimization so as to predict a strut-and-tie model. As the name suggests, the reinforced concrete structure is composed of two materials: concrete and steel. Hence, incorporating different mechanical properties of concrete and steel into topology optimization has emerged to gain a more effective design [45, 46, 47]. Luo and Kang [48] developed a two-material topology optimization with volume constraint on steel and strength constraint on concrete. The resulting topology is much like a steel-concrete composite structure. Instead of imposing stress constraints, the complete non-linear elasto-plastic response for both concrete and steel were modelled in Bogomolny and Amir et al. [25]. Also, Luo et al. [49] proposed an effective continuum topology optimization method, aiming to minimize the cost of steel reinforcements, subjected to a shrinkage volume constraint and yield constraint for concrete phases.

Reviewing these works, RC structure is generally regarded as two-phase continuum, however, in real application, the volumetric ratio of steel used into the continuous concrete is rarely over 1% [37], which cannot be achieved properly by modelling steel reinforcements as continuous elements in topology optimization design. Also, from a construction perspective, the required postprocessing of continuous members in tension regions to discrete bars is less practical.

In order to benefit from both continuum and truss topology optimization, the truss ground structure and continuous finite elements are combined onto a mesh of shared nodes where tension members are presented by truss elements resulting in reinforcing steel design while continuum elements are implemented as concrete to carry compression. This idea was initially proposed in Moen and Guest et al. [50] and then topology optimization of using a hybrid truss-continuum model was further developed in Gaynor et al. [51] to prevent the strut-only solution from missing transverse tensile stresses caused by load spreading. Also, it has been extended to 3D design models by Yang, Moen and Guest [52] and developed to generate a structural system performing practically in construction by considering a tradeoff between material and construction cost [53].

However, the stiffness of truss steel element modeled in the hybrid approach is high in tension but negligible in compression, just as in most previous studies with the goal of achieving a strut-and-tie model. It is important to point out that although it opposes to the STM mechanism, both tension and compression are acceptable in steel in the real application.

As a result of this, the current work develops a truss-continuum embedded model that reinforcing bars are modeled as truss elements embedded onto the continuum concrete. Furthermore, it focus on obtaining an optimized steel reinforcement layout accepting both tension and compression within a constant concrete domain. The optimization variables are only applicable to steel reinforcements. The main contribution of this study is that a heuristic orientation finding scheme is proposed to be employed into a 2D BESO algorithm. This enables the reinforcing bar can adjust itself to an efficient orientation based on the principal strain direction in each iterative design, which get rid of the drawback of conventional truss topology optimization that the layout for reinforcing bars is dominantly influenced by the predefined truss layout.

BESO method is an improvement of evolutionary structural optimization (ESO), which removes the unnecessary material from a structure while the efficient ones to be added. Apart from the gradient based method, e.g. the Solid Isotropic Material with Penalization method (SIMP), the heuristic BESO method is another promising choice. More recently, the solution to problems of checkerboard pattern, mesh-dependence and non-convergence, and a material interpolation scheme with penalization was employed in the BESO technique [54]. Its simple concept and easy implementation has gained widespread popularity among researchers and designers and has been used for a wide range of applications in engineering field [55]. For these reasons, the author decides to achieve the goal by using the BESO approach in this paper. Moreover, due to the property of concrete that is strong in compression but weak in tension, a modified design variable updating scheme is developed, based on the allowable strain for concrete in tension and compression.

3.2 Modelling of reinforcing bars

The reinforcing bar placed in the concrete is used to strengthen structure by minimizing deformation, crack or high stress of concrete. There are generally two methods to model reinforcements: smeared model and embedded model. In the smeared model, the overall constitutive relationship is simply evaluated by adding the material matrix for concrete and steel together as

$$\mathbf{D} = \rho_c \mathbf{D}_c + \rho_s \mathbf{D}_s \tag{3.1}$$

where ρ_c and ρ_s are the volume ratio for concrete and steel in one element, respectively. To solve the distinct scale problem, the embedded model is adopted in this study by modelling the reinforcing bar as truss that contribute to its resistance only in the longitudinal direction. The material matrix of steel and concrete for the plane stress case can be expressed as

$$\mathbf{D}_s = \begin{bmatrix} E_s & 0 & 0 \\ 0 & 0 & 0 \\ 0 & 0 & 0 \end{bmatrix} \tag{3.2}$$

$$\mathbf{D}_c = \frac{E_c}{1-v^2}\begin{bmatrix} 1 & v & 0 \\ v & 1 & 0 \\ 0 & 0 & \frac{1-v}{2} \end{bmatrix} \tag{3.3}$$

The discrete modeling of steel reinforcements was initially proposed by Kwak and Filippou et al. [56]. Perfect bond between steel and concrete is assumed, so that the displacement of truss (steel) elements are consistent with those of the surrounding continuum (concrete) elements. Also, the location and orientation of the steel bar superimposed on a concrete element is arbitrary, not necessarily sharing the same nodes, hence the orientation of the truss element is ideally flexible during the optimization process. The elemental stiffness of each individual steel bar can be added to nodes of concrete elements, in other words, the strain energy of the embedded steel bar can be evaluated through the nodal displacements and its elemental stiffness at a global coordinate system.

Here, I derived the stiffness assembly of truss element and continuum element for a particular embedded model where the reinforcing bar presented in red is embedded arbitrarily into a 4-node quadrilateral element shown in black (Fig.3.1). Based on the assumption that the reinforcing bar only has stiffness along the longitudinal axial direction with a constant cross-sectional area, the elemental stiffness matrix for a 1D steel bar is given by,

$$\mathbf{K}_{sl} = \frac{A_s E_s}{L_e}\begin{bmatrix} 1 & -1 \\ -1 & 1 \end{bmatrix}. \tag{3.4}$$

Where A_s, E_s and L_e represent the cross-sectional area, the elastic Young's modulus and the length of an individual bar, respectively.

As presented in Fig.3.2, the nodal axial force (F_{s1}, F_{s2}) of an elastic reinforcing bar can be formulated as

$$\begin{bmatrix} F_{s1} \\ F_{s2} \end{bmatrix} = \mathbf{K}_{sl}\begin{bmatrix} u_{s1} \\ u_{s2} \end{bmatrix} \tag{3.5}$$

Fig.3.3 presents the nodal axial force and displacement in a global coordinate, then Eq.(3.5) can be further formulated as

$$\begin{bmatrix} F_{sx1} \\ F_{sy1} \\ F_{sx2} \\ F_{sy2} \end{bmatrix} = \mathbf{K}_{sg}\begin{bmatrix} u_{sx1} \\ u_{sy1} \\ u_{sx2} \\ u_{sy2} \end{bmatrix} \tag{3.6}$$

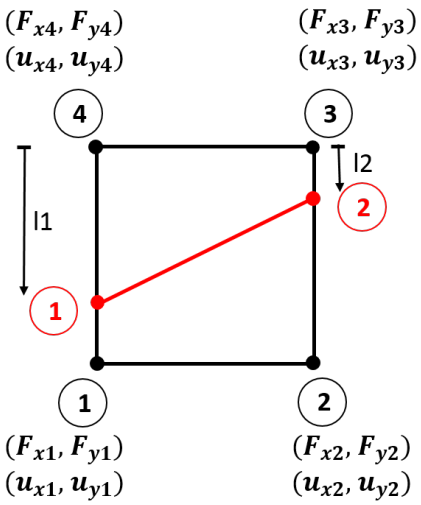

Figure 3.1: Reinforcement embedded model

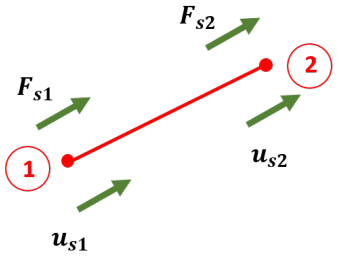

Figure 3.2: 1D truss element in local coordinate

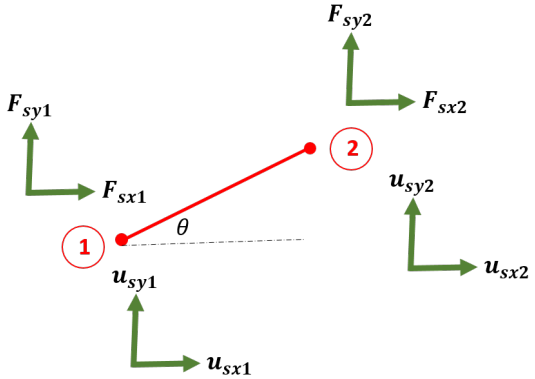

Figure 3.3: 1D truss element in global coordinate

with

$$\mathbf{K}_{sg} = \mathbf{N_1}^T \mathbf{K}_{sl} \mathbf{N_1} \tag{3.7}$$

$$\mathbf{N_1} = \begin{bmatrix} \cos\theta & \sin\theta & 0 & 0 \\ 0 & 0 & \cos\theta & \sin\theta \end{bmatrix}. \tag{3.8}$$

where θ expresses the angle between the axis of the reinforcing bar and the x-axial direction. Therefore, the local elemental stiffness matrix $\mathbf{K}_{sl}$ can be transformed to $\mathbf{K}_{sg}$ in a global coordinates through a transformation matrix $\mathbf{N_1}$. The transformation matrix $\mathbf{N_1}$ relates the local truss elements to a global coordinate system by applying a rotation θ. As the location of the truss element embedded in the continuum element is arbitrary that the truss nodes may not coincide with the continuum nodes, another transformation matrix $\mathbf{N_2}$ is needed to map $\mathbf{K}_{sg}$ to a stiffness matrix $\mathbf{K}_s$ in terms of the degree of freedoms (DOFs) of continuum nodes. Based on the principle of energy conservation, $\mathbf{N_2}$ can be derived as

$$\mathbf{U}_{sg}^T \mathbf{K}_{sg} \mathbf{U}_{sg} = \mathbf{U}_e^T \mathbf{K}_s \mathbf{U}_e \tag{3.9}$$

where $\mathbf{U}_e$ represents a nodal displacement vector associated with continuum nodes. Due to the assumption that the displacement of the embedded reinforcing bar is compatible with those of the continuum concrete elements, the global displacement vector $\mathbf{U}_{sg}$ at the end nodes for a truss element can be expressed in terms of $\mathbf{U}_e$ through shape functions $\mathbf{N}_2$ as

$$\mathbf{U}_{sg} = \mathbf{N}_2 \mathbf{U}_e \tag{3.10}$$

In this particular example as presented in Fig.3.1, it can be described more specifically as

$$\begin{bmatrix} u_{sx1} \\ u_{sy1} \\ u_{sx2} \\ u_{sy2} \end{bmatrix} = \mathbf{N}_2 \begin{bmatrix} u_{x1} \\ u_{y1} \\ u_{x2} \\ u_{y2} \\ u_{x3} \\ u_{y3} \\ u_{x4} \\ u_{y4} \end{bmatrix} \tag{3.11}$$

with

$$p = \frac{l1}{l} \quad q = \frac{l2}{l} \tag{3.12}$$

$$\mathbf{N}_2 = \begin{bmatrix} 1-p & 0 & 0 & 0 & 0 & 0 & p & 0 \\ 0 & 1-p & 0 & 0 & 0 & 0 & 0 & p \\ 0 & 0 & 1-q & 0 & q & 0 & 0 & 0 \\ 0 & 0 & 0 & 1-q & 0 & q & 0 & 0 \end{bmatrix} \tag{3.13}$$

Note that matrix $\mathbf{N_2}$ varies subject to the rotation of reinforcing bar from axis x within the continuum element. By substituting Eq.(3.11) into Eq.(3.6), the nodal force vector of the bar in a global coordinate can be further obtained as

$$\begin{bmatrix} F_{sx1} \\ F_{sy1} \\ F_{sx2} \\ F_{sy2} \end{bmatrix} = \mathbf{K}_{sg}\mathbf{N}_2 \begin{bmatrix} u_{x1} \\ u_{y1} \\ u_{x2} \\ u_{y2} \\ u_{x3} \\ u_{y3} \\ u_{x4} \\ u_{y4} \end{bmatrix} \tag{3.14}$$

And the nodal force of the bar in terms of the continuum nodes can also be achieved through the transposed form of $\mathbf{N}_2$ as

$$\begin{bmatrix} F_{x1} \\ F_{y1} \\ F_{x2} \\ F_{y2} \\ F_{x3} \\ F_{y3} \\ F_{x4} \\ F_{y4} \end{bmatrix} = \mathbf{N}_2^T \begin{bmatrix} f_{sx1} \\ f_{sy1} \\ f_{sx2} \\ f_{sy2} \end{bmatrix} \tag{3.15}$$

By substituting Eq.(3.15) into Eq.(3.14),

$$\begin{bmatrix} F_{x1} \\ F_{y1} \\ F_{x2} \\ F_{y2} \\ F_{x3} \\ F_{y3} \\ F_{x4} \\ F_{y4} \end{bmatrix} = \mathbf{N}_2^T\mathbf{K}_{sg}\mathbf{N}_2 \begin{bmatrix} u_{x1} \\ u_{y1} \\ u_{x2} \\ u_{y2} \\ u_{x3} \\ u_{y3} \\ u_{x4} \\ u_{y4} \end{bmatrix} \tag{3.16}$$

Therefore, a fully description of stiffness matrix $\mathbf{K_s}$ can be summarized as

$$\mathbf{K}_s = \mathbf{N}_2^T\mathbf{K}_{sg}\mathbf{N}_2 = \mathbf{N_2}^T\mathbf{N_1}^T\mathbf{K}_{sl}\mathbf{N_1}\mathbf{N_2} \tag{3.17}$$

As a result, the assembled stiffness $\mathbf{K}_e$ can be obtained by adding $\mathbf{K}_s$ to the elemental concrete stiffness matrix $\mathbf{K}_c$ to model the reinforced concrete element in a finite element method, which is given by

$$\mathbf{K}_e = \mathbf{K}_s + \mathbf{K}_c \tag{3.18}$$

Regarding the orientation of reinforcing bar, it is simplified to consider only four types of rotation allowed from axis x within the continuum element in this study. As shown in Fig.3.4, the grey area denotes the continuum concrete element while reinforcing bar is represented by black bold line.

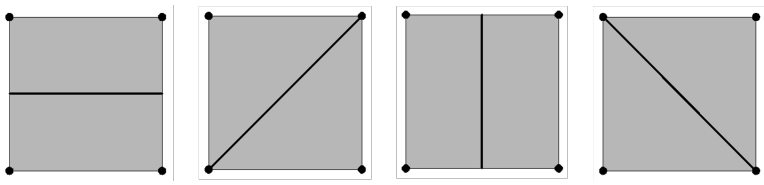

Figure 3.4: Four different types of reinforcing bar embedded in a continuum element

3.3 Topology optimization algorithm

The optimization algorithm applied in this work is explored dominantly based on the BESO optimization approach [30]. Although the hosting concrete is taken into account in the finite element analysis, the optimization design domain is only applicable to the steel reinforcement layout. As mentioned that topology optimization technique is nowadays widely used to design RC structures to gain a truss-like layout. However, the achieved topology cannot be applied straightforwardly to the real design problem due to the requirement for structural integrity and the minimum reinforcing ratio in some specific regions. Therefore, here steel distribution is the only target of optimizing within a constant amount of concrete domain.

3.3.1 Problem statement and design parametrization

The problem is formulated with the objective of maximizing the stiffness of reinforcement layout in a RC design domain and a constraint on the amount of steel to be used

$$\begin{aligned} \min \quad & c(\mathbf{x}) = \frac{1}{2}\mathbf{U}^T\mathbf{K}\mathbf{U} \\ s.t. \quad & \sum_{e=1}^{N_{ele}} v_e x_e = V_s^* \\ & x_e = 0 \ \ or \ \ 1, \quad (e = 1, 2, ..., N_{ele}) \end{aligned} \tag{3.19}$$

where c denotes the mean compliance; $\mathbf{U}$ is the vector of nodal displacement obtained from FEA of the reinforced concrete model; $\mathbf{K}$ is the global stiffness matrix of the structure; V_s^* is the prescribed target volume fraction of the design domain which corresponds to the realistic reinforcement volume ratio into the concrete domain; v_e is the volume of each truss element; x_e is the design variable that are restricted to be either lower-bound x_{min} (0.001) or 1 throughout this study.

As elements are defined without intermediate density, only one type of steel bar is considered. The evolutionary optimization starts from a full design domain, which means that the continuum concrete is initially over-reinforced by steel, and the amount of reinforcement decreases gradually by applying an evolutionary ratio (R_{er}) till the target volume V_s^* is achieved. In order to avoid the results being influenced by R_{er}, a constant value of 2% that has been widely tested in previous studies is adopted herein. Furthermore, a convergence criterion is required to terminate the optimization algorithm. In this research, the optimization stops when a change of 0.01% is satisfied in the mean compliance over the last 10 iterations.

3.3.2 Reinforcing bar orientation

Amir and Sigmund et al. [37] states the outcome of optimization is obviously influenced by the selection of the ground structure. Therefore, it is vital to consider the efficient orientation of steel without establishing a very dense ground

structure. As a heuristic approach, BESO provides researchers a promising basis of extending to various design problems and implementing ideas into its algorithm.

This research focus on the optimization of both orientation and topology of steel layout in concrete structure. The reinforcing bars are modeled as discrete truss elements and accept both tension and compression. At the initial design domain, two reinforcing bars are embedded into each concrete continuum element along the longitudinal axis x and y respectively, as presented in Fig.3.7(a). After the first iteration, their orientation will be adjusted according to the maximum and minimum principal strain direction, respectively. Although the angle of rotation from x axis can also be obtained by the direction of principal stresses, achieving the principal stress is not as easy as strain based on this finite element embedded model that consists of both discrete and continuum elements. Four different 2D principal strain states are shown in Fig.3.5.

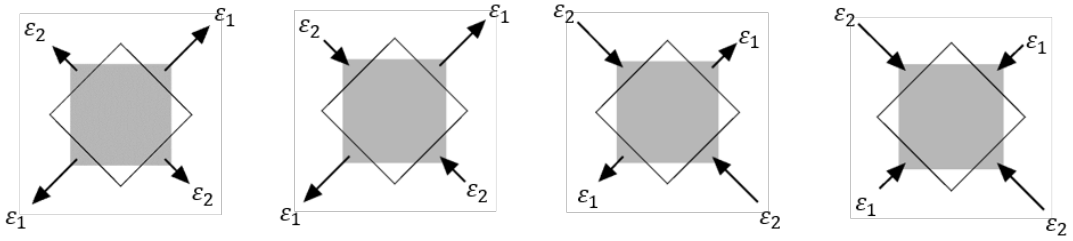

Figure 3.5: 2D principal strain states

As the purpose of the initial research is to verify the proposed heuristic orientation finding system rather than generate a very complicated reinforcement layout, only two types of embedded model are considered in which reinforcing bars are located horizontally and vertically or in a diagonal form. Hence, the maximum principal strain orientation is defined approximately equal to: 0° (180°), 45°, 90° or 135°, in terms of rotating anticlockwise from x axis (see Fig.3.6). For example, when the direction of maximum principle strain at the centroid of element is 50° from the positive x axis, which appears in the range between 22.5° and 67.5°, then it assumbed equal to 45° to simplify the problem. Fig.3.7 shows the reinforcing bar in black following these four possible orientations, while the bar in blue which is perpendicular to the black, is parallel to the minimum principal strain direction.

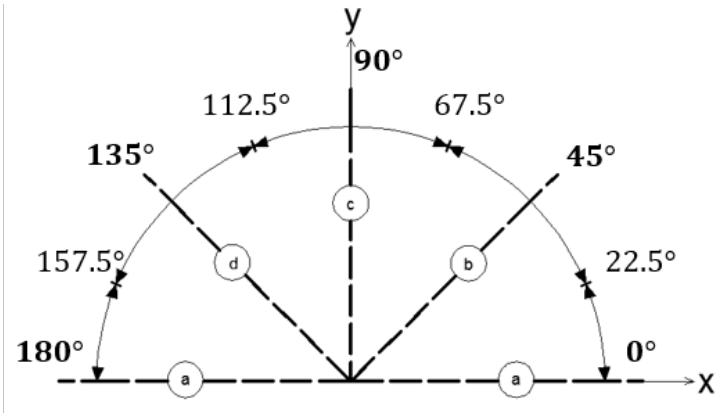

Figure 3.6: Four simplified maximum principal strain orientation rotating anti-clockwise from x axis

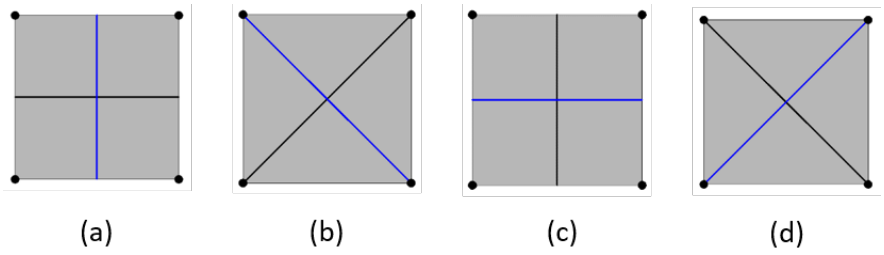

Figure 3.7: Presentation of embedded model

For the problems encountered in topology optimization design, e.g., checkerboard pattern or mesh-dependency, Huang and Xie et al. [18] proposed filtering scheme for sensitivity numbers to address the numerical instabilities. Since the orientation of reinforcing bar is considered based the strain states, the strain obtained from structural analysis of the current structure is modified by a filtering scheme before being used to define the orientation. The influence from neighboring elements within the filtering circle are taken into account as

$$\boldsymbol{\epsilon}_e = \frac{\sum_{i=1}^{N} w_{ei}\boldsymbol{\epsilon}_i}{\sum_{i=1}^{N} w_{ei}} \tag{3.20}$$

with

$$w_{ei} = max(0, r_{min} - dis(e,i)) \tag{3.21}$$

where $\boldsymbol{\epsilon}_e$ and $\boldsymbol{\epsilon}_i$ are the vectors representing the strian components at the centroid of element e and element i, respectively. w_{ei} is the weight factor, r_{min} is the filter radius and the item $dis(e,i)$ represents the distance between of centers of element e and element i. A Pseudocode for the bar orientation finding scheme is depicted as follows:

For each truss-continuum element **do**
  Calculate the centroid strain components ε_x, ε_y, γ_{xy}
  Apply filtering to ε_x, ε_y, γ_{xy}
  Calculate principal strain ε_1, ε_2
  Apply filtering to ε_1, ε_2
  Calculate angle θ between maximum principal strain direction and x axis in terms of anticlockwise rotation
  If $\theta \leq 22.5^\circ$ or $157.5^\circ \leq \theta \leq 180^\circ$ **then**
    $\theta = 0^\circ$
  Else if $22.5^\circ < \theta \leq 67.5^\circ$ **then**
    $\theta = 45^\circ$
  Else if $67.5^\circ < \theta \leq 112.5^\circ$ **then**
    $\theta = 90^\circ$

Else if $112.5° < \theta \leq 157.5°$ **then**
$\theta = 135°$
End if
Rotate reinforcing bar in black by θ
Locate reinforcing bar in blue perpendicular to the one in black
End for

However, from numerical studies, I observed that results may fail to converge after satisfying the volume constraint in optimization, which is possibly due to the oscillation of rotation angle θ. This leads to a non-convergence results and non-optimal bar orientation. At this point, a possible solution to this problem is proposed to stabilize the orientation. The rotation angle is defined by weighting the current orientation θ and the orientation obtained in last iteration θ_{old} to a threshold θ_{th} (that possibly equal to 22.5°, 67.5°, 112.5° or 157.5° as introduced above). The following pseudocode describes one situation which may occur. Although, it cannot guarantee an optimal solution but play a positive role in converging material orientation for all examples in this paper.

Do while $\theta \leq \theta_{th}$ and $\theta_{old} > \theta_{th}$
If $\frac{\theta_{th}-|\theta|}{\theta_{th}} \leq \frac{|\theta_{old}|-\theta_{th}}{\theta_{th}}$ **then**
$\theta = \theta_{old}$
Else if
$\theta = \theta$
End if
End do

3.3.3 Update Scheme

As the optimized topology is achieved by the relative ranking of sensitivity numbers in BESO method, no matter an individual truss element acting in tension or compression, its corresponding sensitivity is involved in the optimization algorithm. However, the resulting topology based on the contribution of steel reinforcement to the objective function may not reflect the real design problem. Some

steel reinforcements may be remained in regions where concrete itself can withstand the compression. This is due to its higher sensitivity than that of those in tension areas. Opposed to steel having constant and high strength in all direction, concrete is strong in compression but very weak in tension due to its quasi-brittle nature. Therefore, a proposed scheme updating the design variables while taking the host concrete into consideration is applied into the BESO algorithm in this study. Homogenized average strain is derived from a truss-continuum combined element model. When the maximum principal strain or the minimum principal strain of an element exceeds the threshold value of the allowable tensile or compressive strain that measured from uniaxial tension and compression tests, it is considered prior in the sensitivity analysis, and ranked over elements with strain less than the allowable value. Here, the threshold values for concrete in tension and compression are set to be 1×10^{-4} and -3×10^{-3} respectively throughout the paper. The sensitivity modification formulation is constructed as

$$s_i = s_h - 0.001 \times (s_h - s_i) \quad (i = 1, 2) \tag{3.22}$$

where s_i is the sensitivity number with respect to the reinforcing bar being placed based on the maximum ($i = 1$) or minimum ($i = 2$) principal strain direction. And s_h is the highest sensitivity value among those of all the candidate truss elements. Note that the sensitivities of elements having allowable strain do not need undergo this artificial modification. The examples given in the next section show different topologies obtained from the optimization algorithm with and without adding this heuristic update scheme and prove its capacity in achieving a reasonable reinforcement layout.

As a result, the proposed evolutionary optimization procedure based on BESO algorithm is summarised as follows:

1. Define mesh condition and initial truss layout.

2. Assign design variable for each truss element.

3. Set up BESO parameters (target volume V_s^*, evolutionary removal ratio R_{er}, filtering radius r_{min}, convergent tolerance τ and maximum optimization iterations).

4. Perform FE analysis of current truss-embedded-continuum structure to obtain the nodal displacements **U**.
5. Calculate sensitivity number of every truss element.
6. Filter sensitivity numbers and average them based on evolutionary history.
7. Define desired volume of next iteration.
8. Update design variables of truss elements based on the modified updating system using Eq.(3.22).
9. Check the target volume are reached and the convergence criterion or determined total iterations are satisfied.
10. If not, calculate the magnitude and direction of principle strain based on the output **U**, and construct a new truss layout.
11. Return to step 4 until step 9 is satisfied.

3.4 Examples

Two 2D cases were tested in this section to present the implementation of the proposed optimization algorithm in obtaining steel reinforcement layout for concrete structure design. The Young's modulus for steel and concrete $E_s = 210Gpa$, $E_c = 25Gpa$ and the poisson ratio for both concrete and steel $v = 0.3$ are constant throughout all examples. Four-node quadrilateral plane-stress elements are used to model the 2D continuum concrete element. The filter radius applied in the filtering scheme is equal to 3 times of the element size. Since reinforcing bars are embedded into individual continuum element, using smaller element size leading to a denser reinforcement layout while reinforcements are placed with larger space based on a coarser FE mesh. In all simulations, the thickness of a 2D structure is 0.001m and the volumetric ratio of steel used in a continuum element is set to 2%. Although the cross-sectional area of the reinforcing bar cannot subject to more than one type, there would not be a significant influence on determining the regions where to be reinforced by compressive or tensile bars. In the resulting

topologies, black solid line represents reinforcing bar in tension while the one in compression is described by blue solid line.

3.4.1 A 2D cantilever beam

A cantilever short beam with length-to-height ratio equal to 8/4 is shown in Fig.3.8. It is fully clamped along the left edge and a downward concentrated load F=300N is applied at the centroid of the right edge. Using an element size of 20mm, the whole domain is discretized into 800 (40×20) continuum finite elements. It is aiming to achieve a practical volumetric ratio of 0.48% from an initial over-reinforced reinforcing ratio (2%), in other words, only 24% of the total amount of reinforcing bars remain in the continuum concrete through optimization. Firstly, the influence of the implementation of the proposed update

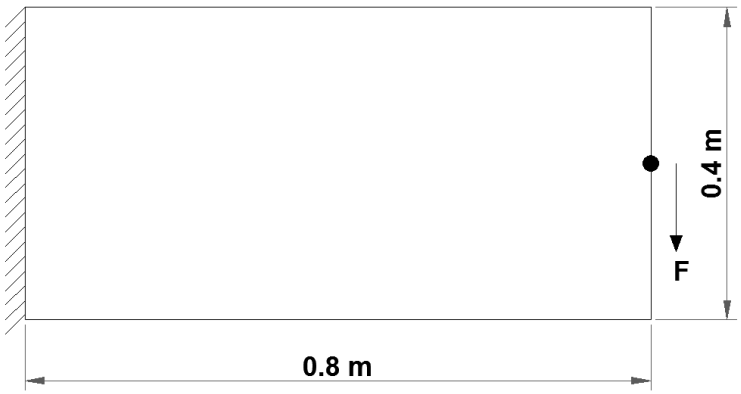

Figure 3.8: A 2D cantilever beam design domain

scheme in the optimization algorithm on the resulting topology is studied. As shown in Fig.3.9 (a), a symmetric layout of reinforcing bars located in tension and compression regions is achieved for this particular case. Same amount of steel bars are distributed in the upper and lower parts of the cantilever beam when the asymmetric property of concrete is not considered. While in Fig.3.9 (b), taking the allowable tensile and compressive strain for concrete into account in the variable updating system, more reinforcing bars are distributed in tension regions which is due to concrete has a strong strength in compression. Also, it should be pointed out that a small amount of bars perpendicular to the compressive

reinforcing bars exist in the left lower area of the domain to reduce the concrete potential crack widths due to tensile stresses. Furthermore, the cantilever beam with various length-to-height ratio of 9/4 and 10/4 are tested respectively, under the same loading and boundary conditions. The resulting topologies are plotted in Fig.3.9 (c) and (d). Through comparison with the result shown in Fig.3.9 (a), an increasing amount of vertical tensile steel bars are distributed to reinforce concrete in compression-dominant regions. Moreover, the length of the horizontal bar acting in both tension and compression are extended along the geometrical increase in length of the domain. And rows of compressive horizontal bar located at the bottom area increase from four (Fig.3.9 (b)) to five (Fig.3.9 (d)). However, the limitation of the target volume of steel used and high demanding in other critical bar positions reduce the amount of diagonal reinforcements.

3.4.2 A 2D deep beam

This example considers the layout design of steel reinforcing bars in a deep beam as shown in Fig.3.10. It has fixed support at left and roller at right that allow to move along the positive x axial direction. And a downwards point load of 1500N is applied on top central surface. Also, the effect of the mesh size of continuum elements on the resulting optimized reinforcement layout is investigated. The target volumetric ratio of 0.4% for steel embedded into the continuum concrete are constant in all cases. Initially, the concrete domain is discretized by 2100 continuum elements where the element size equal to 20mm. From the results presented in Fig.3.11 (a), it can be observed that large amount of tensile reinforcing bars are located at the bottom of the concrete domain where flexural failure easily exist. While the top middle zone in which the downwards pressure is applied, a group of steel bars are remained to strengthen concrete and act in compression. Also, double reinforcements are placed in the boundary support regions due to their high concentrated stress. As expected, there is an obvious distribution of diagonal reinforcing bars in tension appears to reinforce the shear part of the deep beam. Since the reinforcing bars are embedded in continuum elements, a denser mesh for a continuum domain leads to a denser truss layout. The cross-sectional area of a bar decreases with the reduction of element size to

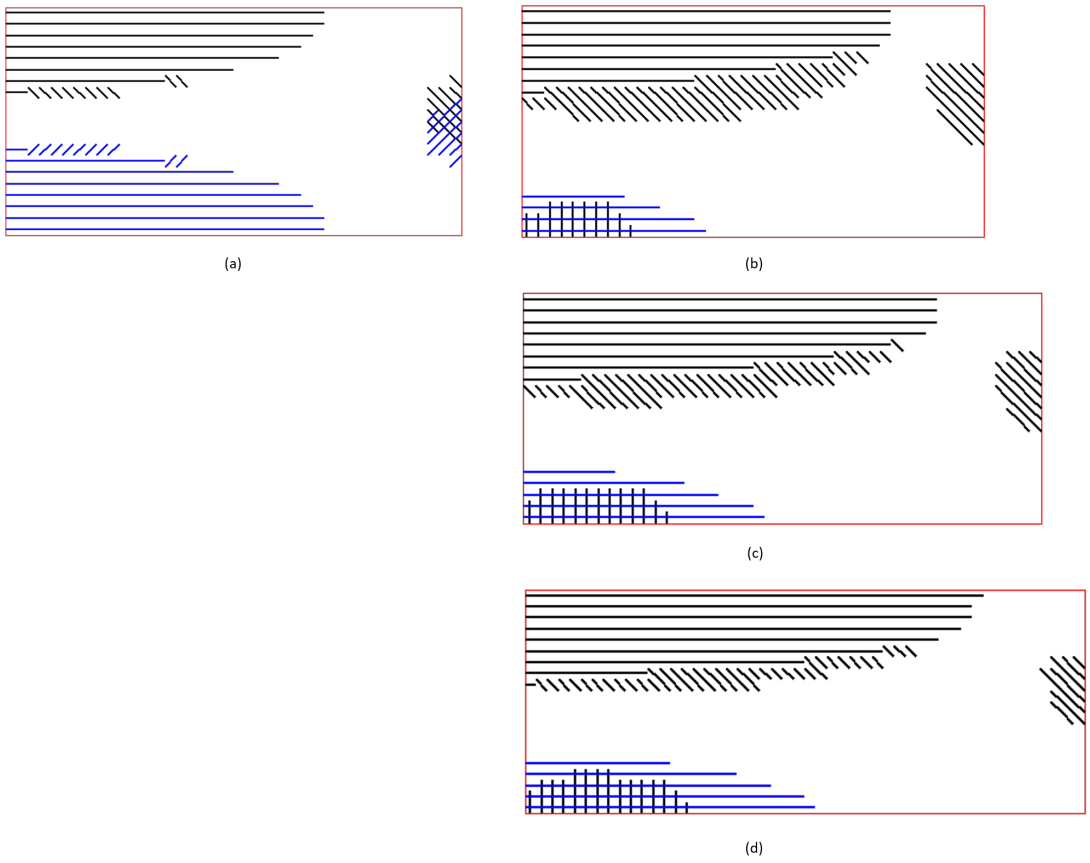

Figure 3.9: Comparison of resulting topologies. (a) Optimized layout without applying the novel update scheme into BESO algorithm. (b) Optimized layout with applying the novel update scheme into BESO algorithm: 2D structure with length-to-height ratio of 8/4. (c) 2D structure with length-to-height ratio of 9/4. (d) 2D structure with length-to-height ratio of 10/4.

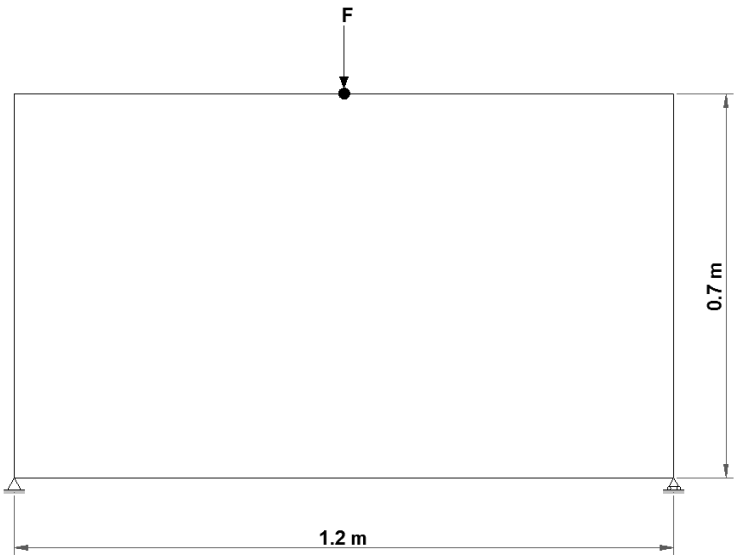

Figure 3.10: A 2D deep beam design domain

ensure the reinforcing ratio in an individual concrete element is constant. It can be observed from Fig.3.11 (a-d) that using a finer finite element mesh, more discrete tension-reinforced bars are distributed to prevent from missing any tensile strain developed in a compression-dominated phase that exceeds the allowable tensile strain for concrete. Simultaneously, for some areas where concrete itself can suffer from the pressure, the volume of steel bar resisting to compression decreases. Particularly in Fig.3.11 (d), tensile-load carrying reinforcing bars exist around the top central region, where the point load applied, which does not exist in other obtained topologies. As mentioned above, although the cross-sectional area of the reinforcing bar may be unrealistic in this paper, it provides a rational reinforcement layout under a limited amount of steel used for designers.

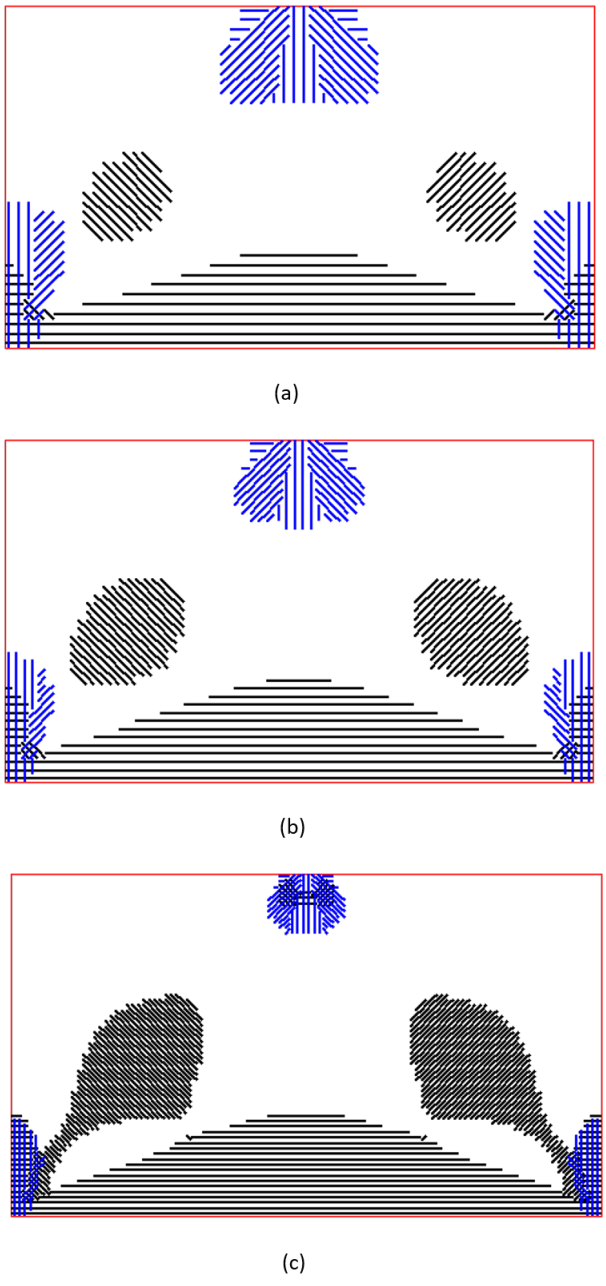

Figure 3.11: Reinforcement layout obtained with various mesh dense discretization for the continuum domain. (a) 2100 (60×35) finite elements. (b) 3024 (72×42) finite elements. (c) 6804 (108×63) finite elements

3.5 Conclusions and discussions

This work proposed an optimization procedure on the basis of BESO approach to design reinforcement layout within a constant concrete domain. Two reinforcing bars modeled as 1D truss elements are embedded in each continuum element along the maximum principal strain and minimum principal strain direction, respectively. A heuristic orientation scheme is designed for rotating the bar into its most efficient orientation so that the resulting reinforcement topology is not limited by the initial truss layout. To just corroborate the implementation of the proposed orientation finding system, only two types of embedded model in which reinforcing bars are located horizontally and vertically or in a diagonal form are considered. Furthermore, a novel scheme of updating design variables apart from the relative ranking of sensitivity numbers is applied to the BESO algorithms to avoid reinforcing regions where concrete can withstand itself, especially for regions suffering from compression.

The optimization algorithms that incorporates volume constraint on steel are implemented in two 2D examples. From the results, it can be observed that reinforcing bars in tension are mainly distributed due to high tensile strains, while in order to strength some critical area with high compressive strain, reinforcement bars in compression are also distributed. Also, the homogenized average strain of each element in a finer mesh condition is more accurate, hence, more truss-continuum elements are detected to have the maximum tensile strain exceeding the allowable tensile strain of concrete. And reinforcing bar appears in more compression-dominant area acting in tension.

Although the cross-sectional area of steel bar that restricted to one type is possibly not practical, the total volumetric ratio of steel amount into the continuum concrete is realistic and the orientation of steel bar is determined. Nevertheless, the current study succeeds in achieving both location and orientation of reinforcing bars playing roles in tension or compression, which provides a valuable suggestion for the regions in a concrete structure to be reinforced by steel.

4

Using Continuous Density-based Optimization Method for Nonlinear Composite Structure

4.1 Introduction

Composite structure has drawn a wide attention from both research and design communities in various areas such as structural engineering and aerospace fields due to the diverse design purpose and increasingly high demand on mechanical characteristic and weight savings. In other words, materials constituting the composites can be placed easily into a free-form combination to achieve a specific and more desirable design, e.g. increase in strength, toughness, erosion resistance and anti-fatigue ability compared to using single material. Currently, a two-phase composite in which one of the materials as a reinforcing part embedded into the other material matrix in the form of strips, sheet, or grids, has become attractive for many practical applications. The material candidates for both phases can be steel, aluminium, polymer, wood or concrete, etc. Therefore, a concurrent need of distributing materials of composites efficiently arises in order to maximize contribution of each material.

The topology optimization technique as an effective tool has been used to design a conceptual structural layout especially with a complex boundary and loading conditions. Initially, extensive research works on implementing topology

optimization on single material with linear elastic property [42, 43, 57]. The resulting truss-like topology can be regarded as a strut-and-tie model based on the compression and tension regions. Also, multiphase linear elastic material optimization has been developed by interpolating the lower bond of design variable to a second material candidate [11, 17]. However, linear-elastic material modeling is inadequate for the realistic design problem when the structural behaviour exceeds the elastic range. Realizing the problem, especially for those material such concrete or soil having unequal strength in compression and tension, studies emerged incorporating different mechanical properties of composite materials into topology optimization[45, 46, 47, 48, 49]. Also, in recent decades, the nonlinear material behaviour has been considered in order to achieve a more reliable design by topology optimization. Initial studies considering topology optimization with material nonlinearity focus on single material problem [27, 58, 59, 60]. In the most recent research, Wallin et al. [61] succeed in combing the finite strain isotropic hardening plasticity with topology optimization. Zhang and Lei [62] take into account the plastic anisotropy when in conjunction with topology optimization. The BESO optimization method is also applied in layout design considering the von Mises isotropic hardening plasticity in [29]. Li et al. [63] proposed a topology optimization procedure incorporated with the von Mises criteria employing various hardening rules to maximize the energy dissipation under cyclic loading.

In the two-phase elastoplastic material optimization, the obtained toplogy significantly depends on the loading condition where is elastic or plastic dominated [24]. However there are few studies considering material nonlinearity for a multiphase optimization problem. For example, Swan and Kosaka [26] presented a framework of continuous structural topology optimization for elasoplastic applications based on the Voigt and Reuss mixing formulation. An approach presented in Bogomolny and Amir's work [25] applied topology optimization method in concrete and steel layout design taking into account both the yield criteria and the post yielding performance. Nakshatrala and Tortorelli [64] stated a framework of distributing the two elastoplastic material phases to optimize energy dissipation under impact loading. Kato et al.[24] developed an analytical sensitivity approach for nonlinear composites topology optimization. However, the von Mises plastic material modeling is adopted in majority aforementioned studies and all

works employ the isotropic hardening rule in which the radius of the yield surface increases based on the accumulated effective plastic strain. While in the kinematic hardening, it remains constant but the centre subsequent yield surface are moved by a shift stress. Particularly, many practical materials such as polycrystalline metals exhibit a combined property of isotropic and kinematic hardenings. In addition, except for the common used yielding criterion of von Mises that is widely applied to model the metal materials, the Drucker-Prager yield criterion is usually used to describe the pressure-dependent material such as concrete or soil [25, 48].

Therefore, due to the increasing demanding of topology optimization technique in efficiently distributing material phases for composite structure, it is necessary to consider more types of hardening rules following multiple yield criteria and incorporate with topology optimization method to achieve a more realistic and reliable design. This study proposed a topology optimization procedure for multiphase material distribution problem when the material candidates are associated with kinematic hardening or mixed isotropic and kinematic hardening with the flexibility of accommodating with different plasticity models. Moreover, the proposed framework also offers the flexibility of assigning different hardening rule to each single material phase by using the design variables to interpolate the permissible yielding stress surface into the topology optimization. For example, the von Mises or the Drucker-Prager plasticity model are applied to both phases but one following the isotropic hardening rule while the kinematic hardening is assigned to the other. To illustrate the advantage of the proposed framework and method, three design examples are tested and the results are presented in this paper. In the first two examples, several material models created in this paper include: 1) the von Mises and the Drucker-Prager yield criterion applied to each phase respectively; 2) the von Mises yield criterion applied to both phases; 3) the Drucker-Prager yield criterion applied to both phases, and particularly, all cases in example 1 employ the kinematic hardening, while in example 2, they employ the combined isotropic/kinematic hardening rule, which enables to investigate the influence of plasticity model on the resulting topology. In the third example, several material models using the same plasticity model for the composite structure but following with various hardening rules, i.e., isotropic, kinematic or

mixed isotropic and kinematic hardening are performed to study whether the post yielding behaviour would affect the optimization results of multiphase material distribution. This work succesfully achieved the above initiatives of incorporating structural analysis with specific multiphase plasticity into topology optimization. The residual equilibriums on an integration point level is defined based on various plastic material modeling. And the corresponding path-dependent sensitivity analysis expression is derived in this paper, by using a path-dependent adjoint method that following the framework described by Michaleris et al. [65]. The method of moving asymptotes (MMA) [66] is utilized to update design variables. Through a comparative study, it points out the importance of considering material properties precisely for multiphase optimization design.

4.2 Material Elastoplasticity

The behavior of some material is initially elastic and become plastic with existence of the irreversible strain when the applied force exceeds the elastic limit, which is known as the elastoplasticity.

4.2.1 Yield Criteria

To describe the material elastoplasticity in this study, two types of yield criterion are considered: the von Mises yield criterion and the Drucker-Prager yield criterion.

The von Mises yielding criterion is widely used to predict the yielding of metals that having equal strength in compression and tension. Whereas for those materials, e.g. rock or soil, the Drucker-Prager yielding criterion is generally employed to consider the hydrostatic pressure dependence. It is obtained by adding a mean stress term on the von Mises yielding based formulation as

$$f = \sqrt{3J_2} + \alpha I_1 - k, \tag{4.1}$$

where the material constant α is equal to zero when it corresponds to the von Mises yield function. And k represents the permissible yielding stress surface, which will be discussed in the next subsection. The first invariant of the stress

tensor I_1 and the second invariant of the deviatoric stress tensor J_2 are written as

$$J_2 = \frac{1}{6}[(\sigma_x - \sigma_y)^2 + (\sigma_y - \sigma_z)^2 + (\sigma_x - \sigma_z)^2] + \tau_{xy}^2 + \tau_{yz}^2 + \tau_{xz}^2, \tag{4.2}$$

and

$$I_1 = \sigma_x + \sigma_y + \sigma_z. \tag{4.3}$$

4.2.2 Hardening Rules

When the plastic loading progresses, the yield stress may increase rather than remain constant according to the plastic deformation, which is called strain hardening. For some applications, the ideal assumption of material with elastic-perfectly-plasticity may not be adequate to simulate the problem, therefore the strain-hardening is essentially to be considered in a two-material topology optimization. Here, three types of hardening models are applied: isotropic, kinematic and combined hardening. In the isotropic hardening model, the yield surface with a fixed central location grows uniformly according to the effective plastic strain. However, the kinematic hardening rule enables the elastic domain stays constant while the subsequent yield surface moves following the strain hardening. Moreover, some materials are generally described by a combination of these two models as follows:

$$k = \sigma_Y + (1 - \phi)H_p e_p, \tag{4.4}$$

where σ_Y denotes the initial yield stress, e_p is the effective plastic strain and the plastic modulus H_p is a constant, as all hardening rules are assumed to be linear in this paper. ϕ is a parameter representing the combined effect for a mixed isotropic/kinematic hardening model. For the isotropic hardening, ϕ equals 0 and 1 for the kinematic hardening.

4.2.3 Elastoplasticity Model

According to the assumption in the small deformation elastoplasticity, the rate of the total strain $\dot{\boldsymbol{\varepsilon}}$ can be decomposed into the rate of the elastic strain $\dot{\boldsymbol{\varepsilon}}^e$ and the plastic strain $\dot{\boldsymbol{\varepsilon}}^p$ as

$$\dot{\boldsymbol{\varepsilon}} = \dot{\boldsymbol{\varepsilon}}^e + \dot{\boldsymbol{\varepsilon}}^p. \tag{4.5}$$

The elastic strain relates to the stress by using the fourth-order constitutive tensor $\mathbf{D}$. And the plastic strain evolves in the direction normal to the flow potential that is associated to the yield function f in this study, which is given by

$$\dot{\boldsymbol{\varepsilon}}^p = \gamma \frac{\partial f}{\partial \boldsymbol{\sigma}}, \tag{4.6}$$

where γ is the non-negative plastic consistency parameter. It is governed by the Kuhn-Tucker conditions, i.e.

$$\gamma f = 0; \quad \gamma \geq 0; \quad f \leq 0. \tag{4.7}$$

4.3 Structural Analysis

4.3.1 Global and Local Residuals

The global equilibrium for the complete structure should be satisfied in the finite element analysis, it can be expressed as

$$\mathbf{R}^n = \mathbf{R}^n_{ext} - \mathbf{R}^n_{int} \tag{4.8}$$

with

$$\begin{aligned} \mathbf{R}^n_{int} &= \sum_{e=1}^{nele} \left(\int_{V_e} \mathbf{B}^T \boldsymbol{\sigma}^n dV_e \right) \\ \mathbf{R}^n_{ext} &= \sum_{e=1}^{nele} \left(\int_{V_e} f^n_B dV_e + \int_{S_e} f^n_S dS_e \right) + P^n \end{aligned} \tag{4.9}$$

where $\mathbf{R}^n$ represents the residual on the global level in loading step n, which equals to the difference of the external applied force $\mathbf{R}^n_{ext}$ and the internal force $\mathbf{R}^n_{int}$ in the same step. $\mathbf{B}$ is the strain-displacement matrix. f_B, f_S and P denote the internal body force, surface traction and the external concentrated load respectively.

Also, the local residuals on each integration point are constructed and required to be sufficiently small throughout the analysis. In this study, four-node quadrilateral plane-stress element with four integration points is utilized. Thus, the

expression of residual $\mathbf{H}$ on the loading increment n for a full structure is formed by embedding the local residuals on each integration point of each element into a global matrix.

$$\begin{aligned}\mathbf{H}^n &= [\mathbf{H}_1^n, \mathbf{H}_2^n, ..., \mathbf{H}_{nele}^n]^T \\ \mathbf{H}_e^n &= [\mathbf{H}_{e1}^n, \mathbf{H}_{e2}^n, \mathbf{H}_{e3}^n, \mathbf{H}_{e4}^n]^T \\ \mathbf{H}_{ei}^n &= \left[\mathbf{H}_{ei1}^n, \mathbf{H}_{ei2}^n, ..., \mathbf{H}_{eij}^n\right]^T\end{aligned} \tag{4.10}$$

where e is the number of elements, i represents the number of integration points, and j corresponds to the number of local residual required on an integration point level based on the specified plastic model and hardening rule.

In the elastic incremental stage, for the material candidate modeled with either the von Mises or the Drucker-Prager yielding criterion, the local residuals $\mathbf{H}_{eij}^n$ are defined in the same formulations. When the elastoplastic material model follows the kinematic or combined hardening rule,

$$\mathbf{H}_{eij}^n = \begin{bmatrix}\mathbf{H}_{ei1}^n \\ \mathbf{H}_{ei2}^n \\ \mathbf{H}_{ei3}^n \\ \mathbf{H}_{ei4}^n\end{bmatrix} = \begin{bmatrix}\boldsymbol{\sigma}_{ei}^n - \boldsymbol{\sigma}_{ei}^{n-1} - \mathbf{D}_e^0 : (\mathbf{B}_e\mathbf{U}_e^n - \mathbf{B}_e\mathbf{U}_e^{n-1}) = 0 \\ \mathbf{a}_{ei}^n - \mathbf{a}_{ei}^{n-1} = 0 \\ e_{p_{ei}}^{\ n} - e_{p_{ei}}^{\ n-1} = 0 \\ \Delta\gamma_{ei}^n = 0\end{bmatrix}. \tag{4.11}$$

When the elastoplastic material model follows the isotropic hardening rule,

$$\mathbf{H}_{eij}^n = \begin{bmatrix}\mathbf{H}_{ei1}^n \\ \mathbf{H}_{ei2}^n \\ \mathbf{H}_{ei3}^n\end{bmatrix} = \begin{bmatrix}\boldsymbol{\sigma}_{ei}^n - \boldsymbol{\sigma}_{ei}^{n-1} - \mathbf{D}_e^0 : (\mathbf{B}_e\mathbf{U}_e^n - \mathbf{B}_e\mathbf{U}_e^{n-1}) = 0 \\ e_{p_{ei}}^{\ n} - e_{p_{ei}}^{\ n-1} = 0 \\ \Delta\gamma_{ei}^n = 0\end{bmatrix}. \tag{4.12}$$

where $\mathbf{U}_e$ is the elemental nodal displacement vector; $\boldsymbol{\sigma}_{ei}$, $\mathbf{a}_{ei}, e_{p_{ei}}$ represent the stress, back stress and the equivalent plastic strain obtained on each integration point, respectively.

However, in the plastic stage, the local residuals for both materials using the von Mises model with kinematic or combined hardening rule are given by

$$\mathbf{H}_{eij}^n = \begin{bmatrix}\mathbf{H}_{ei1}^n \\ \mathbf{H}_{ei2}^n \\ \mathbf{H}_{ei3}^n \\ \mathbf{H}_{ei4}^n\end{bmatrix} = \begin{bmatrix}\boldsymbol{\sigma}_{ei}^n - \boldsymbol{\sigma}_{ei}^{n-1} - \mathbf{D}_e^0 : (\mathbf{B}_e\mathbf{U}_e^n - \mathbf{B}_e\mathbf{U}_e^{n-1}) + 2\mu_e\Delta\gamma_{ei}^n(\frac{\partial f}{\partial \boldsymbol{\eta}})_{ei}^n = 0 \\ \mathbf{a}_{ei}^n - \mathbf{a}_{ei}^{n-1} - \frac{2}{3}\phi H_{p_e}\Delta\gamma_{ei}^n(\frac{\partial f}{\partial \boldsymbol{\eta}})_{ei}^n = 0 \\ e_{p_{ei}}^{\ n} - e_{p_{ei}}^{\ n-1} - \sqrt{\frac{2}{3}}\Delta\gamma_{ei}^n = 0 \\ ||\boldsymbol{\eta}||_{ei}^n - \sqrt{\frac{2}{3}}[\sigma_{Y_e} + (1-\phi)H_{p_e}e_{p_{ei}}^{\ n}] = 0\end{bmatrix} \tag{4.13}$$

the local residuals for both materials using the von Mises model with isotropic hardening rule are given by

$$\mathbf{H}_{eij}^{n} = \begin{bmatrix} \mathbf{H}_{ei1}^{n} \\ \mathbf{H}_{ei2}^{n} \\ \mathbf{H}_{ei3}^{n} \end{bmatrix} = \begin{bmatrix} \boldsymbol{\sigma}_{ei}^{n} - \boldsymbol{\sigma}_{ei}^{n-1} - \mathbf{D}_{e}^{0} : (\mathbf{B}_{e}\mathbf{U}_{e}^{n} - \mathbf{B}_{e}\mathbf{U}_{e}^{n-1}) + 2\mu_{e}\Delta\gamma_{ei}^{n}(\frac{\partial f}{\partial \mathbf{s}})_{ei}^{n} = 0 \\ e_{p_{ei}}^{n} - e_{p_{ei}}^{n-1} - \sqrt{\frac{2}{3}}\Delta\gamma_{ei}^{n} = 0 \\ ||\mathbf{s}||_{ei}^{n} - \sqrt{\frac{2}{3}}[\sigma_{Y\,e} + H_{p_e} e_{p_{ei}}^{n}] = 0 \end{bmatrix} \tag{4.14}$$

the local residuals for both materials using the Drucker-Prager model with kinematic or combined hardening rule are given by

$$\mathbf{H}_{eij}^{n} = \begin{bmatrix} \mathbf{H}_{ei1}^{n} \\ \mathbf{H}_{ei2}^{n} \\ \mathbf{H}_{ei3}^{n} \\ \mathbf{H}_{ei4}^{n} \end{bmatrix} = \begin{bmatrix} \boldsymbol{\sigma}_{ei}^{n} - \boldsymbol{\sigma}_{ei}^{n-1} - \mathbf{D}_{e}^{0} : (\mathbf{B}_{e}\mathbf{U}_{e}^{n} - \mathbf{B}_{e}\mathbf{U}_{e}^{n-1}) + \mathbf{D}_{e}^{0}\Delta\gamma_{ei}^{n}(\frac{\partial f}{\partial \boldsymbol{\sigma}})_{ei}^{n} = 0 \\ \mathbf{a}_{ei}^{n} - \mathbf{a}_{ei}^{n-1} - \frac{2}{3}\phi H_{p_e}\Delta\gamma_{ei}^{n}(\frac{\partial f}{\partial \boldsymbol{\sigma}})_{ei}^{n} = 0 \\ e_{p_{ei}}^{n} - e_{p_{ei}}^{n-1} - \sqrt{\frac{2}{3}}\Delta\gamma_{ei}^{n} = 0 \\ ||\boldsymbol{\eta}||_{ei}^{n} + \sqrt{\frac{2}{3}}\alpha I_{1\,ei}^{n} - \sqrt{\frac{2}{3}}[\sigma_{Y\,e} + (1-\phi) H_{p_e} e_{p_{ei}}^{n}] = 0 \end{bmatrix} \tag{4.15}$$

the local residuals for both materials using the Drucker-Prager model with isotropic hardening rule are given by

$$\mathbf{H}_{eij}^{n} = \begin{bmatrix} \mathbf{H}_{ei1}^{n} \\ \mathbf{H}_{ei2}^{n} \\ \mathbf{H}_{ei3}^{n} \end{bmatrix} = \begin{bmatrix} \boldsymbol{\sigma}_{ei}^{n} - \boldsymbol{\sigma}_{ei}^{n-1} - \mathbf{D}_{e}^{0} : (\mathbf{B}_{e}\mathbf{U}_{e}^{n} - \mathbf{B}_{e}\mathbf{U}_{e}^{n-1}) + \mathbf{D}_{e}^{0}\Delta\gamma_{ei}^{n}(\frac{\partial f}{\partial \boldsymbol{\sigma}})_{ei}^{n} = 0 \\ e_{p_{ei}}^{n} - e_{p_{ei}}^{n-1} - \sqrt{\frac{2}{3}}\Delta\gamma_{ei}^{n} = 0 \\ ||\mathbf{s}||_{ei}^{n} + \sqrt{\frac{2}{3}}\alpha I_{1\,ei}^{n} - \sqrt{\frac{2}{3}}[\sigma_{Y\,e} + H_{p_e} e_{p_{ei}}^{n}] = 0 \end{bmatrix} \tag{4.16}$$

where $\boldsymbol{\eta}$ is the shifted stress deviator defined as the difference between the stress deviator $\mathbf{s}$ and the back stress deviator $\mathbf{a}$, i.e. $\boldsymbol{\eta} = \mathbf{s} - \mathbf{a}$. When the two material phase are associated with various plastic model(one with Drucker-Prager model and the other with von Mises model), and accompanied with various hardening rule (one with kinematic or combined hardening and the other with isotropic hardening), the corresponding residuals are presented as follows:

$$\mathbf{H}_{eij}^{n} = \begin{bmatrix} \mathbf{H}_{ei1}^{n} \\ \mathbf{H}_{ei2}^{n} \\ \mathbf{H}_{ei3}^{n} \\ \mathbf{H}_{ei4}^{n} \end{bmatrix} = \begin{bmatrix} \boldsymbol{\sigma}_{ei}^{n} - \boldsymbol{\sigma}_{ei}^{n-1} - \mathbf{D}_{e}^{0} : (\mathbf{B}_{e}\mathbf{U}_{e}^{n} - \mathbf{B}_{e}\mathbf{U}_{e}^{n-1}) + \mathbf{D}_{e}^{0}\Delta\gamma_{ei}^{n}(\frac{\partial f}{\partial \boldsymbol{\sigma}})_{ei}^{n} = 0 \\ \mathbf{a}_{ei}^{n} - \mathbf{a}_{ei}^{n-1} - \frac{2}{3}\phi_{e} H_{p_e}\Delta\gamma_{ei}^{n}(\frac{\partial f}{\partial \boldsymbol{\sigma}})_{ei}^{n} = 0 \\ e_{p_{ei}}^{n} - e_{p_{ei}}^{n-1} - \sqrt{\frac{2}{3}}\Delta\gamma_{ei}^{n} = 0 \\ ||\boldsymbol{\eta}||_{ei}^{n} + \sqrt{\frac{2}{3}}\alpha_{e} I_{1\,ei}^{n} - \sqrt{\frac{2}{3}}[\sigma_{Y\,e} + (1-\phi_{e}) H_{p_e} e_{p_{ei}}^{n}] = 0 \end{bmatrix} \tag{4.17}$$

where the material constant α_e and the hardening combined effect parameter ϕ_e corresponding to a specified element e are related to the density design variables. Also, as the nature of the hydrostatic pressure is considered in the Drucker-Prager model, the direction of the plastic strain normal to the flow potential is described as

$$\begin{aligned}\frac{\partial f}{\partial \boldsymbol{\sigma}} &= \frac{\partial f}{\partial \boldsymbol{\eta}}\frac{\partial \boldsymbol{\eta}}{\partial \boldsymbol{\sigma}} + \frac{\partial f}{\partial \mathbf{I}_1}\frac{\partial \mathbf{I}_1}{\partial \boldsymbol{\sigma}} \\ &= \frac{\boldsymbol{\eta}}{||\boldsymbol{\eta}||}\mathbf{I}_{dev} + \sqrt{\frac{2}{3}}\alpha\frac{\partial \mathbf{I}_1}{\partial \boldsymbol{\sigma}}\end{aligned} \tag{4.18}$$

while in the previous case presented in Eq.(5.10), based on the von Mises yield criterion, the yield function is defined in a deviatoric space only as the volumetric stress is independent of plastic deformation. Thus the plastic strain evolves in the direction:
for those with kinematic or combined isotropic-kinematic hardening:

$$\frac{\partial f}{\partial \boldsymbol{\eta}} = \frac{\boldsymbol{\eta}}{||\boldsymbol{\eta}||} \tag{4.19}$$

or for those with isotropic hardening:

$$\frac{\partial f}{\partial \mathbf{s}} = \frac{\mathbf{s}}{||\mathbf{s}||} \tag{4.20}$$

In the case of isotropic hardening applied to both materials, the centre of the yielding surface is fixed on a certain point means that the back stress $\mathbf{a}$ does not exist so as the related residual equation in both elastic and plastic stage is eliminated. Correspondingly, only three variables on each integration point are considered, i.e. $\mathbf{v}^n = [\boldsymbol{\sigma}_{ei}^n \quad e_{p_{ei}}^n \quad \Delta\gamma_{ei}^n]$. However, in the kinematic/combined hardening model, the yielding surface moves following the plastic deformation, therefore the required variables would be defined as $\mathbf{v}^n = [\boldsymbol{\sigma}_{ei}^n \quad \mathbf{a}_{ei}^n \quad e_{p_{ei}}^n \quad \Delta\gamma_{ei}^n]$.

4.3.2 Stress Return-Mapping Algorithm

As the flow potential is associated with the yield function here, the plastic strain is then expressed as

$$\dot{\boldsymbol{\epsilon}_{\boldsymbol{p}}} = \gamma\frac{\partial f(\boldsymbol{\sigma}, \mathbf{a}, e_p)}{\partial \boldsymbol{\sigma}} \tag{4.21}$$

When the value of yield function with trial stress is over 0, the structure enter the plastic loading state. Based on the Kuhn-Tucker condition,

$$\dot{f}(\boldsymbol{\sigma}, \mathbf{a}, e_p) = 0, \quad \gamma > 0 \tag{4.22}$$

which means the yield function remains constant during the plastic loading stage. As required that the yield surface remains 0, the following expression can be achieved:

$$\dot{f}(\boldsymbol{\sigma}, \mathbf{a}, e_p) = \frac{\partial f}{\partial \boldsymbol{\sigma}} : \dot{\boldsymbol{\sigma}} + \frac{\partial f}{\partial \mathbf{a}} : \dot{\mathbf{a}} + \frac{\partial f}{\partial e_p} \dot{e_p} = 0 \tag{4.23}$$

Therefore, the plastic consistency parameter γ can be calculated from the rate form of the yield function by writing the function in terms of γ

$$\begin{aligned} \dot{\boldsymbol{\sigma}} &= \mathbf{D} : (\dot{\boldsymbol{\epsilon}} - \dot{\boldsymbol{\epsilon_p}}) = \mathbf{D} : (\dot{\boldsymbol{\epsilon}} - \gamma \frac{\partial f}{\partial \boldsymbol{\sigma}}) \\ \dot{\mathbf{a}} &= \frac{2}{3} \phi H \gamma \frac{\partial f}{\partial \boldsymbol{\sigma}} \\ e_p &= \sqrt{\frac{2}{3}} \gamma \end{aligned} \tag{4.24}$$

By substituting Eq.(4.24) into Eq.(4.23),

$$\frac{\partial f}{\partial \boldsymbol{\sigma}} : \mathbf{D} : \dot{\boldsymbol{\epsilon}} - \frac{\partial f}{\partial \boldsymbol{\sigma}} : \mathbf{D} : \gamma \frac{\partial f}{\partial \boldsymbol{\sigma}} + \frac{\partial f}{\partial \mathbf{a}} : \frac{2}{3} \phi H \gamma \frac{\partial f}{\partial \boldsymbol{\sigma}} + \frac{\partial f}{\partial e_p} \sqrt{\frac{2}{3}} \gamma = 0 \tag{4.25}$$

The plastic consistency parameter can be obtained by solving the above equation as

$$\gamma = \frac{\frac{\partial f}{\partial \boldsymbol{\sigma}} : \mathbf{D} : \dot{\boldsymbol{\epsilon}}}{\frac{\partial f}{\partial \boldsymbol{\sigma}} : \mathbf{D} : \frac{\partial f}{\partial \boldsymbol{\sigma}} - \frac{\partial f}{\partial \mathbf{a}} : \frac{2}{3} \phi H \frac{\partial f}{\partial \boldsymbol{\sigma}} - \sqrt{\frac{2}{3}} \frac{\partial f}{\partial e_p}} \tag{4.26}$$

where the derivative of the yield function with respect to the stress components $\frac{\partial f}{\partial \boldsymbol{\sigma}}$ is defined based on the type of plastic model adopted. The derivative of the yield function with respect to the back stress components $\frac{\partial f}{\partial \mathbf{a}}$ and the equivalent plastic strain e_p can be derived as follows:

$$\begin{aligned} \frac{\partial f}{\partial \mathbf{a}} &= \frac{\partial f}{\partial \boldsymbol{\eta}} \frac{\partial \boldsymbol{\eta}}{\partial \mathbf{a}} = -\frac{\boldsymbol{\eta}}{||\boldsymbol{\eta}||} \\ \frac{\partial f}{\partial e_p} &= -\sqrt{\frac{2}{3}} (1 - \phi) H \end{aligned} \tag{4.27}$$

Hence, by substituting Eq.(4.27), Eq.(4.26) can be further modified as

$$\gamma = \frac{\frac{\partial f}{\partial \boldsymbol{\sigma}} : \mathbf{D} : \dot{\boldsymbol{\epsilon}}}{\frac{\partial f}{\partial \boldsymbol{\sigma}} : \mathbf{D} : \frac{\partial f}{\partial \boldsymbol{\sigma}} + \frac{\boldsymbol{\eta}}{||\boldsymbol{\eta}||} : \frac{2}{3}\phi H \frac{\partial f}{\partial \boldsymbol{\sigma}} + \frac{2}{3}(1-\phi)H} \tag{4.28}$$

In the return-mapping scheme, the first step is to predict the trial magnitude of stress and plastic variables at time step $n+1$ according to the known variables at the former time step n and the incremental strain calculated from the known incremental displacement at time step $n+1$.

$$\begin{aligned} \boldsymbol{\sigma}^{trial} &= \boldsymbol{\sigma}_n + \mathbf{D} : \boldsymbol{\Delta\epsilon} \\ \mathbf{a}^{trial} &= \mathbf{a}_n \\ e_p^{trial} &= e_{p_n} \\ \boldsymbol{\eta}^{trial} &= \mathbf{I}_{dev} : \boldsymbol{\sigma}^{trial} - \mathbf{a}^{trial} \end{aligned} \tag{4.29}$$

If the trial yield function $f^{trial} \leq 0$, the stress and plastic variables are updated equal to the trial values as

$$\begin{aligned} \boldsymbol{\sigma}_{n+1} &= \boldsymbol{\sigma}^{trial} \\ \mathbf{a}_{n+1} &= \mathbf{a}^{trial} \\ e_{p_{n+1}} &= e_p^{trial} \end{aligned} \tag{4.30}$$

If the trial yield function $f^{trial} \geq 0$, then the status of material become plastic, and the stress and plastic variables are corrected by considering the plastic deformation as

$$\begin{aligned} \boldsymbol{\sigma}_{n+1} &= \boldsymbol{\sigma}_n + \mathbf{D} : (\boldsymbol{\Delta\epsilon} - \Delta\gamma \frac{\partial f}{\partial \boldsymbol{\sigma}}) \\ \mathbf{a}_{n+1} &= \mathbf{a}_n + \frac{2}{3}\phi H \Delta\gamma \frac{\partial f}{\partial \boldsymbol{\sigma}} \\ e_{p_{n+1}} &= e_{p_n} + \sqrt{\frac{2}{3}}\Delta\gamma \\ \boldsymbol{\eta}_{n+1} &= \mathbf{I}_{dev} : \boldsymbol{\sigma}_{n+1} - \mathbf{a}_{n+1} \end{aligned} \tag{4.31}$$

Therefore, the yield function at the updated state of the return-mapped point is

$$f_{n+1} = ||\boldsymbol{\eta}_{n+1}|| - \sqrt{\frac{2}{3}}[\sigma_y^0 + (1-\phi)H e_{p_{n+1}}] = 0 \tag{4.32}$$

4.3.3 Elastoplastic Tangent Stiffness

Due to the plastic state, the elastic stiffness in a multidimensional system must be modified to represent the relation between the rates of stress and strain. Following the constitutive relation in a rate form:

$$\dot{\boldsymbol{\sigma}} = \mathbf{D} : \dot{\boldsymbol{\epsilon}} - \mathbf{D} : \dot{\boldsymbol{\epsilon}}_p \tag{4.33}$$

By substituting Eq.(4.28) into Eq.(4.33),

$$\begin{aligned} \dot{\boldsymbol{\sigma}} &= \mathbf{D} : \dot{\boldsymbol{\epsilon}} - \mathbf{D} : \frac{\partial f}{\partial \boldsymbol{\sigma}} \frac{\frac{\partial f}{\partial \boldsymbol{\sigma}} : \mathbf{D} : \dot{\boldsymbol{\epsilon}}}{\frac{\partial f}{\partial \boldsymbol{\sigma}} : \mathbf{D} : \frac{\partial f}{\partial \boldsymbol{\sigma}} + \frac{\boldsymbol{\eta}}{||\boldsymbol{\eta}||} : \frac{2}{3}\phi H \frac{\partial f}{\partial \boldsymbol{\sigma}} + \frac{2}{3}(1-\phi)H} \\ &= [\mathbf{D} - \frac{\mathbf{D} : \frac{\partial f}{\partial \boldsymbol{\sigma}} \otimes \frac{\partial f}{\partial \boldsymbol{\sigma}} : \mathbf{D}}{\frac{\partial f}{\partial \boldsymbol{\sigma}} : \mathbf{D} : \frac{\partial f}{\partial \boldsymbol{\sigma}} + \frac{\boldsymbol{\eta}}{||\boldsymbol{\eta}||} : \frac{2}{3}\phi H \frac{\partial f}{\partial \boldsymbol{\sigma}} + \frac{2}{3}(1-\phi)H}] : \dot{\boldsymbol{\epsilon}} \end{aligned} \tag{4.34}$$

where $\mathbf{D}$ is the elastic stiffness and reduced by the plastic consistency parameter. Therefore, the elastoplastic tangent stiffness can be obtained as

$$\mathbf{D}^{ep} = [\mathbf{D} - \frac{\mathbf{D} : \frac{\partial f}{\partial \boldsymbol{\sigma}} \otimes \frac{\partial f}{\partial \boldsymbol{\sigma}} : \mathbf{D}}{\frac{\partial f}{\partial \boldsymbol{\sigma}} : \mathbf{D} : \frac{\partial f}{\partial \boldsymbol{\sigma}} + \frac{\boldsymbol{\eta}}{||\boldsymbol{\eta}||} : \frac{2}{3}\phi H \frac{\partial f}{\partial \boldsymbol{\sigma}} + \frac{2}{3}(1-\phi)H}] \tag{4.35}$$

Note the expression of the plastic consistency parameter γ and the elastoplastic tangent stiffness $\mathbf{D}^{ep}$ can be determined explicitly by the specified plastic model and hardening.

4.4 Topology Optimization Procedure

4.4.1 Problem statement

For the linear elastic material topology optimization, minimizing the mean compliance is often used as the objective function. While for elastoplastic materials, minimizing the end-compliance or maximizing the total plastic energy is commonly used as the objective function in topology optimization. In this study, the displacement loading method is applied throughout the nonlinear analysis due to its relative stability. And the end-compliance related objective function is achieved by maximizing the final equivalent external load corresponding to the

prescribed displacement. Also, based on the consideration of the material nonlinearity, the optimization statement should be coupled with the global equilibrium and the local residual conditions that satisfied at each step as shown below:

$$\begin{aligned} \min \quad & c(\mathbf{x}) = -\varphi^N \mathbf{P}_{ref} \mathbf{u}^N \\ s.t. \quad & \sum_{e=1}^{nele} v_e x_e \leq V^* \\ & x_{\min} \leq x_e \leq 1, \quad (e = 1, 2, ..., nele) \\ & \mathbf{R}^n(\mathbf{u}^n, \mathbf{u}^{n-1}, \mathbf{v}^n, \mathbf{v}^{n-1}, \mathbf{x}) = 0 \\ & \mathbf{H}^n(\mathbf{u}^n, \mathbf{u}^{n-1}, \mathbf{v}^n, \mathbf{v}^{n-1}, \mathbf{x}) = 0 \\ & n = 1, 2, ..., N, \end{aligned} \tag{4.36}$$

where x_e depicts the elemental design variable updated in each iteration and V^* is the prescribed target volume fraction of the design domain. $\mathbf{P}_{ref}$ is a constant external load vector in which each element corresponding to a degree of freedom. When there is a prescribed displacement applied on a degree of freedom, the corresponding element equals to 1 otherwise will be 0. φ^N denotes the load factor at the final loading step calculated from the global equilibrium, and it is a scalar. The objective function stated in Eq.(6.12) only valid under certain load conditions, and will lead to a complicated sensitivity analysis. Thus, Amir et al. [25] proposed a simplified hybrid approach using the load-controlled concept to generate a more applicable objective function as following: $c(\mathbf{x}) = \mathbf{P}^N \mathbf{u}^N$, but the actual nonlinear analysis is performed through a displacement-controlled method.

4.4.2 Material Interpolation

In this paper, the elastoplastic behaviour of a two-material-phase problem will be interpolated into topology optimization by utilizing the design variable. The elastic constitutive tensor can be written as

$$\mathbf{D} = \lambda \mathbf{1} \otimes \mathbf{1} + 2\mu \mathbf{I} \tag{4.37}$$

with

$$\begin{aligned}
\lambda &= \frac{Ev}{(1+v)(1-2v)} \\
\mu &= \frac{E}{2(1+v)} \\
\mathbf{1} &= [\delta_{ij}] \\
\mathbf{I} &= [I_{ijkl}] = [\frac{1}{2}(\delta_{ik}\delta_{jl} + \delta_{il}\delta_{jk})]
\end{aligned} \tag{4.38}$$

where $\mathbf{1}$ is the second-order unit tensor and $\mathbf{I}$ is the symmetric fourth-order unit tensor. v is the poisson ratio, and from the relationship presented above, it can be observed that the Lame's constants λ and μ are proportional to the Young's modulus E. The following shows the interpolating functions:

$$\begin{aligned}
\lambda_e &= \lambda_{min} + (\lambda_{max} - \lambda_{min})x_e^{p^\lambda} \\
\mu_e &= \mu_{min} + (\mu_{max} - \mu_{min})x_e^{p^\mu} \\
\sigma_{Ye} &= \sigma_{Ymin} + (\sigma_{Ymax} - \sigma_{Ymin})x_e^{p^{\sigma_Y}} \\
H_{p_e} &= H_{p_{min}} + (H_{p_{max}} - H_{p_{min}})x_e^{p^{H_p}},
\end{aligned} \tag{4.39}$$

Particularly, when different plasticity model and hardening rules are adopted by each material phase, e.g., the von Mises model with kinematic hardening is applied to the first material and the second material employs the Drucker-Prager model with isotropic hardening, two more interpolation functions need to be considered as:

$$\begin{aligned}
\alpha_e &= \alpha_{max} - (\alpha_{max} - \alpha_{min})x_e^{p^\alpha} \\
\phi_e &= \phi_{min} + (\phi_{max} - \phi_{min})x_e^{p^\phi},
\end{aligned} \tag{4.40}$$

where the penalization value $p^\lambda = p^\mu = p^{\sigma_Y} = p^{H_p} = p^\alpha = p^\phi = 3$ is assumed throughout this study. Eq.(6.14) is one of the important interpolations proposed in this paper which develops a straightforward approach for adopting different plasticity model and hardening rules for each material phase. In particular, a specific yielding criterion or strain hardening model can be derived as a special case of Eq.(6.14), i.e.when $x_e = 1$ yields a material phase with von Mises yielding criterion ($\alpha_e = \alpha_{min} = 0$) and kinematic hardening ($\phi_e = \phi_{max} = 1$).

4.5 Sensitivity analysis

4.5.1 Adjoint sensitivity analysis

The path-dependent adjoint method is applied to compute the sensitivity of the objective with respect to the design variables. The augmented objective function can be built by adding the global and the local residuals that are infinitely approaching to zero. Also, the objective function c and the global residual $\mathbf{R}$ only depend on the nodal displacement $\mathbf{u}$ and the variable $\mathbf{v}$ respectively.

$$\begin{aligned}\hat{c} &= c(\mathbf{x},\mathbf{u}) + \sum_{n=1}^{N} \boldsymbol{\xi}^{nT}\mathbf{R}^n(\mathbf{u}^n,\mathbf{u}^{n-1},\mathbf{v}^n,\mathbf{v}^{n-1},\mathbf{x}) + \sum_{n=1}^{N} \boldsymbol{\theta}^{nT}\mathbf{H}^n(\mathbf{u}^n,\mathbf{u}^{n-1},\mathbf{v}^n,\mathbf{v}^{n-1},\mathbf{x}) \\ &= c(\mathbf{u}) + \sum_{n=1}^{N} \boldsymbol{\xi}^{nT}\mathbf{R}^n(\mathbf{v}^n) + \sum_{n=1}^{N} \boldsymbol{\theta}^{nT}\mathbf{H}^n(\mathbf{u}^n,\mathbf{u}^{n-1},\mathbf{v}^n,\mathbf{v}^{n-1},\mathbf{x}),\end{aligned} \tag{4.41}$$

where $\boldsymbol{\xi}^n$ and $\boldsymbol{\theta}^n$ are the adjoint vectors calculated during the sensitivity analysis. The differentiation of the objective function c is equivalent to the derivative of the augmented function $\hat{c}$ with respect to design variables, and it can be decomposed into an explicit term and an implicit term

$$\frac{\partial c}{\partial \mathbf{x}} = \frac{\partial \hat{c}}{\partial \mathbf{x}} = \frac{\partial \hat{c}_{exp}}{\partial \mathbf{x}} + \frac{\partial \hat{c}_{imp}}{\partial \mathbf{x}}. \tag{4.42}$$

In order to eliminate the unknown term of derivatives $\frac{\partial \mathbf{u}^n}{\partial \mathbf{x}}$ and $\frac{\partial \mathbf{v}^n}{\partial \mathbf{x}}$, the backward incremental calculation approach is applied to obtain the Lagrange multipliers $\boldsymbol{\theta}^n, \boldsymbol{\xi}^n$ for all increments $n = 1, ..., N$

$$\begin{aligned}\frac{\partial \hat{c}_{imp}}{\partial \mathbf{x}} =& \frac{\partial \hat{c}^N_{imp}}{\partial \mathbf{x}} + \sum_{n=1}^{N-1} \frac{\partial \hat{c}^n_{imp}}{\partial \mathbf{x}} \\ \frac{\partial \hat{c}^N_{imp}}{\partial \mathbf{x}} =& \left(\frac{\partial c}{\partial \mathbf{u}^N} + \boldsymbol{\theta}^{NT}\frac{\partial \mathbf{H}^N}{\partial \mathbf{u}^N}\right)\frac{\partial \mathbf{u}^N}{\partial \mathbf{x}} + \\ & \left(\boldsymbol{\xi}^{NT}\frac{\partial \mathbf{R}^N}{\partial \mathbf{v}^N} + \boldsymbol{\theta}^{NT}\frac{\partial \mathbf{H}^N}{\partial \mathbf{v}^N}\right)\frac{\partial \mathbf{v}^N}{\partial \mathbf{x}} \\ \frac{\partial \hat{c}^n_{imp}}{\partial \mathbf{x}} =& \left(\frac{\partial c}{\partial \mathbf{u}^n} + \boldsymbol{\theta}^{nT}\frac{\partial \mathbf{H}^n}{\partial \mathbf{u}^n} + \boldsymbol{\theta}^{n+1T}\frac{\partial \mathbf{H}^{n+1}}{\partial \mathbf{u}^n}\right)\frac{\partial \mathbf{u}^n}{\partial \mathbf{x}} + \\ & \left(\boldsymbol{\xi}^{nT}\frac{\partial \mathbf{R}^n}{\partial \mathbf{v}^n} + \boldsymbol{\theta}^{nT}\frac{\partial \mathbf{H}^n}{\partial \mathbf{v}^n} + \boldsymbol{\theta}^{n+1T}\frac{\partial \mathbf{H}^{n+1}}{\partial \mathbf{v}^n}\right)\frac{\partial \mathbf{v}^n}{\partial \mathbf{x}}\end{aligned} \tag{4.43}$$

For the final step N:

$$\begin{cases} \dfrac{\partial c}{\partial \mathbf{u}^N} + \boldsymbol{\theta}^{N^T} \dfrac{\partial \mathbf{H}^N}{\partial \mathbf{u}^N} = 0 \\ \boldsymbol{\xi}^{N^T} \dfrac{\partial \mathbf{R}^N}{\partial \mathbf{v}^N} + \boldsymbol{\theta}^{N^T} \dfrac{\partial \mathbf{H}^N}{\partial \mathbf{v}^N} = 0 \end{cases} \tag{4.44}$$

For steps from $n = 1$ to $N - 1$:

$$\begin{cases} \dfrac{\partial c}{\partial \mathbf{u}^n} + \boldsymbol{\theta}^{n^T} \dfrac{\partial \mathbf{H}^n}{\partial \mathbf{u}^n} + \boldsymbol{\theta}^{n+1^T} \dfrac{\partial \mathbf{H}^{n+1}}{\partial \mathbf{u}^n} = 0 \\ \boldsymbol{\xi}^{n^T} \dfrac{\partial \mathbf{R}^n}{\partial \mathbf{v}^n} + \boldsymbol{\theta}^{n^T} \dfrac{\partial \mathbf{H}^n}{\partial \mathbf{v}^n} + \boldsymbol{\theta}^{n+1^T} \dfrac{\partial \mathbf{H}^{n+1}}{\partial \mathbf{v}^n} = 0 \end{cases} \tag{4.45}$$

Therefore, based on the obtained adjoint vector and the derivative of the explicit term, the design sensitivity with respect to the design variables can be written as follows:

$$\frac{\partial c}{\partial \mathbf{x}} = \frac{\partial \hat{c}_{exp}}{\partial \mathbf{x}} = \sum_{n=1}^{N} \boldsymbol{\theta}^{n^T} \frac{\partial \mathbf{H}^n}{\partial \mathbf{x}} \tag{4.46}$$

Furthermore, the derivatives $\frac{\partial c}{\partial \mathbf{u}^N}$, $\frac{\partial \mathbf{H}^n}{\partial \mathbf{u}^n}$, $\frac{\partial \mathbf{H}^{n+1}}{\partial \mathbf{u}^n}$, $\frac{\partial \mathbf{H}^n}{\partial \mathbf{v}^n}$, $\frac{\partial \mathbf{H}^{n+1}}{\partial \mathbf{v}^n}$ and $\frac{\partial \mathbf{R}^n}{\partial \mathbf{v}^n}$ are required to solve the above equilibriums presented in Eq. (6.23) and Eq. (6.24). This will be discussed in the next subsection.

4.5.2 Derivatives calculation

When the elastoplastic material employing kinematic or combined hardening rule, the variables $\mathbf{v}^n$ on integration-point level consist of stresses $\boldsymbol{\sigma}^n$, back stresses $\mathbf{a}^n$, equivalent plastic strain e_p^n and the plastic multiplier $\Delta\gamma^n$, whereas the back stress $\mathbf{a}^n$ is neglected when the isotropic hardening is applied. Corresponding to the material with elasoplastic kinematic or combined hardening, the derivatives in matrix form are given as follows

$$\frac{\partial \mathbf{H}_{ei}^n}{\partial \mathbf{v}_{ei}^n} = \begin{bmatrix} \frac{\partial \mathbf{H}_{ei1}^n}{\partial \boldsymbol{\sigma}_{ei}^n} & \frac{\partial \mathbf{H}_{ei1}^n}{\partial \mathbf{a}_{ei}^n} & \frac{\partial \mathbf{H}_{ei1}^n}{\partial e_{p_{ei}}^n} & \frac{\partial \mathbf{H}_{ei1}^n}{\Delta\gamma_{ei}^n} \\ \frac{\partial \mathbf{H}_{ei2}^n}{\partial \boldsymbol{\sigma}_{ei}^n} & \frac{\partial \mathbf{H}_{ei2}^n}{\partial \mathbf{a}_{ei}^n} & \frac{\partial \mathbf{H}_{ei2}^n}{\partial e_{p_{ei}}^n} & \frac{\partial \mathbf{H}_{ei2}^n}{\Delta\gamma_{ei}^n} \\ \frac{\partial \mathbf{H}_{ei3}^n}{\partial \boldsymbol{\sigma}_{ei}^n} & \frac{\partial \mathbf{H}_{ei3}^n}{\partial \mathbf{a}_{ei}^n} & \frac{\partial \mathbf{H}_{ei3}^n}{\partial e_{p_{ei}}^n} & \frac{\partial \mathbf{H}_{ei3}^n}{\Delta\gamma_{ei}^n} \\ \frac{\partial \mathbf{H}_{ei4}^n}{\partial \boldsymbol{\sigma}_{ei}^n} & \frac{\partial \mathbf{H}_{ei4}^n}{\partial \mathbf{a}_{ei}^n} & \frac{\partial \mathbf{H}_{ei4}^n}{\partial e_{p_{ei}}^n} & \frac{\partial \mathbf{H}_{ei4}^n}{\Delta\gamma_{ei}^n} \end{bmatrix} \tag{4.47}$$

$$\frac{\partial \mathbf{H}_{ei}^n}{\partial \mathbf{u}_e^n} = \begin{bmatrix} \frac{\partial \mathbf{H}_{ei1}^n}{\partial \mathbf{u}_e^n} & \frac{\partial \mathbf{H}_{ei2}^n}{\partial \mathbf{u}_e^n} & \frac{\partial \mathbf{H}_{ei3}^n}{\partial \mathbf{u}_e^n} & \frac{\partial \mathbf{H}_{ei4}^n}{\partial \mathbf{u}_e^n} \end{bmatrix}^T \tag{4.48}$$

$$\frac{\partial \mathbf{H}_{ei}^{n}}{\partial x_e} = \begin{bmatrix} \frac{\partial \mathbf{H}_{ei1}^{n}}{\partial x_e} & \frac{\partial \mathbf{H}_{ei2}^{n}}{\partial x_e} & \frac{\partial \mathbf{H}_{ei3}^{n}}{\partial x_e} & \frac{\partial \mathbf{H}_{ei4}^{n}}{\partial x_e} \end{bmatrix}^T \tag{4.49}$$

$$\frac{\partial \mathbf{R}_{e}^{n}}{\partial \mathbf{v}_{ei}^{n}} = \begin{bmatrix} \frac{\partial \mathbf{R}_{e}^{n}}{\partial \boldsymbol{\sigma}_{ei}^{n}} & \frac{\partial \mathbf{R}_{e}^{n}}{\partial \mathbf{a}_{ei}^{n}} & \frac{\partial \mathbf{R}_{e}^{n}}{\partial e_{p_{ei}}^{n}} & \frac{\partial \mathbf{R}_{e}^{n}}{\Delta \gamma_{ei}^{n}} \end{bmatrix} \tag{4.50}$$

When the material response stays in the elastic stage:

$$\frac{\partial \mathbf{H}_{ei}^{n}}{\partial \mathbf{v}_{ei}^{n}} = \begin{bmatrix} \mathbf{I} & \mathbf{0} & \mathbf{0} & \mathbf{0} \\ \mathbf{0} & \mathbf{I} & \mathbf{0} & \mathbf{0} \\ \mathbf{0} & \mathbf{0} & 1 & 0 \\ \mathbf{0} & \mathbf{0} & 0 & 1 \end{bmatrix} \tag{4.51}$$

$$\frac{\partial \mathbf{H}_{ei}^{n}}{\partial x_e} = \begin{bmatrix} -\frac{\partial \mathbf{D}_{e}^{0}}{\partial x_e} : (\mathbf{B}_{ei}\mathbf{u}_{e}^{n} - \mathbf{B}_{ei}\mathbf{u}_{e}^{n-1}) & \mathbf{0} & 0 & 0 \end{bmatrix}^T \tag{4.52}$$

Corresponding to the material with elasoplastic isotropic hardening, the derivatives in matrix form are given as follows

$$\frac{\partial \mathbf{H}_{ei}^{n}}{\partial \mathbf{v}_{ei}^{n}} = \begin{bmatrix} \frac{\partial \mathbf{H}_{ei1}^{n}}{\partial \sigma_{ei}^{n}} & \frac{\partial \mathbf{H}_{ei1}^{n}}{\partial e_{p_{ei}}^{n}} & \frac{\partial \mathbf{H}_{ei1}^{n}}{\Delta \gamma_{ei}^{n}} \\ \frac{\partial \mathbf{H}_{ei3}^{n}}{\partial \sigma_{ei}^{n}} & \frac{\partial \mathbf{H}_{ei3}^{n}}{\partial e_{p_{ei}}^{n}} & \frac{\partial \mathbf{H}_{ei3}^{n}}{\Delta \gamma_{ei}^{n}} \\ \frac{\partial \mathbf{H}_{ei4}^{n}}{\partial \sigma_{ei}^{n}} & \frac{\partial \mathbf{H}_{ei4}^{n}}{\partial e_{p_{ei}}^{n}} & \frac{\partial \mathbf{H}_{ei4}^{n}}{\Delta \gamma_{ei}^{n}} \end{bmatrix} \tag{4.53}$$

$$\frac{\partial \mathbf{H}_{ei}^{n}}{\partial \mathbf{u}_{e}^{n}} = \begin{bmatrix} \frac{\partial \mathbf{H}_{ei1}^{n}}{\partial \mathbf{u}_{e}^{n}} & \frac{\partial \mathbf{H}_{ei2}^{n}}{\partial \mathbf{u}_{e}^{n}} & \frac{\partial \mathbf{H}_{ei3}^{n}}{\partial \mathbf{u}_{e}^{n}} \end{bmatrix}^T \tag{4.54}$$

$$\frac{\partial \mathbf{H}_{ei}^{n}}{\partial x_e} = \begin{bmatrix} \frac{\partial \mathbf{H}_{ei1}^{n}}{\partial x_e} & \frac{\partial \mathbf{H}_{ei2}^{n}}{\partial x_e} & \frac{\partial \mathbf{H}_{ei3}^{n}}{\partial x_e} \end{bmatrix}^T \tag{4.55}$$

$$\frac{\partial \mathbf{R}_{e}^{n}}{\partial \mathbf{v}_{ei}^{n}} = \begin{bmatrix} \frac{\partial \mathbf{R}_{e}^{n}}{\partial \sigma_{ei}^{n}} & \frac{\partial \mathbf{R}_{e}^{n}}{\partial e_{p_{ei}}^{n}} & \frac{\partial \mathbf{R}_{e}^{n}}{\Delta \gamma_{ei}^{n}} \end{bmatrix} \tag{4.56}$$

When the material response stays in the elastic stage:

$$\frac{\partial \mathbf{H}_{ei}^{n}}{\partial \mathbf{v}_{ei}^{n}} = \begin{bmatrix} \mathbf{I} & \mathbf{0} & \mathbf{0} \\ \mathbf{0} & 1 & 0 \\ \mathbf{0} & 0 & 1 \end{bmatrix} \tag{4.57}$$

$$\frac{\partial \mathbf{H}_{ei}^{n}}{\partial x_e} = \begin{bmatrix} -\frac{\partial \mathbf{D}_{e}^{0}}{\partial x_e} : (\mathbf{B}_{ei}\mathbf{u}_{e}^{n} - \mathbf{B}_{ei}\mathbf{u}_{e}^{n-1}) & 0 & 0 \end{bmatrix}^T \tag{4.58}$$

In the plastic stage, for both material modelled with von Mises yield criterion employing kinematic or combined hardening, the derivatives of the local residual

with respect to the variable $\mathbf{v}$ and the design variable $\mathbf{x}$ can be derived as follows

$$\frac{\partial \mathbf{H}_{ei}^{n}}{\partial \mathbf{v}_{ei}^{n}} = \begin{bmatrix} \mathbf{I} + 2\mu_e \Delta\gamma_{ei}^{n} (\frac{\partial f}{\partial \boldsymbol{\eta}\partial \boldsymbol{\sigma}})_{ei}^{n} & 2\mu_e \Delta\gamma_{ei}^{n} (\frac{\partial f}{\partial \boldsymbol{\eta}\partial \mathbf{a}})_{ei}^{n} & \mathbf{0} & 2\mu_e (\frac{\partial f}{\partial \boldsymbol{\eta}})_{ei}^{n} \\ -\frac{2}{3}\phi H_{p_e} \Delta\gamma_{ei}^{n} (\frac{\partial f}{\partial \boldsymbol{\eta}\partial \boldsymbol{\sigma}})_{ei}^{n} & \mathbf{I} - \frac{2}{3}\phi H_{p_e} \Delta\gamma_{ei}^{n} (\frac{\partial f}{\partial \boldsymbol{\eta}\partial \mathbf{a}})_{ei}^{n} & \mathbf{0} & -\frac{2}{3}\phi H_{p_e} (\frac{\partial f}{\partial \boldsymbol{\eta}})_{ei}^{n} \\ \mathbf{0} & \mathbf{0} & 1 & -\sqrt{\frac{2}{3}} \\ (\frac{\partial f}{\partial \boldsymbol{\eta}})_{ei}^{n} & -(\frac{\partial f}{\partial \boldsymbol{\eta}})_{ei}^{n} & -\sqrt{\frac{2}{3}}(1-\phi) H_{p_e} & 0 \end{bmatrix} \tag{4.59}$$

$$\frac{\partial \mathbf{H}_{ei}^{n}}{\partial x_e} = \begin{bmatrix} -\frac{\partial \mathbf{D}_e^0}{\partial x_e} : (\mathbf{B}_{ei}\mathbf{u}_e^n - \mathbf{B}_{ei}\mathbf{u}_e^{n-1}) + 2\Delta\gamma_{ei}^{n} (\frac{\partial f}{\partial \boldsymbol{\eta}})_{ei}^{n} \frac{\partial \mu_e}{\partial x_e} \\ -\frac{2}{3}\phi \frac{\partial H_{p_e}}{\partial x_e} \Delta\gamma_{ei}^{n} (\frac{\partial f}{\partial \boldsymbol{\eta}})_{ei}^{n} \\ 0 \\ -\sqrt{\frac{2}{3}} \frac{\partial \sigma_{y_e}}{\partial x_e} - \sqrt{\frac{2}{3}}(1-\phi) \frac{\partial H_{p_e}}{\partial x_e} {e_p}_{ei}^{n} \end{bmatrix} \tag{4.60}$$

For both material modelled with von Mises yield criterion employing isotropic hardening, the corresponding derivatives become

$$\frac{\partial \mathbf{H}_{ei}^{n}}{\partial \mathbf{v}_{ei}^{n}} = \begin{bmatrix} \mathbf{I} + 2\mu_e \Delta\gamma_{ei}^{n} (\frac{\partial f}{\partial \mathbf{s}\partial \boldsymbol{\sigma}})_{ei}^{n} & \mathbf{0} & 2\mu_e (\frac{\partial f}{\partial \mathbf{s}})_{ei}^{n} \\ \mathbf{0} & 1 & -\sqrt{\frac{2}{3}} \\ (\frac{\partial f}{\partial \mathbf{s}})_{ei}^{n} & -\sqrt{\frac{2}{3}} H_{p_e} & 0 \end{bmatrix} \tag{4.61}$$

$$\frac{\partial \mathbf{H}_{ei}^{n}}{\partial x_e} = \begin{bmatrix} -\frac{\partial \mathbf{D}_e^0}{\partial x_e} : (\mathbf{B}_{ei}\mathbf{u}_e^n - \mathbf{B}_{ei}\mathbf{u}_e^{n-1}) + 2\Delta\gamma_{ei}^{n} (\frac{\partial f}{\partial \boldsymbol{s}})_{ei}^{n} \frac{\partial \mu_e}{\partial x_e} \\ 0 \\ -\sqrt{\frac{2}{3}} \frac{\partial \sigma_{y_e}}{\partial x_e} - \sqrt{\frac{2}{3}} \frac{\partial H_{p_e}}{\partial x_e} {e_p}_{ei}^{n} \end{bmatrix} \tag{4.62}$$

For both material modelled with von Mises yield criterion employing isotropic hardening for one phase and kinematic hardening for the other, the corresponding derivatives become

$$\frac{\partial \mathbf{H}_{ei}^{n}}{\partial \mathbf{v}_{ei}^{n}} = \begin{bmatrix} \mathbf{I} + 2\mu_e \Delta\gamma_{ei}^{n} (\frac{\partial f}{\partial \boldsymbol{\eta}\partial \boldsymbol{\sigma}})_{ei}^{n} & 2\mu_e \Delta\gamma_{ei}^{n} (\frac{\partial f}{\partial \boldsymbol{\eta}\partial \mathbf{a}})_{ei}^{n} & \mathbf{0} & 2\mu_e (\frac{\partial f}{\partial \boldsymbol{\eta}})_{ei}^{n} \\ -\frac{2}{3}\phi_e H_{p_e} \Delta\gamma_{ei}^{n} (\frac{\partial f}{\partial \boldsymbol{\eta}\partial \boldsymbol{\sigma}})_{ei}^{n} & \mathbf{I} - \frac{2}{3}\phi_e H_{p_e} \Delta\gamma_{ei}^{n} (\frac{\partial f}{\partial \boldsymbol{\eta}\partial \mathbf{a}})_{ei}^{n} & \mathbf{0} & -\frac{2}{3}\phi_e H_{p_e} (\frac{\partial f}{\partial \boldsymbol{\eta}})_{ei}^{n} \\ \mathbf{0} & \mathbf{0} & 1 & -\sqrt{\frac{2}{3}} \\ (\frac{\partial f}{\partial \boldsymbol{\eta}})_{ei}^{n} & -(\frac{\partial f}{\partial \boldsymbol{\eta}})_{ei}^{n} & -\sqrt{\frac{2}{3}}(1-\phi_e) H_{p_e} & 0 \end{bmatrix} \tag{4.63}$$

$$\frac{\partial \mathbf{H}_{ei}^{n}}{\partial x_e} = \begin{bmatrix} -\frac{\partial \mathbf{D}_e^0}{\partial x_e} : (\mathbf{B}_{ei}\mathbf{u}_e^n - \mathbf{B}_{ei}\mathbf{u}_e^{n-1}) + 2\Delta\gamma_{ei}^{n} (\frac{\partial f}{\partial \boldsymbol{\eta}})_{ei}^{n} \frac{\partial \mu_e}{\partial x_e} \\ -\frac{2}{3}\phi_e \frac{\partial H_{p_e}}{\partial x_e} \Delta\gamma_{ei}^{n} (\frac{\partial f}{\partial \boldsymbol{\eta}})_{ei}^{n} - \frac{2}{3} \frac{\partial \phi_e}{\partial x_e} H_{p_e} \Delta\gamma_{ei}^{n} (\frac{\partial f}{\partial \boldsymbol{\eta}})_{ei}^{n} \\ 0 \\ -\sqrt{\frac{2}{3}} \frac{\partial \sigma_{y_e}}{\partial x_e} - \sqrt{\frac{2}{3}}(1-\phi_e) \frac{\partial H_{p_e}}{\partial x_e} {e_p}_{ei}^{n} + \sqrt{\frac{2}{3}} \frac{\partial \phi_e}{\partial x_e} H_{p_e} {e_p}_{ei}^{n} \end{bmatrix} \tag{4.64}$$

According to Eq.(4.19) and Eq.(4.20), the derivatives shown below can be derived as

$$
\begin{aligned}
(\frac{\partial f}{\partial \boldsymbol{\eta}\partial \boldsymbol{\sigma}})^n_{ei} &= \frac{1}{||\boldsymbol{\eta}||^n_{ei}}[\mathbf{I}_{dev} - (\frac{\boldsymbol{\eta}}{||\boldsymbol{\eta}||})^n_{ei} \otimes (\frac{\boldsymbol{\eta}}{||\boldsymbol{\eta}||})^n_{ei}] \\
(\frac{\partial f}{\partial \boldsymbol{\eta}\partial \mathbf{a}})^n_{ei} &= -\frac{1}{||\boldsymbol{\eta}||^n_{ei}}[\mathbf{I} - (\frac{\boldsymbol{\eta}}{||\boldsymbol{\eta}||})^n_{ei} \otimes (\frac{\boldsymbol{\eta}}{||\boldsymbol{\eta}||})^n_{ei}] \\
(\frac{\partial f}{\partial \mathbf{s}\partial \boldsymbol{\sigma}})^n_{ei} &= \frac{1}{||\mathbf{s}||^n_{ei}}[\mathbf{I}_{dev} - (\frac{\mathbf{s}}{||\mathbf{s}||})^n_{ei} \otimes (\frac{\mathbf{s}}{||\mathbf{s}||})^n_{ei}]
\end{aligned}
\tag{4.65}
$$

where $\mathbf{I}_{dev} = \mathbf{I} - \frac{1}{3}\mathbf{1} \otimes \mathbf{1}$ is the unit deviatoric tensor of the fourth-order.

For both material modelled with Drucker-Prager yield criterion employing kinematic or combined hardening, the corresponding derivatives become

$$
\frac{\partial \mathbf{H}^n_{ei}}{\partial \mathbf{v}^n_{ei}} = \begin{bmatrix}
\mathbf{I} + \mathbf{D}^0_e \Delta\gamma^n_{ei}(\frac{\partial f}{\partial \boldsymbol{\sigma}\partial \boldsymbol{\sigma}})^n_{ei} & \mathbf{D}^0_e \Delta\gamma^n_{ei}(\frac{\partial f}{\partial \boldsymbol{\sigma}\partial \mathbf{a}})^n_{ei} & \mathbf{0} & \mathbf{D}^0_e(\frac{\partial f}{\partial \boldsymbol{\sigma}})^n_{ei} \\
-\frac{2}{3}\phi H_{p_e}\Delta\gamma^n_{ei}(\frac{\partial f}{\partial \boldsymbol{\sigma}\partial \boldsymbol{\sigma}})^n_{ei} & \mathbf{I} - \frac{2}{3}\phi H_{p_e}\Delta\gamma^n_{ei}(\frac{\partial f}{\partial \boldsymbol{\sigma}\partial \mathbf{a}})^n_{ei} & \mathbf{0} & -\frac{2}{3}\phi H_{p_e}(\frac{\partial f}{\partial \boldsymbol{\sigma}})^n_{ei} \\
\mathbf{0} & \mathbf{0} & 1 & -\sqrt{\frac{2}{3}} \\
(\frac{\partial f}{\partial \boldsymbol{\eta}})^n_{ei} + \sqrt{\frac{2}{3}}\alpha\frac{\partial {I_1}^n_{ei}}{\partial \boldsymbol{\sigma}^n_{ei}} & -(\frac{\partial f}{\partial \boldsymbol{\eta}})^n_{ei} & -\sqrt{\frac{2}{3}}(1-\phi)H_{p_e} & 0
\end{bmatrix}
\tag{4.66}
$$

$$
\frac{\partial \mathbf{H}^n_{ei}}{\partial x_e} = \begin{bmatrix}
-\frac{\partial \mathbf{D}^0_e}{\partial x_e} : (\mathbf{B}_{ei}\mathbf{u}^n_e - \mathbf{B}_{ei}\mathbf{u}^{n-1}_e) + \frac{\partial \mathbf{D}^0_e}{\partial x_e}\Delta\gamma^n_{ei}(\frac{\partial f}{\partial \boldsymbol{\sigma}})^n_{ei} \\
-\frac{2}{3}\phi\frac{\partial H_{p_e}}{\partial x_e}\Delta\gamma^n_{ei}(\frac{\partial f}{\partial \boldsymbol{\sigma}})^n_{ei} \\
0 \\
-\sqrt{\frac{2}{3}}\frac{\partial \sigma_{y_e}}{\partial x_e} - \sqrt{\frac{2}{3}}(1-\phi)\frac{\partial H_{p_e}}{\partial x_e}{e_p}^n_{ei}
\end{bmatrix}
\tag{4.67}
$$

For both material modelled with Drucker-Prager yield criterion employing isotropic hardening, the corresponding derivatives become

$$
\frac{\partial \mathbf{H}^n_{ei}}{\partial \mathbf{v}^n_{ei}} = \begin{bmatrix}
\mathbf{I} + \mathbf{D}^0_e \Delta\gamma^n_{ei}(\frac{\partial f}{\partial \boldsymbol{\sigma}\partial \boldsymbol{\sigma}})^n_{ei} & \mathbf{0} & \mathbf{D}^0_e(\frac{\partial f}{\partial \boldsymbol{\sigma}})^n_{ei} \\
\mathbf{0} & 1 & -\sqrt{\frac{2}{3}} \\
(\frac{\partial f}{\partial \mathbf{s}})^n_{ei} + \sqrt{\frac{2}{3}}\alpha\frac{\partial {I_1}^n_{ei}}{\partial \boldsymbol{\sigma}^n_{ei}} & -\sqrt{\frac{2}{3}}H_{p_e} & 0
\end{bmatrix}
\tag{4.68}
$$

$$
\frac{\partial \mathbf{H}^n_{ei}}{\partial x_e} = \begin{bmatrix}
-\frac{\partial \mathbf{D}^0_e}{\partial x_e} : (\mathbf{B}_{ei}\mathbf{u}^n_e - \mathbf{B}_{ei}\mathbf{u}^{n-1}_e) + \frac{\partial \mathbf{D}^0_e}{\partial x_e}\Delta\gamma^n_{ei}(\frac{\partial f}{\partial \boldsymbol{\sigma}})^n_{ei} \\
0 \\
-\sqrt{\frac{2}{3}}\frac{\partial \sigma_{y_e}}{\partial x_e} - \sqrt{\frac{2}{3}}\frac{\partial H_{p_e}}{\partial x_e}{e_p}^n_{ei}
\end{bmatrix}
\tag{4.69}
$$

For both material modelled with Drucker-Prager yield criterion employing isotropic hardening for one phase and kinematic hardening for the other, the corresponding

derivatives become

$$\frac{\partial \mathbf{H}_{ei}^n}{\partial \mathbf{v}_{ei}^n} = \begin{bmatrix} \mathbf{I} + \mathbf{D}_e^0 \Delta\gamma_{ei}^n (\frac{\partial f}{\partial \boldsymbol{\sigma} \partial \boldsymbol{\sigma}})_{ei}^n & \mathbf{D}_e^0 \Delta\gamma_{ei}^n (\frac{\partial f}{\partial \boldsymbol{\sigma} \partial \mathbf{a}})_{ei}^n & \mathbf{0} & \mathbf{D}_e^0 (\frac{\partial f}{\partial \boldsymbol{\sigma}})_{ei}^n \\ -\frac{2}{3}\phi_e H_{p_e} \Delta\gamma_{ei}^n (\frac{\partial f}{\partial \boldsymbol{\sigma} \partial \boldsymbol{\sigma}})_{ei}^n & \mathbf{I} - \frac{2}{3}\phi_e H_{p_e} \Delta\gamma_{ei}^n (\frac{\partial f}{\partial \boldsymbol{\sigma} \partial \mathbf{a}})_{ei}^n & \mathbf{0} & -\frac{2}{3}\phi_e H_{p_e} (\frac{\partial f}{\partial \boldsymbol{\sigma}})_{ei}^n \\ \mathbf{0} & \mathbf{0} & 1 & -\sqrt{\frac{2}{3}} \\ (\frac{\partial f}{\partial \boldsymbol{\eta}})_{ei}^n + \sqrt{\frac{2}{3}} \alpha \frac{\partial {I_1}_{ei}^n}{\partial \boldsymbol{\sigma}_{ei}^n} & -(\frac{\partial f}{\partial \boldsymbol{\eta}})_{ei}^n & -\sqrt{\frac{2}{3}}(1-\phi_e) H_{p_e} & 0 \end{bmatrix} \tag{4.70}$$

$$\frac{\partial \mathbf{H}_{ei}^n}{\partial x_e} = \begin{bmatrix} -\frac{\partial \mathbf{D}_e^0}{\partial x_e} : (\mathbf{B}_{ei}\mathbf{u}_e^n - \mathbf{B}_{ei}\mathbf{u}_e^{n-1}) + \frac{\partial \mathbf{D}_e^0}{\partial x_e} \Delta\gamma_{ei}^n (\frac{\partial f}{\partial \boldsymbol{\sigma}})_{ei}^n \\ -\frac{2}{3}\phi_e \frac{\partial H_{p_e}}{\partial x_e} \Delta\gamma_{ei}^n (\frac{\partial f}{\partial \boldsymbol{\sigma}})_{ei}^n - \frac{2}{3}\frac{\partial \phi_e}{\partial x_e} H_{p_e} \Delta\gamma_{ei}^n (\frac{\partial f}{\partial \boldsymbol{\sigma}})_{ei}^n \\ 0 \\ -\sqrt{\frac{2}{3}}\frac{\partial \sigma_{y_e}}{\partial x_e} - \sqrt{\frac{2}{3}}(1-\phi_e)\frac{\partial H_{p_e}}{\partial x_e} {e_p}_{ei}^n + \sqrt{\frac{2}{3}}\frac{\partial \phi_e}{\partial x_e} H_{p_e} {e_p}_{ei}^n \end{bmatrix} \tag{4.71}$$

Since the volumetric parts of stress (first invariant of stress tensor) I_1 is a first-order differential equation in terms of σ, the following expression $\frac{\partial f}{\partial \sigma \partial \sigma}$ and $\frac{\partial f}{\partial \sigma \partial \mathbf{a}}$ are equivalent to $\frac{\partial f}{\partial \eta \partial \sigma}$ and $\frac{\partial f}{\partial \eta \partial \mathbf{a}}$ as stated in Eq.(6.35).

When each material phase adopts a different plastic model (e.g. the von Mises model for one phase while the Drucker-Prager model for the other) and both phases employ kinematic or combined hardening, the corresponding derivatives become

$$\frac{\partial \mathbf{H}_{ei}^n}{\partial \mathbf{v}_{ei}^n} = \begin{bmatrix} \mathbf{I} + \mathbf{D}_e^0 \Delta\gamma_{ei}^n (\frac{\partial f}{\partial \boldsymbol{\sigma} \partial \boldsymbol{\sigma}})_{ei}^n & \mathbf{D}_e^0 \Delta\gamma_{ei}^n (\frac{\partial f}{\partial \boldsymbol{\sigma} \partial \mathbf{a}})_{ei}^n & \mathbf{0} & \mathbf{D}_e^0 (\frac{\partial f}{\partial \boldsymbol{\sigma}})_{ei}^n \\ -\frac{2}{3}\phi H_{p_e} \Delta\gamma_{ei}^n (\frac{\partial f}{\partial \boldsymbol{\sigma} \partial \boldsymbol{\sigma}})_{ei}^n & \mathbf{I} - \frac{2}{3}\phi H_{p_e} \Delta\gamma_{ei}^n (\frac{\partial f}{\partial \boldsymbol{\sigma} \partial \mathbf{a}})_{ei}^n & \mathbf{0} & -\frac{2}{3}\phi H_{p_e} (\frac{\partial f}{\partial \boldsymbol{\sigma}})_{ei}^n \\ \mathbf{0} & \mathbf{0} & 1 & -\sqrt{\frac{2}{3}} \\ (\frac{\partial f}{\partial \boldsymbol{\eta}})_{ei}^n + \sqrt{\frac{2}{3}} \alpha_e \frac{\partial {I_1}_{ei}^n}{\partial \boldsymbol{\sigma}_{ei}^n} & -(\frac{\partial f}{\partial \boldsymbol{\eta}})_{ei}^n & -\sqrt{\frac{2}{3}}(1-\phi) H_{p_e} & 0 \end{bmatrix} \tag{4.72}$$

$$\frac{\partial \mathbf{H}_{ei}^n}{\partial x_e} = \begin{bmatrix} -\frac{\partial \mathbf{D}_e^0}{\partial x_e} : (\mathbf{B}_{ei}\mathbf{u}_e^n - \mathbf{B}_{ei}\mathbf{u}_e^{n-1}) + \mathbf{D}_e^0 \Delta\gamma_{ei}^n (\frac{\partial f}{\partial \boldsymbol{\sigma}_{ei} \partial x_e})^n + \frac{\partial \mathbf{D}_e^0}{\partial x_e} \Delta\gamma_{ei}^n (\frac{\partial f}{\partial \boldsymbol{\sigma}})_{ei}^n \\ -\frac{2}{3}\phi \frac{\partial H_{p_e}}{\partial x_e} \Delta\gamma_{ei}^n (\frac{\partial f}{\partial \boldsymbol{\sigma}})_{ei}^n - \frac{2}{3}\phi H_{p_e} \Delta\gamma_{ei}^n (\frac{\partial f}{\partial \boldsymbol{\sigma}_{ei} \partial x_e})^n \\ 0 \\ -\sqrt{\frac{2}{3}}\frac{\partial \sigma_{y_e}}{\partial x_e} - \sqrt{\frac{2}{3}}(1-\phi)\frac{\partial H_{p_e}}{\partial x_e} {e_p}_{ei}^n + \sqrt{\frac{2}{3}} {I_1}_{ei}^n \frac{\partial \alpha_e}{\partial x_e} \end{bmatrix} \tag{4.73}$$

When each material phase adopts a different plastic model and both phases employ isotropic hardening, the corresponding derivatives become

$$\frac{\partial \mathbf{H}_{ei}^n}{\partial \mathbf{v}_{ei}^n} = \begin{bmatrix} \mathbf{I} + \mathbf{D}_e^0 \Delta\gamma_{ei}^n (\frac{\partial f}{\partial \boldsymbol{\sigma} \partial \boldsymbol{\sigma}})_{ei}^n & \mathbf{0} & \mathbf{D}_e^0 (\frac{\partial f}{\partial \boldsymbol{\sigma}})_{ei}^n \\ \mathbf{0} & 1 & -\sqrt{\frac{2}{3}} \\ (\frac{\partial f}{\partial \mathbf{s}})_{ei}^n + \sqrt{\frac{2}{3}} \alpha_e \frac{\partial {I_1}_{ei}^n}{\partial \boldsymbol{\sigma}_{ei}^n} & -\sqrt{\frac{2}{3}} H_{p_e} & 0 \end{bmatrix} \tag{4.74}$$

$$\frac{\partial \mathbf{H}_{ei}^{n}}{\partial x_e} = \begin{bmatrix} -\frac{\partial \mathbf{D}_e^0}{\partial x_e} : (\mathbf{B}_{ei}\mathbf{u}_e^n - \mathbf{B}_{ei}\mathbf{u}_e^{n-1}) + \mathbf{D}_e^0 \Delta\gamma_{ei}^n (\frac{\partial f}{\partial \boldsymbol{\sigma}_{ei} \partial x_e})^n + \frac{\partial \mathbf{D}_e^0}{\partial x_e} \Delta\gamma_{ei}^n (\frac{\partial f}{\partial \boldsymbol{\sigma}})_{ei}^n \\ 0 \\ -\sqrt{\frac{2}{3}} \frac{\partial \sigma_{y_e}}{\partial x_e} - \sqrt{\frac{2}{3}} \frac{\partial H_{p_e}}{\partial x_e} e_{p_{ei}}^n + \sqrt{\frac{2}{3}} I_{1ei}^n \frac{\partial \alpha_e}{\partial x_e} \end{bmatrix} \tag{4.75}$$

When each material phase adopts a different plastic model and coupled with various hardening rules (e.g. isotropic hardening for one phase and the other with kinematic or combined hardening), the corresponding derivatives become

$$\frac{\partial \mathbf{H}_{ei}^{n}}{\partial \mathbf{v}_{ei}^{n}} = \begin{bmatrix} \mathbf{I} + \mathbf{D}_e^0 \Delta\gamma_{ei}^n (\frac{\partial f}{\partial \boldsymbol{\sigma} \partial \boldsymbol{\sigma}})_{ei}^n & \mathbf{D}_e^0 \Delta\gamma_{ei}^n (\frac{\partial f}{\partial \boldsymbol{\sigma} \partial \mathbf{a}})_{ei}^n & \mathbf{0} & \mathbf{D}_e^0 (\frac{\partial f}{\partial \boldsymbol{\sigma}})_{ei}^n \\ -\frac{2}{3}\phi_e H_{p_e} \Delta\gamma_{ei}^n (\frac{\partial f}{\partial \boldsymbol{\sigma} \partial \boldsymbol{\sigma}})_{ei}^n & \mathbf{I} - \frac{2}{3}\phi_e H_{p_e} \Delta\gamma_{ei}^n (\frac{\partial f}{\partial \boldsymbol{\sigma} \partial \mathbf{a}})_{ei}^n & \mathbf{0} & -\frac{2}{3}\phi_e H_{p_e} (\frac{\partial f}{\partial \boldsymbol{\sigma}})_{ei}^n \\ \mathbf{0} & \mathbf{0} & 1 & -\sqrt{\frac{2}{3}} \\ (\frac{\partial f}{\partial \boldsymbol{\eta}})_{ei}^n + \sqrt{\frac{2}{3}} \alpha_e \frac{\partial {I_1}_{ei}^n}{\partial \boldsymbol{\sigma}_{ei}^n} & -(\frac{\partial f}{\partial \boldsymbol{\eta}})_{ei}^n & -\sqrt{\frac{2}{3}}(1-\phi_e) H_{p_e} & 0 \end{bmatrix} \tag{4.76}$$

$$\frac{\partial \mathbf{H}_{ei}^{n}}{\partial x_e} = \begin{bmatrix} -\frac{\partial \mathbf{D}_e^0}{\partial x_e} : (\mathbf{B}_{ei}\mathbf{u}_e^n - \mathbf{B}_{ei}\mathbf{u}_e^{n-1}) + \mathbf{D}_e^0 \Delta\gamma_{ei}^n (\frac{\partial f}{\partial \boldsymbol{\sigma}_{ei} \partial x_e})^n + \frac{\partial \mathbf{D}_e^0}{\partial x_e} \Delta\gamma_{ei}^n (\frac{\partial f}{\partial \boldsymbol{\sigma}})_{ei}^n \\ -\frac{2}{3}\phi_e \frac{\partial H_{p_e}}{\partial x_e} \Delta\gamma_{ei}^n (\frac{\partial f}{\partial \boldsymbol{\sigma}})_{ei}^n - \frac{2}{3}\phi_e H_{p_e} \Delta\gamma_{ei}^n (\frac{\partial f}{\partial \boldsymbol{\sigma}_{ei} \partial x_e})^n - \frac{2}{3}\frac{\partial \phi_e}{\partial x_e} H_{p_e} \Delta\gamma_{ei}^n (\frac{\partial f}{\partial \boldsymbol{\sigma}})_{ei}^n \\ 0 \\ -\sqrt{\frac{2}{3}} \frac{\partial \sigma_{y_e}}{\partial x_e} - \sqrt{\frac{2}{3}}(1-\phi_e) \frac{\partial H_{p_e}}{\partial x_e} e_{p_{ei}}^n + \sqrt{\frac{2}{3}} I_{1ei}^n \frac{\partial \alpha_e}{\partial x_e} + \sqrt{\frac{2}{3}} \frac{\partial \phi_e}{\partial x_e} H_{p_e} e_{p_{ei}}^n \end{bmatrix} \tag{4.77}$$

with

$$\frac{\partial f}{\partial \boldsymbol{\sigma}_{ei} \partial x_e}^{n} = \sqrt{\frac{2}{3}} \frac{\partial I_{1ei}}{\partial \boldsymbol{\sigma}_{ei}} \frac{\partial \alpha_e}{\partial x_e}^{n} \tag{4.78}$$

where

$$\frac{\partial \mathbf{D}_e^0}{\partial x_e} = \frac{\partial \lambda_e^0}{\partial x_e} \mathbf{1} \otimes \mathbf{1} + 2 \frac{\partial \mu_e^0}{\partial x_e} \mathbf{I} \tag{4.79}$$

Opposite to the derivatives of $\mathbf{H}^n$ with respect to the internal variable $\mathbf{v}^n$ and the design variable $\mathbf{x}$ are different for materials incorporating with various yielding function in the elastic and plastic step, the following derivatives (i.e. $\frac{\partial \mathbf{H}_{ei}^{n+1}}{\partial \mathbf{v}_{ei}^n}, \frac{\partial \mathbf{H}_{ei}^n}{\partial \mathbf{u}_e^n}, \frac{\partial \mathbf{R}_e^n}{\partial \mathbf{v}_{ei}^n}, \frac{\partial \mathbf{R}_e^n}{\partial \mathbf{v}_{ei}^n}$) do not depend on the finite element analysis response. When the structure is associated with kinematic or combined hardening, the derivatives mentioned above are described as follows:

$$\frac{\partial \mathbf{H}_{ei}^{n+1}}{\partial \mathbf{v}_{ei}^n} = \begin{bmatrix} -\mathbf{I} & \mathbf{0} & \mathbf{0} & \mathbf{0} \\ \mathbf{0} & -\mathbf{I} & \mathbf{0} & \mathbf{0} \\ \mathbf{0} & \mathbf{0} & -1 & 0 \\ \mathbf{0} & \mathbf{0} & 0 & 0 \end{bmatrix} \tag{4.80}$$

$$\frac{\partial \mathbf{H}_{ei}^{n}}{\partial \mathbf{u}_e^n} = \begin{bmatrix} -\mathbf{D}_e^0 \mathbf{B}_{ei} & \mathbf{0} & 0 & 0 \end{bmatrix}^T \tag{4.81}$$

$$\frac{\partial \mathbf{H}_{ei}^{n+1}}{\partial \mathbf{u}_e^n} = \begin{bmatrix} \mathbf{D}_e^0 \mathbf{B}_{ei} & \mathbf{0} & 0 & 0 \end{bmatrix}^T \tag{4.82}$$

$$\frac{\partial \mathbf{R}_e^n}{\partial \mathbf{v}_{ei}^n} = \begin{bmatrix} \mathbf{B}_{ei}^T w_{ei} & \mathbf{0} & 0 & 0 \end{bmatrix} \tag{4.83}$$

When the structure is associated with isotropic hardening, the corresponding derivatives become:

$$\frac{\partial \mathbf{H}_{ei}^{n+1}}{\partial \mathbf{v}_{ei}^n} = \begin{bmatrix} -\mathbf{I} & \mathbf{0} & \mathbf{0} \\ \mathbf{0} & -1 & 0 \\ \mathbf{0} & 0 & 0 \end{bmatrix} \tag{4.84}$$

$$\frac{\partial \mathbf{H}_{ei}^{n}}{\partial \mathbf{u}_e^n} = \begin{bmatrix} -\mathbf{D}_e^0 \mathbf{B}_{ei} & 0 & 0 \end{bmatrix}^T \tag{4.85}$$

$$\frac{\partial \mathbf{H}_{ei}^{n+1}}{\partial \mathbf{u}_e^n} = \begin{bmatrix} \mathbf{D}_e^0 \mathbf{B}_{ei} & 0 & 0 \end{bmatrix}^T \tag{4.86}$$

$$\frac{\partial \mathbf{R}_e^n}{\partial \mathbf{v}_{ei}^n} = \begin{bmatrix} \mathbf{B}_{ei}^T w_{ei} & 0 & 0 \end{bmatrix} \tag{4.87}$$

Therefore the matrix of the differentiation of $\mathbf{H}^n$ need to be adjusted according to the trial elastic condition, which keep consistency with the analysis at each increment. Also, for the yield criterion incorporating with isotropic hardening, the derivatives of the global residual $\mathbf{R}^n$ and the local residual $\mathbf{H}^n$ are matrices of smaller size due to the elimination of one variable (back stress $\mathbf{a}^n$).

4.6 Examples

Three numerical examples, a simply supported beam, a cantilever beam with a circular opening and a L-shaped bracket, are examined to evaluate the impacts of different yielding criterion and hardening rules on the resulting topologies through the proposed optimization framework for structure with two elastoplastic material phases. All examples are assumed to be in plane stress condition. Due to the design variable for continuous density-based optimization method can vary from 0 to 1, "gray" regions of intermediate density may exist in the resulting topology. Also, this may cause difficulty in achieving a convergent results. A filtering scheme of gradually reducing the filter radius is implemented in this study to remove "gray" areas. The optimization procedure is either stopped by the limiting convergence tolerance (10^{-4} in our case) or a stable topology achieved after an adequate number of iterations (300 to 500 in our case).

4.6.1 Simply supported beam

A simply supported beam, length-to-height ratio equals to 4, is shown in Fig.4.1. A downward distributed prescribed displacement is applied to the central portion of the top edge. The whole design domain is discretized into 3600 (120 x 30) elements. And the desired volume fraction to the whole design domain is 30%. The prescribed displacement $U^* = 0.5mm$ is assumed throughout this example to achieve a plastic design.

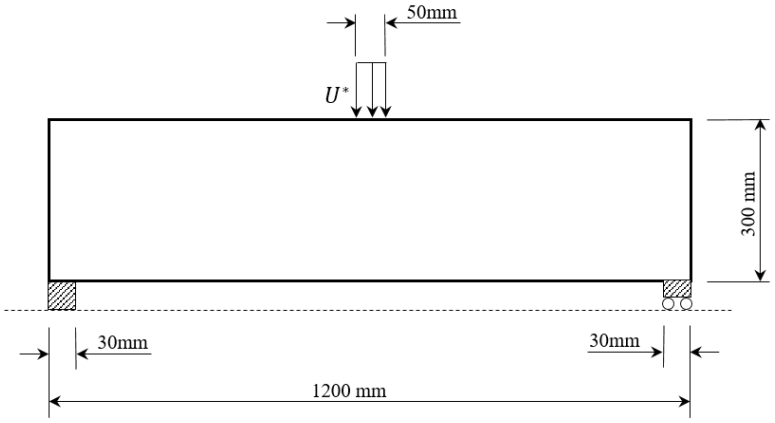

Figure 4.1: Design domain of the simply supported beam

In this example, each material phase has the flexibility of adopting different elastic and plastic material model accompany with various hardening rules. The cases examined in this example include: 1) both material with elastic model; 2) both material phases with the von Mises plasticity model and the kinematic hardening; 3) both material phases with the Drucker-Prager plasticity model and the kinematic hardening; 4) one material phase with the von Mises plasticity model while the other with the Drucker-Prager plasticity model and the post yielding behaviour, both following the kinematic hardening, as detailed in Table 4.1. The purpose of this example is to investigate the influence of the plasticity model on the results of the optimization design. The mechanical properties of the two material candidates are detailed as follows:

$$E_1 = 206GPa;\ H_{p1} = 2060MPa;\ \sigma^0_{Y1} = 250MPa;$$
$$E_2 = 30GPa;\ H_{p2} = 300MPa;\ \sigma^0_{Y2} = 7MPa.$$

Table 4.1: Summary of test set up in Example 1

	plasticity model for material phase 1	plasticity model for material phase 2	Strain-hardening for both material phases
Case A	Elastic	Elastic	-
Case B	von Mises	von Mises	Kinematic ($\phi = 1$)
Case C	Drucker-Prager	Drucker-Prager	Kinematic ($\phi = 1$)
Case D	von Mises	Drucker-Prager	Kinematic ($\phi = 1$)

Poisson ratio $v = 0.3$ is adopted for both material candidates. If the Drucker-Prager model is adopted, the material parameter α is required and assumed to be equal to 0.8 in this example. To maintain the comparability, the values of the material properties remain constant for all cases.

The resulting distribution of two material phases are shown in black and white in Fig.4.2. The first material is presented in black while the second material is presented in white. Using the resulting topology as the final design, the contour plots of the second principal stress for case A-D are shown in Fig.4.3, which are able to highlight the micro-structure of the final design. For clarity, only the stresses of material 2 is plotted, and that of material 1 is plotted as void.

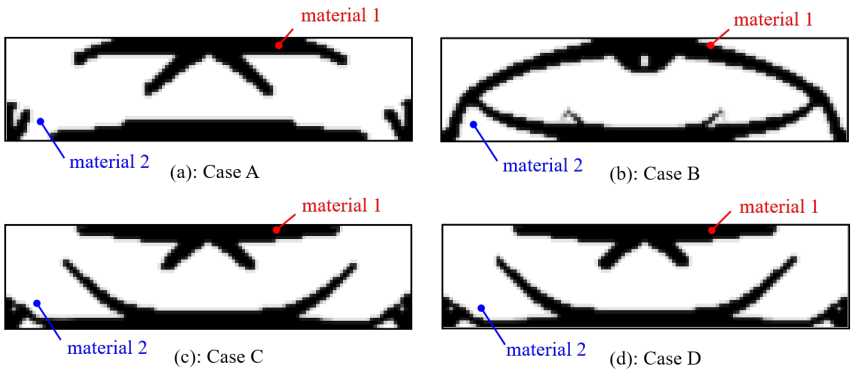

Figure 4.2: Optimized layouts of case A-D

Several important findings are summarised below:

1) Adopting different plasticity models for material 2 result in different final

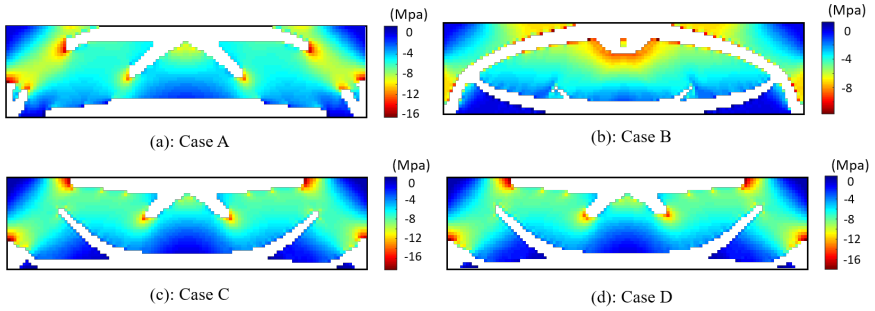

Figure 4.3: The corresponding contour plots of the second principal stress for Case A-D

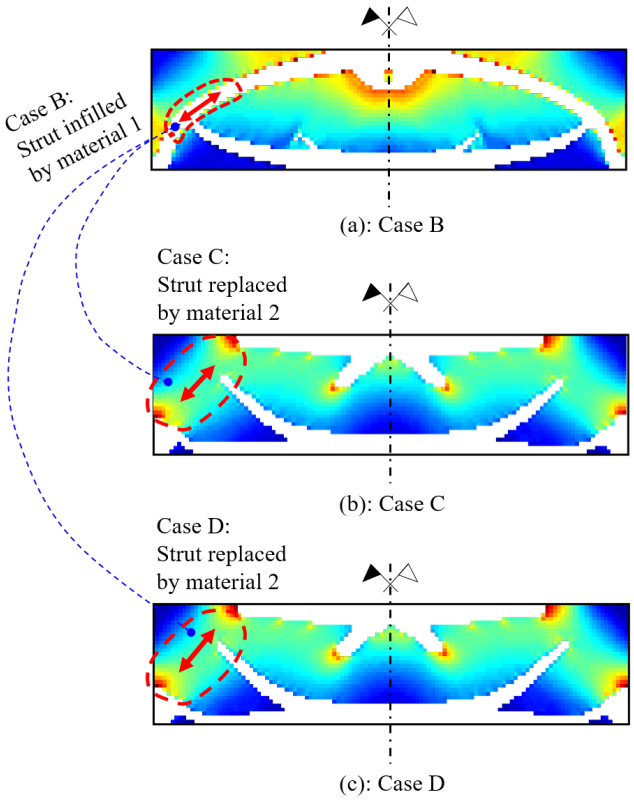

Figure 4.4: Comparison of the arch components of case B to case C and D

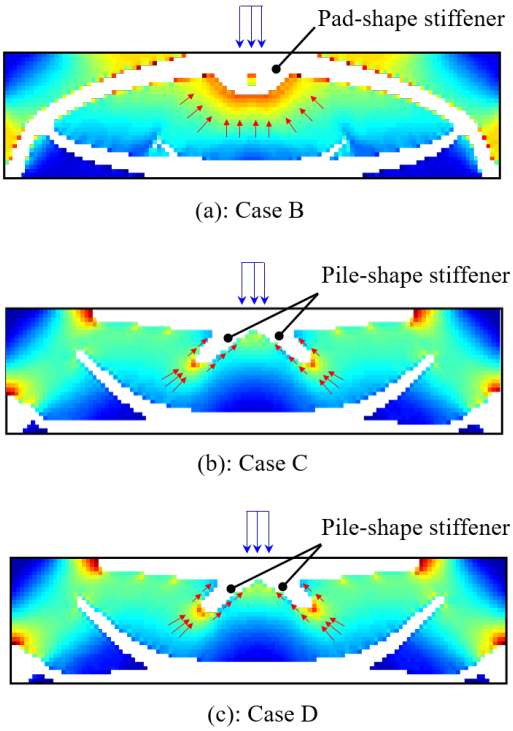

Figure 4.5: Comparison of the punching stiffeners of case B to case C and D

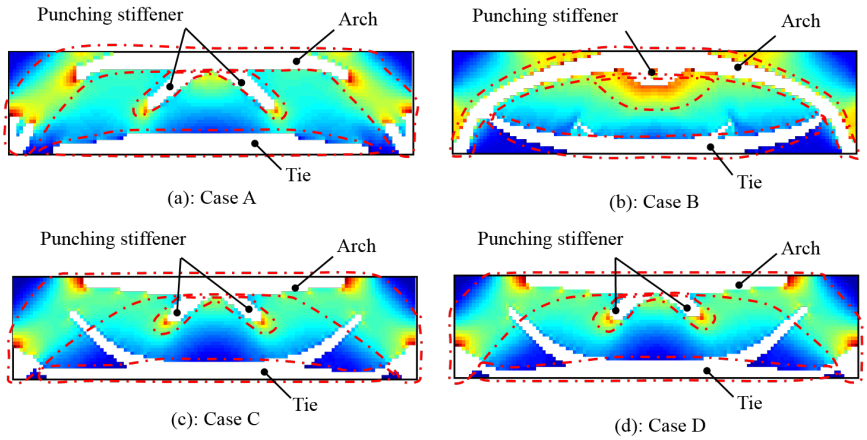

Figure 4.6: Summary of micro-structures in the resulting topology for Case A-D

topologies. When von Mises plasticity model is used, the mechanical properties are symmetrical in tension and compression, and both of them are much weaker than phase material 1. This leads to a arch-shape of topology as shown in Fig.4.6(b) in which the structural skeleton, no matter in compression (the arch) and tension (the tie), are all made of material 1 as material 2 is not able to take the loading. As shown in Fig.4.3(b), it is noticeable that around the top-middle area of the beam where the prescribed loading applied, there is a chuck of material 1 allocated due to the high compressive stress concentration in this area.
2) In case C and D, while using Drucker-Prager plasticity model for the second material, empowered with the ability of modelling the relatively higher compressive and lower tensile yielding strength, different resulting topologies are obtained as shown in Fig.4.2(c) and (d). In comparison with Fig.4.2(b), there are two main differences that can be observed from the contour plots, i) some parts of the structural members, as shown in Fig.4.4(a), filled with material 1 suffering from compression are replaced by a block of material 2, as shown in Fig.4.4(b-c), acting as struts; ii) The resulting topologies developed in different cases demonstrate different ways to address the compressive stress concentration around the loading area. A pad-shape structure as shown in Fig.4.5(a) is formed by stiff material 1 supported by soft material 2 under. While in Fig.4.5(c) and (d), showing the results of case C and D respectively, the material 2 are modelled with the Drucker-Prager yielding criterion, which allows material 2 to sustain a much higher compression, a pile-shape structure is evolved taking the advantage of the end support underpinned by the Drucker-Prager model.
3) Although adopting different plasticity model for material phase 2 leads to noticeable different topologies as shown in Fig.4.2, the fundamental principle of loading transfer through the structure and optimized topology constituted are quite similar. As shown in Fig.4.6, the components of the beam can be easily identified in three common parts: the arch, the tie and the punching stiffener. The arch is spanning between the two supports demonstrating the arch effect. In Fig.4.6(b), case B, when material 2 is modelled by von Mises plasticity model with a relatively lower compressive strength, the arch is formed by material 1 only. While in case C and D, as shown in Fig.4.6(c) and (d), the parts of arch between the structural support and the upper chord of the arch are replaced by

material 2. Same situation can be observed in case A as shown in Fig.4.6(a), in which both material are simulated with linear elastic model. In this model without considering the yielding behaviour, the compressive stress in material 2 can become infinitely large, which allows material 2 to replace material 1 in some regions of the arch. Although the models used in case A, C and D are different, the reason for material 2 distributing in these regions is the same: compressive strength. In all the four cases, the bottom ties are all made of material 1, and the plasticity model of material 2 has strong impact on the shape of tie in the resulting topology. Apart from the arch and tie, the punching stiffener is another important component in this structure. Their shapes are similar in case A, C and D, all are pile-shape structures. For case B, it is a pad-shape structure instead. It can be concluded that although the obtained topologies look different, the optimized micro-architecture of the internal mechanical system will not change fundamentally.

4.6.2 optimization of a cantilever beam with circular opening

In this example, the design of the two-phase material layout for a cantilever beam with a circular opening is considered, as shown in Fig.4.7. The radius of the hole R=60 mm and the distance from the centre of the opening to the left and the top edge are 400 mm and 150 mm, respectively. The beam is subjected to a prescribed distributed displacement of 2 mm applied at 50 mm long central region of the right side edge. The left side edge is fully clamped. The FE mesh with element size of 10mm is shown in Fig.4.8. The design variables for the elements within the circular opening are equal to zero and not updated during the optimization procedure. The percentage of material 1 used in the whole domain is limited to 50%. The mechanical properties of the two material candidates are same as those presented in the previous example. The poisson ratio and the material parameter α for the Drucker-Prager model remain unchanged. All the plasticity model adopt a combined isotropic and kinematic hardening rule with the combined effect parameter $\phi = 0.5$. The cases examined in this example are detailed in Table 4.2.

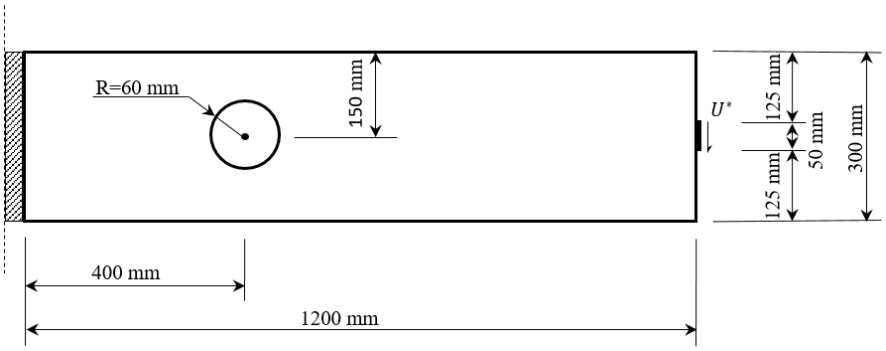

Figure 4.7: Design domain of the cantilever beam with a circular opening

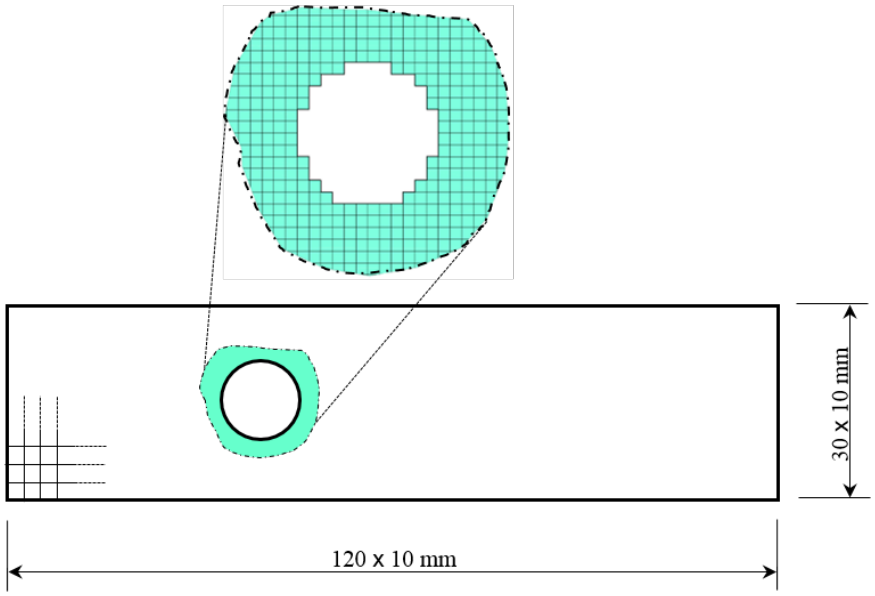

Figure 4.8: Mesh condition of the cantilever beam with a circular opening

Table 4.2: Summary of test set up in Example 2

	plasticity model for material phase 1	plasticity model for material phase 2	Strain-hardening for both material phases
Case A	Elastic	Elastic	-
Case B	von Mises	von Mises	Combined isotropic/kinematic hardening ($\phi = 0.5$)
Case C	Drucker-Prager	Drucker-Prager	Combined isotropic/kinematic hardening ($\phi = 0.5$)
Case D	von Mises	Drucker-Prager	Combined isotropic/kinematic hardening ($\phi = 0.5$)

The resulting topologies of different cases are shown in Fig.4.9 and the corresponding contour of the second principle stress are shown in Fig.4.10. For sake of clarity of the following discussion, all the areas filled with material 1 are removed, and only the stress distribution of material 2 is plotted. Several important

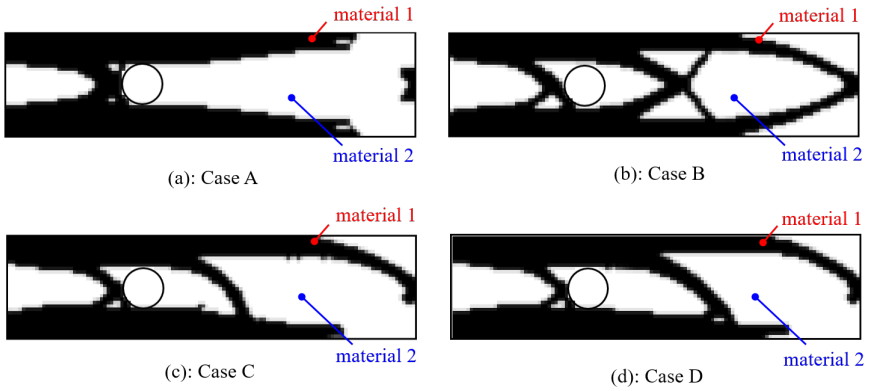

Figure 4.9: Optimized layouts of case A-D

findings are presented as follows:
1) When material elastoplasticity is considered, i.e. case B, C and D, similar to previous example, the type of plasticity model adopted for material 2 has great impact on the design results. As indicated in Fig.4.10(b) (case B), when von Mises plasticity model is applied to material 2, a truss-shaped skeleton of material 1 is generated to contribute more in resisting the structural response, due to its stiffer material property and equivalent strength in compression and tension. While in Case C and D, when using the Drucker-Prager model for material 2, their resulting topologies are remarkably different from the case B results, though the two topologies themselves are quite similar to each other. One noticeable minor difference between case C and D is the shape and pitch of the diagonal bar made of material 1 located at the middle of the beam, which hints that the plasticity model of material 1 do have some level of influence on the final topology, but less intensive than the choice of model for material 2.
2) As shown in Fig.4.10, when using Drucker-Prager model to simulate the material 2 with a higher compressive strength but lower tensile strength, a leg of the truss member in compression made of material 1, as shown in Fig.4.10(b) (case B), is replaced by material 2 to take the advantage of its compressive strength that

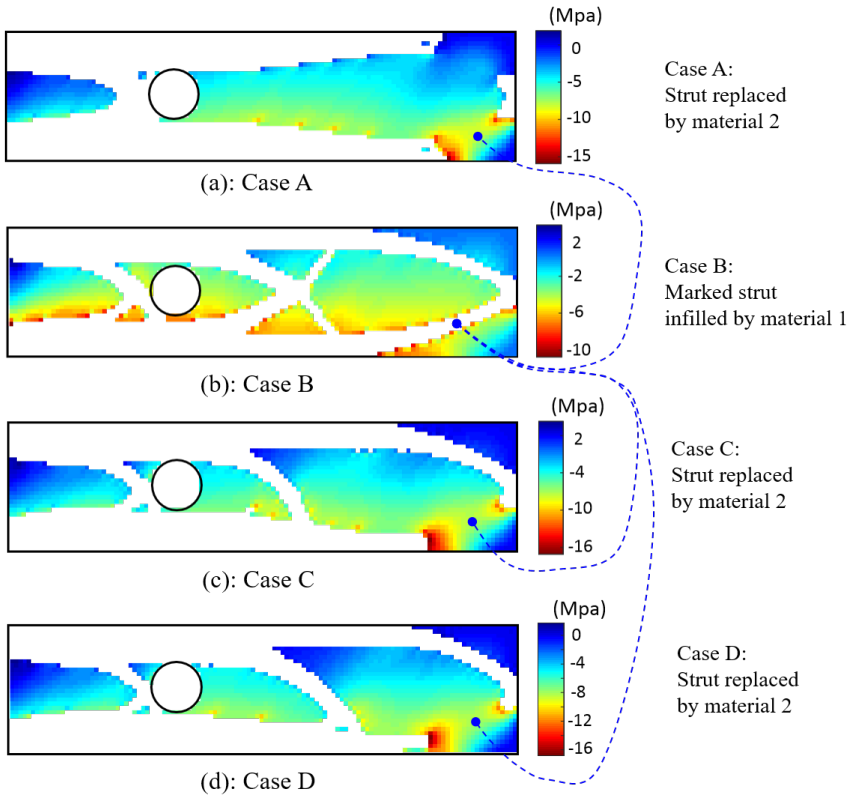

Figure 4.10: The corresponding contour plots of the second principal stress for Case A-D

come with Drucker-Prager model. This similar situation is noticed in example 1. Results of both examples revealed the impact of the type of plasticity models on the material distribution for a nonlinear multi-material-phase optimization design.

Also, the influence of filtering scheme on the resulting topology for two-phase material nonlinear optimization design is investigated here. As mentioned that by gradually reducing the filter radius during the optimization procedure, a distinct layout can be achieved within 300 iterations, which means that afterwards, there is no significant change in topology. To demonstrate its effectiveness of the proposed scheme, optimized design of using a constant filter radius throughout 300 iterations is also produced. The comparison of topology designs for different filter radius adopted is presented in Fig.4.11. It can be observed that for optimization design of two-phase structure taking into account the material elastoplasticity, the filtering scheme considerably effects the resulting topology. When a gradual refinement is used, the optimization benefits from obtaining a distinct layout as well as saving computational cost by quickly escaping from the emergence of 'gray' areas.

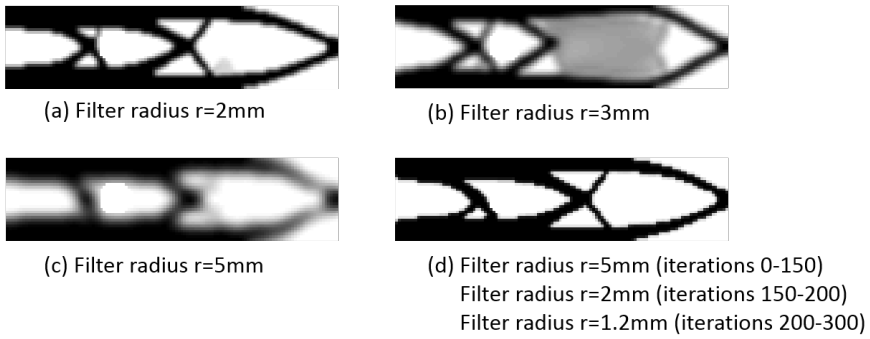

Figure 4.11: Comparison of Optimized layouts of two-phase nonliear design for different filter radius adopted within 300 design iterations

Also, optimized design of using constant filter radius equal to 2 and 3 respectively for a single-phase nonlinear structure is conducted to evaluate whether same phenomenon can be observed. The resulting topologies are shown in Fig.4.12. It

can be seen that though the design with r=3mm does not show a layout as distinct as that of using r=2mm, it can be concluded that, in this particular case, nonlinear single-phase optimization problem is filter-independent.

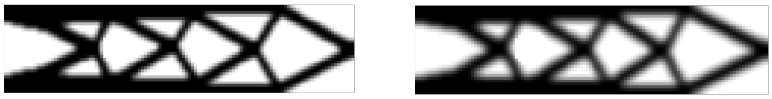

Figure 4.12: Comparison of Optimized layouts of single-phase nonliear design for different filter radius adopted within 300 design iterations

4.6.3 optimization of a L-shape bracket

The purpose of this example is to investigate the impact of the post-yielding behaviour on the resulting topology. As there are few previous studies on the impact of the post-yielding hardening model on the resulting topologies even for single material nonliear optimization design, it is the intention to evaluate the significance of its impact on the optimized layout for both single and two-material phase optimization.

As shown in Fig.4.13, a L-shape bracket with $600mm$ equal length of legs is subjected to a prescribed $1mm$ uniform displacement applied to the $3.75mm$ long centre region of the right-end surface of the horizontal leg. The top surface of the vertical leg is fully clamped. The FE mesh is shown in Fig.4.14. The volume fraction of the first material to the whole composite domain is limited to 40%.

For single material design problem, the von Mises plasticity model is adopted in all three cases, while each case is coupled with isotropic, kinematic, and combined isotropic/kinematic hardening ($\phi = 0.5$) respectively. The initial stiffness $E = 30GPa$ and yield stress $\sigma_Y^0 = 7MPa$ are set up the same as for the second material in the next step. For two materials design problem, both materials phases adopt the von Mises plasticity model to eliminate the influence of the plasticity model so that the impact of the hardening rule can be insulated. In the three cases considered, the first material phase employs the isotropic hardening while the second phase is associated with various hardening models: 1) elastic-perfectly-plastic(without strain hardening); 2) isotropic hardening; 3) kinematic

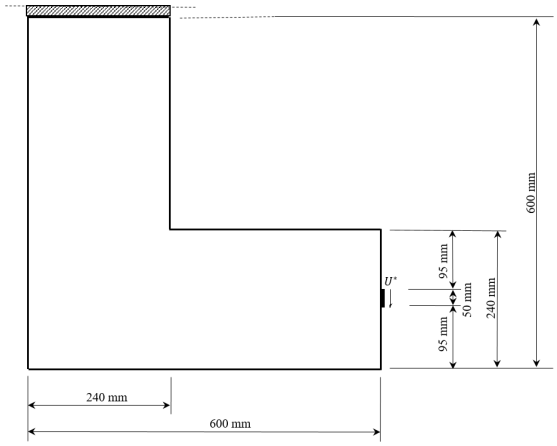

Figure 4.13: Design Domain of the L-shaped bracket

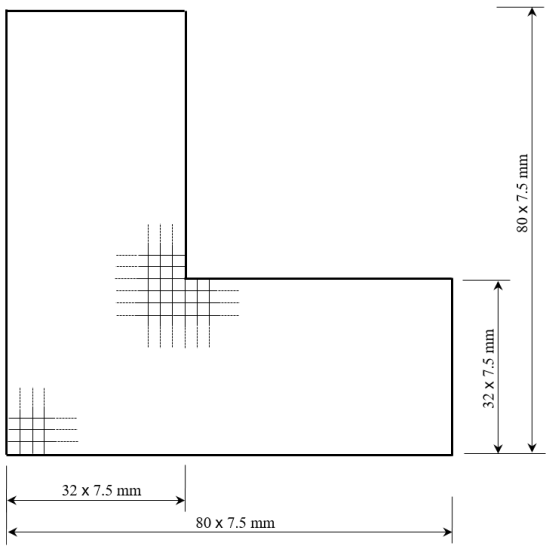

Figure 4.14: Mesh condition of the L-shaped bracket

Table 4.3: Summary of test set up in Example 3

	Hardening model for material phase 1	Hardening model for material phase 2
Case A	-	Isotropic
Case B	-	Kinematic
Case C	-	Combined Isotropic/Kinematic ($\phi = 0.5$)
Case D	Isotropic	Elastic-perfectly-plastic
Case E	Isotropic	Isotropic
Case F	Isotropic	Kinematic

hardening. The plastic modulus H_p is equal to 2060MPa for both materials and not modified by the design variables, while all the value of the other plastic material parameters are exactly the same as the previous examples. A summary of hardening rule employed is presented in Table 4.3.

Several important findings are concluded as follows:

1) The results obtained from the single material design case A, B and C are presented in Fig.4.15(a), (b) and (c), respectively. It can be easily found that the resulting topologies are similar. Hence, in single material design cases, where the design material is associated with the same plasticity model but follow different strain-hardening rule, the impact of the post-yielding hardening on the resulting topology is not significant.

2) Contrary to the single material cases, different post yielding hardening model do produce obvious differences among the resulting topologies in the case D, E and F examined in this example for two material phase optimization. The optimized layout and the corresponding contour of the first principle stress for part of the lower horizontal structure marked in red rectangular box are presented in Fig.4.16. The contour plot of the first principal stress can clearly reveal the tensile zone in the part of the structure. It can be observed from Fig.4.16(a-c) that the two vertical branches in the left upper structure end up with similar material distributions, and for the inclined branch in between, its position and the amount of material used show a remarkable difference in Fig.4.16(a) in comparison with the other two designs where the strain-hardening is considered for the second material. Also, the optimised layouts of the lower structure of the bracket are

obviously different in these three cases. Fig.4.16(a) shows the result of case D in which the second material is described as elastic-perfectly-plastic, i.e. no hardening after yielding, the tensile tie at the top of the horizontal leg and the compressive strut at the bottom are made of material 1, as material 2 is limited by its weaker yielding strength. While for case E and F, as shown in Fig.4.16(b) and (c), in which isotropic and kinematic hardening are applied to material 2 respectively, a noticeable change can be observed in the final topologies. The top ties is replaced by a smeared-strut-and-tie micro-structure as illustrated in Fig.4.17.

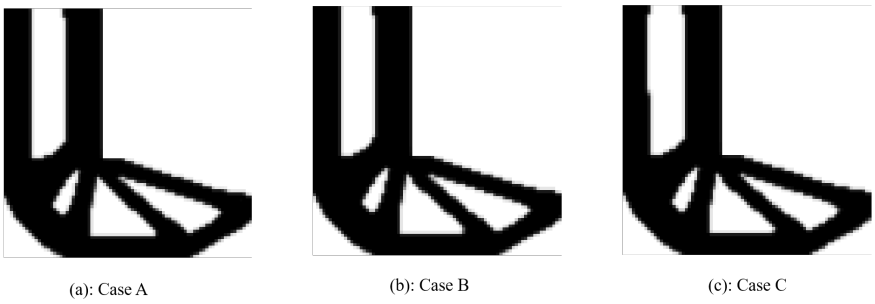

Figure 4.15: Optimized layouts of case A-C

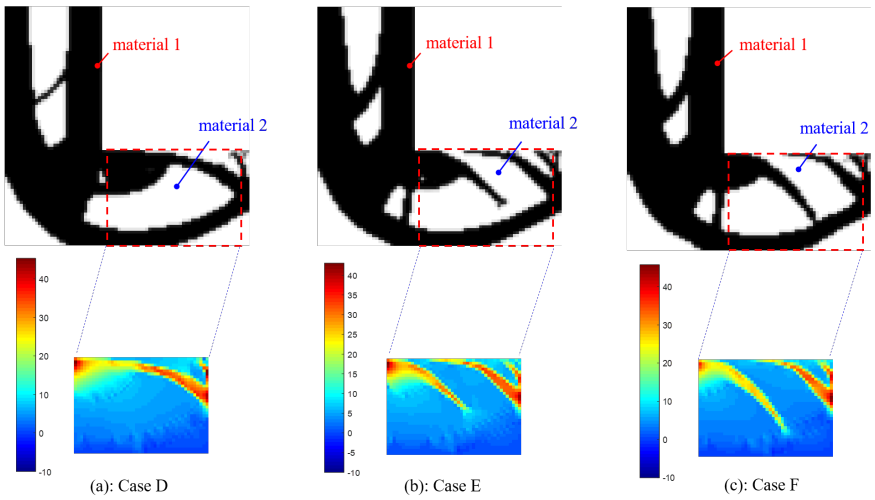

Figure 4.16: Optimized layouts and the corresponding contour plots of the first principal stress for Case D-F

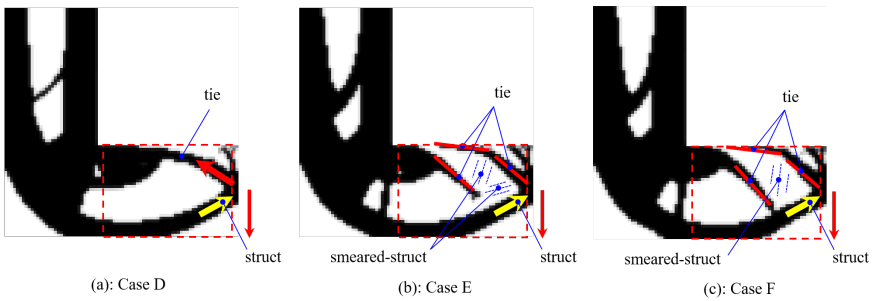

Figure 4.17: Strut-and-tie, smeared-strut-and-tie analogy for Case D-F

4.7 Conclusion and discussion

In this research study, a framework for multiphase material nonlinear topology optimization is developed, implemented and validated. This new framework offers the flexibility that highly desired in complex composite structural optimization when each material has different nonlinear characteristics and hardening behaviours. As in this type of multiphase material nonlinear optimization, each material phase will not only associate with different plasticity model but also following different hardening rule so that each material elastoplastic properties can be closely characterized during the optimization process. In some practical design optimization, having the flexibility of modeling the different actual material elastoplasticity, for example, von Mises plasticity with isotropic hardening for one material, while Drucker-Prager plasticity with kinematic hardening for the other will lead to a better approximation of the real optimum design. Few studies focused on this area, even fewer studies achieved this level of flexibilities that come with the proposed framework.

In supporting the proposed framework, a modified path-dependent adjoint sensitivity analysis is developed for calculating the design sensitivities when the two-phase elastoplastic materials are associated with various hardening rules.

As demonstrated in the examples, the proposed framework is effective, versatile and highly adaptive to the different elastoplastic and hardening models. The results of the example presented in this paper have also revealed the impact on the resulting topology when adopting different plasticity models and hardening rules in a composite structural optimization which has also demonstrated the flexibility of adapting to different material combinations for modern composite structures. Some of the topologies produced by the proposed method are novel yet fulfil the engineering common sense when looking into the details of micro-structures.

5

Using Discrete Density-based Optimization Method for Nonlinear Structure

5.1 Introduction

Topology optimization has been widely used in mechanical designs and has become an extremely active research area in recent decades and been applied to many other design fields [5]. It is mainly classified into three approaches: continuously density-based method [8, 10, 67], evolutionary optimization technique [14, 17] and level-set method [3, 21].

Initial works implement topology optimization method into the linear elastic design and the optimized layout are then post-processed [42, 43, 57]. However, it is far from the practical design where the material cannot be assumed purely linear elastic. To achieve a more reliable optimized design, topology optimization considering material nonlinearity has received more attention in recent decades, e.g. hyperelasticity [68, 69, 70], path-dependent elastoplasticity [24, 25, 27, 59, 61, 63].

However, there are still limited research studies incorporating material nonlinearity with topology optimization due to the high computational cost and difficulty in convergence. And most of the aforementioned works use the continuous density-based optimization method for the plastic structural design. The

evolutionary structural optimization (ESO) method seems to be an effective alternative, which is developed from the concept of gradually removing the inefficient materials in the design domain. A further improved evolutionary method bi-directional evolutionary structural optimization (BESO) method is developed with the capability of allowing elements to be removed and added simultaneously. Its nature of achieving a discrete layout avoids the grey-scale problem caused by the material with intermediate density, especially for a nonlinear optimization design. Also, opposite to linear elastic optimization design, computational burden emerges due to the nonlinear finite element analysis ahead the optimization algorithm, which highly depend on the mesh generation size. ESO/BESO is relatively advantageous in reducing the computational cost by achieving a distinct layout in a certain number of optimization iterations.

The capacity of using BESO method for structural nonlinear design has been evaluated in optimization of monoscale structures considering both material and geometrical nonlinearity[71], multiscale nonlinear structures[72, 73], and elasto-plastic structures[29]. In order to stabilize the topology optimization process for nonlinear design, apart from the mesh-independency filter scheme and consideration of sensitivity history of each element [18], additional approaches are developed to smooth the sensitivity number and improve the topology convergence, e.g., an admission volume ratio is introduced to control the number of elements recovered in each iteration [29, 71, 72], a damping scheme on sensitivity numbers and a modified filtering scheme of gradually decreasing filtering radius are proposed [29]. Also, due to the fact that using BESO method for nonlinear structure design may not lead to a convergent solution, a maximum number of iterations is considered to terminate the optimization process rather than by satisfying the convergence criterion with an allowable convergent tolerance [71]. Hence, using BESO evolutionary method in particular for plastic design is still a field of on-going research due to the difficulties arising from uncertain stabilization and convergence.

In the BESO optimization process, sensitivity numbers are used to determine the removal and addition of each element through a ranking system. Hence, sensitivity analysis is particularly important as it straightforwardly affect the accuracy and stabilization of the optimization procedure. The recipes for path-dependent

sensitivity analyses of inelastic structures can be traced back to 1990s, which has also been implemented into the elastoplastic mathematical-based topology optimization in recent works. However, refer to the previous works of using BESO method for nonlinear structural design, the sensitivity analysis were simplified and approximated during the optimization process where the calculation of sensitivity the objective function with respect to the design variables only take the global constitutive equation into account. This equation represents the difference between the internal force and the external force, which is normally achieved in an iterative manner using the Newton-Raphson method. However, the discrete mechanical balance laws on a local material level is also necessarily considered in the elastoplastic material optimization design. An inaccurate approximated sensitivities may lead to incorrect topologies and unstable optimization process. Therefore, In this paper, the sensitivity number used in the BESO algorithm is calculated based on the transient nonlinear coupled systems proposed in Michaleris et al [65]. The global residual force as well as the local residual on integration point level are simultaneously satisfied and both are defined as functions of time. The objective of this study is using evolutionary optimization method to design elastoplastic structure where the material path-dependency is directly taken into account through an adjoint sensitivity analysis based on a transient coupled nonlinear system.

The elastoplastic material model adopted in this paper is using von Mises material model with linear isotropic hardening rule. Three examples are conducted to verify the efficiency and effectiveness of the proposed BESO procedure for elstoplastic structural design. In the optimization procedure, only a general filtering scheme that consider the factor from the neighbouring elements within a constant filtering radius is applied. The results are successfully converged which denotes the accuracy and robustness of the sensitivity analysis that implemented in the BESO algorithm. Also, a prescribed displacement governed analysis shows the impact of prescribed displacement on the history evolutionary topology and the final topology for the plastic optimization design.

5.2 Nonlinear Finite Element Analysis

5.2.1 Elastoplastic Material Model

In this study, the von Mises plastic model with isotropic hardening is adopted to exhibit the elastoplastic behaviour for some ductile material, e.g. metal, which is given by

$$f = ||\mathbf{s}|| - \sqrt{\frac{2}{3}}(\sigma_Y + H_p e_p) \tag{5.1}$$

where $||\mathbf{s}|| = \sqrt{\mathbf{s} : \mathbf{s}}$ is the norm of the deviatoric stress. And

$$\sqrt{\mathbf{s} : \mathbf{s}} = \sqrt{2J_2} \tag{5.2}$$

where J_2 represents the second invariant of the deviatoric stress tensor, σ_Y denotes the initial yield stress, e_p is the effective plastic strain and H_p is the constant plastic modulus which means the hardening model is assumed to be linear here.

According to the assumption of small deformation elastoplasticity, the rate of the total strain $\dot{\boldsymbol{\varepsilon}}$ can be decomposed into the rate of the elastic strain $\dot{\boldsymbol{\varepsilon}}^e$ and the plastic strain $\dot{\boldsymbol{\varepsilon}}^p$ as

$$\dot{\boldsymbol{\varepsilon}} = \dot{\boldsymbol{\varepsilon}}^e + \dot{\boldsymbol{\varepsilon}}^p. \tag{5.3}$$

The elastic strain relates to the stress by using the fourth-order constitutive tensor $\mathbf{D}$. And the plastic strain evolves in the direction normal to the associated flow potential (yield function f) in this study, which is given by

$$\dot{\boldsymbol{\varepsilon}}^p = \gamma \frac{\partial f(\mathbf{s}, e_p)}{\partial \mathbf{s}} = \gamma \frac{\mathbf{s}}{||\mathbf{s}||} = \gamma \mathbf{N} \tag{5.4}$$

where $\mathbf{N}$ is a unit deviatoric tensor normal to the yield surface. γ is the non-negative plastic consistency parameter and it is governed by the Kuhn-Tucker conditions, i.e.

$$\gamma f = 0; \quad \gamma \geq 0; \quad f \leq 0. \tag{5.5}$$

5.2.2 Global and local residuals

The global equilibrium for the complete structure should be satisfied in the finite element analysis, can be expressed as

$$\mathbf{R}^n = \mathbf{R}^n_{ext} - \mathbf{R}^n_{int} \tag{5.6}$$

where $\mathbf{R}^n$ represents the residual on the global level at the loading step n, which equals to the difference of the external applied force $\mathbf{R}^n_{ext}$ and the internal force $\mathbf{R}^n_{int}$ at the loading step n. In the force-incremental analysis, the external force vector is known, while in the displacement-incremental analysis, the unknown load factor need to be solved through the coupled equation system for each increment and then multiply with the reference load vector only with non-zero entries at the loaded degrees of freedom. The internal force can be expressed as

$$\mathbf{R}^n_{int} = \sum_{e=1}^{nele} (\int_{V_e} \mathbf{B}^T \boldsymbol{\sigma}^n dV_e) \tag{5.7}$$

where $\mathbf{B}$ is the strain-displacement matrix. Additionally, the local residuals on the integration point level are required to be sufficiently small throughout the nonliear analysis. Here, four-node quadrilateral plane-stress element with four integration points is utilized for design problems. Thus, the residual $\mathbf{H}$ at the loading increment n is formed by embedding the local residuals on each integration point of each element into a global matrix as

$$\begin{aligned} \mathbf{H}^n &= [\mathbf{H}^n_1, \mathbf{H}^n_2, ..., \mathbf{H}^n_{nele}]^T \\ \mathbf{H}^n_e &= [\mathbf{H}^n_{e1}, \mathbf{H}^n_{e2}, \mathbf{H}^n_{e3}, \mathbf{H}^n_{e4}]^T \\ \mathbf{H}^n_{ei} &= \left[\mathbf{H}^n_{ei1}, \mathbf{H}^n_{ei2}, ..., \mathbf{H}^n_{eij}\right]^T \end{aligned} \tag{5.8}$$

where e is the number of elements, i represents the number of integration points, and j corresponds to the number of local residual required on an integration point level based on the specified plastic model and hardening rule. In the elastic incremental stage, the local residuals $\mathbf{H}^n_{eij}$ are defined as

$$\mathbf{H}^n_{eij} = \begin{bmatrix} \mathbf{H}^n_{ei1} \\ \mathbf{H}^n_{ei2} \\ \mathbf{H}^n_{ei3} \end{bmatrix} = \begin{bmatrix} \boldsymbol{\sigma}^n_{ei} - \boldsymbol{\sigma}^{n-1}_{ei} - \mathbf{D}^0_e : (\mathbf{B}_e \mathbf{U}^n_e - \mathbf{B}_e \mathbf{U}^{n-1}_e) = 0 \\ e^n_{p_{ei}} - e^{n-1}_{p_{ei}} = 0 \\ \Delta\gamma^n_{ei} = 0 \end{bmatrix} \tag{5.9}$$

where $\mathbf{U}_e$ is the nodal displacement vector of element e; $\boldsymbol{\sigma}_{ei}$ and $e_{p_{ei}}$ represent the stress and the equivalent plastic strain obtained at each integration point of element e respectively.

However, in the plastic stage, the local residuals $\mathbf{H}_{eij}^{n}$ are given by

$$\mathbf{H}_{eij}^{n} = \begin{bmatrix} \mathbf{H}_{ei1}^{n} \\ \mathbf{H}_{ei2}^{n} \\ \mathbf{H}_{ei3}^{n} \end{bmatrix} = \begin{bmatrix} \boldsymbol{\sigma}_{ei}^{n} - \boldsymbol{\sigma}_{ei}^{n-1} - \mathbf{D}_{e}^{0} : (\mathbf{B}_{e}\mathbf{U}_{e}^{n} - \mathbf{B}_{e}\mathbf{U}_{e}^{n-1}) + 2\mu_{e}\Delta\gamma_{ei}^{n}\mathbf{N}_{ei}^{n} = 0 \\ e_{p_{ei}}{}^{n} - e_{p_{ei}}{}^{n-1} - \sqrt{\frac{2}{3}}\Delta\gamma_{ei}^{n} = 0 \\ ||\mathbf{s}||_{ei}^{n} - \sqrt{\frac{2}{3}}[\sigma_{Y\,e} + H_{p_e} e_{p_{ei}}{}^{n}] = 0 \end{bmatrix} \tag{5.10}$$

It can be observed that three variables on each integration point are considered, i.e. $\mathbf{v}^{n} = [\boldsymbol{\sigma}_{ei}^{n} \quad e_{p_{ei}}{}^{n} \quad \Delta\gamma_{ei}^{n}]$.

5.2.3 Consistent tangent stiffness

Although a general description of stress return-mapping algorithm and calculation of plastic variables and tangent stiffness for elstoplastic material is given in Chapter 4 Section 4.3.2 and Section 4.3.3, here, a more straightforward description of calculation for the specified material modelled by von Mises yield criterion and isotropic hardening is given. As known that the stress rate can be written as

$$\dot{\boldsymbol{\sigma}} = \mathbf{D} : (\dot{\boldsymbol{\epsilon}} - \dot{\boldsymbol{\epsilon}}^{p}) = \mathbf{D} : \dot{\boldsymbol{\epsilon}} - \dot{\gamma}\mathbf{D} : \mathbf{N} \tag{5.11}$$

In the von Mises plastic model, the hydrostatic pressure (volumetric stress) is independent of plastic deformation, therefore, the yield function is defined using the deviatoric stress alone. Since $\mathbf{N}$ is a unit deviatoric tensor, and based on Eq.(1.14), the following derivation can be obtained as

$$\mathbf{D} : \mathbf{N} = 2\mu\mathbf{N} \tag{5.12}$$

Therefore, Eq.(5.11) can be further written as

$$\dot{\boldsymbol{\sigma}} = \mathbf{D} : \dot{\boldsymbol{\epsilon}} - 2\mu\dot{\gamma}\mathbf{N} \tag{5.13}$$

The rate of change of yield function is given by

$$\dot{f} = \frac{\partial f}{\partial \mathbf{s}} : \dot{\mathbf{s}} + \frac{\partial f}{\partial e_{p}}\dot{e_{p}} = 0 \tag{5.14}$$

with

$$\begin{aligned}
&\frac{\partial f}{\partial \mathbf{s}} = \frac{1}{2}\frac{1}{\sqrt{\mathbf{s}:\mathbf{s}}}2\mathbf{s} = \frac{\mathbf{s}}{\sqrt{\mathbf{s}:\mathbf{s}}} = \frac{\mathbf{s}}{||\mathbf{s}||} = \mathbf{N} \\
&\frac{\partial f}{\partial e_p} = -\sqrt{\frac{2}{3}}H_p \\
&\dot{\mathbf{s}} = 2\mu(\dot{\mathbf{e}} - \dot{\mathbf{e}_p}) = 2\mu\dot{\mathbf{e}} - 2\mu\gamma\mathbf{N} \\
&\dot{e_p} = \sqrt{\frac{2}{3}}\gamma
\end{aligned} \tag{5.15}$$

Hence, the rate of yield function can be written into a function in terms of the plastic consistency parameter as

$$\dot{f} = 2\mu\mathbf{N} : \dot{\boldsymbol{\epsilon}} - 2\mu\gamma\mathbf{N} : \mathbf{N} - \frac{2}{3}H_p\gamma = 0 \tag{5.16}$$

The plastic consistency parameter γ is obtained as

$$\gamma = \frac{2\mu\mathbf{N} : \dot{\boldsymbol{\epsilon}}}{2\mu + \frac{2}{3}H_p} \tag{5.17}$$

By substituting Eq.(5.17) into Eq.(5.13), the tangent stiffness can be derived as

$$\begin{aligned}
\dot{\boldsymbol{\sigma}} &= \mathbf{D} : \dot{\boldsymbol{\epsilon}} - 2\mu\dot{\gamma}\mathbf{N} \\
&= \mathbf{D} : \dot{\boldsymbol{\epsilon}} - 2\mu\mathbf{N}\frac{2\mu\mathbf{N} : \dot{\boldsymbol{\epsilon}}}{2\mu + \frac{2}{3}H_p} \\
&= [\mathbf{D} - \frac{4\mu^2}{2\mu + \frac{2}{3}H_p}\mathbf{N} \otimes \mathbf{N}] : \dot{\boldsymbol{\epsilon}}
\end{aligned} \tag{5.18}$$

Thus, the elastoplastic tangent stiffness $\mathbf{D}^{ep}$ can be achieved by

$$\mathbf{D}^{ep} = \mathbf{D} - \frac{4\mu^2}{2\mu + \frac{2}{3}H_p}\mathbf{N} \otimes \mathbf{N} \tag{5.19}$$

The computational cost for nonlinear analysis is dominantly determined by the convergence during Newton-Raphson iteration. And when the structure partially enter the plastic state, the tangent stiffness representing the relation between the stress rate and strain rate straightforwardly effect the speed of convergence. When use the elastoplastic tangent stiffness $\mathbf{D}^{ep}$, Newton-Raphson iteration does not show a quadratic convergence. According to Simo and Taylor [74], this is due to $\mathbf{D}^{ep}$ is not consistent with the time itegration algorithm. And the consistent

tangent stiffness can be achieved by differentiating the incremental stress with respect to the incremental strain, which provides a consistent constitutive relation with the return-mapping algorithm as

$$\begin{aligned}\mathbf{D}^{cs} = \frac{\partial \Delta\boldsymbol{\sigma}}{\partial \Delta\boldsymbol{\epsilon}} &= \frac{\partial(\mathbf{D} : \Delta\boldsymbol{\epsilon} - 2\mu\Delta\gamma\mathbf{N})}{\partial \Delta\boldsymbol{\epsilon}} \\ &= \mathbf{D} - 2\mu\mathbf{N} \otimes \frac{\partial \Delta\gamma}{\partial \Delta\boldsymbol{\epsilon}} - 2\mu\Delta\gamma\frac{\partial \mathbf{N}}{\partial \Delta\boldsymbol{\epsilon}}\end{aligned} \tag{5.20}$$

where $\mathbf{D}^{cs}$ represents the consistent tangent stiffness. As known that during the return-mapping algorithm, the deviatoric stress, and the equivalent plastic strain at time t_{n+1} can be calculated as

$$\begin{aligned}\mathbf{s}_{n+1} &= \mathbf{s}_{trial} - 2\mu\Delta\gamma\mathbf{N} \\ e_{p_{n+1}} &= e_{p_n} + \sqrt{\frac{2}{3}}\Delta\gamma\end{aligned} \tag{5.21}$$

where the deviatoric unit tensor $\mathbf{N} = \frac{\mathbf{s}_{n+1}}{||\mathbf{s}_{n+1}||} = \frac{\mathbf{s}^{trial}}{||\mathbf{s}^{trial}||}$ means that the final updated deviatoric stress $\mathbf{s}_{n+1}$ moves in the same direction of the trial deviatoric stress $\mathbf{s}^{trial}$ which is parallel to $\mathbf{N}$. Hence, the following yielding function for a certain material point at time t_{n+1} must be satisfied

$$\begin{aligned}f_{n+1} &= ||\mathbf{s}_{n+1}|| - \sqrt{\frac{2}{3}}(\sigma_Y + H_p e_{p_{n+1}}) \\ &= ||\mathbf{s}^{trial}|| - 2\mu\Delta\gamma - \sqrt{\frac{2}{3}}(\sigma_Y + H_p e_{p_{n+1}}) = 0\end{aligned} \tag{5.22}$$

Thus, in order to solve Eq.(5.20) to achieve the consistent tangent stiffness, the unknown derivative $\frac{\partial \mathbf{N}}{\partial \Delta\boldsymbol{\epsilon}}$ can be obtained as follows:

$$\begin{aligned}\frac{\mathbf{N}}{\Delta\boldsymbol{\epsilon}} &= \frac{\partial \mathbf{N}}{\partial \mathbf{s}^{trial}} : \frac{\partial \mathbf{s}^{trial}}{\Delta\boldsymbol{\epsilon}} \\ &= \frac{\partial \frac{\mathbf{s}^{trial}}{||\mathbf{s}^{trial}||}}{\partial \mathbf{s}^{trial}} : \frac{\partial(\boldsymbol{\sigma}^{trial} : \mathbf{I}_{dev})}{\partial \Delta\boldsymbol{\epsilon}} \\ &= [\frac{\mathbf{I}}{||\mathbf{s}^{trial}||} - \frac{\mathbf{s}^{trial} \otimes \mathbf{s}^{trial}}{||\mathbf{s}^{trial}||^3}] : 2\mu\mathbf{I}_{dev} \\ &= \frac{2\mu}{||\mathbf{s}^{trial}||}[\mathbf{I}_{dev} - \mathbf{N} \otimes \mathbf{N}]\end{aligned} \tag{5.23}$$

And the unknown derivative $\frac{\partial \Delta\gamma}{\partial \boldsymbol{\Delta\epsilon}}$ can be calculated through differentiating the yield function in Eq.(5.22) with respect to the incremental strain

$$\frac{f}{\boldsymbol{\Delta\epsilon}} = \frac{\partial ||\mathbf{s}^{trial}||}{\partial \boldsymbol{\Delta\epsilon}} - 2\mu \frac{\partial \Delta\gamma}{\partial \boldsymbol{\Delta\epsilon}} - \sqrt{\frac{2}{3}} H_p \frac{\partial e_{p_{n+1}}}{\partial \Delta\gamma} \frac{\partial \Delta\gamma}{\partial \boldsymbol{\Delta\epsilon}} = 0 \tag{5.24}$$

with

$$\begin{aligned} \frac{\partial ||\mathbf{s}^{trial}||}{\partial \boldsymbol{\Delta\epsilon}} = \frac{\partial \frac{\mathbf{s}^{trial}}{\mathbf{N}}}{\partial \boldsymbol{\Delta\epsilon}} &= \frac{\frac{\partial \mathbf{s}^{trial}}{\partial \boldsymbol{\Delta\epsilon}} \mathbf{N} - \mathbf{s}^{trial} \frac{\partial \mathbf{N}}{\partial \boldsymbol{\Delta\epsilon}}}{\mathbf{N}^2} \\ &= \frac{2\mu \mathbf{I}_{dev} \mathbf{N} - \mathbf{s}^{trial} \frac{2\mu}{||\mathbf{s}^{trial}||} [\mathbf{I}_{dev} - \mathbf{N} \otimes \mathbf{N}]}{\mathbf{N}^2} \\ &= 2\mu \mathbf{N} \end{aligned} \tag{5.25}$$

Hence, Eq.(5.24) can be further modified as

$$\frac{f}{\boldsymbol{\Delta\epsilon}} = 2\mu \mathbf{N} - 2\mu \frac{\partial \Delta\gamma}{\partial \boldsymbol{\Delta\epsilon}} - \frac{2}{3} H_p \frac{\partial \Delta\gamma}{\partial \boldsymbol{\Delta\epsilon}} = 0 \tag{5.26}$$

Thus, the derivative of the plastic consistency parameter with respect to the incremental strain $\frac{\partial \Delta\gamma}{\partial \boldsymbol{\Delta\epsilon}}$ is then obtained as

$$\frac{\partial \Delta\gamma}{\partial \boldsymbol{\Delta\epsilon}} = \frac{2\mu \mathbf{N}}{2\mu + \frac{2}{3} H_p} \tag{5.27}$$

By substituting Eq.(5.23) and Eq.(5.27) into Eq.(5.20), the consistent tangent stiffness is achieved as

$$\mathbf{D}^{cs} = \mathbf{D} - \frac{4\mu^2}{2\mu + \frac{2}{3} H_p} \mathbf{N} \otimes \mathbf{N} - \frac{4\mu^2 \Delta\gamma}{||\mathbf{s}^{trial}||} [\mathbf{I}_{dev} - \mathbf{N} \otimes \mathbf{N}] \tag{5.28}$$

In comparison with Eq.(5.19), it can be observed that an additional term is added in Eq.(5.28) where the change in direction for the strain increment is also taken into account. When the strain increment is large, the direction of deviatoric stress may change. Note that when the material stay in elastic state where the trial value of yield function is less than 0, either elastoplastic tangent stiffness $\mathbf{D}^{ep}$ or consistent tangent stiffness $\mathbf{D}^{cs}$ become identical and equal to the elastic tangent stiffness $\mathbf{D}$.

5.3 BESO optimization procedure

5.3.1 Problem statement

In this study, BESO optimization method is used to maximize the external force at the final incremental loading step with material volume constraint for elasto-plastic structure. And the displacement-incremental method is applied throughout the nonlinear analysis. The optimization objective function, volume constraint and coupled mechanical equilibrium in both global and local level are presented as follows:

$$\begin{aligned} \min \quad & f(\mathbf{x}) = -\varphi^N \mathbf{P}_{ref} \mathbf{u}^N \\ s.t. \quad & \sum_{e=1}^{nele} v_e x_e = V^* \\ & x_e = 0 \ \ or \ \ 1, \quad (e = 1, 2, ..., nele) \\ & \mathbf{R}^n(\mathbf{u}^n, \mathbf{u}^{n-1}, \mathbf{v}^n, \mathbf{v}^{n-1}, \mathbf{x}) = 0 \\ & \mathbf{H}^n(\mathbf{u}^n, \mathbf{u}^{n-1}, \mathbf{v}^n, \mathbf{v}^{n-1}, \mathbf{x}) = 0 \\ & n = 1, 2, ..., N, \end{aligned} \tag{5.29}$$

where x_e depicts the elemental design variable updated in each iteration and V^* is the prescribed target volume fraction of the design domain. $\mathbf{P}_{ref}$ is a constant external load vector with non-zero entries only at loaded degrees of freedom. φ^N denotes the unknown load factor at the final loading step N. The objective function stated in Eq.(6.12) only valid under certain load conditions, and will lead to a complicated sensitivity analysis. Therefore, Amir et al. [75] proposed a simplified hybrid approach using the load-controlled concept to generate a more applicable objective function as following: $f(\mathbf{x}) = \mathbf{P}^N \mathbf{u}^N$, but the actual nonlinear analysis is performed through a displacement-controlled method.

5.3.2 Sensitivity analysis

5.3.2.1 Adjoint method

The path-dependent adjoint method is applied to compute the elemental sensitivity numbers. The objective function is augmented by adding the global and

the local residuals due to their infinitesimal value. In this study, the only variable associated with the objective function f is nodal displacement $\mathbf{u}$ and the global residual $\mathbf{R}$ only depend on the variable $\mathbf{v}$. Hence the simplified augmented objective function is written as:

$$\begin{aligned}\hat{c} &= c(\mathbf{x},\mathbf{u}) + \sum_{n=1}^{N} \boldsymbol{\xi}^{nT}\mathbf{R}^n(\mathbf{u}^n,\mathbf{u}^{n-1},\mathbf{v}^n,\mathbf{v}^{n-1},\mathbf{x}) + \sum_{n=1}^{N} \boldsymbol{\theta}^{nT}\mathbf{H}^n(\mathbf{u}^n,\mathbf{u}^{n-1},\mathbf{v}^n,\mathbf{v}^{n-1},\mathbf{x}) \\ &= c(\mathbf{u}) + \sum_{n=1}^{N} \boldsymbol{\xi}^{nT}\mathbf{R}^n(\mathbf{v}^n) + \sum_{n=1}^{N} \boldsymbol{\theta}^{nT}\mathbf{H}^n(\mathbf{u}^n,\mathbf{u}^{n-1},\mathbf{v}^n,\mathbf{v}^{n-1},\mathbf{x}),\end{aligned} \tag{5.30}$$

where $\boldsymbol{\xi}^n$ and $\boldsymbol{\theta}^n$ are two adjoint vectors to be calculated through the sensitivity analysis. The differentiation of the objective function c with respect to design variables $\mathbf{x}$ is equivalent to the derivative of the augmented function $\hat{c}$, and it can be decomposed into an explicit term and an implicit term

$$\frac{\partial c}{\partial \mathbf{x}} = \frac{\partial \hat{c}}{\partial \mathbf{x}} = \frac{\partial \hat{c}_{exp}}{\partial \mathbf{x}} + \frac{\partial \hat{c}_{imp}}{\partial \mathbf{x}}. \tag{5.31}$$

In order to eliminate the unknown term of derivatives $\frac{\partial \mathbf{u}^n}{\partial \mathbf{x}}$ and $\frac{\partial \mathbf{v}^n}{\partial \mathbf{x}}$, the backward incremental calculation approach is applied to obtain the Lagrange multipliers $\boldsymbol{\theta}^n, \boldsymbol{\xi}^n$ for all increments $n = 1, ..., N$

$$\begin{aligned}&\frac{\partial \hat{c}_{imp}}{\partial \mathbf{x}} = \frac{\partial \hat{c}^N_{imp}}{\partial \mathbf{x}} + \sum_{n=1}^{N-1} \frac{\partial \hat{c}^n_{imp}}{\partial \mathbf{x}} \\ &\frac{\partial \hat{c}^N_{imp}}{\partial \mathbf{x}} = (\frac{\partial c}{\partial \mathbf{u}^N} + \boldsymbol{\theta}^{NT}\frac{\partial \mathbf{H}^N}{\partial \mathbf{u}^N})\frac{\partial \mathbf{u}^N}{\partial \mathbf{x}} + (\boldsymbol{\xi}^{NT}\frac{\partial \mathbf{R}^N}{\partial \mathbf{v}^N} + \boldsymbol{\theta}^{NT}\frac{\partial \mathbf{H}^N}{\partial \mathbf{v}^N})\frac{\partial \mathbf{v}^N}{\partial \mathbf{x}} \\ &\frac{\partial \hat{c}^n_{imp}}{\partial \mathbf{x}} = (\frac{\partial c}{\partial \mathbf{u}^n} + \boldsymbol{\theta}^{nT}\frac{\partial \mathbf{H}^n}{\partial \mathbf{u}^n} + \boldsymbol{\theta}^{n+1T}\frac{\partial \mathbf{H}^{n+1}}{\partial \mathbf{u}^n})\frac{\partial \mathbf{u}^n}{\partial \mathbf{x}} \\ &+ (\boldsymbol{\xi}^{nT}\frac{\partial \mathbf{R}^n}{\partial \mathbf{v}^n} + \boldsymbol{\theta}^{nT}\frac{\partial \mathbf{H}^n}{\partial \mathbf{v}^n} + \boldsymbol{\theta}^{n+1T}\frac{\partial \mathbf{H}^{n+1}}{\partial \mathbf{v}^n})\frac{\partial \mathbf{v}^n}{\partial \mathbf{x}}\end{aligned} \tag{5.32}$$

For the final step N:

$$\begin{cases}\dfrac{\partial c}{\partial \mathbf{u}^N} + \boldsymbol{\theta}^{NT}\dfrac{\partial \mathbf{H}^N}{\partial \mathbf{u}^N} = 0 \\ \boldsymbol{\xi}^{NT}\dfrac{\partial \mathbf{R}^N}{\partial \mathbf{v}^N} + \boldsymbol{\theta}^{NT}\dfrac{\partial \mathbf{H}^N}{\partial \mathbf{v}^N} = 0\end{cases} \tag{5.33}$$

For steps from $n = 1$ to $N - 1$:

$$\begin{cases} \dfrac{\partial c}{\partial \mathbf{u}^n} + \boldsymbol{\theta}^{nT} \dfrac{\partial \mathbf{H}^n}{\partial \mathbf{u}^n} + \boldsymbol{\theta}^{n+1T} \dfrac{\partial \mathbf{H}^{n+1}}{\partial \mathbf{u}^n} = 0 \\ \boldsymbol{\xi}^{nT} \dfrac{\partial \mathbf{R}^n}{\partial \mathbf{v}^n} + \boldsymbol{\theta}^{nT} \dfrac{\partial \mathbf{H}^n}{\partial \mathbf{v}^n} + \boldsymbol{\theta}^{n+1T} \dfrac{\partial \mathbf{H}^{n+1}}{\partial \mathbf{v}^n} = 0 \end{cases} \tag{5.34}$$

Therefore based on the obtained adjoint vector and the derivative of the explicit term, the design sensitivity with respect to the design variables can be written as

$$\frac{\partial c}{\partial \mathbf{x}} = \frac{\partial \hat{c}_{exp}}{\partial \mathbf{x}} = \sum_{n=1}^{N} \boldsymbol{\theta}^{nT} \frac{\partial \mathbf{H}^n}{\partial \mathbf{x}} \tag{5.35}$$

Furthermore, the derivatives $\frac{\partial c}{\partial \mathbf{u}^N}$, $\frac{\partial \mathbf{H}^n}{\partial \mathbf{u}^n}$, $\frac{\partial \mathbf{H}^{n+1}}{\partial \mathbf{u}^n}$, $\frac{\partial \mathbf{H}^n}{\partial \mathbf{v}^n}$, $\frac{\partial \mathbf{H}^{n+1}}{\partial \mathbf{v}^n}$ and $\frac{\partial \mathbf{R}^n}{\partial \mathbf{v}^n}$ are required to solve the above equilibriums presented in Eq. (6.23) and Eq. (6.24). This will be discussed in the next subsection. Note that since x_e equals to either 1 or 0, the sensitivities are actually only evaluated for solid elements wheras zero for void elements.

5.3.2.2 Derivatives calculation

The variables $\mathbf{v}^n$ on integration-point level consist of stress $\boldsymbol{\sigma}^n$, equivalent plastic strain e_p^n and the plastic multiplier $\Delta\gamma^n$. The required derivatives in matrix form are given as follows

$$\frac{\partial \mathbf{H}_{ei}^n}{\partial \mathbf{v}_{ei}^n} = \begin{bmatrix} \frac{\partial \mathbf{H}_{ei1}^n}{\partial \boldsymbol{\sigma}_{ei}^n} & \frac{\partial \mathbf{H}_{ei1}^n}{\partial e_{p_{ei}}^n} & \frac{\partial \mathbf{H}_{ei1}^n}{\Delta\gamma_{ei}^n} \\ \frac{\partial \mathbf{H}_{ei3}^n}{\partial \boldsymbol{\sigma}_{ei}^n} & \frac{\partial \mathbf{H}_{ei3}^n}{\partial e_{p_{ei}}^n} & \frac{\partial \mathbf{H}_{ei3}^n}{\Delta\gamma_{ei}^n} \\ \frac{\partial \mathbf{H}_{ei4}^n}{\partial \boldsymbol{\sigma}_{ei}^n} & \frac{\partial \mathbf{H}_{ei4}^n}{\partial e_{p_{ei}}^n} & \frac{\partial \mathbf{H}_{ei4}^n}{\Delta\gamma_{ei}^n} \end{bmatrix} \tag{5.36}$$

$$\frac{\partial \mathbf{H}_{ei}^n}{\partial \mathbf{u}_e^n} = \begin{bmatrix} \frac{\partial \mathbf{H}_{ei1}^n}{\partial \mathbf{u}_e^n} & \frac{\partial \mathbf{H}_{ei2}^n}{\partial \mathbf{u}_e^n} & \frac{\partial \mathbf{H}_{ei3}^n}{\partial \mathbf{u}_e^n} \end{bmatrix}^T \tag{5.37}$$

$$\frac{\partial \mathbf{H}_{ei}^n}{\partial x_e} = \begin{bmatrix} \frac{\partial \mathbf{H}_{ei1}^n}{\partial x_e} & \frac{\partial \mathbf{H}_{ei2}^n}{\partial x_e} & \frac{\partial \mathbf{H}_{ei3}^n}{\partial x_e} \end{bmatrix}^T \tag{5.38}$$

$$\frac{\partial \mathbf{R}_e^n}{\partial \mathbf{v}_{ei}^n} = \begin{bmatrix} \frac{\partial \mathbf{R}_e^n}{\partial \boldsymbol{\sigma}_{ei}^n} & \frac{\partial \mathbf{R}_e^n}{\partial e_{p_{ei}}^n} & \frac{\partial \mathbf{R}_e^n}{\Delta\gamma_{ei}^n} \end{bmatrix} \tag{5.39}$$

When the material response stays in the elastic stage:

$$\frac{\partial \mathbf{H}_{ei}^n}{\partial \mathbf{v}_{ei}^n} = \begin{bmatrix} \mathbf{I} & \mathbf{0} & \mathbf{0} \\ \mathbf{0} & 1 & 0 \\ \mathbf{0} & 0 & 1 \end{bmatrix} \tag{5.40}$$

$$\frac{\partial \mathbf{H}_{ei}^{n}}{\partial x_e} = \left[-\frac{\partial \mathbf{D}_e^0}{\partial x_e} : (\mathbf{B}_{ei}\mathbf{u}_e^n - \mathbf{B}_{ei}\mathbf{u}_e^{n-1}) \quad 0 \quad 0 \right]^T \tag{5.41}$$

In the plastic stage, the derivatives of the local residual with respect to the variable $\mathbf{v}$ and the design variable $\mathbf{x}$ can be derived as follows

$$\frac{\partial \mathbf{H}_{ei}^{n}}{\partial \mathbf{v}_{ei}^{n}} = \begin{bmatrix} \mathbf{I} + 2\mu_e \Delta\gamma_{ei}^n (\frac{\partial \mathbf{N}}{\partial \boldsymbol{\sigma}})_{ei}^n & \mathbf{0} & 2\mu_e \mathbf{N}_{ei}^n \\ \mathbf{0} & 1 & -\sqrt{\frac{2}{3}} \\ \mathbf{N}_{ei}^n & -\sqrt{\frac{2}{3}} H_{p_e} & 0 \end{bmatrix} \tag{5.42}$$

$$\frac{\partial \mathbf{H}_{ei}^{n}}{\partial x_e} = \begin{bmatrix} -\frac{\partial \mathbf{D}_e^0}{\partial x_e} : (\mathbf{B}_{ei}\mathbf{u}_e^n - \mathbf{B}_{ei}\mathbf{u}_e^{n-1}) + 2\Delta\gamma_{ei}^n \mathbf{N}_{ei}^n \frac{\partial \mu_e}{\partial x_e} \\ 0 \\ -\sqrt{\frac{2}{3}} \frac{\partial \sigma_{y_e}}{\partial x_e} - \sqrt{\frac{2}{3}} \frac{\partial H_{p_e}}{\partial x_e} e_{p}{}_{ei}^{n} \end{bmatrix} \tag{5.43}$$

with

$$(\frac{\partial \mathbf{N}}{\partial \boldsymbol{\sigma}})_{ei}^n = \frac{1}{||\mathbf{s}||_{ei}^n} [\mathbf{I}_{dev} - \mathbf{N}_{ei}^n \otimes \mathbf{N}_{ei}^n] \tag{5.44}$$

where $\mathbf{I}_{dev} = \mathbf{I} - \frac{1}{3}\mathbf{1} \otimes \mathbf{1}$ is the unit deviatoric tensor of the fourth-order. Opposite to the derivatives of $\mathbf{H}^n$ with respect to the internal variable $\mathbf{v}^n$ and the design variable $\mathbf{x}$ are different in the elastic and plastic step, the following derivatives do not depend on the finite element analysis response

$$\frac{\partial \mathbf{H}_{ei}^{n+1}}{\partial \mathbf{v}_{ei}^{n}} = \begin{bmatrix} -\mathbf{I} & \mathbf{0} & \mathbf{0} \\ \mathbf{0} & -1 & 0 \\ \mathbf{0} & 0 & 0 \end{bmatrix} \tag{5.45}$$

$$\frac{\partial \mathbf{H}_{ei}^{n}}{\partial \mathbf{u}_{e}^{n}} = \begin{bmatrix} -\mathbf{D}_e^0 \mathbf{B}_{ei} & 0 & 0 \end{bmatrix}^T \tag{5.46}$$

$$\frac{\partial \mathbf{H}_{ei}^{n+1}}{\partial \mathbf{u}_{e}^{n}} = \begin{bmatrix} \mathbf{D}_e^0 \mathbf{B}_{ei} & 0 & 0 \end{bmatrix}^T \tag{5.47}$$

$$\frac{\partial \mathbf{R}_{e}^{n}}{\partial \mathbf{v}_{ei}^{n}} = \begin{bmatrix} \mathbf{B}_{ei}^T w_{ei} & 0 & 0 \end{bmatrix} \tag{5.48}$$

Therefore the matrix of the differentiation of $\mathbf{H}^n$ need to be adjusted according to the trial elastic condition, which keep consistency with the analysis at each increment.

5.3.3 Update of design variables

BESO design starts from the full structural domain and its volume gradually decreases until the target volume is reached. The evolutionary function is given by

$$V^l = V^{l-1}(1 - R_{er}), \qquad l = 1, 2, 3... \tag{5.49}$$

where R_{er} is the evolutionary ratio, l represents the current optimization iteration.

The elemental sensitivity number derived in Eq.(6.25) cannot be applied directly to the BESO updating scheme. To address the mesh-dependent and convergence problem, a filtering scheme [76] is utilized to smooth the sensitivity numbers by taking the surrounding sensitivities into account.

$$a_e = \frac{\sum_{i=1}^{N} w_{ei} a_i}{\sum_{i=1}^{N} w_{ei}} \tag{5.50}$$

with

$$w_{ei} = max(0, r_{min} - dis(e, i)) \tag{5.51}$$

where a_e and a_i denote the design sensitivity of element e and element i, respectively. w_{ei} is the weight factor, r_{min} is the filter radius and the item $dis(e, i)$ represents the distance between of centres of element e and element i. Moreover, a scheme of averaging the sensitivity numbers in the current iteration with that in the previous iteration is normally implemented to further improve the optimization stability [18].

$$a_e^l = \frac{a_e^l + a_e^{l-1}}{2} \tag{5.52}$$

In most previous studies on BESO plastic design, a threshold parameter a_{add}^{th} is also considered in order to control the recovered number of elements from voids [29, 71, 72]. This is mainly due to extensive elements readded to the structure may deteriorate the optimization design and result in difficulty in solution convergence. Here, in this paper, only one threshold parameter a^{th} is set up iteratively, which is to some extent simplify the algorithm of updating design variables. The value of the parameter a^{th} is determined based on the prescribed volume required in the current iteration. When the sensitivity number of an element is higher than

a^{th}, as shown in Eq.(6.42), the corresponding design variable remains equal to 1 for solid element or change from 0 to 1 for the void.

$$a_e > a^{th} \tag{5.53}$$

While for those elements with the sensitivity numbers lower than a^{th}, as shown in Eq.(6.43), they are removed from the current design domain.

$$a_e \leq a^{th} \tag{5.54}$$

Once the prescribed volume is satisfied, the optimization procedure repeats with a constant volume and stopped by the following convergence criterion:

$$\frac{|\sum_{j=1}^{N}(C_{i-j+1} - C_{i-N-j+1})|}{\sum_{j=1}^{N} C_{i-j+1}} \leq \tau \tag{5.55}$$

where N is an integral number defined as 5 in this study. And τ is the allowable convergence tolerance relating to the change in objective function. It is set up equal to $10e-4$ for all examples examined here. In summary, a flowchart describing the BESO optimization procedure is presented in Fig.5.1.

5.4 Examples

5.4.1 Design of a cantilever beam

A benchmark design of a cantilever beam, as presented in the previous study [29], is examined here to verify the proposed BESO optimization framework. Fig.5.2 shows the design domain where the left edge is fully clamped and a downward prescribed displacement is distributed along the distance of 200mm at the center of the right side. The whole design domain is discretized into 5000 (100 x 50) elements. The mechanical property of the material candidate employing an isotropic hardening von Mises plastic model is detailed as follows: Young's modulus $E = 75GPa$; initial yielding stress $\sigma_y = 100MPa$; plastic modulus $H_p = 1000MPa$ and poisson ratio $v = 0.3$. The target volume fraction to the

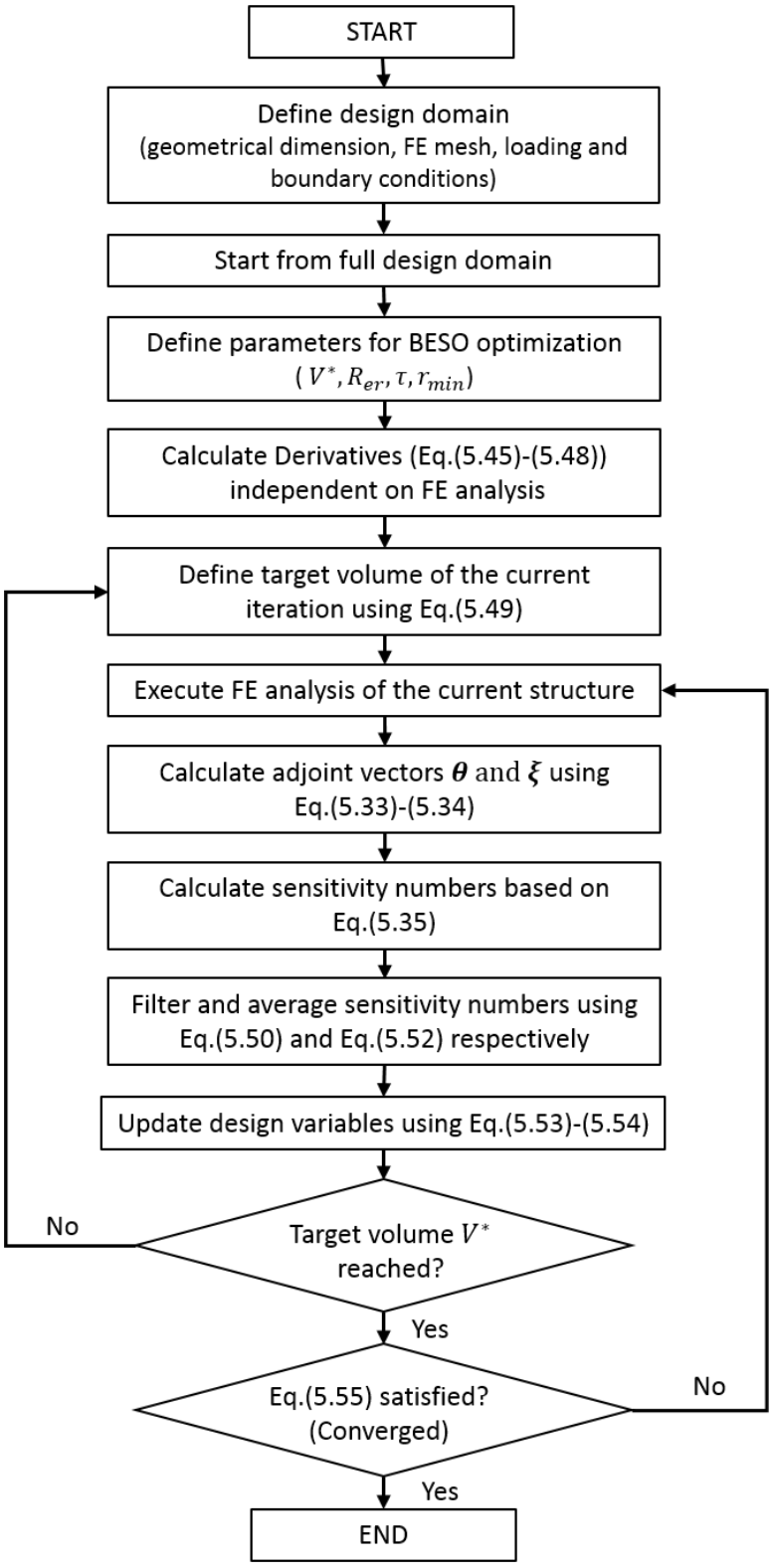

Figure 5.1: Flowchart of BESO optimization procedure

whole design domain is assumed to be 60%. The filtering radius (r_{min}) is set up as 4 size of the element length and remain constant in the optimization procedure. The evolutionary ratio (R_{er}) is defined equal to 2%.

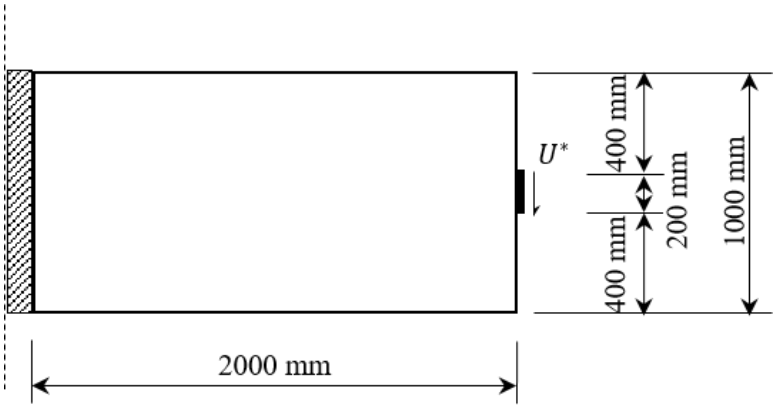

Figure 5.2: Design domain of the cantilever beam

In this example, four cases with the prescribed displacement assumed to be $1mm$, $5mm$, $7mm$ and $10mm$, respectively, are examined. Five loading time steps are considered, which means the incremental displacement is equal to 20% of the total displacement. Fig.5.3 presents the resulting topologies. It can be observed that the remaining elements serving in tension and compression are symmetrically distributed at the top and the bottom of the beam for all cases. Apart from the design layout shown in Fig.5.3 (c) where an extra cross branches appears, same number of structural branches are developed through the optimization design as presented in Fig.5.3 (a), (b) and (d). Note that with the increase in the applied prescribed displacement, the whole internal skeleton resisting to the plastic response moves approaching to the left boundary to strength the beam. Fig.5.4 highlights that all the cases succeed in achieving a convergent solution that satisfy the tolerance error of $10e-4$. Particularly, for the case applied with the prescribed displacement of $10mm$ fails to converge in the previous study [29], while it converges successfully in 32 steps here, which demonstrates the robustness of the proposed BESO framework for the plastic design. The evolutionary histories of topology are also recorded in some typical iterations and presented in Fig.5.4. It can be seen that during the approximate initial 20 iterations, the objective function decreases monotonically in a stable pace. The topology at iterations 7 and 15

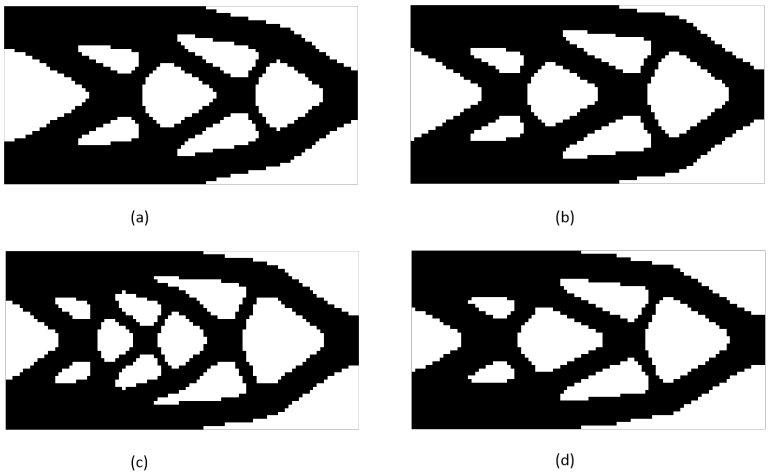

Figure 5.3: Resulting topologies for the cantilever beam optimization design when subjected to the prescribed displacement (a) 1mm; (b) 5mm; (c) 7mm; (d) 10mm

are plotted for all cases to compare the evolutionary difference at the beginning stage. When $u^* = 1mm$ is applied, the optimization problem is nearly belong to a linear elastic design, low efficient elements are removed simultaneously at the right front and the left back of the structure. However, following the growth of the displacement, less elements are removed at the back and the main evolution occurs at the front void areas. Furthermore, with the volume reduction, extensive holes are formed due to the existing of small structural branches. And after the target volume is reached, the redundant branches are eliminated and then added in essential places to adjust the topology and enhance the most needed branches. In this example, based on the evolutionary ratio of 0.02, the desired volume fraction of 60% to the complete design domain is satisfied at iteration 26. Obvious fluctuations can be observed in the objective function when existing branches are removed from the structure, as shown in Fig.5.4 (a) (iteration 26-27), Fig.5.4 (b) (iteration 37-38) and Fig.5.4 (d) (iteration 27). Whereas in Fig.5.4 (c), after the volume usage is reached, there is no oscillation occurring in the plot due to rare alteration in the topology is developed afterwards. The solution of cases applied with prescribed displacement of $1mm$, $5mm$, $7mm$ and $10mm$ converge at the optimization iteration 60, 59, 42, and 32, respectively. Hence, it can be concluded that the design topology convergence is independent of the prescribed

displacement (elastic or plastic dominated design).

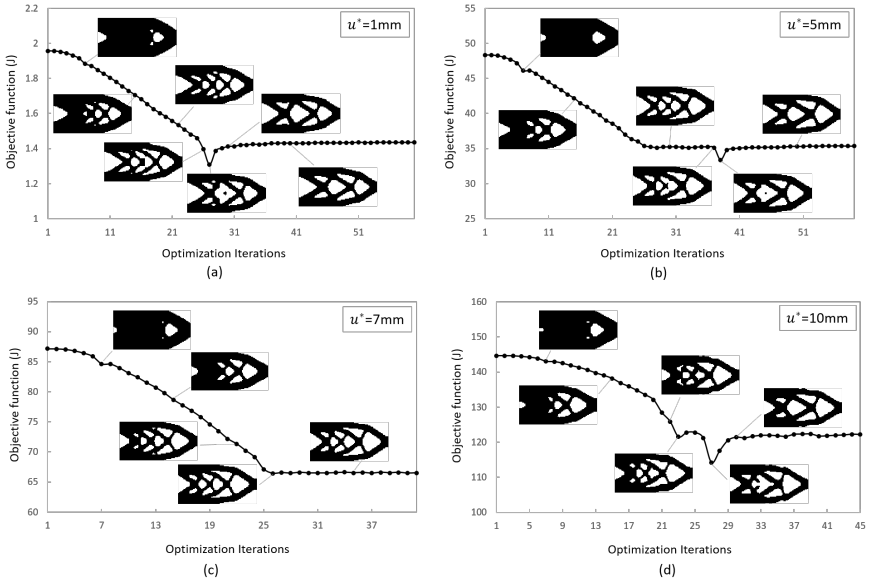

Figure 5.4: Evolutionary histories of objective function and topology for the cantilever beam subjected to various prescribed displacement in four cases

Then, for the purpose of evaluating the reasonability and reliability of the resulting topologies, the design layouts obtained in Fig.5.3 (a-d) are reanalysed when they are subjected to the same loading condition (i.e. prescribed displacement of $10mm$). Fig.5.5 (a-d) shows the equivalent stress distribution, and Fig.5.6 presents the maximum equivalent stress and plastic strain achieved in these four cases. It can be observed in Fig.5.5 (a) that high stress mainly concentrate around the boundary edge, while in Fig.5.5 (d), all the structural branches, especially for those placed at the middle and right front zones, are sufficiently involved in taking the von Mises stress. Apparently, using the design topology obtained in the case of $u^* = 10mm$ produces the most effective stress distribution. Also, as expected that the lowest efficient structure obtained from the case of $u^* = 1mm$, resulting in the highest maximum equivalent stress (172.34MPa) and plastic strain (0.0097mm), while the design of the case undertaking the plastic loading ($u^* = 10mm$) attains the lowest value of equivalent stress (143.10MPa) and plastic strain (0.0047mm). This may mitigate the stress concentration problem to some extent, in comparison with the other three designs in this case.

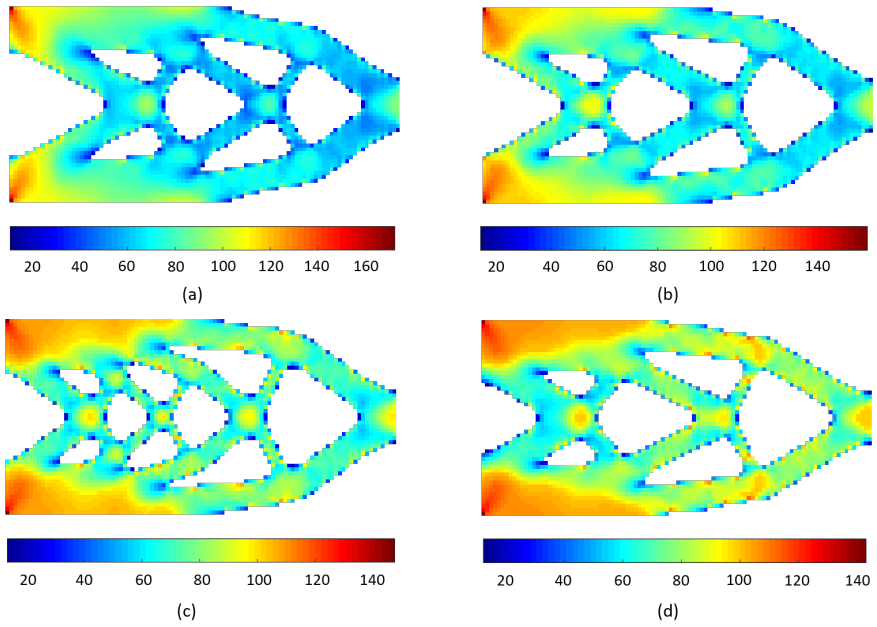

Figure 5.5: Equivalent stress distribution of different design layouts obtained in Fig.5.3 (a-d) subjected to displacement loading $u^* = 10mm$

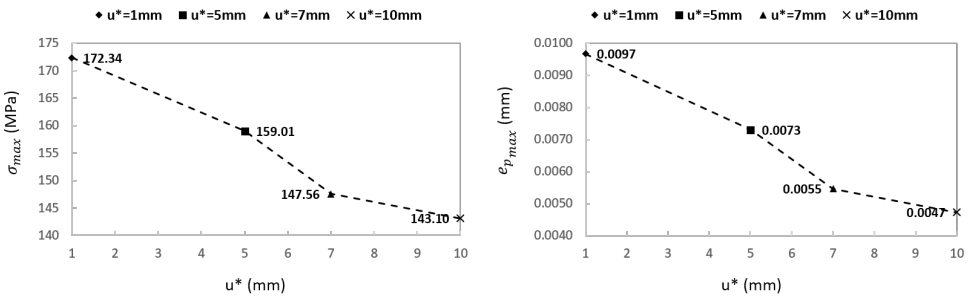

Figure 5.6: Maximum equivalent stress (left) and maximum equivalent plastic strain (right) of different design layouts obtained in Fig.5.3 (a-d) subjected to displacement loading $u^* = 10mm$

Additionally, a plot of force against displacement is presented in Fig.5.7. A prescribed displacement of u^*=20mm is applied to the four designs respectively to compare thier loading capacity at each stage. Firstly, when the displacement u=10mm, the corresponding force of the optimized design model achieved under the plastic design of u^*=10mm is the highest, followed by that of the optimized model with u^*=7mm, 5mm, and 1mm, and this trend become more obviously afterwards. Also, I compared the external force of each design when the displacement loading reach 1mm, 5mm, and 7mm respectively. To achieve a distinct comparison, the results of four designs on those specified points are presented in zoom in views (the red dot rectangular box). It shows when subjected to a small deformation (elastic loading condition), a pure elastic design is more efficient than a fully plastic or a plastic dominated design model. However, when the structure get into the plastic phase, its loading capacity decrease, which is possibly due to the high plastic strain or von Mises stress concentrate on some structural elements rather than that are more evenly distributed in the whole structure. Hence, it can be found that the loading capacity of each design model become the most effective when their deformation reach equivalent to the prescribed loading value, which also further demonstrate the reliability and accuracy of the proposed BESO method when taking the material elasoplasticity into account.

5.4.2 Design of a beam

An optimization design of a beam with length-to-height equal to three is considered here. As presented in Fig.5.8, both sides of the beam is fully clamped and a distributed prescribed displacement is applied at the central top surface along a distance of 50mm. The beam is discretized using 120×40 quadrilateral bilinear elements where the elemental length equals to 20mm. The associated material property is described as follows: Young's modulus $E = 200GPa$; initial yielding stress $\sigma_y = 250MPa$; plastic modulus $H_p = 200MPa$ and poisson ratio $v = 0.3$. The proposed BESO method starts from a complete design domain with an evolutionary removal ratio of 0.02 until the desired volume of 60% is achieved and then the convergent tolerance of $10e-4$ is satisfied. Also, the filtering radius

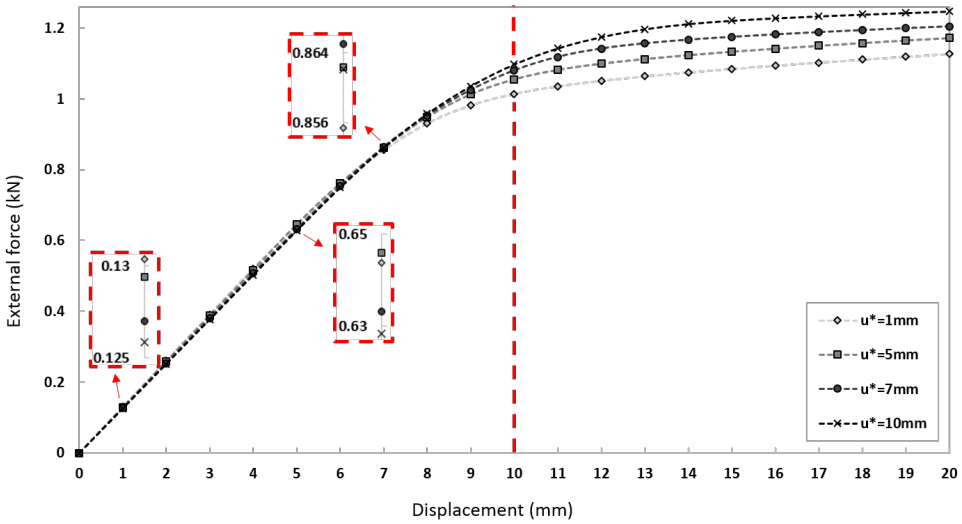

Figure 5.7: Comparison of external force against displacement of different design layouts obtained in Fig.5.3 (a-d) subjected to displacement loading $u^* = 20mm$

set up the same as that in the former example (4 times of the elemental length).

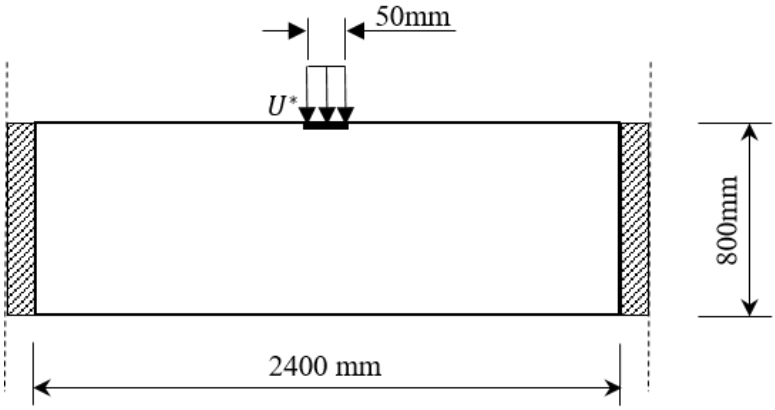

Figure 5.8: Design domain of the harf MMB beam

Four cases applied with the prescribed displacement of 1mm, 2mm, 3mm and 4mm respectively are conducted to validate the effectiveness of the proposed BESO framework for either nearly elastic design or a fully plastic design. The resulting topologies are presented in Fig.5.9. It can be observed that the design

layouts are remarkably different in the material distribution around the top central area of the beam where the prescribed loading is applied. With the increase of the displacement, larger amount of material are placed for compressive resistance. And the two inclined struts connecting the top stiffener and the bottom curve shaped tie become thicker. Fig.5.10 plots the change of the value of objective

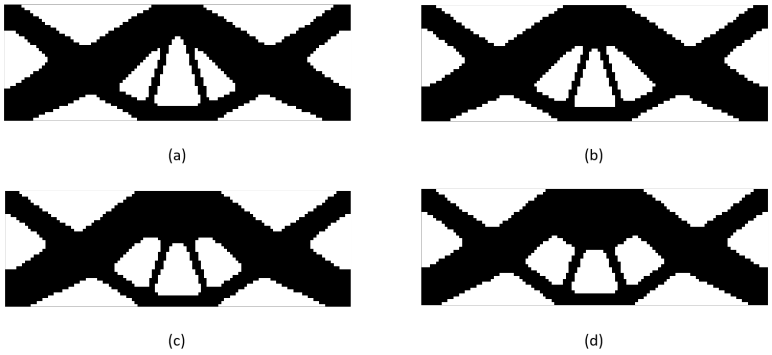

Figure 5.9: Resulting topologies for the cantilever beam optimization design when subjected to the prescribed displacement (a) 1mm; (b) 2mm; (c) 3mm; (d) 4mm

function throughout the optimization iterations. It should be pointed out that all designs successfully converged at iteration 39, 37, 40 and 61, respectively. Also, For sake of comparing the topology evolutionary history, the topologies obtained at iterations 8, 15, 20 and 30 are presented. In this example, opposite to the phenomenon observed from the first example in which obvious small branches are developed initially and gradually eliminated in the subsequent optimization iterations, there is no apparent new branches exist before or after reaching the target volume, especially for the first three cases (See Fig.5.10(a-c)). As shown in Fig.5.10(d), when the prescribed displacement u^*=4mm is applied, two tiny struts are developed beside the middle inner struts at iteration 15 and then removed afterwards. Hence, the elimination of redundant elements during optimization process may due to volume reduction or the structural self-adjustment before satisfying the convergence criterion.

To further validate the design models obtained in Fig.5.9 under different magnitude of deformation loading, I compared the von Mises stress distribution of the four designs when being applied with the same prescribed displacement of 4mm. The comparison is given in Fig.5.11, where total number of 66 elements

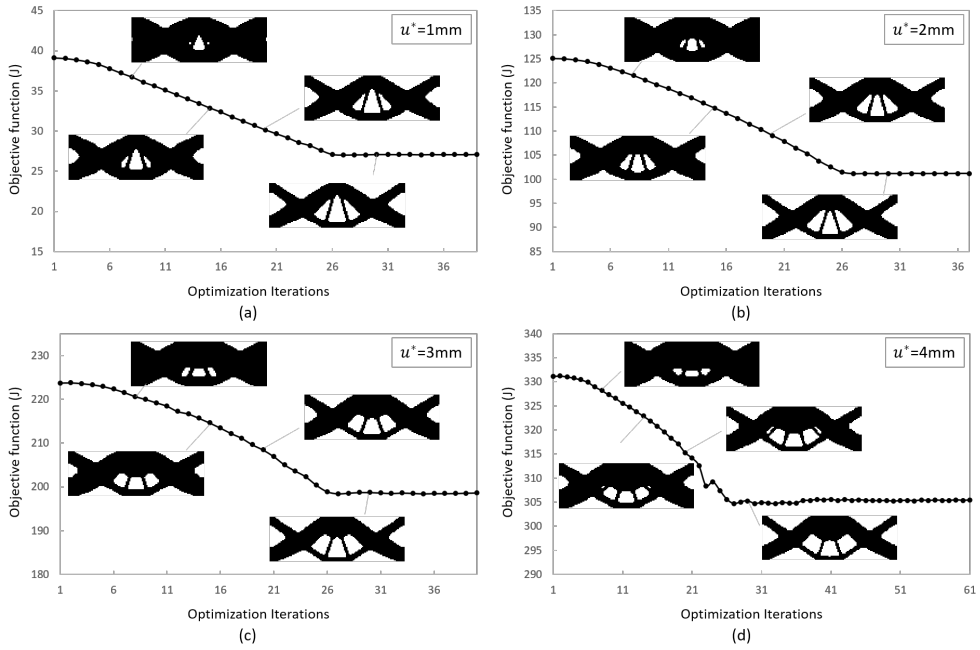

Figure 5.10: Evolutionary histories of objective function and topology for the cantilever beam subjected to various prescribed displacement in four cases

surrounding the loading area with high concentration stress are removed from the stress plot for the purpose of description. Also, Fig.5.12 demonstrates the the maximum equivalent stress (left) and plastic strain (right) of each design. It can be observed when the applied displacement load is 4mm for all the optimized models presented in Fig.5.9, the lowest σ_{max}=311.08MPa and $e_{p_{max}}$=0.0027mm is achieved by using Fig.5.9(d) design as the objective structure, whereas the highest σ_{max}=326.84MPa and $e_{p_{max}}$=0.0042mm is achieved based on Fig.5.9(a) model. Moreover, through comparing the stress plots in Fig.5.11 (d) with that in Fig.5.11 (a-c), it can seen that the von Mises stress is more equally distributed in more areas surrounding the loading points, and, the structural struts and ties contribute more in withstanding compression and tension. This implies that a small adjust in topology can reduce stress concentration and improve the involvement of structural elements in taking the stress and resistance to structural response.

The force-displacement relation of the four designs are plotted in Fig.5.13, where the prescribed displacement applied to the four optimized models equal to

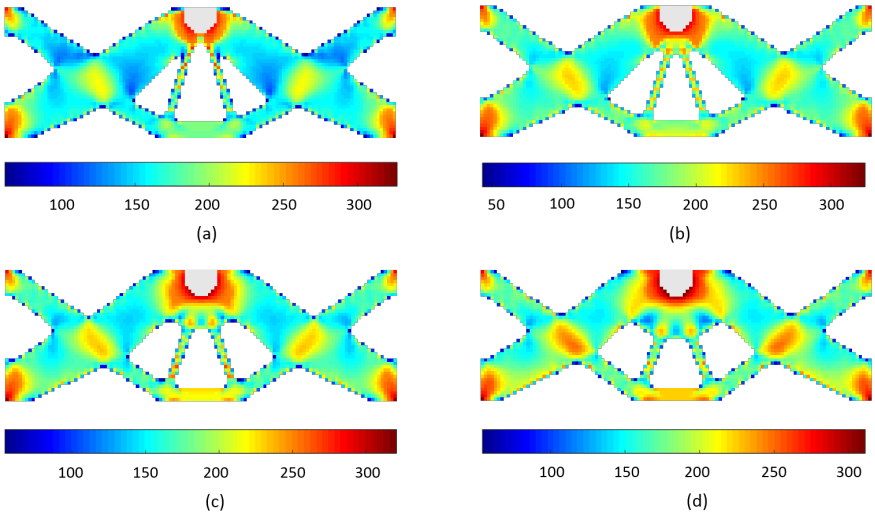

Figure 5.11: Equivalent stress distribution of different design layouts obtained in Fig.5.9 (a-d) subjected to displacement loading u^*=4mm

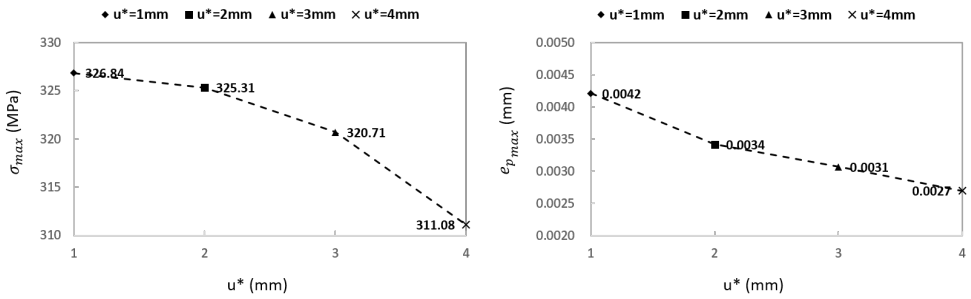

Figure 5.12: Maximum equivalent stress (left) and maximum equivalent plastic strain (right) of different design layouts obtained in Fig.5.9 (a-d) subjected to displacement loading u^*=4mm

8mm. Also, I zoomed up the external force corresponding to the tip deformation at 1mm, 2mm and 3mm for the four designs respectively to compare their loading capacity. As can be observed, the nearly elastic design (u^*=1mm) has the best performance at the initial deformation (up to approx. 1mm) and following the increase in tip deformation, it is surpassed by the plastic design with u^*=2mm that is subsequently transcended by the plastic design with u^*=3mm. As expected, the plastic design (u^*=4mm) starts to perform exceeds the other three designs at 3.5mm deflection and remain this tendency up to 8mm. This agrees well with the observation achieved in Example 1 (Fig.5.7) that the elastic or plastic governed design have significant impact on the resulting topology.

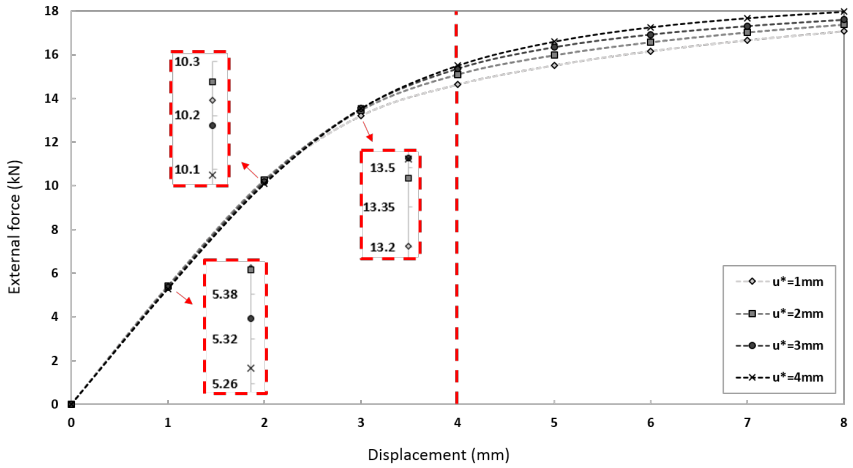

Figure 5.13: Comparison of external force against displacement of different design layouts obtained in Fig.5.9 (a-d) subjected to displacement loading u^*=8mm

5.5 Conclusion and discussion

In this study, an elastoplastic BESO method is proposed where the transition between the elastic and plastic state is considered in the sensitivity analysis. sensitivity numbers are calculated by considering both satisfaction of the equilibrium between the external and internal force, and the local residual on each integration point. In the BESO procedure, only an evolutionary removal ratio without setting up a recovered ratio is applied in the elemental sensitivity ranking system. Also, a simple linear filtering scheme for smoothing sensitivity numbers is considered where taking the weight factor of the neighbouring sensitivities within a constant radius. The robustness and effectiveness of the proposed BESO method for elastoplastic material optimization problem are presented through two numerical examples.

The displacement governed analysis is conducted to compare different topologies obtained from linear elastic design, elastic dominated, plastic dominated or fully plastic design. They all successfully converged demonstrate the sensitivity stabilization when implementing the transit coupled nonlinear system in BESO sensitivity analysis. And the number of interactions for achieving a convergent result is found independent on the material property. From the evolutionary histories of topology, it can be observed that some small branches emerge initially and gradually removed following the volume reduction or move to the area surrounding the most requisite branch to strength the structure. To further investigate the reliability of the proposed method, the von Mises stress distribution of designs achieved in different cases when subjected to the same loading condition is plotted and discussed. It is found that the stress of nearly elastic design mainly concentrate at some areas, e.g., loading applied points. This may result in only parts of the structure enter the plastic design leading to an early failure whereas others remain in the elastic state. However, the plastic design enables to distribute the stress more evenly in the whole structure, which alleviate the stress concentration at some point. Also, the load-displacement curve presents the significant influence of the prescribed displacement on the results.

6

Plastic Strain-based Topology Optimization for Nonliear Structure

6.1 Introduction

Topology optimization technique has been widely used to provide a preliminary conceptual design in the engineering field [12]. Initially, extensive research studies implement topology optimization method into linear elastic structural design with the purpose of minimizing the compliance as well as restricting to the material usage. And the resulting truss-like topology is possibly regarded as a strut-and-tie model based on the regions suffering from tension or compression. However, the linear elastic optimization design is generally far from valid design, continuous studies have emerged to consider more realistic material performance for topology optimization design problem, such as material nonlinearity, geometrical nonlinearity or both material and geometrical nonlinearity.

The energy absorption capacity for a nonlinear structure is generally taken into account. As opposite to linear elastic material quantity complimentary energy is equal to that of strain energy, the purpose of maximizing energy absorption capacity for nonlinear structure can be achieved by either maximizing the total strain energy [24, 26, 27, 28, 29], or minimizing complementary elastic work [54, 77], with a given amount of material. Alternatively, for energy absorbing

elastoplastic structures design, the optimization problem can be formulated by maximizing the absorbed plastic work in the design domain under the prescribed loading condition [62, 63]. Furthermore, the objective can also be set up as the maximization of the end-compliance with a prescribed displacement or minimization of the end-compliance with a prescribed force [25].

Apart from the extensive studies on the compliance topology optimization problem, the stress-based topology optimization problem is another attractive topic. Three main challenges concluded from literature [78, 79] are summarized as follows: (i) the "singularity" phenomenon; (ii) the local nature of stress constraint, and (iii) nonlinear dependence of stress behavior on design topology. Many efforts have been conducted to deal with these technical and computational difficulties regarding to stress-constrained design [80, 81, 82] or stress-minimized design [79, 83].

Opposite to linear or non-linear elastic material that the type of deformation is reversible, most materials, such as metals, soils and concrete, etc., undergo non-reversible deformation in response to the applied force. Once the loading exceeds the yielding point of the material, the extension of material increases more rapidly than that in the elastic region. And the remaining extension after load removal is so called as permanent or plastic deformation. For a given total strain, stress in the material relates to the elastic strain while is independent of the plastic strain. For example, for material with elastic-perfectly-plastic property, the stress is always brought back to the fixed yielding surface through the return-mapping algorithm in the plastic phase, whereas the corresponding plastic strain keep increasing under further loading and deformation. Additionally, for elastoplastic material followed by a strain hardening model, the plastic strain also affect its yield stress. In one-dimensional case, plastic strain is easily to be defined by the permanent part of the strain. However, for arbitrary stress state rather than uniaxial stress state, the equivalent plastic strain is considered by calculated from the components of the plastic strain, as it is a scalar. In a stress-strain curve, the plastic part of the curve can be described by a function of equivalent plastic strain, presenting the behaviour of material against further loading. Hence, for most engineering materials, particularly in a nonlinear design phase, equivalent plastic strain is among the most important internal state variables. However, to authors'

best knowledge, there is lack of studies considering plastic strain associated design objective or constraint in the elastoplastic topology optimization design problem.

This is possibly due to the challenges may be encountered in the optimization procedure. Firstly, the local nature of strain enables the equivalent plastic strain to be considered on every material point in a continuum structure. And it only exist on material entering plastic stage and equals to 0 for material staying in elastic stage. Therefore, unlike the computational burden from stress-based optimization that depends on the number of material points considered alone, it is highly associated with the material response to the applied loading. The second challenge is that the element with low density may present high equivalent plastic strain, leading to the 'singularity' phenomenon and resisting the optimization procedure from removing them. This paper proposed an optimization method with the purpose of minimizing the maximum equivalent plastic strain of elastoplastic continuum structure within a given amount of material volume. Also, effective schemes are introduced to remedy the aforementioned difficulties.

Noticed that the continuous density-based topology optimization method is utilized in most previous works for plastic structural design. However, the evolutionary structural optimization (ESO) method seems to be an effective alternative, which is developed from the concept of gradually removing the inefficient materials in the design domain and further improved by allowing elements to be removed and recovered simultaneously, so called the bi-directional evolutionary structural optimization (BESO) method. Particularly, its nature of achieving a discrete black-and-white layout avoids the 'singularity' problem raised from material with intermediate density. An global quantity of accumulating all the equivalent plastic strain on every finite element of the descretized structure is used to approximate local plastic strain. In other words, the optimization problem is formulated with the objective of minimizing the total equivalent plastic strain at the final loading step and a constraint on material usage. This global function may be difficult to consider all the plastic strain on a local level, however, the influence on the local peak values of plastic strain of the design can be investigated by comparing the results with that achieved from compliance-based optimization without plastic strain minimization. Also, as the challenges mentioned above, the sensitivity numbers may vary by several orders of magnitude due to high

dependence on structural analysis and be delicate to change of design topology. A damping scheme is proposed in this paper to smooth sensitivity numbers and stabilize the evolutionary process. The effectiveness and robustness of the proposed method for plastic strain minimization design is validated through three examples in this paper.

The work is organized as follows: Section 6.2 presents the elasto-plastic model adopted and the nonlinear finite element analysis. Section 6.3 gives the optimization formulations for end-compliance minimization problem and equivalent plastic strain minimization problem, respectively. The detailed sensitivity analysis for the global function of equivalent plastic strain minimization is derived in Section 6.4. Section 6.5 describes the modified BESO method and the proposed damping system embedded in the optimization algorithms. Three examples are conducted in Section 6.6 and conclusion are discussed in Section 6.7.

6.2 Nonlinear Finite Element Analysis

This section presents the elasto-plastic model used and the corresponding nonlinear finite element problem to be solved. The von Mises plastic model with isotropic hardening that commonly used to model ductile metal material is adopted here and is given by

$$f = ||\mathbf{s}|| - \sqrt{\frac{2}{3}}(\sigma_Y + H_p e_p) \tag{6.1}$$

where $\mathbf{s}$ is the deviatoric stress tensor; σ_Y is the initial yield stress; e_p is the effective plastic strain and H_p denotes the plastic modulus of a linear isotropic hardening which is constant in this paper. Assuming small deformation elasto-plasticity, the rate of the total strain $\dot{\boldsymbol{\varepsilon}}$ is decomposed into the rate of the elastic strain $\dot{\boldsymbol{\varepsilon}}^e$ and the plastic strain $\dot{\boldsymbol{\varepsilon}}^p$ as

$$\dot{\boldsymbol{\varepsilon}} = \dot{\boldsymbol{\varepsilon}}^e + \dot{\boldsymbol{\varepsilon}}^p \tag{6.2}$$

The stress relates to the elastic strain by the fourth-order constitutive tensor $\mathbf{D}$

$$\dot{\boldsymbol{\sigma}} = \mathbf{D} : \dot{\boldsymbol{\varepsilon}}^e \tag{6.3}$$

And the flow potential is associated with the yielding function f here, and the plastic strain evolves in the direction normal to the associated flow rule

$$\dot{\boldsymbol{\varepsilon}}^p = \gamma \frac{\partial f}{\partial \boldsymbol{\sigma}} = \gamma \frac{\mathbf{s}}{||\mathbf{s}||} = \gamma \mathbf{N} \tag{6.4}$$

where $\mathbf{N}$ is a unit deviatoric tensor and denotes the flow direction of plastic strain. γ is the non-negative plastic consistency parameter, which is governed by the Kuhn-Tucker conditions

$$\gamma f = 0; \quad \gamma \geq 0; \quad f \leq 0 \tag{6.5}$$

The finite element analysis for a complete structure should be satisfied on both global equilibrium and local residuals.

$$\mathbf{R}^n = \mathbf{R}^n_{ext} - \mathbf{R}^n_{int} \tag{6.6}$$

$$\mathbf{R}^n_{int} = \sum_{e=1}^{nele} (\int_{V_e} \mathbf{B}^T \boldsymbol{\sigma}^n dV_e) \tag{6.7}$$

where $\mathbf{R}^n$ represents the equilibrium between the external force $\mathbf{R}^n_{ext}$ and the internal force $\mathbf{R}^n_{int}$ at loading step n. $\mathbf{B}$ is the strain-displacement matrix. In this study, four-node quadrilateral plane-stress element with four integration points is adopted. Residuals on every integration point is infinitely approaching to zero during the nonlinear analysis at each loading step, which is given by,
for elastic step

$$\mathbf{H}^n_{eij} = \begin{bmatrix} \boldsymbol{\sigma}^n_{ei} - \boldsymbol{\sigma}^{n-1}_{ei} - \mathbf{D}^0_e : (\mathbf{B}_e \mathbf{u}^n_e - \mathbf{B}_e \mathbf{u}^{n-1}_e) = 0 \\ e_{p_{ei}}{}^n - e_{p_{ei}}{}^{n-1} = 0 \\ \Delta\gamma^n_{ei} = 0 \end{bmatrix} \tag{6.8}$$

and for plastic step

$$\mathbf{H}^n_{eij} = \begin{bmatrix} \boldsymbol{\sigma}^n_{ei} - \boldsymbol{\sigma}^{n-1}_{ei} - \mathbf{D}^0_e : (\mathbf{B}_e \mathbf{u}^n_e - \mathbf{B}_e \mathbf{u}^{n-1}_e) + 2\mu_e \Delta\gamma^n_{ei} \mathbf{N}^n_{ei} = 0 \\ e_{p_{ei}}{}^n - e_{p_{ei}}{}^{n-1} - \sqrt{\frac{2}{3}} \Delta\gamma^n_{ei} = 0 \\ ||\mathbf{s}||^n_{ei} - \sqrt{\frac{2}{3}} [\sigma_{Y\,e} + H_{p_e} e_{p_{ei}}{}^n] = 0 \end{bmatrix} \tag{6.9}$$

where $\mathbf{u}_e$ is the elemental nodal displacement vector; $\boldsymbol{\sigma}_{ei}$ and $e_{p_{ei}}$ represent the stress and the equivalent plastic strain obtained on each integration point respectively. e is the number of elements, i represents the number of integration

points, and j corresponds to the number of local residuals required according to the plastic model adopted. The variables $\mathbf{v}_{ei}^n$ within one integration point are defined as

$$\mathbf{v}_{ei}^n = [\boldsymbol{\sigma}_{ei}^n \quad e_{p_{ei}}^n \quad \Delta\gamma_{ei}^n] \tag{6.10}$$

The expression of residual $\mathbf{H}$ at the loading increment n for a complete structure is formed by embedding the local residuals on each integration point of each element into a global matrix, as follows:

$$\begin{aligned} \mathbf{H}^n &= [\mathbf{H}_1^n, \mathbf{H}_2^n, ..., \mathbf{H}_{nele}^n]^T \\ \mathbf{H}_e^n &= [\mathbf{H}_{e1}^n, \mathbf{H}_{e2}^n, \mathbf{H}_{e3}^n, \mathbf{H}_{e4}^n]^T \\ \mathbf{H}_{ei}^n &= \left[\mathbf{H}_{ei1}^n, \mathbf{H}_{ei2}^n, ..., \mathbf{H}_{eij}^n\right]^T \end{aligned} \tag{6.11}$$

6.3 Optimization Formulations

In this study, the elastoplastic structure is subjected to a prescribed displacement loading condition, and the optimization problem for minimizing the plastic deformation is formulated with a constraint on material usage. The objective is achieved by minimizing the total equivalent plastic strain at the final step of prescribed loading history (see Section 6.3.2). Additionally, for the purpose of comparison, the end-compliance based objective function (see Section 6.3.1) is created and applied to the same design optimization problem. The BESO optimization formulation is presented as follows

$$\begin{aligned} \min \quad & c(\mathbf{x}) \\ s.t. \quad & \sum_{e=1}^{nele} v_e x_e = v^* \\ & x_e = 0 \ \ or \ \ 1, \quad (e = 1, 2, ..., nele) \\ & \mathbf{R}^n(\mathbf{u}^n, \mathbf{u}^{n-1}, \mathbf{v}^n, \mathbf{v}^{n-1}, \mathbf{x}) = 0 \\ & \mathbf{H}^n(\mathbf{u}^n, \mathbf{u}^{n-1}, \mathbf{v}^n, \mathbf{v}^{n-1}, \mathbf{x}) = 0 \\ & n = 1, 2, ..., N, \end{aligned} \tag{6.12}$$

where x_e is the discrete density variable that is updated in each iteration; $c(\mathbf{x})$ is the corresponding objective function to be solved, and v^* is the prescribed target volume fraction of the design domain.

The BESO method can also be regarded as discrete density based optimization approach, using element as the design variable assigned with material density to show absence or presence. Generally, in linear elastic optimization design, only the elastic Young's modulus of material is interpolated by design variables, while for nonlinear design, more associated elastoplastic behaviour are taken into account in the material interpolation scheme. The fourth-order constitutive tensor is given by

$$\mathbf{D} = \lambda \mathbf{1} \otimes \mathbf{1} + 2\mu \mathbf{I} \tag{6.13}$$

where λ and μ, so called Lame's constants, are functions of Young's modulus and possion ratio; $\mathbf{1}$ is the second-order unit tensor, and $\mathbf{I}$ is the symmetric fourth-order unit tensor. And the following shows the interpolating functions:

$$\begin{aligned} \lambda_e &= \lambda_{min} + (\lambda_{max} - \lambda_{min}) x_e^{p^\lambda} \\ \mu_e &= \mu_{min} + (\mu_{max} - \mu_{min}) x_e^{p^\mu} \\ \sigma_{Ye} &= \sigma_{Ymin} + (\sigma_{Ymax} - \sigma_{Ymin}) x_e^{p^{\sigma_Y}} \\ H_{p_e} &= H_{p_{min}} + (H_{p_{max}} - H_{p_{min}}) x_e^{p^{H_p}}, \end{aligned} \tag{6.14}$$

where the penalization values (p^λ, p^μ, p^{σ_Y}, p^{H_p}) are assumed equal to 3 throughout this study.

6.3.1 End-compliance Minimization Problem (ECM)

An optimization problem for maximizing stiffness is the most common in the literature. Here, the compliance based objective is achieved by maximizing the force applied on the specified degree of freedom for a nonlinear structure, subjected to prescribed displacement loading, which is expressed as

$$c(\mathbf{x}) = -\varphi^N \mathbf{P}_{ref} \mathbf{u}^N \tag{6.15}$$

where $\mathbf{P}_{ref}$, a constant external load vector, equals to 1 only on the degree of freedom where prescribed displacement is applied, otherwise equals to 0; φ^N is a scalar and denotes the load factor at the final step. Note that the objective function stated in Eq.(6.15) only valid under certain loading circumstances. Thus, Amir et al. [25] proposed to modify the function as: $f(\mathbf{x}) = \mathbf{P}^N \mathbf{u}^N$, in which seems to use a load-controlled analysis while the actual nonlinear analysis is performed by displacement governed method.

6.3.2 Equivalent Plastic Strain Minimization Prolem (EPSM)

A global function of accumulating all the equivalent plastic strain on every integrated point entering plastic state within the design domain is constructed to approximate the local strain problem, which is expressed as

$$c(\mathbf{x}) = \sum_{e=1}^{nele}(\sum_{i=1}^{4}(e_{p_{e,i}}^{N}) \tag{6.16}$$

where $e_{p_{e,i}}^{N}$ is the equivalent plastic strain at i-th integration point of e-th element at the final loading step N. In terms of rate, the equivalent plastic strain can be defined as

$$\dot{e_p} = \sqrt{\frac{2}{3}\dot{\boldsymbol{\varepsilon}}^p : \dot{\boldsymbol{\varepsilon}}^p} \tag{6.17}$$

by substituting Eq.(6.4) into Eq.(6.17), the equivalent plastic strain rate can be formulated as a function of plastic consistency parameter γ as

$$\dot{e_p} = \sqrt{\frac{2}{3}\gamma^2\mathbf{N} : \mathbf{N}} = \sqrt{\frac{2}{3}}\gamma \tag{6.18}$$

where the contraction of unit tensor $(\mathbf{N} : \mathbf{N})$ equals to 1.

6.4 Sensitivity analysis for EPSM problem

In this section, a detailed sensitivity analysis of calculating sensitivity numbers for EPSM problem is expressed and derived using the adjoint method. The sensitivity analysis for ECM problem has been given in Chapter 5. Also, due to the elastoplasticity that is path-dependent, the entire path from $n = 1$ to N is considered in the analysis. Firstly, following the framework [65] for transient, nonlinear coupled problems, the original objective function is extended by adding two adjoint items defined by the product of the adjoint variables and the mechanical balance law on both global and local level

$$\begin{aligned}\hat{c} =& c(\mathbf{x}, \mathbf{u}, \mathbf{v}) + \sum_{n=1}^{N} \boldsymbol{\xi}^{nT}\mathbf{R}^n(\mathbf{u}^n, \mathbf{u}^{n-1}, \mathbf{v}^n, \mathbf{v}^{n-1}, \mathbf{x}) \\ &+ \sum_{n=1}^{N} \boldsymbol{\theta}^{nT}\mathbf{H}^n(\mathbf{u}^n, \mathbf{u}^{n-1}, \mathbf{v}^n, \mathbf{v}^{n-1}, \mathbf{x})\end{aligned} \tag{6.19}$$

where $\boldsymbol{\xi}$ and $\boldsymbol{\theta}$ are two adjoint vectors. And as described in Eq.(6.6-6.9) and Eq.(6.17), it can be concluded that the global equilibrium $\mathbf{R}$ only depend on the internal variable $\mathbf{v}$ of the current loading step, while the local residuals $\mathbf{H}$ associated with variables $\mathbf{u}$, $\mathbf{v}$ of current and former step and design variables $\mathbf{x}$

$$\hat{c} = c(\mathbf{x}, \mathbf{v}) + \sum_{n=1}^{N} \boldsymbol{\xi}^{nT} \mathbf{R}^n(\mathbf{v}^n) + \sum_{n=1}^{N} \boldsymbol{\theta}^{nT} \mathbf{H}^n(\mathbf{u}^n, \mathbf{u}^{n-1}, \mathbf{v}^n, \mathbf{v}^{n-1}, \mathbf{x}) \tag{6.20}$$

Hence, if the design variables are assumed to vary continuously from 1 to 0, the sensitivity of the objective function with respect to a change in design variable can be derived as

$$\begin{aligned}\frac{\partial \hat{c}}{\partial \mathbf{x}} =& \frac{\partial c}{\partial \mathbf{x}} + \sum_{n=1}^{N} (\frac{\partial c}{\partial \mathbf{v}^n} \frac{\partial \mathbf{v}^n}{\partial \mathbf{x}}) + \sum_{n=1}^{N} \boldsymbol{\xi}^{nT} (\frac{\partial \mathbf{R}^n}{\partial \mathbf{v}^n} \frac{\partial \mathbf{v}^n}{\partial \mathbf{x}}) \\ &+ \sum_{n=1}^{N} \boldsymbol{\theta}^{nT} (\frac{\partial \mathbf{H}^n}{\partial \mathbf{u}^n} \frac{\partial \mathbf{u}^n}{\partial \mathbf{x}} + \frac{\partial \mathbf{H}^n}{\partial \mathbf{u}^{n-1}} \frac{\partial \mathbf{u}^{n-1}}{\partial \mathbf{x}} + \frac{\partial \mathbf{H}^n}{\partial \mathbf{v}^n} \frac{\partial \mathbf{v}^n}{\partial \mathbf{x}} + \frac{\partial \mathbf{H}^n}{\partial \mathbf{v}^{n-1}} \frac{\partial \mathbf{v}^{n-1}}{\partial \mathbf{x}} + \frac{\partial \mathbf{H}^n}{\partial \mathbf{x}})\end{aligned} \tag{6.21}$$

The initial response $\mathbf{u^0}$ and $\mathbf{v^0}$ are equal to 0. To eliminate the unknown term of derivatives $\frac{\partial \mathbf{u}^n}{\partial \mathbf{x}}$, $\frac{\partial \mathbf{u}^{n-1}}{\partial \mathbf{x}}$, $\frac{\partial \mathbf{v}^n}{\partial \mathbf{x}}$, $\frac{\partial \mathbf{v}^{n-1}}{\partial \mathbf{x}}$, Eq. (6.21) is rewritten as

$$\begin{aligned}\frac{\partial \hat{c}}{\partial \mathbf{x}} =& (\frac{\partial c}{\partial \mathbf{v}^N} + \boldsymbol{\xi}^{NT} \frac{\partial \mathbf{R}^N}{\partial \mathbf{v}^N} + \boldsymbol{\theta}^{NT} \frac{\partial \mathbf{H}^N}{\partial \mathbf{v}^N}) \frac{\partial \mathbf{v}^N}{\partial \mathbf{x}} + (\boldsymbol{\theta}^{NT} \frac{\partial \mathbf{H}^N}{\partial \mathbf{u}^N}) \frac{\partial \mathbf{u}^N}{\partial \mathbf{x}} \\ &+ \sum_{n=1}^{N-1} (\frac{\partial c}{\partial \mathbf{v}^n} + \boldsymbol{\xi}^{nT} \frac{\partial \mathbf{R}^n}{\partial \mathbf{v}^n} + \boldsymbol{\theta}^{nT} \frac{\partial \mathbf{H}^n}{\partial \mathbf{v}^n} + \boldsymbol{\theta}^{n+1T} \frac{\partial \mathbf{H}^{n+1}}{\partial \mathbf{v}^n}) \frac{\partial \mathbf{v}^n}{\partial \mathbf{x}} \\ &+ \sum_{n=1}^{N-1} (\boldsymbol{\theta}^{nT} \frac{\partial \mathbf{H}^n}{\partial \mathbf{u}^n} + \boldsymbol{\theta}^{n+1T} \frac{\partial \mathbf{H}^{n+1}}{\partial \mathbf{u}^n}) \frac{\partial \mathbf{u}^n}{\partial \mathbf{x}} + \sum_{n=1}^{N} \boldsymbol{\theta}^{nT} \frac{\partial \mathbf{H}^n}{\partial \mathbf{x}}\end{aligned} \tag{6.22}$$

To achieve the Lagrange multipliers $\boldsymbol{\theta}^n, \boldsymbol{\xi}^n$ for all steps, backward incremental calculation method is applied through the following equations
N^{th} step:

$$\begin{cases} \boldsymbol{\theta}^{NT} \dfrac{\partial \mathbf{H}^N}{\partial \mathbf{u}^N} = 0 \\ \dfrac{\partial c}{\partial \mathbf{v}^N} + \boldsymbol{\xi}^{NT} \dfrac{\partial \mathbf{R}^N}{\partial \mathbf{v}^N} + \boldsymbol{\theta}^{NT} \dfrac{\partial \mathbf{H}^N}{\partial \mathbf{v}^N} = 0 \end{cases} \tag{6.23}$$

n^{th} step ($n = N-1, ..., 1$):

$$\begin{cases} \boldsymbol{\theta}^{nT}\dfrac{\partial \mathbf{H}^n}{\partial \mathbf{u}^n} + \boldsymbol{\theta}^{n+1T}\dfrac{\partial \mathbf{H}^{n+1}}{\partial \mathbf{u}^n} = 0 \\ \boldsymbol{\xi}^{nT}\dfrac{\partial \mathbf{R}^n}{\partial \mathbf{v}^n} + \boldsymbol{\theta}^{nT}\dfrac{\partial \mathbf{H}^n}{\partial \mathbf{v}^n} + \boldsymbol{\theta}^{n+1T}\dfrac{\partial \mathbf{H}^{n+1}}{\partial \mathbf{v}^n} = 0 \end{cases} \tag{6.24}$$

Once these arbitrary Lagrange multipliers are determined, the final design sensitivity with respect to the design variables can be further expressed with only the explicit terms of derivatives displayed as

$$\frac{\partial c}{\partial \mathbf{x}} = \sum_{n=1}^{N} \boldsymbol{\theta}^{nT}\frac{\partial \mathbf{H}^n}{\partial \mathbf{x}} \tag{6.25}$$

Furthermore, the derivatives $\frac{\partial c}{\partial \mathbf{v}^N}$, $\frac{\partial \mathbf{R}^n}{\partial \mathbf{v}^n}$, $\frac{\partial \mathbf{H}^n}{\partial \mathbf{u}^n}$, $\frac{\partial \mathbf{H}^{n+1}}{\partial \mathbf{u}^n}$, $\frac{\partial \mathbf{H}^n}{\partial \mathbf{v}^n}$, $\frac{\partial \mathbf{H}^{n+1}}{\partial \mathbf{v}^n}$ need to be calculated to solve the adjoint equations presented in Eq. (6.23) and Eq. (6.24), which are given as follows:

$$\frac{\partial c}{\partial \mathbf{v}_{ei}^N} = \begin{bmatrix} \frac{\partial \mathbf{c}}{\partial \boldsymbol{\sigma}_{ei}^N} & \frac{\partial \mathbf{c}}{\partial e_{p_{ei}}^N} & \frac{\partial \mathbf{c}}{\Delta\gamma_{ei}^N} \end{bmatrix} = \begin{bmatrix} \mathbf{0} & 1 & 0 \end{bmatrix} \tag{6.26}$$

$$\frac{\partial \mathbf{R}_e^n}{\partial \mathbf{v}_{ei}^n} = \begin{bmatrix} \frac{\partial \mathbf{R}_e^n}{\partial \boldsymbol{\sigma}_{ei}^n} & \frac{\partial \mathbf{R}_e^n}{\partial e_{p_{ei}}^n} & \frac{\partial \mathbf{R}_e^n}{\Delta\gamma_{ei}^n} \end{bmatrix} = \begin{bmatrix} \mathbf{B}_{ei}^T w_{ei} & 0 & 0 \end{bmatrix} \tag{6.27}$$

$$\frac{\partial \mathbf{H}_{ei}^n}{\partial \mathbf{u}_e^n} = \begin{bmatrix} \frac{\partial \mathbf{H}_{ei1}^n}{\partial \mathbf{u}_e^n} & \frac{\partial \mathbf{H}_{ei2}^n}{\partial \mathbf{u}_e^n} & \frac{\partial \mathbf{H}_{ei3}^n}{\partial \mathbf{u}_e^n} \end{bmatrix}^T = \begin{bmatrix} -\mathbf{D}_e^0\mathbf{B}_{ei} & 0 & 0 \end{bmatrix}^T \tag{6.28}$$

$$\frac{\partial \mathbf{H}_{ei}^{n+1}}{\partial \mathbf{u}_e^n} = \begin{bmatrix} \frac{\partial \mathbf{H}_{ei1}^{n+1}}{\partial \mathbf{u}_e^n} & \frac{\partial \mathbf{H}_{ei2}^{n+1}}{\partial \mathbf{u}_e^n} & \frac{\partial \mathbf{H}_{ei3}^{n+1}}{\partial \mathbf{u}_e^n} \end{bmatrix}^T = \begin{bmatrix} \mathbf{D}_e^0\mathbf{B}_{ei} & 0 & 0 \end{bmatrix}^T \tag{6.29}$$

$$\frac{\partial \mathbf{H}_{ei}^{n+1}}{\partial \mathbf{v}_{ei}^n} = \begin{bmatrix} \frac{\partial \mathbf{H}_{ei1}^{n+1}}{\partial \boldsymbol{\sigma}_{ei}^n} & \frac{\partial \mathbf{H}_{ei1}^{n+1}}{\partial e_{p_{ei}}^n} & \frac{\partial \mathbf{H}_{ei1}^{n+1}}{\Delta\gamma_{ei}^n} \\ \frac{\partial \mathbf{H}_{ei3}^{n+1}}{\partial \boldsymbol{\sigma}_{ei}^n} & \frac{\partial \mathbf{H}_{ei3}^{n+1}}{\partial e_{p_{ei}}^n} & \frac{\partial \mathbf{H}_{ei3}^{n+1}}{\Delta\gamma_{ei}^n} \\ \frac{\partial \mathbf{H}_{ei4}^{n+1}}{\partial \boldsymbol{\sigma}_{ei}^n} & \frac{\partial \mathbf{H}_{ei4}^{n+1}}{\partial e_{p_{ei}}^n} & \frac{\partial \mathbf{H}_{ei4}^{n+1}}{\Delta\gamma_{ei}^n} \end{bmatrix} = \begin{bmatrix} -\mathbf{I} & \mathbf{0} & \mathbf{0} \\ \mathbf{0} & -1 & 0 \\ \mathbf{0} & 0 & 0 \end{bmatrix} \tag{6.30}$$

The above derivatives are independent to the finite element analysis response, whereas the derivatives of $\mathbf{H}^n$ with respect to the internal variable $\mathbf{v}^n$ and the design variable $\mathbf{x}$ are produced variously when the point of material stays in the elastic and plastic phase.

Elastic phase:

$$\frac{\partial \mathbf{H}_{ei}^n}{\partial \mathbf{v}_{ei}^n} = \begin{bmatrix} \frac{\partial \mathbf{H}_{ei1}^n}{\partial \boldsymbol{\sigma}_{ei}^n} & \frac{\partial \mathbf{H}_{ei1}^n}{\partial e_{p_{ei}}^n} & \frac{\partial \mathbf{H}_{ei1}^n}{\Delta\gamma_{ei}^n} \\ \frac{\partial \mathbf{H}_{ei3}^n}{\partial \boldsymbol{\sigma}_{ei}^n} & \frac{\partial \mathbf{H}_{ei3}^n}{\partial e_{p_{ei}}^n} & \frac{\partial \mathbf{H}_{ei3}^n}{\Delta\gamma_{ei}^n} \\ \frac{\partial \mathbf{H}_{ei4}^n}{\partial \boldsymbol{\sigma}_{ei}^n} & \frac{\partial \mathbf{H}_{ei4}^n}{\partial e_{p_{ei}}^n} & \frac{\partial \mathbf{H}_{ei4}^n}{\Delta\gamma_{ei}^n} \end{bmatrix} = \begin{bmatrix} \mathbf{I} & \mathbf{0} & \mathbf{0} \\ \mathbf{0} & 1 & 0 \\ \mathbf{0} & 0 & 1 \end{bmatrix} \tag{6.31}$$

$$\frac{\partial \mathbf{H}_{ei}^{n}}{\partial x_e} = \left[\frac{\partial \mathbf{H}_{ei1}^{n}}{\partial x_e} \quad \frac{\partial \mathbf{H}_{ei2}^{n}}{\partial x_e} \quad \frac{\partial \mathbf{H}_{ei3}^{n}}{\partial x_e}\right]^T = \left[-\frac{\partial \mathbf{D}_e^0}{\partial x_e} : (\mathbf{B}_{ei}\mathbf{u}_e^n - \mathbf{B}_{ei}\mathbf{u}_e^{n-1}) \quad 0 \quad 0\right]^T \tag{6.32}$$

Plastic phase:

$$\frac{\partial \mathbf{H}_{ei}^{n}}{\partial \mathbf{v}_{ei}^{n}} = \begin{bmatrix} \mathbf{I} + 2\mu_e \Delta\gamma_{ei}^{n} (\frac{\partial \mathbf{N}}{\partial \boldsymbol{\sigma}})_{ei}^{n} & \mathbf{0} & 2\mu_e \mathbf{N}_{ei}^{n} \\ \mathbf{0} & 1 & -\sqrt{\frac{2}{3}} \\ \mathbf{N}_{ei}^{n} & -\sqrt{\frac{2}{3}} H_{p_e} & 0 \end{bmatrix} \tag{6.33}$$

$$\frac{\partial \mathbf{H}_{ei}^{n}}{\partial x_e} = \begin{bmatrix} -\frac{\partial \mathbf{D}_e^0}{\partial x_e} : (\mathbf{B}_{ei}\mathbf{u}_e^n - \mathbf{B}_{ei}\mathbf{u}_e^{n-1}) + 2\Delta\gamma_{ei}^{n}\mathbf{N}_{ei}^{n}\frac{\partial \mu_e}{\partial x_e} \\ 0 \\ -\sqrt{\frac{2}{3}}\frac{\partial \sigma_{y_e}}{\partial x_e} - \sqrt{\frac{2}{3}}\frac{\partial H_{p_e}}{\partial x_e} e_{p}{}_{ei}^{n} \end{bmatrix} \tag{6.34}$$

with

$$(\frac{\partial \mathbf{N}}{\partial \boldsymbol{\sigma}})_{ei}^{n} = \frac{1}{||\mathbf{s}||_{ei}^{n}} [\mathbf{I}_{dev} - \mathbf{N}_{ei}^{n} \otimes \mathbf{N}_{ei}^{n}] \tag{6.35}$$

where $\mathbf{I}_{dev} = \mathbf{I} - \frac{1}{3}\mathbf{1}\otimes\mathbf{1}$ is the unit deviatoric tensor of the fourth-order. Therefore differentiation of $\mathbf{H}^n$ with respect to variables $\mathbf{v}^n$ and $\mathbf{x}$ need to be consistent with the analysis at every loading step.

6.5 Modified BESO update of design variables

Due to the instability in the topology evolutionary procedure for plastic strain minimization design of elastoplastic materials, the basic BESO method proposed in [18] is modified by adding a damping scheme on the resulting sensitivity numbers to improve its effectiveness and robustness.

BESO design starts from the full structural domain and its volume gradually decreases until the target volume is reached. The evolutionary function is given by

$$v^l = v^{l-1}(1 - R_{er}), \qquad l = 1, 2, 3... \tag{6.36}$$

where R_{er} is the evolutionary ratio, l represents the current optimization iteration. To ensure only elements with density design variable $x = 1$ taken into the update scheme at the current iteration, the sensitivities obtained directly from Eq. (6.25) are further evaluated as

$$\mathbf{a} = \mathbf{x} \sum_{n=1}^{N} \boldsymbol{\theta}^{nT} \frac{\partial \mathbf{H}^n}{\partial \mathbf{x}} \tag{6.37}$$

where $\mathbf{x}$ play the role of avoiding void elements participating in the rank system of deciding element's removal and addition. Moreover, a damping scheme is proposed for all sensitivity numbers to improve the evolutionary topological stability. This is due to, firstly, the plastic strain in a total strain is uncertain on a local level, which highly rely on the material elastoplasticity and loading condition. Elements with material exceeding yielding point is developed with plastic strain while those staying in elastic stage with plastic strain equal to 0. Also, the void elements assigned with extremely small material properties (e.g., Young's modulus, hardening modulus and initial yielding stress) may present high plastic strain. As a result, the sensitivity numbers may vary with large difference in quantity orders during the evolutionary process. To solve this, Eq. (6.37) is continued to be modified as

$$\mathbf{a} = (\mathbf{x}\sum_{n=1}^{N}\theta^{nT}\frac{\partial \mathbf{H}^n}{\partial \mathbf{x}})^{\phi} \tag{6.38}$$

where ϕ is the damping parameter. Additionally, to address the mesh-dependent and convergence problem, a filtering scheme [76] is utilized to smooth the sensitivity numbers by taking the surrounding sensitivities into account.

$$a_e = \frac{\sum_{i=1}^{N} w_{ei} a_i}{\sum_{i=1}^{N} w_{ei}} \tag{6.39}$$

with

$$w_{ei} = max(0, r_{min} - dis(e,i)) \tag{6.40}$$

where a_e and a_i denote the design sensitivity of element e and element i, respectively. w_{ei} is the weight factor, r_{min} is the filter radius and the item $dis(e,i)$ represents the distance between of centres of element e and element i. And, a scheme of averaging the sensitivity numbers in the current iteration with that in the previous iteration is normally implemented to futher improve the optimization stability [18].

$$a_e^l = \frac{a_e^l + a_e^{l-1}}{2} \tag{6.41}$$

Then, all elements are sorted based on their magnitude of design sensitivity from the highest to the lowest, and a threshold parameter a^{th} is set up according to the prescribed volume desired at the current iteration. Specifically, elements with sensitivity value higher than a^{th}, as shown in Eq. (6.42), are regarded as the solid where the corresponding design variable equals to 1, while those with that lower than a^{th}, as given in Eq. (6.43), represent the void and are removed from the current design domain.

$$a_e > a^{th} \tag{6.42}$$

$$a_e \leq a^{th} \tag{6.43}$$

Once the prescribed volume for material usage is reached, design variables are only updated for satisfying the convergence criterion as

$$\frac{|\sum_{j=1}^{m}(c_{i-j+1} - c_{i-N-j+1})|}{\sum_{j=1}^{m} c_{i-j+1}} \leq \tau \tag{6.44}$$

where m is an integral number equals to 5 in this study, and τ is the allowable convergence tolerance relating to the change in objective function. In this paper, the optimization procedure is either stopped by achieving a convergent result or an adequate number of iteration in which a stable topology raised. In summary, the BESO optimization procedure is described as follows:

1. Define geometrical dimension, FE mesh, loading and boundary conditions for design domain.

2. Assign all elements with design variable equal to 1.

3. Set up BESO parameters (target volume v^*, evolutionary removal ratio R_{er}, filtering radius r_{min}, damping parameter ϕ, convergent tolerance τ).

4. Calculate derivatives presented in Eq. (6.26)-(6.30), that are independent to the finite element analysis response.

5. Perform nonlinear finite element analysis of the current structure, and compute the derivatives presented in Eq. (6.31)-(6.34), that are consistent with respect to the analysis for all loading steps.

6. Calculate the Lagrange multipliers $\boldsymbol{\theta}^n, \boldsymbol{\xi}^n$ for all steps using Eq. (6.23)-(6.24).

7. Obtain design sensitivity numbers by Eq. (6.25).

8. Further evaluate, damp, filter and average the sensitivity number using Eq. (6.37), Eq. (6.38), Eq. (6.39), Eq. (6.41), respectively, and save the sensitivity number as history information for next iteration.

9. Define desired volume of next iteration using Eq. (6.36).

10. Update design variables and material properties for solid and void elements using Eq. (6.42) and (6.43).

11. Construct a new design domain with solid elements and repeat steps 5-10 until the target volume are reached and the convergence criterion or determined total iterations are satisfied.

6.6 Examples

Two numerical examples are conducted to present the effectiveness of the proposed optimization algorithm. A cantilever beam with $2m$ in length and $1m$ in height is applied under two loading cases. In all cases, the Young's moduli, poisson's ratios, initial yielding stress, plastic moduli are given as $E^0 = 80GPa$, $v = 0.3$, $\sigma_Y^0 = 120MPa$, $H_p^0 = 1000MPa$. BESO parameters set up in all cases are $R_{er} = 2\%$, $v^* = 60\%$, $r_{min} = 4$ and $\tau = 1 \times 10^{-4}$. Additionally, the damping parameter ϕ is defined equal to 0.1 for EPSM design and 0.4 for ECM design, considering more uncertainty may be encountered in EPSM design as not all elements are developed with sensitivities (plastic deformation). The full design domain is discretized into 200×100 elements and the uniform size of element is $10mm$.

6.6.1 Case 1

Fig.6.1 shows the design domain, boundary and loading condition for the first case. The cantilever beam is fully clamped at the left edge, and a downwards prescribed displacement of $20mm$ is applied over 21 nodes (20 elements) along the central right edge to eliminate stress concentration.

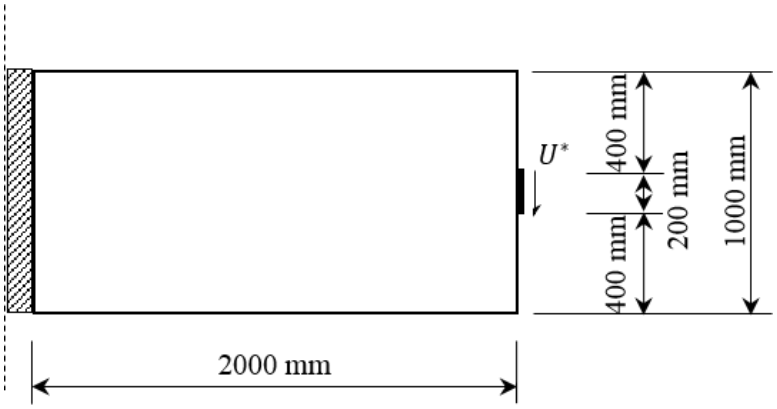

Figure 6.1: Design domain of Case 1

The results in terms of resulting topology, equivalent plastic strain and von Mises distribution obtained from stiffness design, ECM design and EPSM design are presented in Fig.6.2. Also, a modified design domain without considering elements at the structural support and load applied regions is used in order to avoid the effect of stress/strain concentration. $\tilde{e_p}$ and $\tilde{\sigma}$ demonstrate the equivalent plastic strain and von Mises stress for the modified design domain respectively. As can be observed, three distinct topologies are obtained through various design purposes. For stiffness design, the structure is assumed to be linear elastic by defining the yield stress of material is infinitely large. Thus, no plastic deformation occurs and the maximum stress in the full design domain grows without restriction up to $774.22MPa$. The maximum stress reduced to $249.22MPa$ and the von Mises stresses are more evenly diffused in the whole structure in the ECM design, which demonstrates the advantages of considering nonlinear performance. In the EPSM design where the maximum equivalent plastic strain is aiming to be minimized, either the maximum von Mises stress or equivalent plastic strain

is lower than that of the ECM design. This is possibly due to more structural elements are involved in sharing the plastic deformation.

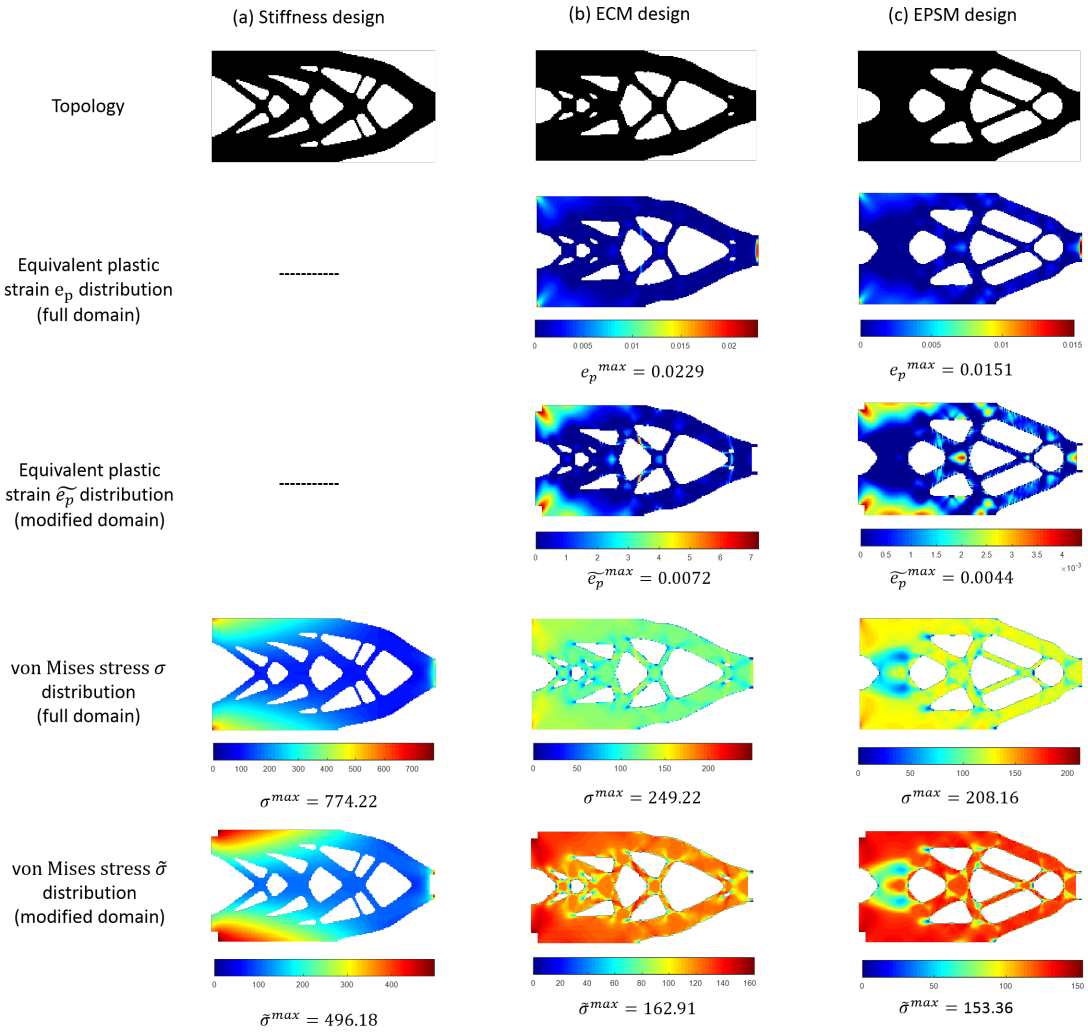

Figure 6.2: Comparison of results achieved from stiffness design, ECM design and EPSM design of Case 1

The evolutionary history regarding to the equivalent plastic strain and von Mises stress fields for ECM design and EPSM design are shown in Fig.(6.3-6.6) and Fig.(6.7-6.10), respectively.

It can be observed from the Fig.6.3 that along the topological evolution, the maximum equivalent plastic strain e_p^{max} decreases from 0.034mm to 0.0229mm. However, at iteration 25, e_p^{max} reaches to 0.0576mm existing at the thin branches

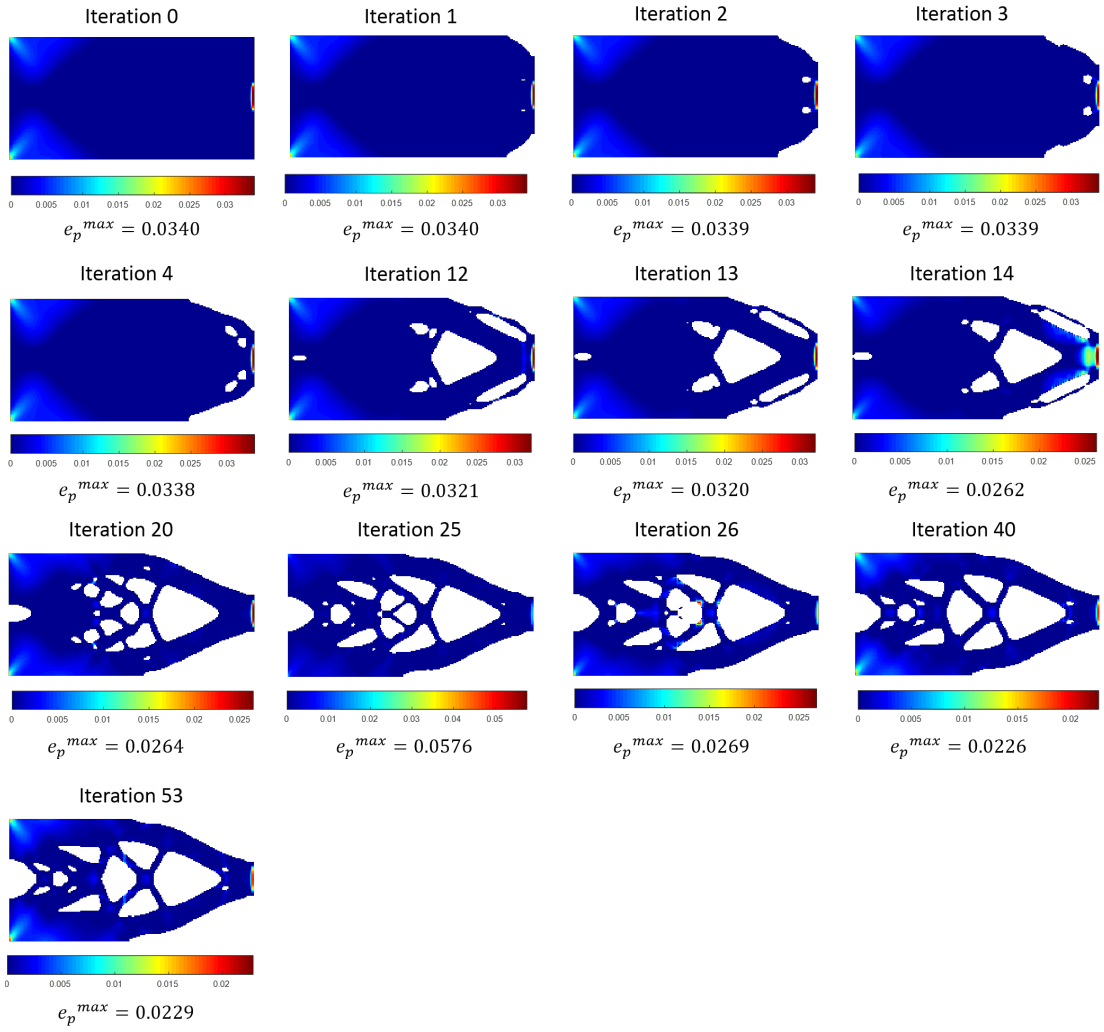

Figure 6.3: The topological evolution with equivalent plastic strain distribution plot of full domain of ECM design

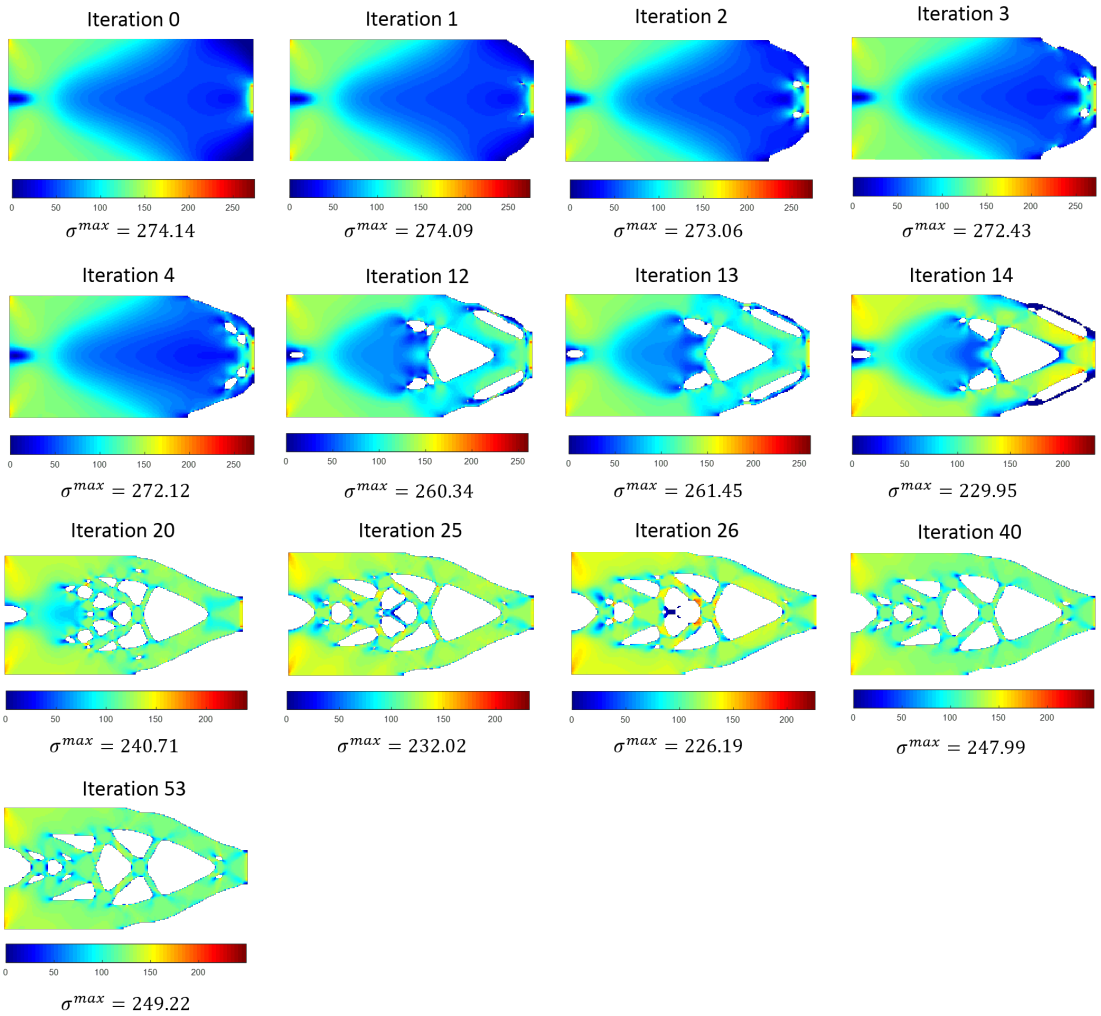

Figure 6.4: The topological evolution with von Mises stress distribution plot of full domain of ECM design

in the central area of domain and then drop to 0.0269mm at iteration 26 where those branches are removed from the structure. Regarding to the von Mises stress plots (Fig.6.4) at iteration 24 to 26, the maximum von Mises stress σ^{max} reduces from 240.71MPa to 226.19MPa, which is not consistent with the plastic strain distribution.

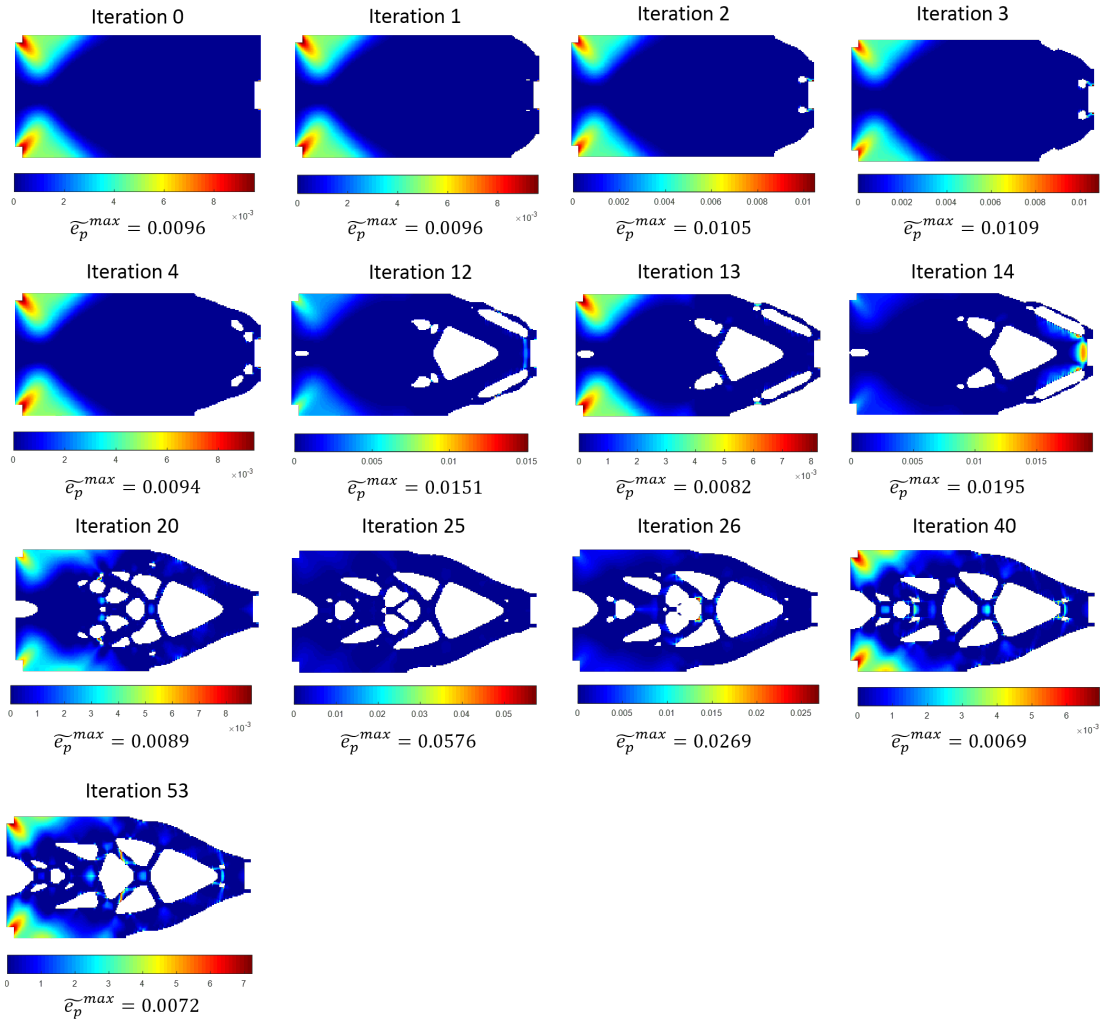

Figure 6.5: The topological evolution with equivalent plastic strain distribution plot of the modified domain of ECM design

Fig.6.5 and Fig.6.6 show the equivalent plastic strain and von Mises distribution at the modified domain where elements at boundary and loading regions are neglected, receptively. This helps to observe the change of stress of remaining

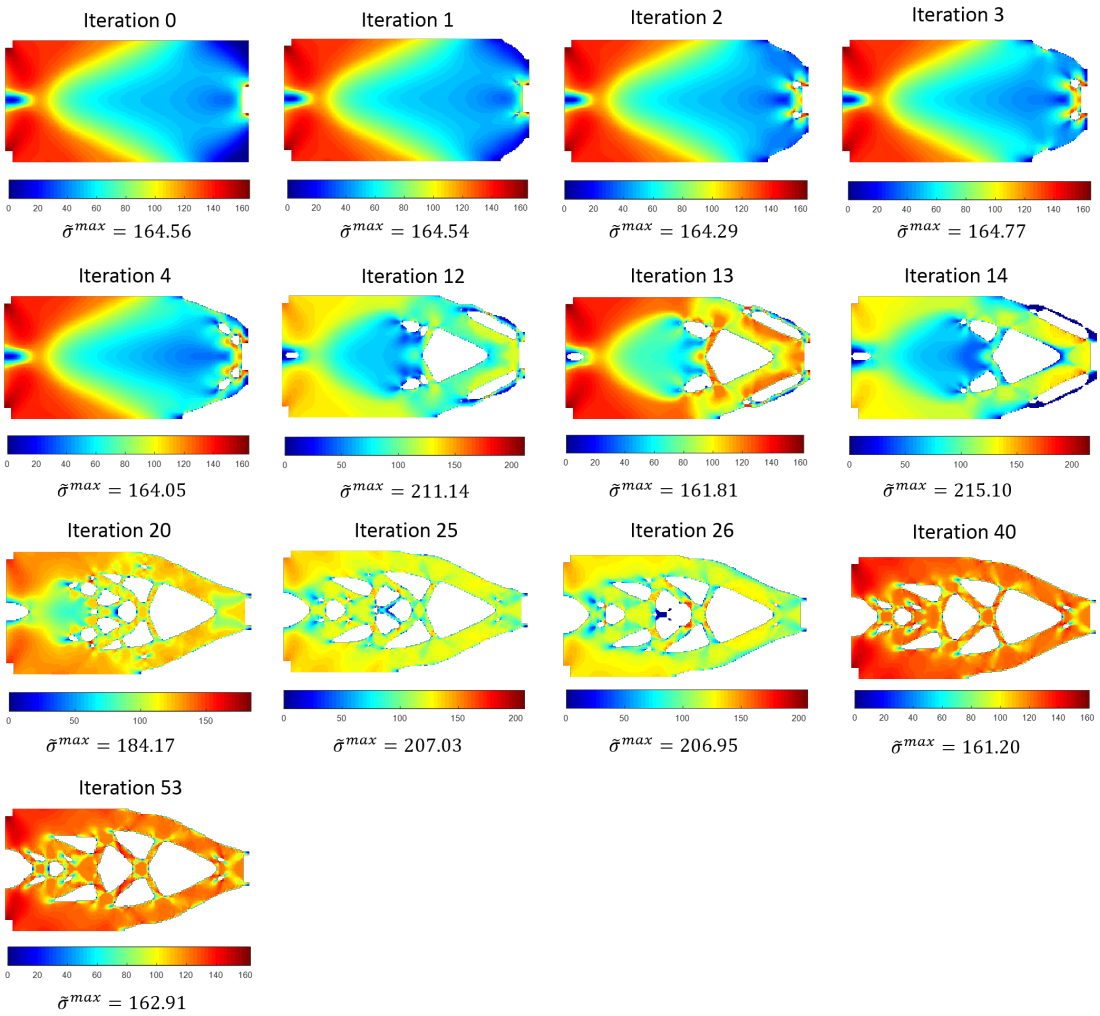

Figure 6.6: The topological evolution with von Mises stress distribution plot of the modified domain of ECM design

elements with the topology evolutionary. For example, topologies at iteration 12 and 13 are nearly the same, while $\tilde{e_p}^{max}$ decreases from 0.0151 to 0.0082 and $\tilde{\sigma}^{max}$ drops around 25%, when two thin branches are eliminated at iteration 13. Also, it is interesting to find that the inefficient materials to be removed in the subsequent iteration can be predicted from the stress distribution of the current topology. For instance, elements with lowest von Mises stress at the design of iteration 14 disappear in the later iteration.

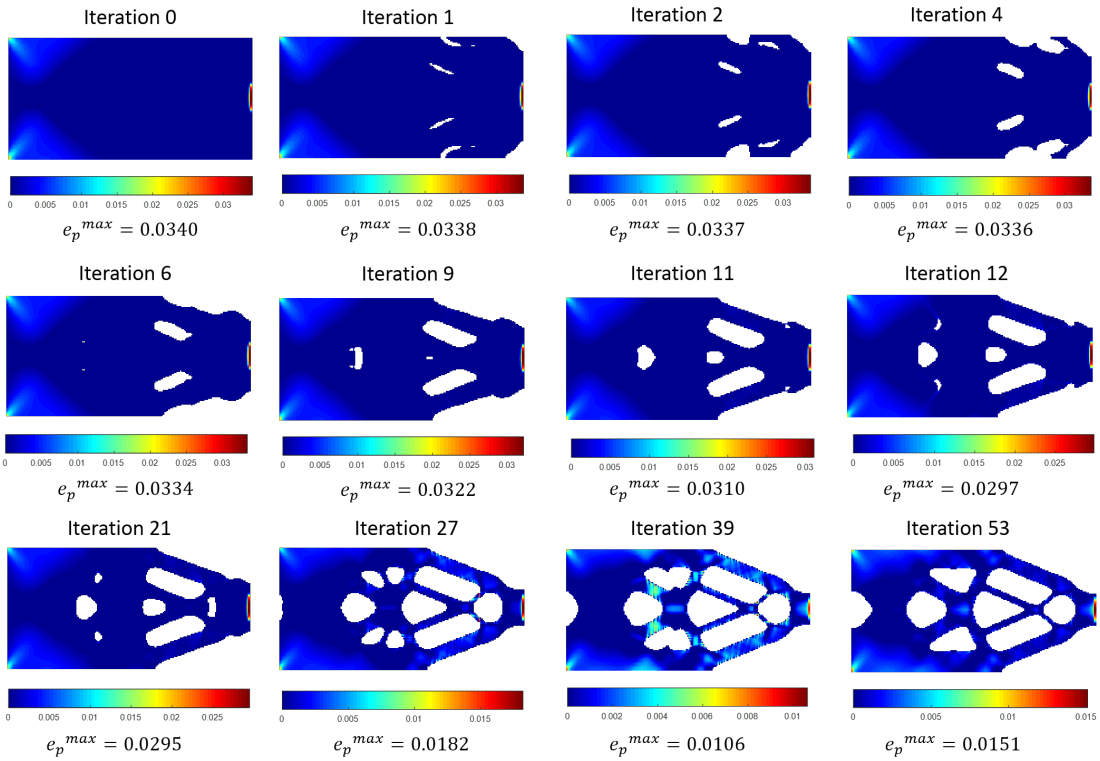

Figure 6.7: The topological evolution with equivalent plastic strain distribution plot of full domain of EPSM design

In the EPSM design, as can be observed from Fig.6.2 that the results of e_p^{max}, σ^{max}, $\tilde{e_p}^{max}$, $\tilde{\sigma}^{max}$ are obviously less than those obtained through ECM design. This demonstrates that the proposed optimization algorithm achieves the goal of minimizing the plastic deformation. Furthermore, the maximum von Mises stress and plastic strain generally decrease along the volume reduction to the lowest while may increase a bit at the converged design (see iterations 39 and

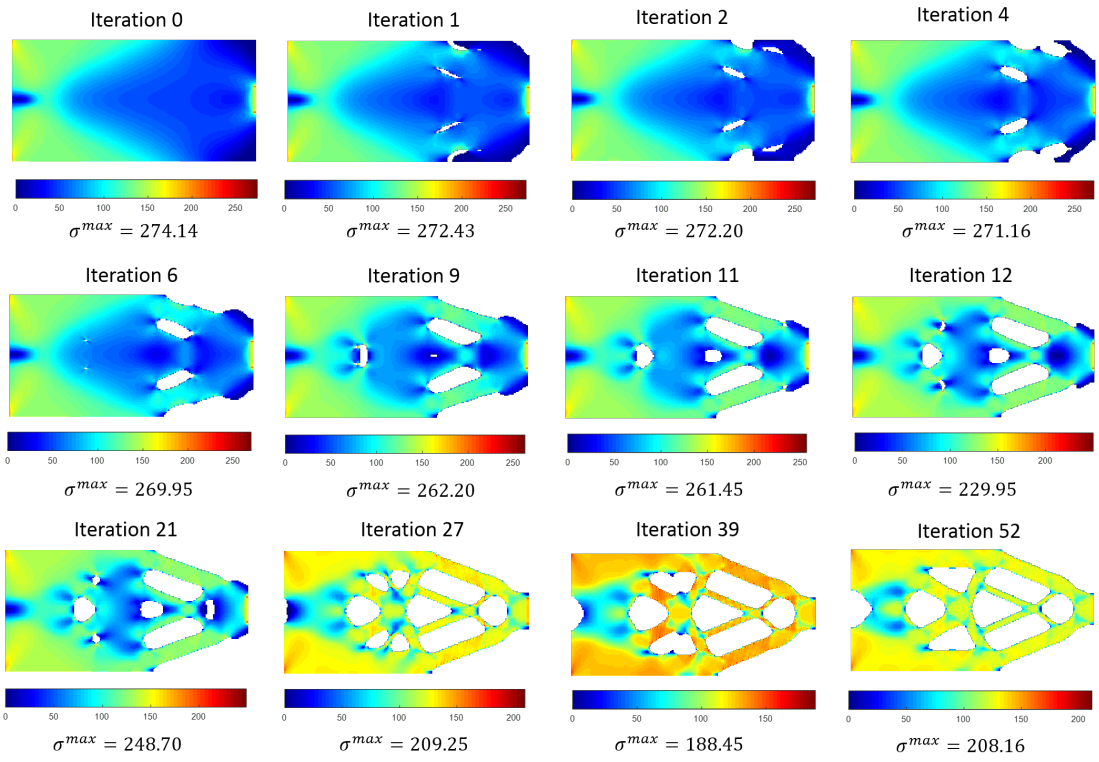

Figure 6.8: The topological evolution with von Mises stress distribution plot of full domain of EPSM design

53 in Fig.6.7 and Fig.6.8). This is possible caused by the stress concentration at 'singular' areas or a compromise from the converged results, though the increase can be negligible.

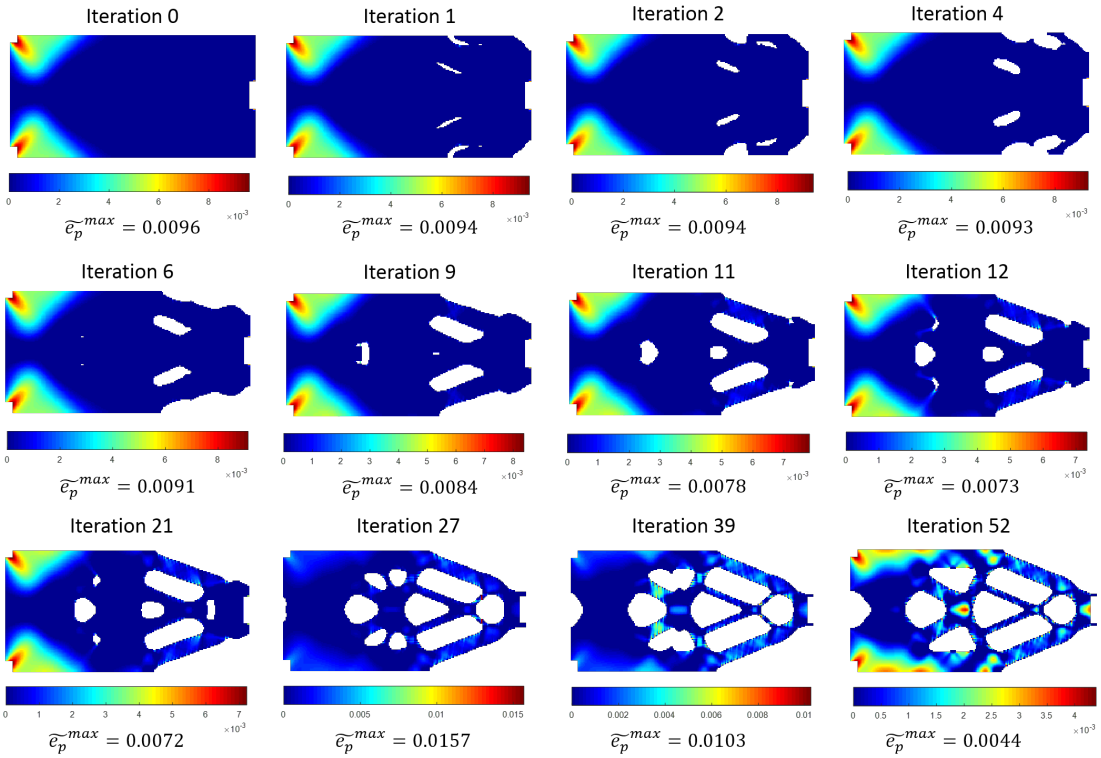

Figure 6.9: The topological evolution with equivalent plastic strain distribution plot of the modified domain of EPSM design

For this particular case, as can be seen from Fig.6.9 and Fig.6.10 where 'singular' areas are removed, that the maximum plastic strain and stress are the lowest at iteration 52 when the results converged. Most importantly, more evenly distribution has been developed to disperse the high stress through structural self-adjustment till a converged topology is achieved.

Relation between the objective functions and iterations of EPSM design is plotted in Fig.6.12 where a stable evolutionary history is observed and the topology converges within 52 iterations, which state the effectiveness and feasibility of the proposed algorithms.

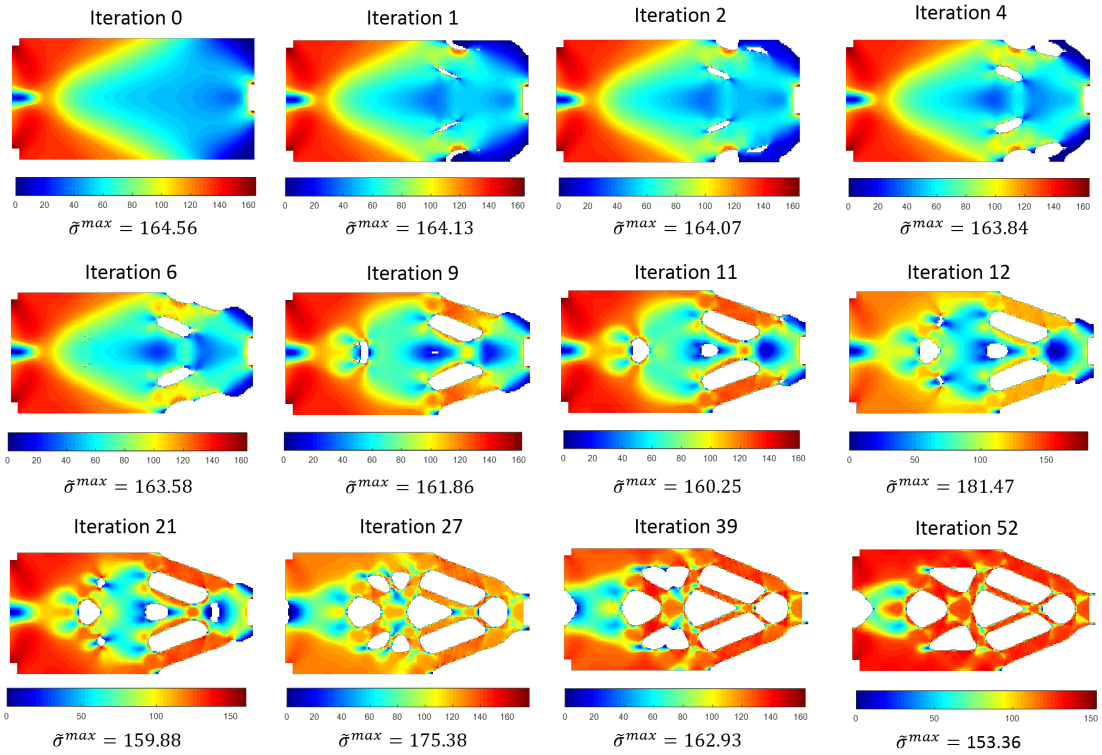

Figure 6.10: The topological evolution with von Mises stress distribution plot of the modified domain of EPSM design

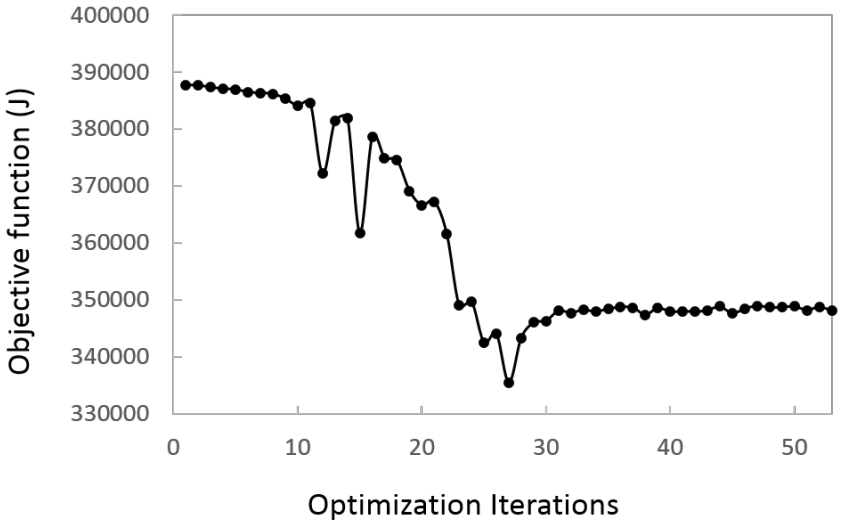

Figure 6.11: Plot of objective functions and iterations of ECM design of Case 1

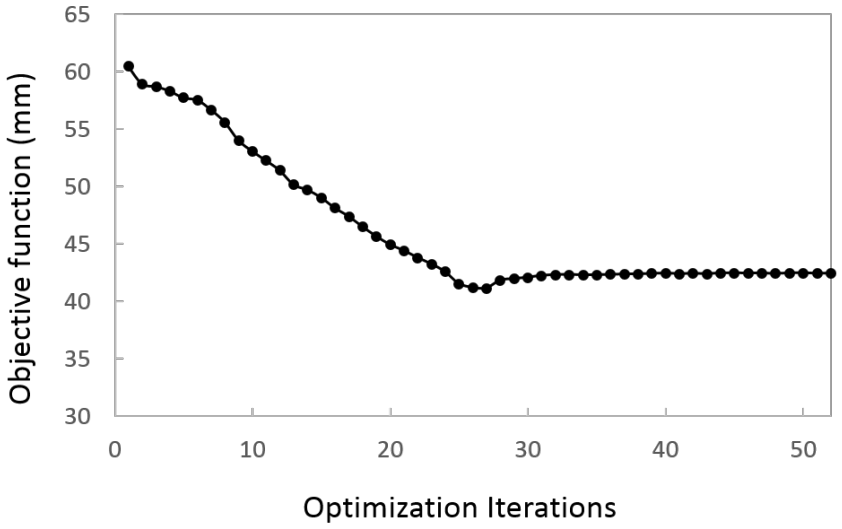

Figure 6.12: Plot of objective functions and iterations of EPSM design of Case 1

6.6.2 Case 2

In the second case, a cantilever beam with same dimension and boundary condition as presented in case 1 is adopted but applied with distributed prescribed displacements over 21 nodes at the right end of the top surface (see Fig.6.13).

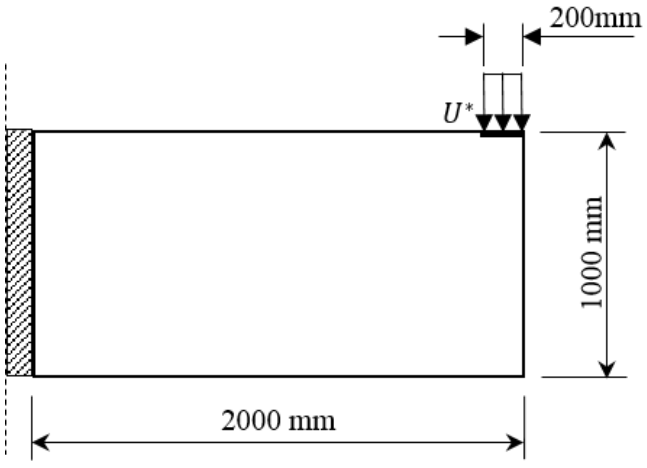

Figure 6.13: Design domain of Case 2

To show the difference between the elastoplastic design and linear design, the problem is solved first using linear FEA and the results are shown in Fig.6.14(a).

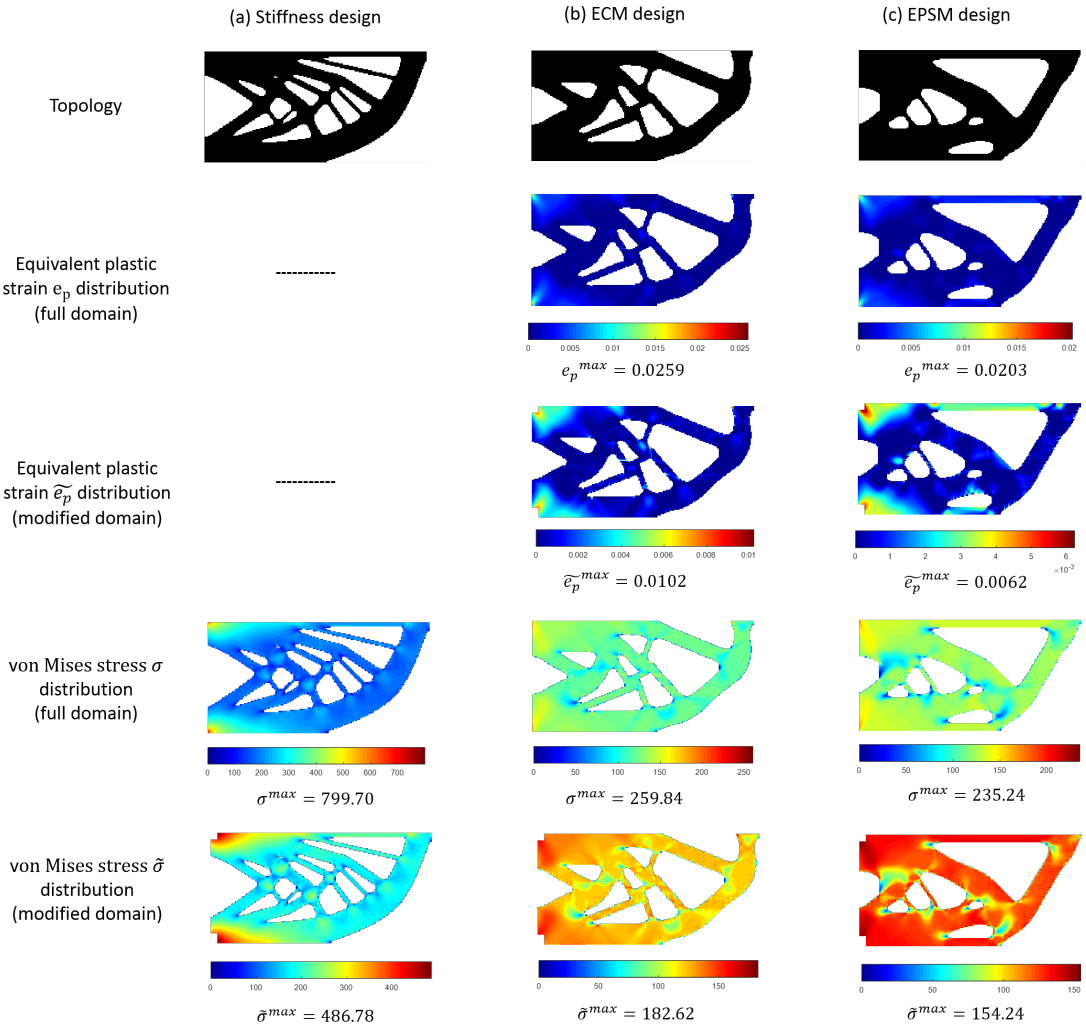

Figure 6.14: Comparison of results achieved from stiffness design, ECM design and EPSM design of Case 2

When the problem is solved using nonlinear FEA, the optimized design has different topology presented in Fig.6.14(b). Comparing the topology obtained from linear design, the nonlinear design has one segment near the loading points along the top surface is void. And, more material is moved to the clamped end, avoiding the von Mises stress only concentrate in specific areas. However, both these linear and nonlinear design are associated with compliance-based optimization design. Plastic strain-based optimization design is conducted and the results are shown in Fig.6.14(c). Though both Fig.6.14(b) and Fig.6.14(c) design taking the material elastoplasticity into account, the optimized layouts are different due to various objective of optimization. From the equivalent plastic strain and von Mises stress plots, as can be observed that values of e_p^{max} and σ^{max} of EPSM design (0.0203mm and 235.24MPa) are less than that of ECM design (0.0259mm and 259.84MPa). And material is moved even further towards the left edge to enable the plastic strains and stresses are more equally dispersed over the full structure.

The detailed evolution of the topology together with the equivalent plastic stain and the von Mises stress distribution for the case of design Fig.6.14 (b) and (c) are given in Fig.(6.15-6.18) and Fig.(6.19-6.22), respectively.

For the ECM design, similar to previous cases, the maximum equivalent plastic strain gradually decreases with the topological evolution from 0.034mm (iteration 0) to 0.0177mm (iteration 24), but jump to 0.0457mm at iteration 27 due to the appearing extremely thin branch that is removed in the subsequent iteration and e_p^{max} drops down to 0.020mm (See Fig.6.15). This demonstrates that within the volume reduction process, plastic strain is dramatically influenced by the material removal and addition.

Fig.6.17 and Fig.6.18 display the results within a modified domain where elements around the left boundary corners are neglected to better present the equivalent plastic strain and von Mises stress distribution. As discussed in the first case that e_p^{max} and σ^{max} of a converged optimized design may not be the lowest. Rather than the fact of arising from the problem of singularity that is found through the distribution of $\tilde{e_p}^{max}$ and $\tilde{\sigma}^{max}$ in the former case, this case has the same trend in both results obtained from unmodified and modified domain, see plots at iteration 45 and 61 in Fig.(6.17-6.18). Thus, it can be concluded that

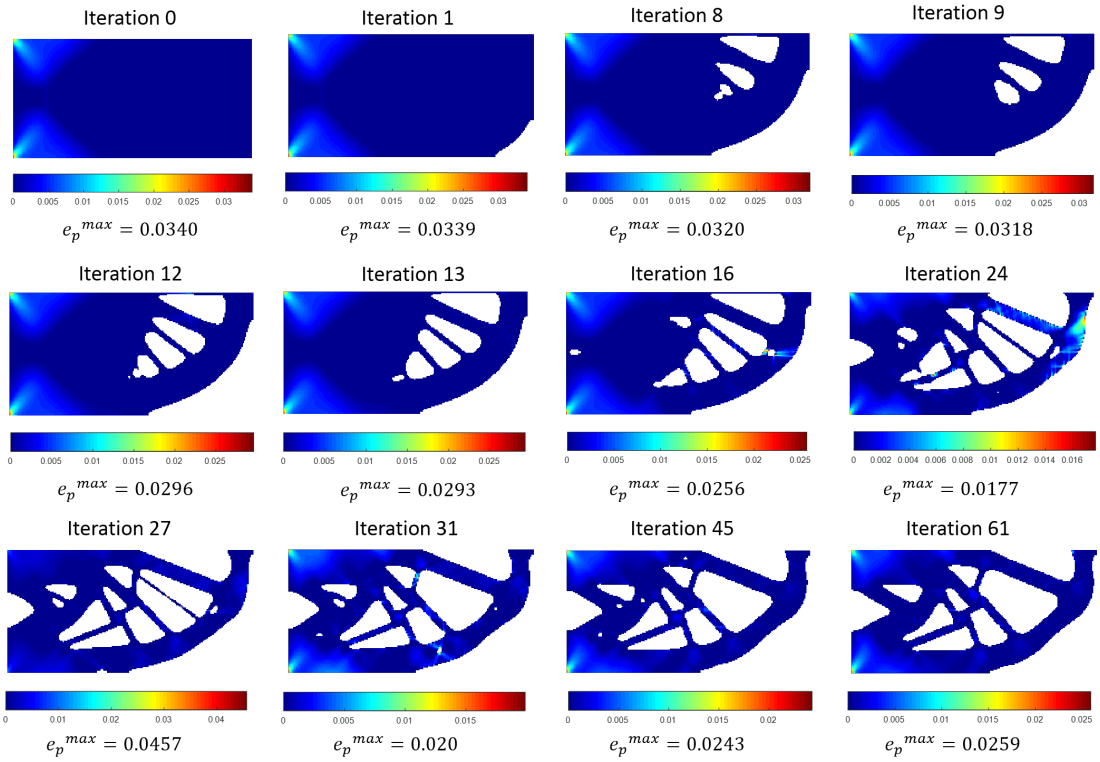

Figure 6.15: The topological evolution with equivalent plastic strain distribution plot of full domain of ECM design

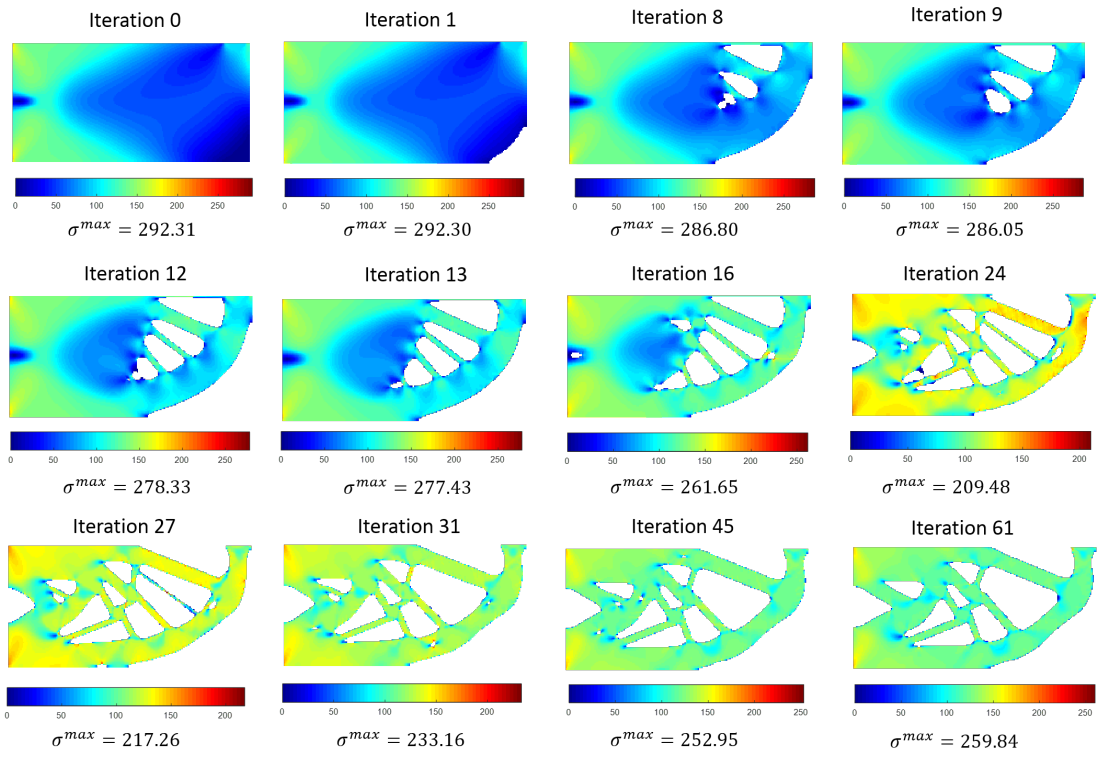

Figure 6.16: The topological evolution with von Mises stress distribution plot of full domain of ECM design

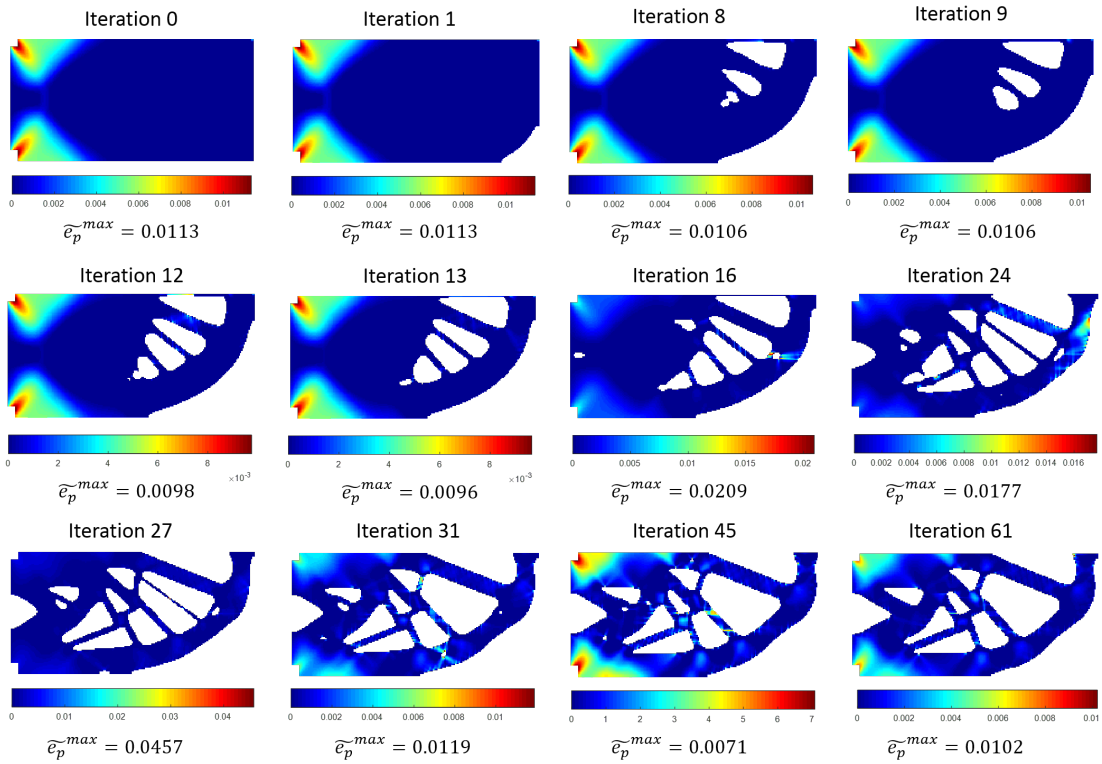

Figure 6.17: The topological evolution with equivalent plastic strain distribution plot of the modified domain of ECM design

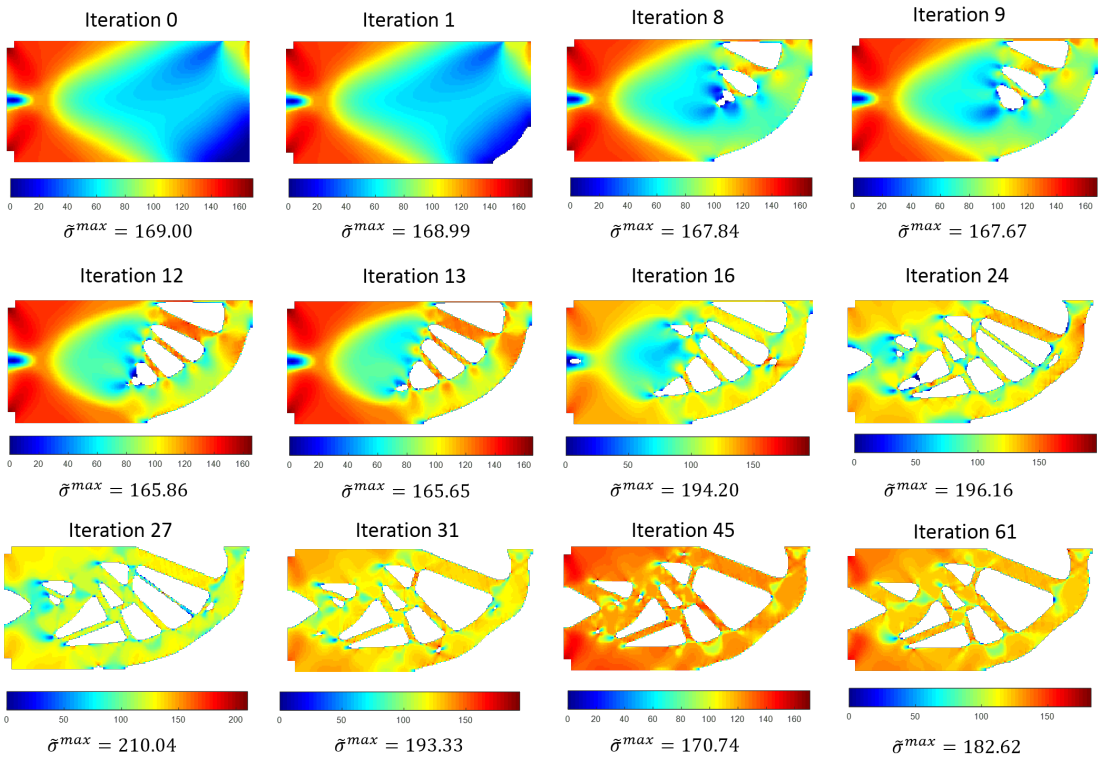

Figure 6.18: The topological evolution with von Mises stress distribution plot of the modified domain of ECM design

the optimal design viewed from a mechanical perspective may be not consistent with that from a manufacturable point of view. A design with some tiny voids may achieve a more desirable structural response but cannot converge due to the fluctuation of elements surrounding the marginal holes, which is also less practical in realistic manufacturing and application.

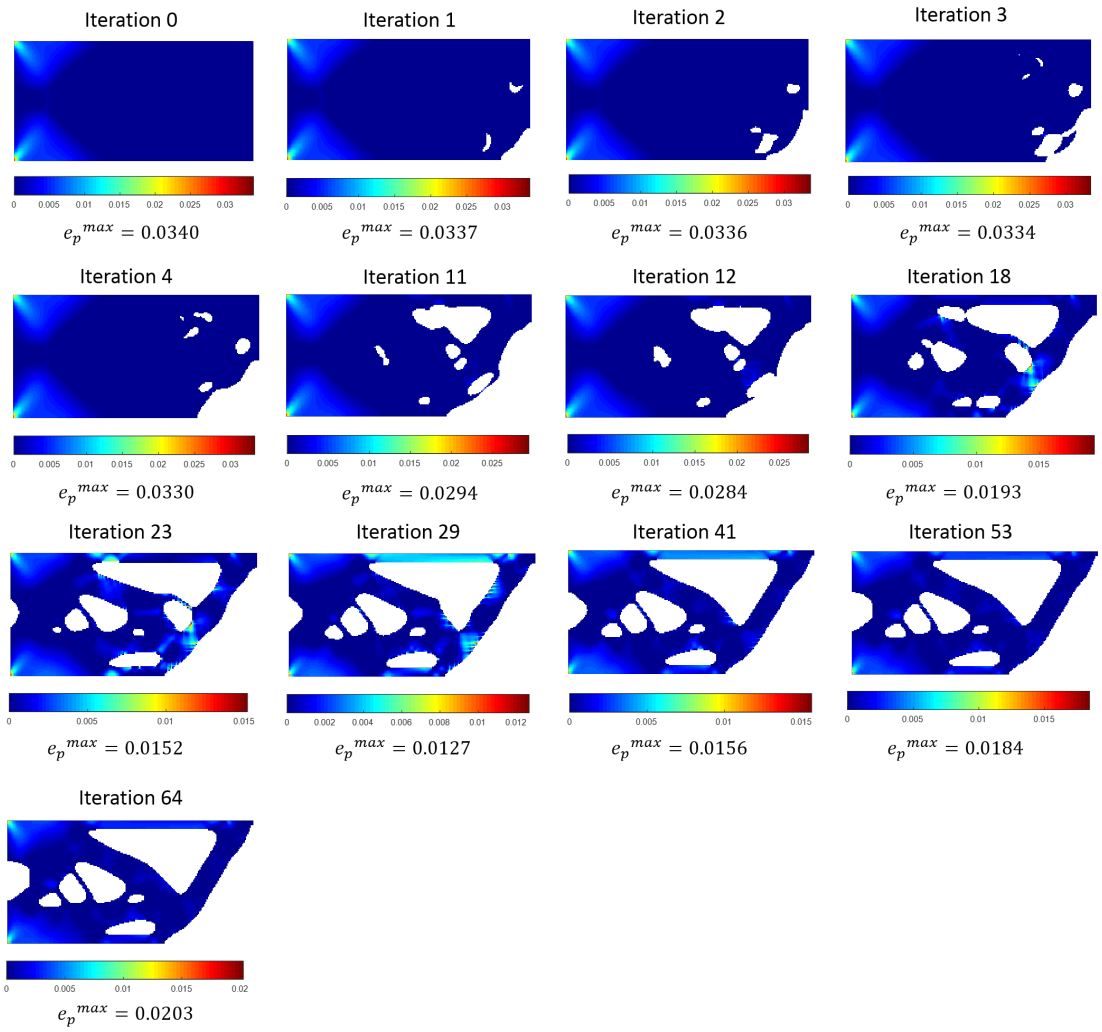

Figure 6.19: The topological evolution with equivalent plastic strain distribution plot of full domain of EPSM design

Regarding to the EPSM design of this case, whose topology at the initial state (iteration 0) is same to the ECM design, however, the void grows mainly from the right bottom, which is unlike the ECM design whose internal void appears

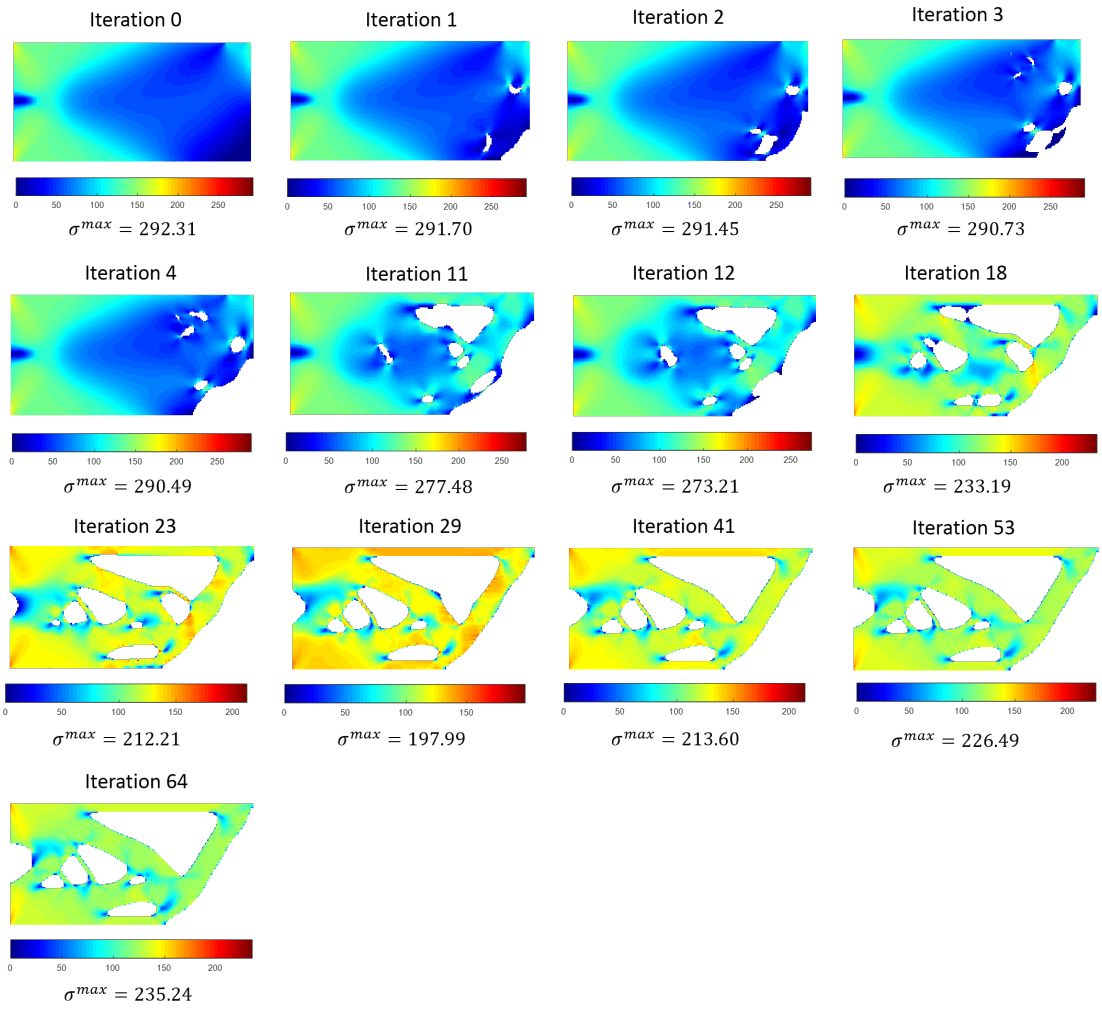

Figure 6.20: The topological evolution with von Mises stress distribution plot of full domain of EPSM design

and is developed from the right top. Also, it can be observed that the topology after the volume constraint has been satisfied (iteration 29) is similar and it took around 30 iterations to obtain a converged result.

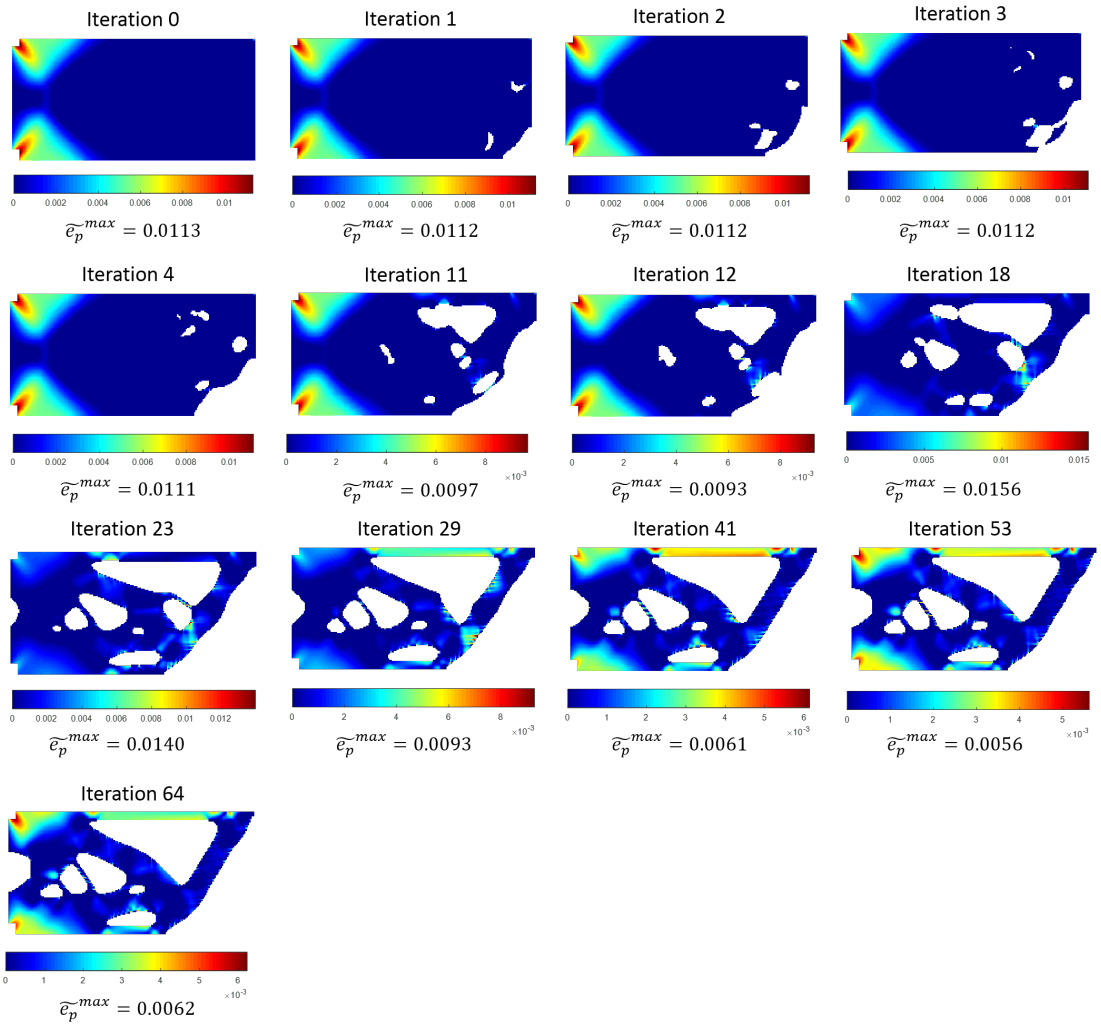

Figure 6.21: The topological evolution with equivalent plastic strain distribution plot of the modified domain of EPSM design

From Fig.6.21 and Fig.6.22, it can be seen that along the result converging procedure, $\tilde{e_p}^{max}$ and $\tilde{\sigma}^{max}$ reduce from 0.0093mm and 164.38MPa (iteration 29) to 0.0056mm and 152.76MPa (iteration 53), and they both rebound slightly at the converged phase (iteration 64) to 0.0062mm and 154.24MPa, respectively.

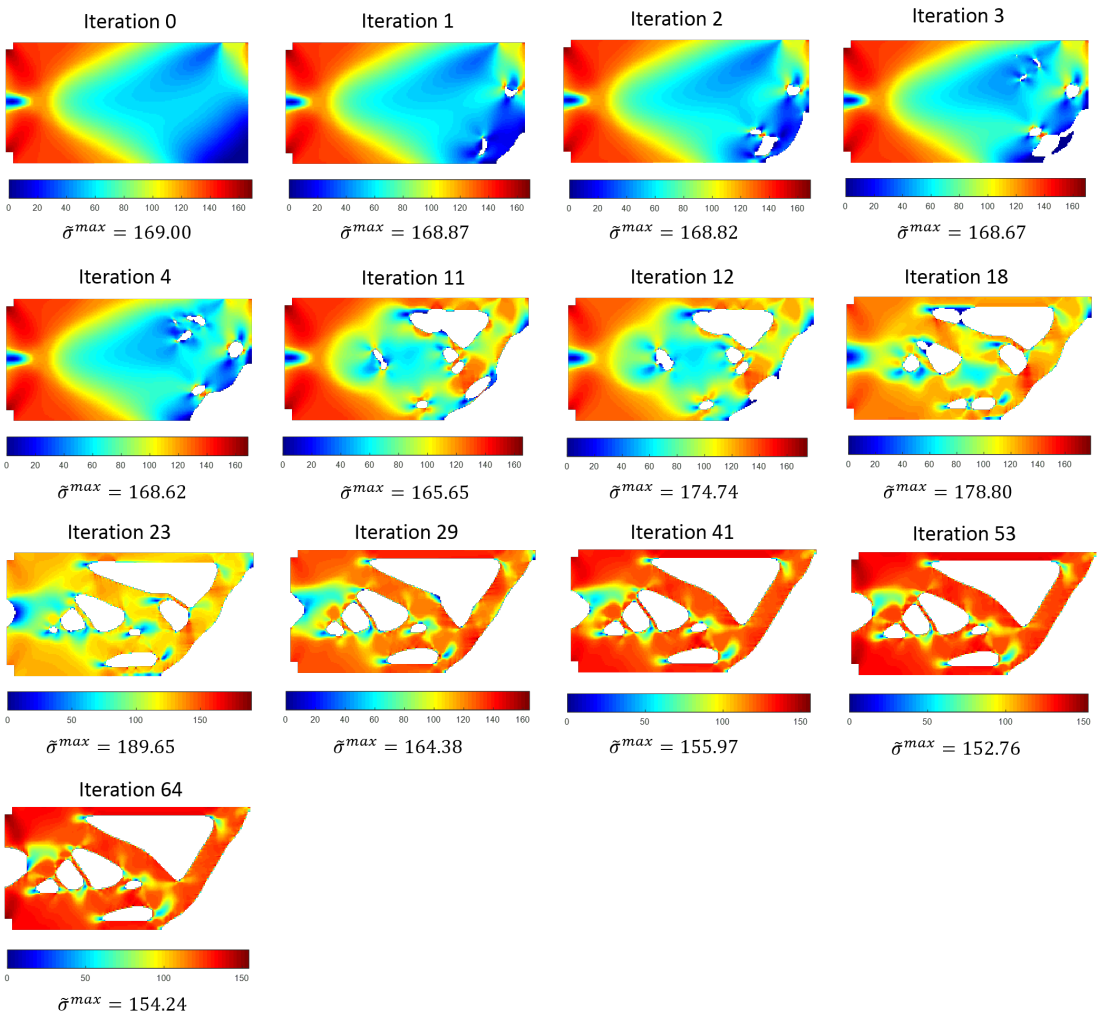

Figure 6.22: The topological evolution with von Mises stress distribution plot of the modified domain of EPSM design

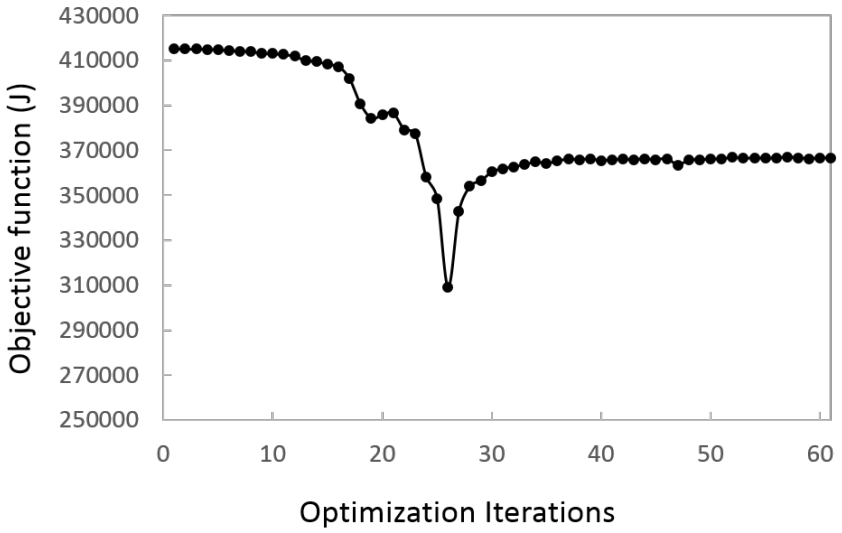

Figure 6.23: Plot of objective functions and iterations of ECM design of Case 2

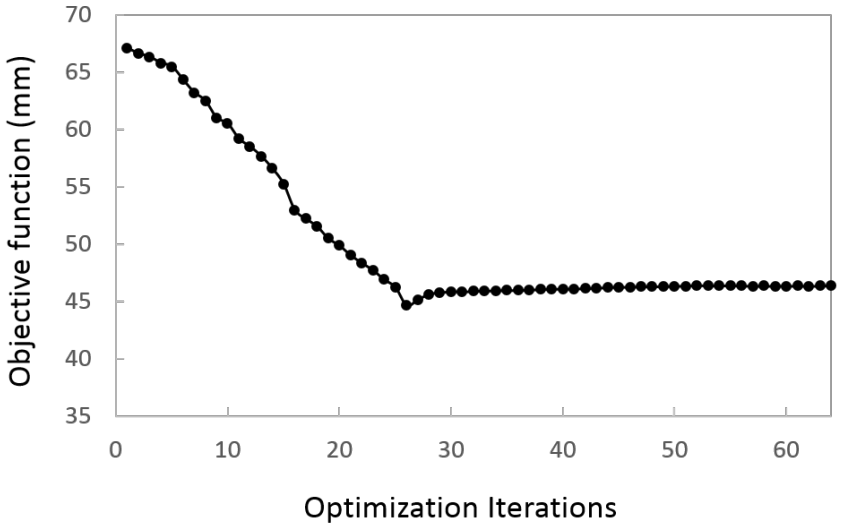

Figure 6.24: Plot of objective functions and iterations of EPSM design of Case 2

6.7 Conclusion and discussion

This study developed a topology optimization method taking into account the material elastoplasticity. And minimizing plastic deformation of a structure is set up as the optimization objective by a global function of accumulating all the equivalent plastic strain of every material (Guass) points. Also, the detailed sensitivity analysis with respect to design variables of the objective function has been presented and derived. A damping system is proposed for all sensitivity numbers, due to plastic strain only appears at partial regions of structure and high sensitivity of local plastic strain to topology changes. This helps to stabilize the evolutionary optimization procedure. Benchmark tests on a cantilever beam design under two cases of loading condition are conducted and compared to the results obtained from elastic stiffness design and elastoplastic stiffness (EPSM) design, have validated the robustness and effectiveness of the proposed plastic strain-based optimization method.

It can be concluded that there are distinct differences in the resulting topologies of three designs, which start to exhibit from the initial topological evolution. Comparing to the results from ECM design, EPSM design has more material moving to the clamped end and their maximum von Mises stress and equivalent plastic strain are the lowest. Also, EPSM design efficiently distribute more material surrounding the highly plastified regions during the optimization process and resulting in a smoother and more evenly distributed stress and plastic strain field.

From the plots of von Mises and equivalent plastic strain distribution at some specified iteration, it can be observed that e_p^{max}, σ^{max}, $\tilde{e_p}^{max}$ and $\tilde{\sigma}^{max}$ reduce gradually along the topological evolution process but are significantly effected by the appearance of thin branches or redundant elements. Furthermore, after the target volume is satisfied, the structure would adjust itself to have the best mechanical response. Without considering the interference from singular area, their maximum equivalent plastic and stress ($\tilde{e_p}^{max}$ and $\tilde{\sigma}^{max}$) develop to the lowest, while they may rebound slightly at the converged phase. This presents that the design may be deteriorated from a mechanical point of view when satisfying the convergence criterion. However, the converged topology is much smoother and

more practical in the real-world design so that the small rebound can be negligible.

7

Conclusion

This chapter summarizes the results obtained from each research aspect and remarks the contribution to applying topology optimization method to nonlinear structural design. Also, future works related to this thesis are discussed in Section 7.2.

7.1 Summary of results

The aim of this research thesis Topology optimization of Elastoplastic Structures is to develop the application of optimization technique to the design of composite structure or structure with D-regions, while considering their material elastoplasticity. Topology optimization technique has been successfully used to elastic structure to obtain a strut-and-tie model (STM), but to date limited further applications applied to nonlinear structural design. For this reason, the author decided to explore further applications, with the aim of describing the suitability of topology optimization approach for further development.

This thesis first uses an evolutionary optimization technique (BESO) to optimize the reinforcement layout within concrete. Though the concrete is still modelled elastic, its asymmetric property in tension and compression has been considered by developing a modified design variable update scheme. In the second stage, the applications to composite structure with various yielding and post yielding behaviours are undertaken, which highlights the importance of considering material ealstoplasticity of each phase in the optimization design. Further-

more, the research study at the third stage presents that evolutionary optimization technique is well suited to optimizing elastoplastic structures after solving its difficulty in convergence and topological instability by applying a transient coupled nonliear system. Finally, the topology optimization method is developed with the objective of minimizing plastic strain for elastoplastic structure. In comparison with results obtained from elastic design and stiffness-based nonliear design, the resulting topology successfully distribute material more efficiently to produce more evenly plastic strain and stress distribution.

The main aim of the thesis has been reached through four aspects of research. The main results and key contribution of each aspect are hereby presented.

Aspect 1: Optimized design of steel layout in RC structure (Chapter 3 of the thesis)
This study modified the conventional BESO approach to optimize both location and orientation of discrete steel bars within the concrete domain. The steel are modelled by truss elements, while the concrete are modelled by continuum elements. Also, the reinforcing bar can be formed freely in any arbitrary orientation. Although the direction of vertical, horizontal and diagonal are considered in this study, the proposed scheme can be extended for a wide range of orientation. Moreover, the nearly equal capacity in tension and compression for steel and the asymmetric property for concrete are both taken into account. As can be concluded from results of two numerical examples, the proposed method can successfully provide designers a valuable suggestion for steel distribution in terms of both orientation and topology, as well as under a realistic amount of steel can be used, which is more approachable to practical design.

The main contributions of this approach can be summarized as follows:

1. In comparison with continuum optimization method, it solves the two distinct scale problem.

2. In comparison with truss optimization method or truss-continuum optimization method, it gets rid of the ground structure theory by distributing truss without being influenced by the initial predefined layout.

Limitations:

1. The type of reinforcing bar is restricted by the nature of evolutionary optimization method (BESO) with design variable of either equalling to "0" or "1". For example, in some high stress concentrating areas, this method would produce two layers of reinforcing bar with same cross-sectional area, however, one layer of reinforcement with larger bar diameter may be preferred to be adopted in the practical design.

Aspect 2: Using continuous density-based optimization method for nonlinear composite structure (Chapter 4 of the thesis)
This study proposed an optimization framework for multiphase elastoplastic structure where each phase can be associated with various yield criterion and hardening model. The investigation of the influence of plastic model on the resulting topology is conducted, which greatly agree with the predicted results from an engineering perspective. And the influence of hardening model on the resulting topology is firstly studied. In single-phase optimization design case, when material employs different hardening rule, the obtained topologies are similar, which presents the effect of post yielding behaviour can be negligible. While it is interesting to observe that there is an obvious distinction in the results for multiphase optimization design case.

The main contributions of this study can be highlighted as follows:

1. Interpolation functions are created to interpolate different plasticity model and hardening rules that are adopted by each material phase into the optimization algorithm.

2. The path-dependent adjoint sensitivity analysis based on the proposed optimization framework is expressed and derived.

3. In-depth analysis to the numerical results emphasizes the importance of considering material nonliearity precisely during the optimization design, especially for multi-phase composite structure.

Limitations:

1. This method is limited to apply to multi-phase (more than two) material optimization. However, it can be extended to solve multi-phase optimization problem by setting up more design variables.

2. In this method, for two-phase structure with different elastoplastic behaviour, a common parameter involved in the function representing the material plasticity of each phase is required to set up the material interpolation function. When there is nothing in common in those functions, the material interpolation function cannot be obtained straightaway.

Aspect 3: Using discrete density-based optimization method for nonlinear structure (Chapter 5 of the thesis)
In this BESO design for elastoplastic structure, I applied the transit coupled nonlinear system for sensitivity analysis rather than the simplified approach where the non-differentiability arising from the elastic-plastic state transition is not considered. The goal is to investigate the performance of the suggested method of sensitivity analysis applied into evolutionary framework. it is shown that the converged results can be obtained within 30 to 60 iterations. Also, the proposed BESO framework is tested under various prescribed displacement loading cases: elastic, elastic-dominated, plastic-dominated and full plastic design. It is interesting to find that the total iterations needed for convergence is independent on the design state, which was expected to have more iterations for plastic design. Additionally, it can be observed that each state level of design may not necessarily have remarkable difference in topology. The structural behaviour could be improved by adjusting the material distribution slightly.

The main contributions of this study can be summarized as follows:

1. When using BESO method for elastoplastic material design, the transit coupled nonlinear system is initially applied to calculate sensitivity numbers.

2. In comparison with the results obtained from previous works of using conventional approximated sensitivity analysis in BESO design, stable evolutionary procedure and converged results are achieved without applying additional stabilizing scheme.

Limitations:

1. More complicated cases such as under multiple loading condition need to be carried out to check the convergence of results and topological stability of applying the transient coupled nonliear scheme to calculate sensitivity numbers.

Aspect 4: Plastic strain-based topology optimization for nonlinear structure (Chapter 6 of the thesis)
Among the limited works concentrating on nonlinear optimization design, this is the first study aiming to minimize plastic deformation as the optimization objective. The encountered challenges, e.g., local nature of plastic strain, 'singular' phenomenon and highly sensitivity to design state during the incremental loading analysis, are naturally avoided and solved by using discrete topology optimization method (BESO), setting up an equivalent global function and proposing a damping scheme for sensitivity analysis.

The proposed approach is validated through two benchmark tests. I compared the results (topology, equivalent plastic strain, von Mises stress distribution) obtained from three types of design: elastic stiffness-based design, elastoplastic stiffness-based design, and elastoplastic plastic strain-based design. Numerical results show that the maximum plastic deformation is always lower and the von Mises stresses are more evenly distributed for elastoplastic structure optimized using plastic strain-based design rather than that using nonlinear stiffness based design.

The main contributions can be listed as follows:

1. A topology optimization method is proposed for plastic deformation minimization design.

2. Previous works stated the difference in results obtained from nonlinear optimization design and linear optimization design. This study demonstrates the significant influence of considering various structural variables (e.g. plastic strain, stress, compliance, etc.) as optimization purpose on the resulting topology for nonlinear optimization design.

Limitations:

1. Due to the limitation of BESO method that is restricted to have multiple constraints, other plastic variables or structural responses cannot be considered by defining as constraints in the optimization design.

7.2 Future works

Several ideas of potential study based on the outcomes achieved from this thesis are hereby presented.

Filtering study of using SIMP based optimization method for multiphase elastoplastic structural design

In the study presented in Chapter.4, an interesting phenomenon has been observed that the optimization design of multiphase nonlinear structure is difficult or may take hundreds of iterations to converge. This is mainly due to that some gray scale areas appear at the elements where it is not clear which material contributes more to the improvement of the objective function. Early studies proposed the filtering scheme to solve checkerboard pattern and mesh-dependency problem, and it is usually set up as 3 times of the size of the element. However, this is developed based on elastic material design. This constant filtering scheme also valid for plastic design of single material, which has been evaluated in this thesis, but do not work for two-phase composite structure. Although a gradual refinement method used in this study helps to achieve a distinct layout, more analytical work is needed in order to discover the initial filter radius, iterations of every refinement and their relation with the structural response.

A comparative study regarding to various sensitivity analysis method when using BESO method for elastoplastic structure optimization design

As known that the sensitivity analysis, as an important section in optimization procedure, significantly influence the accuracy of results and efficiency of convergence. In majority of previous studies, the variational adjoint method with some

simplifications assumed is implemented, while this study (Chapter 5) use an approach considering the consistency of the formulation with the path-dependent behaviour. And converged results are obtained within a limited number of iterations. However, it would be interesting to conduct a comparative study where different approaches for sensitivity analysis are applied to the same design problem to investigate the difference in resulting topology and computational cost.

Compliance and plastic strain-based topology optimization for elasto-plastic tructure

Study presented in Chapter.6 proposes a topology optimization method for plastic strain minimization design. However, due to the fact that evolutionary optimization method (e.g., BESO) are restricted to have multiple constraints, the end-compliance or the total energy absorption cannot be taken into account. Therefore, applying fraction ratio separately for the term of minimizing plastic deformation and the negative of the energy absorption capacity in the objective function can be developed. The ratio accounting the weight of each term can vary based on the design purpose. Then the results can be compared with the fully compliance-based design and fully plastic strain-based design.

References

[1] Peter W Christensen and Anders Klarbring. *An introduction to structural optimization*, **153**. Springer Science & Business Media, 2008. vi, 3, 4, 5

[2] Martin Philip Bendsøe and Noboru Kikuchi. **Generating optimal topologies in structural design using a homogenization method**. *Computer methods in applied mechanics and engineering*, **71**(2):197–224, 1988. vi, 6, 7

[3] Michael Yu Wang, Xiaoming Wang, and Dongming Guo. **A level set method for structural topology optimization**. *Computer methods in applied mechanics and engineering*, **192**(1):227–246, 2003. vi, 10, 89

[4] Nam-Ho Kim. *Introduction to nonlinear finite element analysis*. Springer Science & Business Media, 2014. vi, 15

[5] Joshua D Deaton and Ramana V Grandhi. **A survey of structural and multidisciplinary continuum topology optimization: post 2000**. *Structural and Multidisciplinary Optimization*, **49**(1):1–38, 2014. 5, 89

[6] Martin P Bendsøe and Ole Sigmund. **Topology optimization: theory, methods and applications. 2003**. 5, 6

[7] William S Dorn. **Automatic design of optimal structures**. *Journal de mecanique*, **3**:25–52, 1964. 6

[8] Martin P Bendsøe. **Optimal shape design as a material distribution problem**. *Structural and multidisciplinary optimization*, **1**(4):193–202, 1989. 8, 89

[9] George IN Rozvany, Ming Zhou, and Torben Birker. **Generalized shape optimization without homogenization**. *Structural and Multidisciplinary Optimization*, **4**(3):250–252, 1992. 8

[10] HP Mlejnek. **Some aspects of the genesis of structures**. *Structural and Multidisciplinary Optimization*, **5**(1):64–69, 1992. 8, 89

[11] Martin P Bendsøe and Ole Sigmund. **Material interpolation schemes in topology optimization**. *Archive of applied mechanics*, **69**(9):635–654, 1999. 8, 52

[12] Ole Sigmund and Kurt Maute. **Topology optimization approaches**. *Structural and Multidisciplinary Optimization*, **48**(6):1031–1055, 2013. 8, 116

[13] YM Xie and Grant P Steven. **Shape and layout optimization via an evolutionary procedure**. In *Proceedings of the international conference on computational engineering science*, 1992. 9

[14] Yi M Xie and Grant P Steven. **A simple evolutionary procedure for structural optimization**. *Computers & structures*, **49**(5):885–896, 1993. 9, 89

[15] OM Querin, GP Steven, and YM Xie. **Evolutionary structural optimisation using an additive algorithm**. *Finite Elements in Analysis and Design*, **34**(3):291–308, 2000. 9

[16] Virginia Young, Osvaldo M Querin, GP Steven, and YM Xie. **3D and multiple load case bi-directional evolutionary structural optimization (BESO)**. *Structural and Multidisciplinary Optimization*, **18**(2):183–192, 1999. 9

[17] X Huang and YM Xie. **Bi-directional evolutionary topology optimization of continuum structures with one or multiple materials**. *Computational Mechanics*, **43**(3):393–401, 2009. 9, 52, 89

[18] X Huang and YM Xie. **Convergent and mesh-independent solutions for the bi-directional evolutionary structural optimization method**. *Finite Elements in Analysis and Design*, **43**(14):1039–1049, 2007. 10, 41, 90, 102, 126, 127

[19] James A Sethian and Andreas Wiegmann. **Structural boundary design via level set and immersed interface methods**. *Journal of computational physics*, **163**(2):489–528, 2000. 10

[20] Grégoire Allaire, François Jouve, and Anca-Maria Toader. **A level-set method for shape optimization**. *Comptes Rendus Mathematique*, **334**(12):1125–1130, 2002. 10

[21] Grégoire Allaire, François Jouve, and Anca-Maria Toader. **Structural optimization using sensitivity analysis and a level-set method**. *Journal of computational physics*, **194**(1):363–393, 2004. 10, 89

[22] Jean-Louis Batoz and Gouri Dhatt. **Incremental displacement algorithms for nonlinear problems**. *International Journal for Numerical Methods in Engineering*, **14**(8):1262–1267, 1979. 20

[23] RS Narayanan. *Concise Eurocode 2: For the Design of Insitu Concrete Framed Buildings to BS EN 1992-1-1: 2004 and Its UK National Annex: 2005; a Cement and Concrete Industry Publication*. MPA, the Concrete Centre, 2006. 21

[24] Junji Kato, Hiroya Hoshiba, Shinsuke Takase, Kenjiro Terada, and Takashi Kyoya. **Analytical sensitivity in topology optimization for elastoplastic composites**. *Structural and Multidisciplinary Optimization*, **52**(3):507–526, 2015. 26, 27, 52, 89, 116

[25] Michael Bogomolny and Oded Amir. **Conceptual design of reinforced concrete structures using topology optimization with elastoplastic material modeling**. *International journal for numerical methods in engineering*, **90**(13):1578–1597, 2012. 26, 30, 52, 53, 63, 89, 117, 122

[26] Colby C Swan and Iku Kosaka. **Voigt-Reuss topology optimization for structures with nonlinear material behaviors**. *International Journal for Numerical Methods in Engineering*, **40**(20):3785–3814, 1997. 27, 52, 116

[27] K Maute, S Schwarz, and E Ramm. **Adaptive topology optimization of elastoplastic structures**. *Structural and Multidisciplinary Optimization*, **15**(2):81–91, 1998. 27, 52, 89, 116

[28] Xinyan Huang, YM Xie, and G Lu. **Topology optimization of energy-absorbing structures**. *International Journal of Crashworthiness*, **12**(6):663–675, 2007. 27, 116

[29] Liang Xia, Felix Fritzen, and Piotr Breitkopf. **Evolutionary topology optimization of elastoplastic structures**. *Structural and Multidisciplinary Optimization*, **55**(2):569–581, 2017. 27, 52, 90, 102, 103, 105, 116

[30] Jorg Schlaich and Kurt Schafer. **Design and detailing of structural concrete using strut-and-tie models**. *Structural Engineer*, **69**(6):113–125, 1991. 29

[31] Wilhelm Ritter. **Die bauweise hennebique (hennebiques construction method)**. 1899. 29

[32] Prabhat Kumar. **Optimal force transmission in reinforced concrete deep beams**. *Computers & Structures*, **8**(2):223–229, 1978. 30

[33] Fabio Biondini, Franco Bontempi, and PG Malerba. **Optimal strut-and-tie models in reinforced concrete structures**. *Computer Assisted Mechanics and Engineering Sciences*, **6**(3-4):280–293, 1999. 30

[34] Fabio Biondini, Franco Bontempi, and Pier Giorgio Malerba. **Stress path adapting strut-and-tie models in cracked and uncracked RC elements**. *Structural Engineering and Mechanics*, **12**(6):685, 2001. 30

[35] Mohamed A Ali and Richard N White. **Automatic generation of truss model for optimal design of reinforced concrete structures**. *Structural Journal*, **98**(4):431–442, 2001. 30

[36] Ricardo Perera and Javier Vique. **Strut-and-tie modelling of reinforced concrete beams using genetic algorithms optimization**. *Construction and Building Materials*, **23**(8):2914–2925, 2009. 30

[37] Oded Amir and Ole Sigmund. **Reinforcement layout design for concrete structures based on continuum damage and truss topology optimization**. *Structural and Multidisciplinary Optimization*, **47**(2):157–174, 2013. 30, 31, 38

[38] Qing Quan Liang, Yi Min Xie, and Grant P Steven. *Topology optimization of strut-and-tie models in reinforced concrete structures using an evolutionary procedure*. PhD thesis, American Concrete Institute, 2000. 30

[39] Qing Quan Liang, Yi Min Xie, and Grant P Steven. **Generating optimal strut-and-tie models in prestressed concrete beams by performance-based optimization**. *ACI Structural Journal*, **98**(2):226–232, 2001. 30

[40] Liang-Jenq Leu, Chang-Wei Huang, Chuin-Shan Chen, and Ying-Po Liao. **Strut-and-tie design methodology for three-dimensional reinforced concrete structures**. *Journal of structural engineering*, **132**(6):929–938, 2006. 30

[41] Hyo-Gyoung Kwak and Sang-Hoon Noh. **Determination of strut-and-tie models using evolutionary structural optimization**. *Engineering Structures*, **28**(10):1440–1449, 2006. 30

[42] Matteo Bruggi. **Generating strut-and-tie patterns for reinforced concrete structures using topology optimization**. *Computers & Structures*, **87**(23):1483–1495, 2009. 30, 52, 89

[43] Hong Guan. **Strut-and-tie model of deep beams with web openings-an optimization approach**. *Structural Engineering and Mechanics*, **19**(4):361–380, 2005. 30, 52, 89

[44] Zhi-Qi He and Zhao Liu. **Optimal three-dimensional strut-and-tie models for anchorage diaphragms in externally prestressed bridges**. *Engineering Structures*, **32**(8):2057–2064, 2010. 30

[45] Osvaldo Maximo Querin, Mariano Victoria, and Pascual Martí. **Topology optimization of truss-like continua with different material properties in tension and compression**. *Structural and Multidisciplinary Optimization*, **42**(1):25–32, 2010. 30, 52

[46] Mariano Victoria, Osvaldo M Querin, and Pascual Martí. **Generation of strut-and-tie models by topology design using different material properties in tension and compression**. *Structural and Multidisciplinary Optimization*, **44**(2):247–258, 2011. 30, 52

[47] Shutian Liu and Heting Qiao. **Topology optimization of continuum structures with different tensile and compressive properties in bridge layout design**. *Structural and Multidisciplinary Optimization*, **43**(3):369–380, 2011. 30, 52

[48] Yangjun Luo and Zhan Kang. **Topology optimization of continuum structures with Drucker–Prager yield stress constraints**. *Computers & Structures*, **90**:65–75, 2012. 30, 52, 53

[49] Yangjun Luo, Michael Yu Wang, Mingdong Zhou, and Zichen Deng. **Topology optimization of reinforced concrete structures considering control of shrinkage and strength failure**. *Computers & Structures*, **157**:31–41, 2015. 30, 52

[50] Cristopher D Moen and James K Guest. **Reinforced concrete analysis and design with truss topology optimization**. In *3rd fib international congress*, 2010. 31

[51] Andrew T Gaynor, James K Guest, and Cristopher D Moen. **Reinforced concrete force visualization and design using bilinear truss-continuum topology optimization**. *Journal of Structural Engineering*, **139**(4):607–618, 2012. 31

[52] Yang Yang, Cristopher D Moen, and James K Guest. **Three-dimensional force flow paths and reinforcement design in concrete via stress-dependent truss-continuum topology optimization**. *Journal of Engineering Mechanics*, **141**(1):04014106, 2014. 31

[53] Yang Yang, James Guest, and Cristopher Moen. **Optimizing Reinforcement Layout in Concrete Design Considering Constructability**. In *Convention and national bridge conference*, 2014. 31

[54] X Huang and YM Xie. **Evolutionary topology optimization of geometrically and materially nonlinear structures under prescribed—**. *Structural Engineering and Mechanics*, **34**(5):581–595, 2010. 32, 116

[55] David J Munk, Gareth A Vio, and Grant P Steven. **Topology and shape optimization methods using evolutionary algorithms: a review**. *Structural and Multidisciplinary Optimization*, **52**(3):613–631, 2015. 32

[56] Hyo-Gyoung Kwak and Filip C Filippou. *Finite element analysis of reinforced concrete structures under monotonic loads*. Department of Civil Engineering, University of California Berkeley, CA, 1990. 33

[57] Matteo Bruggi. **On the automatic generation of strut and tie patterns under multiple load cases with application to the aseismic design of concrete structures**. *Advances in Structural Engineering*, **13**(6):1167–1181, 2010. 52, 89

[58] K Yuge and Noboru Kikuchi. **Optimization of a frame structure subjected to a plastic deformation**. *Structural and Multidisciplinary Optimization*, **10**(3):197–208, 1995. 52

[59] Stefan Schwarz, Kurt Maute, and Ekkehard Ramm. **Topology and shape optimization for elastoplastic structural response**. *Computer Methods in Applied Mechanics and Engineering*, **190**(15):2135–2155, 2001. 52, 89

[60] Gil Ho Yoon and Yoon Young Kim. **Topology optimization of material-nonlinear continuum structures by the element connectivity parameterization**. *International journal for numerical methods in engineering*, **69**(10):2196–2218, 2007. 52

[61] Mathias Wallin, Viktor Jönsson, and Eric Wingren. **Topology optimization based on finite strain plasticity**. *Structural and multidisciplinary optimization*, **54**(4):783–793, 2016. 52, 89

[62] Guodong Zhang, Lei Li, and Kapil Khandelwal. **Topology optimization of structures with anisotropic plastic materials using enhanced assumed strain elements**. *Structural and Multidisciplinary Optimization*, **55**(6):1965–1988, 2017. 52, 117

[63] Lei Li, Guodong Zhang, and Kapil Khandelwal. **Design of energy dissipating elastoplastic structures under cyclic loads using topology optimization**. *Structural and Multidisciplinary Optimization*, **56**(2):391–412, 2017. 52, 89, 117

[64] PB Nakshatrala and DA Tortorelli. **Topology optimization for effective energy propagation in rate-independent elastoplastic material systems**. *Computer Methods in Applied Mechanics and Engineering*, **295**:305–326, 2015. 52

[65] Panagiotis Michaleris, Daniel A Tortorelli, and Creto A Vidal. **Tangent operators and design sensitivity formulations for transient non-linear coupled problems with applications to elastoplasticity**. *International Journal for Numerical Methods in Engineering*, **37**(14):2471–2499, 1994. 54, 91, 123

[66] Krister Svanberg. **The method of moving asymptotes—a new method for structural optimization**. *International journal for numerical methods in engineering*, **24**(2):359–373, 1987. 54

[67] M Zhou and GIN Rozvany. **The COC algorithm, Part II: Topological, geometrical and generalized shape optimization**. *Computer Methods in Applied Mechanics and Engineering*, **89**(1-3):309–336, 1991. 89

[68] Anders Klarbring and Niclas Strömberg. **Topology optimization of hyperelastic bodies including non-zero prescribed displacements**. *Structural and Multidisciplinary Optimization*, **47**(1):37–48, 2013. 89

[69] Esben Lindgaard and Jonas Dahl. **On compliance and buckling objective functions in topology optimization of snap-through problems**. *Structural and Multidisciplinary Optimization*, **47**(3):409–421, 2013. 89

[70] Ravi Kiran, Lei Li, and Kapil Khandelwal. **Performance of cubic convergent methods for implementing nonlinear constitutive models**. *Computers & Structures*, **156**:83–100, 2015. 89

[71] X Huang and YM Xie. **Topology optimization of nonlinear structures under displacement loading**. *Engineering structures*, **30**(7):2057–2068, 2008. 90, 102

[72] Felix Fritzen, Liang Xia, Matthias Leuschner, and Piotr Breitkopf. **Topology optimization of multiscale elastoviscoplastic structures**. *International Journal for Numerical Methods in Engineering*, **106**(6):430–453, 2016. 90, 102

[73] Liang Xia and Piotr Breitkopf. **Recent advances on topology optimization of multiscale nonlinear structures**. *Archives of Computational Methods in Engineering*, **24**(2):227–249, 2017. 90

[74] Juan C Simo and Robert Leroy Taylor. **Consistent tangent operators for rate-independent elastoplasticity**. *Computer methods in applied mechanics and engineering*, **48**(1):101–118, 1985. 95

[75] Oded Amir, Mathias Stolpe, and Ole Sigmund. **Efficient reanalysis procedures in structural topology optimization**. 2011. 98

[76] Ole Sigmund. **A 99 line topology optimization code written in Matlab**. *Structural and multidisciplinary optimization*, **21**(2):120–127, 2001. 102, 127

[77] Thomas Buhl, Claus BW Pedersen, and Ole Sigmund. **Stiffness design of geometrically nonlinear structures using topology optimization**. *Structural and Multidisciplinary Optimization*, **19**(2):93–104, 2000. 116

[78] Chau Le, Julian Norato, Tyler Bruns, Christopher Ha, and Daniel Tortorelli. **Stress-based topology optimization for continua**. *Structural and Multidisciplinary Optimization*, **41**(4):605–620, 2010. 117

[79] Liang Xia, Li Zhang, Qi Xia, and Tielin Shi. **Stress-based topology optimization using bi-directional evolutionary structural optimization method**. *Computer Methods in Applied Mechanics and Engineering*, **333**:356–370, 2018. 117

[80] Pierre Duysinx and Martin P Bendsøe. **Topology optimization of continuum structures with local stress constraints**. *International journal for numerical methods in engineering*, **43**(8):1453–1478, 1998. 117

[81] Matteo Bruggi. **On an alternative approach to stress constraints relaxation in topology optimization**. *Structural and multidisciplinary optimization*, **36**(2):125–141, 2008. 117

[82] Matteo Bruggi and Pierre Duysinx. **Topology optimization for minimum weight with compliance and stress constraints**. *Structural and Multidisciplinary Optimization*, **46**(3):369–384, 2012. 117

[83] RJ Yang and CJ Chen. **Stress-based topology optimization**. *Structural optimization*, **12**(2-3):98–105, 1996. 117

Declaration

I herewith declare that I have produced this paper without the prohibited assistance of third parties and without making use of aids other than those specified; notions taken over directly or indirectly from other sources have been identified as such. This work has not been submitted, in whole or in part, in any previous application for a degree.

Edinburgh, September 2018

Mengxiao LI